

**A New Tool for Ultra-Trace Analysis
of Radionuclides**

–

**Setup, Optimization and Characterization
of the Resonant Laser-SNMS System
for IRS Hannover**

Von der

Fakultät für Mathematik und Physik

der Gottfried Wilhelm Leibniz Universität Hannover zur Erlangung des Grades

Doktor der Naturwissenschaften

Dr. rer. nat.

genehmigte Dissertation von

Dipl.-Phys. Michael Franzmann

Erscheinungs- bzw. Druckjahr

2018

Referent: Prof. Dr. Clemens Walther,
Leibniz Universität Hannover
Korreferent: Prof. Dr. Klaus Wendt,
Johannes-Gutenberg Universität Mainz
Tag der Promotion: 20.04.2018

ABSTRACT

Geochemical behavior and transport mechanisms of anthropogenic radionuclides in natural systems are of major importance to evaluate their distribution at contaminated areas and storage sites and for reliable estimation and reduction of radiation hazards for affected, inhabited areas. The research project SIRIUS focuses on the influence of the formation of radionuclide containing nanoparticles and sorption processes of radionuclides in different geological formations. The analysis of composition, spatial distribution and localization of hot particles, sorption and migration processes of trace amounts of radionuclides requires an excellent suppression of organic matrix material and isobaric contamination in combination with high spatial resolution while maintaining the natural structure of the sample. The new resonant Laser-SNMS system at the Institute for Radioecology and Radiation Protection (IRS) in Hannover was developed to meet those demands by an extension of the non-destructive spatially resolved analysis of a static TOF-SIMS with the high element selectivity of resonant laser ionization. This system was planned based on a test installation at the Institute for Nuclear Chemistry of the University Mainz.

The herein presented PhD project comprises the development and installation of a dedicated Ti:sapphire laser system and the adaption, optimization and full characterization of the Laser-SNMS system as well as the first analytical measurements.

The Ti:sapphire laser system was modified in collaboration with the LARISSA group at the Institute of Physics in Mainz to fulfill all requirements for laser post-ionization of a sputtered neutral particle cloud. Besides mechanical modifications of the conventional TOFSIMS 5 by IONTOF to provide access for the focused laser beams, the operational parameters of the TOF mass analyzer required an optimization for Laser-SNMS application. The complexity of the strongly correlated operational parameters necessitated a simulation-based approach, that included the simulation of the sputtered neutral particle cloud, the complete mass analyzer geometry and the resulting ion trajectories of the laser ions through the mass spectrometer. The results of this optimization lead to a gain of Laser-SNMS ion signal and improve the measurement conditions as demonstrated during several tests with uranium, plutonium and technetium samples. The characterization measurements of synthetic samples create a solid basis for future radioanalytical tasks and enabled determination of the influence of laser ionization and of the sensitivity achievable for ultra-trace analysis. The Laser-SNMS mass spectra of synthetic uranium, plutonium and technetium samples demonstrated the expected gain for the signal-to-background ratio in comparison to conventional SIMS. First analytical measurements verify the sufficient suppression of interfering elements and molecular constituents in the sample and prove the applicability of resonant Laser-SNMS on environmental samples. Furthermore, with the ability to record the starting location of every detected resonant laser ion, it was possible to create isotope selective images of hot particles in environmental sample material.

ZUSAMMENFASSUNG

Geochemische Eigenschaften und Transportmechanismen anthropogener Radionuklide in natürlichen Systemen sind von hoher Bedeutung, um deren Verteilung auf kontaminierten Gebieten und Lagerstätten zu ermitteln und um die Strahlungsgefährdung für betroffene, bewohnte Regionen abzuschätzen und zu reduzieren. Das Forschungsprojekt SIRIUS konzentriert sich dabei auf den Einfluss der Entstehung von radionuklidbelasteten Nanopartikeln und auf Sorptionsprozesse von Radionukliden in verschiedenen geologischen Strukturen. Für die Analyse von Zusammensetzung, räumlicher Verteilung und Lokalisierung solcher Nanopartikel, sowie von Sorptions- und Migrationsprozessen geringster Mengen der Radionuklide wird eine herausragende Unterdrückung des organischen Matrixmaterials und isobarer Kontaminationen in Kombination mit hoher Ortsauflösung benötigt, wobei der natürliche Aufbau der Probe erhalten bleiben soll. Das neue System für resonante Laser-SNMS wurde am Institut für Radioökologie und Strahlenschutz (IRS) in Hannover entwickelt um diese Anforderungen zu erfüllen. Dafür wurde die zerstörungsfreie, orts aufgelöste Analyse einer statischen TOF-SIMS um die hohe Elementselektivität der resonanten Laserionisation ergänzt. Die Entwicklung dieses Systems basiert auf einem Testaufbau am Institut für Kernchemie der Universität Mainz.

Das hierin präsentierte Promotionsprojekt umfasst die Entwicklung und den Aufbau eines spezialisierten Ti:Sa-Lasersystems, die Anpassung, Optimierung und komplette Charakterisierung des Laser-SNMS-Systems sowie erste analytische Messungen.

Das Ti:Sa-Lasersystem wurde in Zusammenarbeit mit der LARISSA-Gruppe des Instituts für Physik in Mainz modifiziert, um alle Anforderung der Lasernachionisation einer abgesputterten Neutralteilchenwolke zu erfüllen. Neben mechanischen Umbauten an der konventionellen TOFSIMS 5 der Firma IONTOF zur Einkopplung der fokussierten Laser mussten die Betriebsparameter des Flugzeitmassenspektrometers für den Laser-SNMS-Betrieb optimiert werden. Die Komplexität der stark korrelierten Betriebsparameter erforderte ein simulationsbasiertes Vorgehen, welches die Simulation der abgesputterten Neutralteilchenwolke, der kompletten Geometrie des Flugzeitmassenspektrometers und der resultierenden Trajektorien der Laserionen durch das Spektrometer beinhaltet. Die Ergebnisse dieser Optimierung führen zur Steigerung des Laser-SNMS-Ionensignals und verbessern die Messbedingungen was anhand mehrerer Tests an Uran-, Plutonium- und Technetiumproben gezeigt wurde. Die Charakterisierungsmessungen an künstlichen Proben stellen eine solide Basis für zukünftige, radioanalytische Anwendungen dar und ermöglichten es den Einfluss der Laserionisation und die erreichbare Sensitivität für die Ultraspurenanalyse zu bestimmen. Die mittels Laser-SNMS aufgenommenen Massenspektren von künstlichen Uran-, Plutonium- und Technetiumproben zeigten die erwartete Steigerung des Signal-zu-Untergrund-Verhältnisses gegenüber der konventionellen SIMS-Analyse. Erste analytische Messungen belegen die ausreichende Unterdrückung störender Elemente und molekularer Bestandteile der Proben und bestätigen die Eignung von Laser-SNMS zur Ultraspurenanalyse an Umweltproben. Die zugeordnete Startposition jedes detektierten, resonant angeregten Laserion ermög-

licht es darüber hinaus isotopenselektive Bilder von Partikeln mit Radionuklidgehalten in Umweltproben zu erstellen.

KEYWORDS

Laser-SNMS

Resonant laser ionization

Ultra-trace analysis

CONTENTS

1	Introduction	1
2	Theoretical Background	5
2.1	Sputtering by Ion Bombardment	5
2.1.1	Interaction of ions with condensed matter	5
2.1.2	Distributions of sputtered particles	7
2.2	Laser Ionization	9
2.2.1	Atom-light interaction	9
2.2.2	Laser	10
2.2.3	Non-resonant laser ionization	12
2.2.4	Resonant laser ionization on atoms	13
2.3	Mass Spectrometry	15
2.3.1	Ion sources and methods for mass separation	15
2.3.2	RIMS, SIMS and Laser-SNMS	18
3	Experimental Setup	21
3.1	Ti:sapphire Laser System	21
3.1.1	IRS Ti:sapphire laser	23
3.1.2	Complete laser system for resonance ionization	25
3.2	TOF-SIMS	29
3.2.1	Components	29
3.2.2	Analysis methods and programs	32
3.3	Combined Laser-SNMS System	34
3.3.1	Beam transport, coupling and monitoring	34
3.3.2	Synchronization of all pulsed processes	37
4	Simulation Based Optimization	45
4.1	Simulated Sputtered Particle Cloud	45
4.1.1	Simulation program "Ionengenerator"	46
4.1.2	Expansion behavior and overlap	48
4.2	Mass Analyzer Simulation Model	51
4.3	Optimization Procedure	52
4.3.1	Optimization program	53
4.3.2	Correlation analysis	53
4.4	Verification of Optimized Parameters	56
5	Characterization with Radionuclides	59
5.1	Uranium	60
5.1.1	Characteristic spectrum, laser influence and saturation behavior	61
5.1.2	Decision threshold and efficiency	63

5.2	Plutonium	68
5.2.1	Characteristic spectrum, laser influence and saturation behavior . . .	69
5.2.2	Decision threshold	70
5.3	Technetium	72
5.3.1	Characteristic spectrum, laser influence and saturation behavior . . .	72
5.3.2	Decision threshold	74
5.4	Laser-SNMS in Comparison to Conventional SIMS	76
5.4.1	Ion signal	77
5.4.2	Signal-to-background ratio	77
5.4.3	Mass resolution	78
5.5	Influence of Argon Cluster Sputtering	79
6	Analytical Measurements	81
6.1	MOX Fuel Pellet	81
6.1.1	Verification of element selectivity	82
6.1.2	Influence of lasers and laser power	85
6.1.3	Sputtering behavior	86
6.1.4	Origin of oxides	87
6.2	Kabul Soil Sample	89
6.2.1	Analysis with SIMS and Laser-SNMS	89
6.2.2	Element selective ion images	91
7	Conclusion and Outlook	93
	Appendix	96
A	Photos of the Laser-SNMS Setup	97
A.1	Lasersystem	97
A.2	LabVIEW program interfaces	99
A.3	TOF-SIMS instrument	100
A.4	Beam transport, coupling and monitoring	102
A.5	Sample preparation	104
B	Graphs, Plots and Diagrams	107
B.1	Characterization of the IRS Ti:sapphire laser	107
B.2	Parameter scans	109
B.3	Sputter distributions and laser overlap	111
B.4	Simulation model	113
B.5	Optimization scans	114
B.6	Sputter cleaning	119
B.7	Laser saturation scans	120
B.8	Efficiency measurements	123
B.9	Comparison of Laser-SNMS and SIMS	124
B.10	Argon cluster sputtering	126
B.11	Analysis of a MOX fuel pellet	127
B.12	Analysis of a rock sample from Kabul	131
C	Isotope Shifts of the Applied Excitation Schemes	133

Bibliography	135
List of Publications	141
Curriculum Vitae	143
Acknowledgments	145

LIST OF FIGURES

2.1	Collision cascade in a solid sample	6
2.2	Theoretical Sigmund-Thompson energy distributions	8
2.3	Optical transitions between two discrete electronic states	10
2.4	Four-level laser scheme	11
2.5	Four-level scheme of a Ti:sapphire laser	12
2.6	SPI and REMPI schemes	13
2.7	Three-step excitation scheme	14
2.8	Scheme of a Time-of-Flight mass spectrometer	18
2.9	Selection by RIMS	19
2.10	Laser-SNMS ionization volume	20
3.1	Schematic design of the Ti:sapphire cavity	22
3.2	Photo of the IRS Ti:sapphire laser cavity	23
3.3	CAD scheme of the laser setup	25
3.4	Scheme of the wavelength stabilization system	26
3.5	Scheme of the laser timing control system	27
3.6	Photo of the intra cavity doubling	28
3.7	Photo of the IONTOF TOFSIMS 5	29
3.8	Photo of the sample region in the TOFSIMS 5	31
3.9	Scheme of the combined Laser-SNMS system	34
3.10	Spatial scan of the lasers in x-direction	35
3.11	Spatial scan of the lasers in y-direction	36
3.12	Scheme of the monitoring system	37
3.13	Influence of the extraction delay on the direct sputter ion signal	38
3.14	Shift of the primary ion beam position	39
3.15	Influence of the suppression potential on the sputter ion signal	40
3.16	Influence of the extraction delay on the laser ion signal and the residual background	41
3.17	Influence of the laser delay on the resonant and non-resonant laser ion signal	42
3.18	Relative temporal sequence of the pulsed processes for Laser-SNMS	43
4.1	GUI of the "Ionengenerator" software	47
4.2	Comparison of the theoretical and simulated energy distributions	47
4.3	3D representation of the expanded ion cloud from the simulation	48
4.4	Expansion behavior of the simulated cloud	49
4.5	Ionization yield for different beam heights	50
4.6	Overlap of the ionization lasers and the sputtered particle cloud	50
4.7	3D representation of the TOF mass analyzer	51
4.8	3D simulation model of the mass analyzer	52
4.9	Simulated ion trajectories through the mass analyzer	52

4.10	Scheme of the first part of the mass analyzer with relevant electrodes and test points	54
4.11	3D plot of the dependence of focus, transmission and efficiency	54
4.12	Scheme of the second part of the mass analyzer with relevant electrodes and test points	56
4.13	Comparison of two Laser-SNMS spectra of a synthetic ^{238}U sample for different parameter sets	56
5.1	Resonant 3-step excitation scheme for ^{238}U	60
5.2	Characteristic Laser-SNMS spectrum of the synthetic uranium sample	61
5.3	Influence of the three individual lasers	62
5.4	$^{238}\text{UO}_2$ -ion image of a U_3O_8 particle	64
5.5	Efficiency measurement of a U_3O_8 particle	65
5.6	Laser-SNMS mass spectrum of a 1ppb uranium sample	66
5.7	Resonant 3-step excitation scheme for ^{242}Pu	68
5.8	Characteristic Laser-SNMS spectrum of the synthetic plutonium sample	69
5.9	Influence of the three lasers	69
5.10	Laser-SNMS spectrum of the 10ppb plutonium sample	70
5.11	Resonant 3-step excitation scheme for ^{99}Tc	72
5.12	Characteristic Laser-SNMS spectrum of the synthetic technetium sample	73
5.13	Influence of the three lasers	73
5.14	Laser-SNMS spectrum of the 2ppb plutonium sample	74
5.15	Comparison of SIMS- and Laser-SNMS-spectra for a synthetic technetium sample	76
5.16	Development of uranium ion signals during continuous argon cluster sputtering	79
6.1	Comparison of the MOX mass spectra	83
6.2	Laser power influence on the non-resonant background of the MOX sample	85
6.3	Development of different ion signals during continuous argon cluster sputtering	86
6.4	Ion image comparison of atoms and oxides	87
6.5	Camera image of the sample surface	88
6.6	Comparison of the Kabul mass spectra	90
6.7	Ion image comparison of atoms and oxides	91
6.8	Camera image of the sample surface	92
A.1	Photo of the complete laser system	97
A.2	Photo of the pump laser setup	98
A.3	Photo of the Ti:sapphire laser setup	98
A.4	Screenshot of the GUI of the timing measurement program	99
A.5	Screenshot of the GUI of the wavelength stabilization program	99
A.6	Photo of the liquid metal ion gun (LMIG)	100
A.7	Photo of the dual source column (DSC)	100
A.8	Photo of the gas cluster ion beam (GCIB)	101
A.9	Photo of the time-of-flight mass analyzer	101
A.10	Photo of the modified TOF-SIMS instrument	102
A.11	Photo of the laser coupling and monitoring setup at the TOF-SIMS instrument	102
A.12	Photo of the laser monitoring setup behind the TOF-SIMS	103
A.13	Photo of the sample region seen by the front camera	103
A.14	Photo of the attenuated laser beam seen by the back camera	103
A.15	Photo of the heated sample holder	104
A.16	Photo of the prepared sample before analysis	104

A.17	Photo of the uranium particle containing silicon waver	105
B.1	Power of the IRS Ti:sapphire laser	107
B.2	Pulse width measurement of the IRS Ti:sapphire laser	108
B.3	Beam profile of the IRS Ti:sapphire laser	108
B.4	Influence of the extraction delay on the suppressed sputter ion signal	109
B.5	Influence of the extraction delay on the suppressed sputter ion signal	109
B.6	Influence of the extraction delay on the laser ion signal and the suppressed background	110
B.7	Monitoring of the laser and extraction pulse timing	110
B.8	Influence of the laser delay on the mass resolution of the resonant and non-resonant laser ion signal	111
B.9	Comparison of the theoretical and simulated angular distributions	111
B.10	Comparison of the measured and simulated temporal distribution	112
B.11	Ionization yield for different beam heights with focus of 400 μm	112
B.12	Ionization yield for different beam heights with focus of 500 μm	113
B.13	Differences between automatic and programmed model generation	113
B.14	3D plots of the parameter scans of the first three electrodes	114
B.15	Influence of the drift tube potential	115
B.16	3D plots of the second simulation run	115
B.17	Partial exponential correlation of extraction electrode and einzel lens	116
B.18	Determination of the most efficient extraction potential	116
B.19	3D plots of the final simulation run	117
B.20	Determination of the most efficient Y-deflection potential	117
B.21	Comparison of the Laser-SNMS spectra of a synthetic ^{99}Tc sample for different parameter sets	118
B.22	Comparison of the Laser-SNMS spectra of a synthetic MOX sample for different parameter sets	118
B.23	Ion signal variation during sputtered surface cleaning	119
B.24	Influence on the mass spectrum by sputtered surface cleaning	119
B.25	Saturation scan of the applied laser power for all three steps on ^{238}U	120
B.26	Saturation scan of the laser power for all three steps on ^{242}Pu	121
B.27	Saturation scan of the laser power for all three steps on ^{99}Tc	122
B.28	Efficiency test measurement with SIMS	123
B.29	Comparison of SIMS and Laser-SNMS spectra of a synthetic depleted uranium sample	124
B.30	Comparison of SIMS and Laser-SNMS spectra of a synthetic plutonium sample	125
B.31	Development of plutonium ion signals during continuous argon cluster sputtering	126
B.32	Development of technetium ion signals during continuous argon cluster sputtering	126
B.33	Comparison of the MOX mass spectra	127
B.34	Influence of the three lasers	128
B.35	Saturation scan of the laser power for all three steps on ^{239}Pu	128
B.36	Laser power influence on the non-resonant background of the MOX sample	129
B.37	Development of different ion signals during continuous argon cluster sputtering	129
B.38	Compared ion images of atoms and oxides with Laser-SNMS	130
B.39	Compared ion images of atoms and oxides with SIMS	130
B.40	Camera image of the sample surface	130
B.41	Photo of the sample collection in Kabul	131

B.42 Photo of the milled sample material 131
B.43 Comparison of the signal and background spectrum of the Kabul sample . . . 132

LIST OF TABLES

3.1	Required and tested specifications of the IRS Ti:sapphire laser	25
4.1	Comparison of conventional and optimized parameters for the TOF mass analyzer	55
4.2	Gain by optimized parameters for the TOF mass analyzer	57
5.1	Isotopic composition of the synthetic uranium sample	60
5.2	Saturation powers for resonant Laser-SNMS on ^{238}U	63
5.3	Composition and size of the synthetic uranium particles	64
5.4	Decision threshold based on efficiency measurements	65
5.5	Decision threshold based on the lowest measured quantity	67
5.6	Isotopic composition of the synthetic plutonium sample	68
5.7	Saturation powers for resonant Laser-SNMS on ^{242}Pu	70
5.8	Decision threshold based on the lowest measured quantity	71
5.9	Saturation powers for resonant Laser-SNMS on ^{99}Tc	74
5.10	Decision threshold based on the lowest measured quantity	75
5.11	Comparison of Laser-SNMS and conventional SIMS	78
6.1	Isotopic composition of the MOX sample	81
6.2	Isotope ratios of isobaric contaminations	82
6.3	Comparison of specified and measured isotope ratios of plutonium	84
6.4	Comparison of specified and approximated isotope ratios of uranium	84
6.5	Comparison of specified and measured mass ratios for different laser powers	86
C.1	Isotopic shift of the resonant transitions for uranium	133
C.2	Isotopic shift of the resonant transitions for plutonium	134

INTRODUCTION

Radioactivity is present on earth since its formation 4.5 billion years ago. The discovery of radioactive processes and the resulting radiation was made by Henri Becquerel in 1896 and confirmed by Marie and Pierre Curie in 1898 [1, 2]. Different modes of radioactive decay and the participating particles were identified in the following years and led to advanced theories about specific nuclear reactions and certain peculiarities. In 1939 the work of Hahn, Strassmann, Meitner and Frisch resulted in the discovery of nuclear fission [3, 4], a unique process of radioactive decay, that soon turned out to offer a broad range of applications in various fields. The understanding of neutron induced nuclear fission and the control of the neutrons emitted during the fission process of ^{235}U and ^{239}Pu led to the development of nuclear chain reactions, which are the basis of both, the peaceful use in nuclear reactors as well as the thread of nuclear weapons.

In most nuclear reactors a sustained, stabilized and controlled fission chain reaction of ^{235}U or ^{239}Pu produces a high amount of thermal energy, that is converted into electrical energy by an intense flux of a cooling medium, turbines and generators. In addition to the fission processes, the high neutron flux in nuclear reactors initiates further nuclear reactions, which cause the production of several radionuclides, that are non-existent in nature. Therefore, nuclear reactors are also applied for targeted production of specific radionuclides, which are required in scientific experiments or for medical therapies and diagnostics. A nuclear weapon instead uses a rapidly, under optimum conditions exponentially growing nuclear process chain of fission reactions for instantaneous creation of a huge amount of energy. The nuclear fuel of reactors as well as the material for nuclear weapons requires previous treatment and enrichment of fissionable isotopes. The purification and processing of large amounts of radioactive material to usable fuel as well as the reprocessing of spent nuclear fuel is performed in specialized facilities by different physical and chemical processes. All these individual processes and applications in the nuclear fuel cycle are subject to leakages and accidents and thus sources to release radionuclides in very low up to tremendously high concentrations into the environment.

More than 2000 nuclear weapon tests were conducted by seven countries from 1945 to 1998 and released huge amounts of radionuclides into the atmosphere, into the oceans and into different geological compartments and structures at and around the test sites [5]. Some of the nuclear test sites were analyzed afterwards for quantification and consequences of the released radioactive material [6, 7], others are still today classified and barely even known. Besides these weapon test remainders, large amounts of radionuclides were released into rivers and seas as nuclear waste from the production of weapon-grade nuclear material

during a variety of nuclear weapon development programs of the participating countries [8]. Further strong sources of radionuclides in the environment with anthropogenic origin are releases during several minor incidents as well as a few major catastrophes at nuclear facilities. The reactor accidents that occurred at Chernobyl 1986 and at Fukushima 2011 were the worst scenarios of nuclear power reactor disasters, due to the combination of nuclear meltdowns, hydrogen explosions and failures or even bursts of the reactor containment, that released high amounts of various radionuclides [9, 10]. On the other hand, releases from regular processes of nuclear industry like uranium mining, reprocessing of spent nuclear fuel and the long-term storage of nuclear waste are also major sources of hazardous and well detectable amounts of radionuclides in the environment.

The evaluation of radiation hazards from nuclear materials, that are released into the environment is complex. Risks of radionuclide exposition for human health are based on multiple influences on the human body distinguished by type, energy and absorbed dose of radiation as well as duration and way of the exposition, especially concerning either external contact or ingestion. If radionuclides are incorporated into the human body and possibly even embedded into organs, the health hazard of incidents for cancerous diseases increases drastically. Main candidates for this burden of human health are the radiotoxic isotopes ^{60}Co , ^{90}Sr , ^{99}Tc , ^{131}I , ^{134}Cs , ^{137}Cs , ^{238}Pu and ^{239}Pu , due to their half-life, prevalent occurrence and physiological behavior in the human body. The content of these isotopes in the breathing air is therefore constantly monitored all over the world, while lowest level concentrations in drinking water and in the food chain can only be analyzed for known contaminated sources or areas. This surveillance is limited by incomplete understanding of the transport mechanisms and geochemical behavior of the different radionuclides. The large diversity of geological and organic systems in the environment leads to multiple influencing processes that determine the speciation and migration, i.e. the binding or mobility of radionuclides. Besides decades of scientific investigation on these different transport mechanisms, there are still many not yet studied physical and chemical processes with major influence on the mobility of radionuclides.

The herein presented work focuses on the analysis of radionuclide nanoparticles. These colloidal systems result in highly different transport behavior and bioavailability of the radionuclides in comparison to molecular, ionic or complex species [11–13]. Therefore, the distribution and mobility of radionuclide nanoparticles in environmental ground water systems and the health effects caused by their ingestion are not covered by established standard models and require further research and fundamental data to extend models and improve predictions. Different radioecological analyses of known contaminated sites showed the major influence of colloid-based transport of plutonium, but also the complexity of tracking, identification and analysis of radionuclide nanoparticles [14, 15]. Due to several different formation processes including a variety of matrix materials, also information about size, physical shape and chemical composition of the nanoparticles is required. This prevents the application of conventional chemical separation techniques, that dissolve the sample material before separation as necessary preparation for the majority of standard analysis methods.

The renunciation of chemical separation led to the combined application of different techniques for separation from the surrounding bulk material, nanoparticle sampling, spatially resolved analysis, identification of elemental composition and chemical speciation as well as determination of isotope ratios. Localization of the radionuclide nanoparticle inside a large amount of sample material can be accomplished with different radiometric approaches depending on the sample material and the radioisotope of interest. Simple fixation and cut out

of identified sample areas as well as more complex techniques of micromanipulation allow the handling, separation and relocation of the radioactive particle for analysis. Alternative approaches use electron microscopy techniques like SEM and TEM for the spatial resolved analysis, X-ray spectrometry methods like EDX, μ -XRF and EXAFS for determination of the elemental composition and radiometric techniques for characterization of the radionuclides. The work presented in this thesis, is based on a mass spectrometric approach with the aim of a non-destructive analysis of radioisotope content in particles including chemical, elemental and isotopic composition with high spatial resolution in a single analytical instrument. The chosen technique, which allows the determination of the detailed characteristics of radionuclide nanoparticles, is a combination of secondary ion mass spectrometry and resonant laser ionization, known as resonant Laser-SNMS (secondary neutral mass spectrometry).

The standard technique of SIMS (secondary ion mass spectrometry) provides the required high spatial resolution for nanoparticle analysis of below 1 μm and is able to identify the major components including their chemical configuration. Nevertheless, the high amount of organic background, which can be expected from environmental samples, prevents the application of a conventional SIMS setup for highly sensitive ultra-trace determination of radionuclides. Different instruments based on dynamic SIMS are applied for the purpose of nuclear forensics at a limited number of specialized institutes [16]. The intense primary ion beam of dynamic SIMS consumes the radionuclide nanoparticle completely, which results in suitable sensitivity for detection and quantification of some predefined radioisotopes, but makes further application of other techniques and analyses of the elemental composition and matrix material interaction impossible. In addition, strong isobaric interferences by molecular constituents or neighboring elements are inevitable. Therefore, the focus of the herein presented PhD project was the upgrade of a static TOF-SIMS apparatus by the implementation of element selective resonant laser ionization. The goal of this development is the provision of highest sensitivity, complete suppression of isobaric interferences and an adaptability on different radioecological tasks and possible combination with further analytical techniques.

Following chapter 2, which gives the theoretical foundations on particle sputtering, laser ionization and mass spectrometry, the experimental setup and its development is described in detail in chapter 3. That includes all relevant components of the commercial TOF-SIMS, the adaption of the pulsed high power Ti:sapphire laser system, which was developed by the LARISSA group at the Johannes Gutenberg-Universität Mainz, and the merging of both systems at the Institute for Radioecology and Radiation Protection (IRS) at the Leibniz Universität Hannover. Parallel to the setup, the processes of particle sputtering and ion optical transport through the time-of-flight mass analyzer were simulated in detail for an optimization of the experimental parameters towards enhanced overall efficiency. Chapter 4 comprises these simulations with all applied models and programs, the results of the simulations and the comparison to the first characterizing Laser-SNMS measurements.

An experimental setup for reliable analytical studies requires precise characterization of instrumental performance under real measurement conditions. The characterization of the IRS Laser-SNMS system on the three elements of primary interest uranium, plutonium and technetium involves the properties of the different spectra, the decision thresholds as scale for the sensitivity as well as the study of various influences of the Ti:sapphire laser settings. Further parts of chapter 5 describe the direct comparison of conventional SIMS and resonant Laser-SNMS measurements and discuss the reduction of oxidized surfaces via argon cluster sputtering. The performance during first analytical applications of the new Laser-SNMS

system and their results are presented in chapter 6. The final chapter 7 summarizes all achievements of the development, optimization and characterization procedures of this new tool for radioecology and depicts its future applications while room is also given to further possible extensions of the technique.

THEORETICAL BACKGROUND

The analytical technique of resonant Laser-SNMS (secondary neutral mass spectrometry) consists of three consecutive processes. The first step is the sputtering by ion bombardment which detaches a small fraction of material from the sample surface. After suppression of initially sputtered ions, the neutral fraction of the sputtered sample material is element selectively ionized in the second process step which is the resonant laser ionization. The mass distribution of the generated ions is thereupon analyzed by a conventional mass spectrometer as third and final process of a resonant Laser-SNMS measurement. The following sections summarize the theoretical background of these three individual processes to create a base for the herein presented work.

2.1 Sputtering by Ion Bombardment

Sputtering describes the ablation of material from a solid surface by bombardment with energetic ions. Although this process is known for more than 100 years [17], the fundamental theory is still subject to new technical and scientific findings especially for high energy sputtering and complex sample compositions like organic material [18]. The ablation of atoms, molecules and clusters is only one of the apparent effects which are induced by ion bombardment. The collision of the impacting ions with a solid surface and the transferred kinetic energy causes several processes like backscattering or implantation, structural deformation of the surface layer, emission of electrons and photons and phononic or atomic excitation of both, the bulk as well as the sputtered material.

This sputter excitation, the resulting secondary ionization and the distributions of the sputtered material are of high relevance for the presented work and are therefore described in detail in the following section. A comprehensive description of the theory of sputtering is given in specialized literature [19–21] on which the following overview is based on.

2.1.1 Interaction of ions with condensed matter

The kinetic energy of an ion dissipates during impact and penetration through the surface layers of a solid target by collisions. These collisions between the impacting ion and atoms of the solid surface can initiate secondary and higher order collisions with further atoms and in this way create a collision cascade, as shown in Fig. 2.1. The resulting processes depend on the kinetic energy and mass of the impacting ion and can be distinguished accordingly into three regimes [22].

1. The single knock-on regime covers the impact of light ions or low energy heavy ions ($< \text{keV}$), where no secondary collisions appear and thus no collision cascade is created.

2. In the linear cascade regime collision cascades are produced due to a higher kinetic energy of the impacting ion of up to a few hundred keV. The dominant amount of collisions in this regime occurs to atoms of the solid bulk material at rest, because of the low density of moving atoms in the cascade volume.
3. In the spike regime this density is very high instead. As a result collisions occur predominantly between moving atoms which leads to significant non-linear effects. This applies for heavy and highly energetic ions, molecules or large atom clusters, where an impact produces several cascades in a small volume.

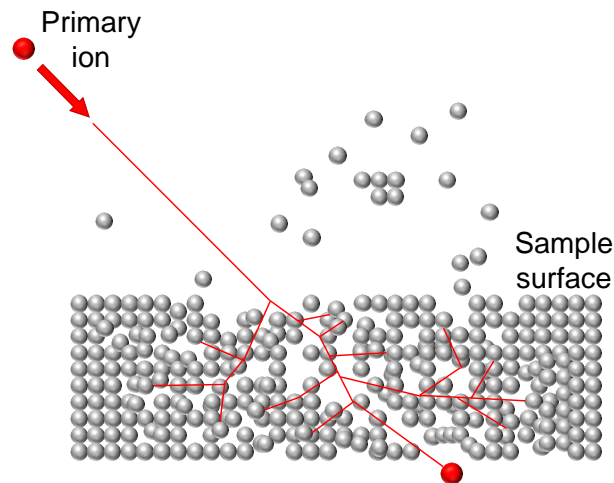


Figure 2.1: Scheme of a linear collision cascade in a solid sample induced by the impact of an accelerated primary ion. Atoms, molecules and clusters are sputtered by the recoil cascades of the impact.

Sputtering is possible in all three regimes if moving atoms in the bulk material reach its surface and their kinetic energy is higher than the surface binding energy E_B . The energy and angular distributions of the sputtered atoms are characteristic for the different collision regimes. The average number of atoms which are removed per incident particle defines the sputtering yield Y . This yield varies widely depending on the kinetic energy, element and mass of the impacting ion, on the incident angle and on the elemental composition, chemical speciation and surface structure of the target. Therefore the determination of the sputtering yield is based on analytic theory, comprehensive computer calculations and specialized experimental setups for sputtering analysis. Nevertheless, it is almost exclusively applicable only for crystalline or complete homogeneous sample surfaces.

Sputtered atoms are ejected via elastic atomic interactions, but additional inelastic processes can cause transitions into atomic excited states. Most of these excited states decay radiatively after a short lifetime and can therefore be identified by the energy of the emitted photon. Longer lived metastable states can be analyzed by laser induced fluorescence or resonance ionization spectroscopy. These experimental studies are currently the only option for determination of the final electronic state population of the sputtering process due to incomplete understanding of the involved processes.

The sputtering process is also directly affecting the electrons of the sputtered atoms. Before the impact of a primary ion, the valence electrons of an atom bound in a solid state structure are located spatially as well as energetically somewhere in the overlapping orbital structures.

During sputtering the electrons of an ejected atom have to rearrange and need to fill the eigenstates of this free atom. In this process a certain fraction of the ejected species are produced as positively or even negatively charged ions due to the short time scale for this electron transition.

2.1.2 Distributions of sputtered particles

The energy and angular distributions of the sputtered atoms are well described for the linear collision cascade by Sigmund and Thompson [23–26]. Their theoretical model was developed for an amorphous, mono-elemental target and forms the basis for refined descriptions. The linear cascade theory separates the sputtering process into three parts:

1. The energy dissipation of the impacting ion
2. The formation of the collision cascade
3. The ejection of atoms from the cascade out of the target

The energy E_i of the cascade atoms inside the target needs to exceed the surface binding energy E_B at the surface for sputtering. The stopping cross section of the target material and the planar energy barrier at the surface transforms the internal energy distribution of the atoms, which is proportional to E_i^{-2} . The resulting differential yield of sputtered atoms $\partial^3 Y$ as function of kinetic emission energy E_{kin} and solid angle Ω ,

$$\frac{\partial^3 Y}{\partial E_{kin} \partial^2 \Omega} \propto \frac{E_{kin}}{(E_B + E_{kin})^{3-2m}} \cdot \cos^n \theta \quad (2.1)$$

m : energy dependent interatomic cross section parameter, $0 \leq m \leq \frac{1}{2}$

n : energy dependent polar distribution parameter, $1 \leq n \leq 2$

was derived by Sigmund and Thompson based on statistical assumptions for the cross section and a cosine-like prediction for the angular distribution. Unlike the monotonously falling internal energy distribution, the sputtered energy distribution shows a maximum of:

$$E_{max} = \frac{E_B}{2(1 - m)} \quad (2.2)$$

The approximation of $m=0$ and $n=1$ matches the majority of the experimental results for sputter energies of a few keV [20, 27]. Simplified distributions for the kinetic emission energy E_{kin} and the polar angle θ of the sputtered atoms demonstrate the independence from the kinetic impact energy and the impact angle of the primary ion as:

$$\frac{\partial Y}{\partial E_{kin}} \propto \frac{E_{kin}}{(E_B + E_{kin})^3} \quad (2.3)$$

$$\frac{\partial^2 Y}{\partial^2 \Omega} \propto \cos \theta \quad (2.4)$$

As shown in Fig. 2.2, the only parameter with major influence on the energy distribution of the sputtered atoms is the surface binding energy E_B . An appropriate value for E_B is often

determined by the cohesive (or sublimation) energy. Experimental studies indicate that this value for E_B is underestimated for quiet some configurations [27] as this assumption neglects specific local interactions for sputtered atoms, which are embedded in different matrix materials [28].

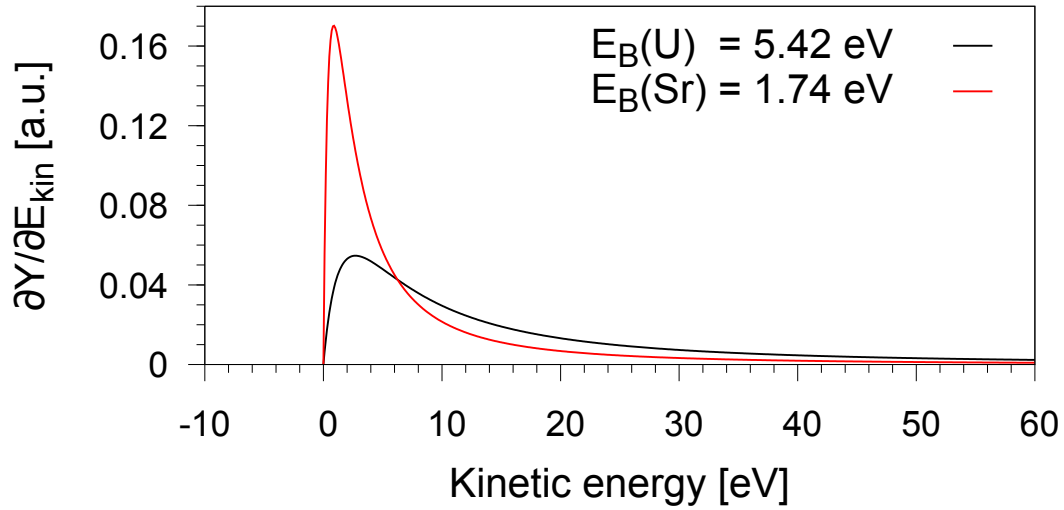


Figure 2.2: Theoretical Sigmund-Thompson energy distributions of sputtered uranium and strontium atoms.

2.2 Laser Ionization

An atom or molecule is ionized if it either loses or gains at least one additional electron and consequently acquires positive or negative charge. The ionization can be initiated by several processes that provide energy transfer to the atom or molecule. The two ionization methods with specific relevance for the herein presented work are sputter ionization, which was described before in section 2.1, and laser ionization, which is explained in detail in this section. The main advantage of laser ionization against most other techniques is the use of well tuned laser radiation, representing a discrete and precisely selected amount of energy. As a consequence, this process is highly selective and laser ionization has become an essential tool for spectroscopic and analytical measurements. The fundamental interaction of atoms and light, the particular properties of laser radiation and different methods of laser ionization are summarized in the following section based on comprehensive literature [29–33].

2.2.1 Atom-light interaction

Every atom is composed of a positively charged nucleus and a surrounding negatively charged electron shell. Energetic position and spatial location of the electrons is not explainable by a classical approach, as the electrons populate specific discrete levels only. Jointly, the quantized energy levels of the individual electrons define the quantum mechanic state, i.e. the configuration, of the atom. They are characterized by the principle, angular and projection quantum numbers n , l and m which describe the quantized interactions between electron and nucleus. The energy of the states for a simple atomic system with only one electron is independent of l and m :

$$E_n = -\frac{\mu Z^2 e^4}{8\epsilon_0^2 h^2 n^2} = -\text{Ry} \frac{Z^2}{n^2} \quad (2.5)$$

Ry = 13.61 eV: the Rydberg unit of energy

This basic model excludes effects, like the fine structure and the hyper-fine structure of this energy levels, which are caused by The consideration of the electron spin s and nuclear spin I . The structure of electronic states of an atom with more than one electron shows higher complexity involving also the electromagnetic interactions between the individual electrons. These states are described by the total quantum numbers of the complete atomic system, abbreviated by a term symbol notation:

$$^{2S+1}L_J \quad (\text{example for LS-coupling}) \quad (2.6)$$

S is the total spin quantum number, L is the total orbital quantum number in spectroscopic notation and J is the total angular momentum quantum number. Descriptions of coupling schemes and term symbols for systems with higher complexity can be found in comprehensive literature [34].

A transition of an atom between its electronic states can be effected by a radiation field with the frequency ν , if it is resonant to the energy difference of the states:

$$\Delta E = |E_1 - E_0| = h \cdot \nu = E_{\text{photon}} \quad (2.7)$$

The three possible processes of atom-light interaction are absorption, stimulated emission and spontaneous emission, which are illustrated in Fig. 2.3. An incoming photon, that fulfills condition (2.7), is either absorbed for a transition from the initial state of the atom E_0 to the energetically higher lying excited state E_1 or, alternatively, it induces emission of an identical photon, whereby the excited state E_1 decays into the energetically lower lying state E_0 . The emitted photon matches the frequency, phase and direction of the incoming photon. In addition, photons are emitted also spontaneously in this decay process without stimulation of an incoming photon. The phase and direction of spontaneously emitted photons is randomly distributed, while the energy is also set by condition (2.7) for the transition of an excited state E_1 to the energetically lower state E_0 .

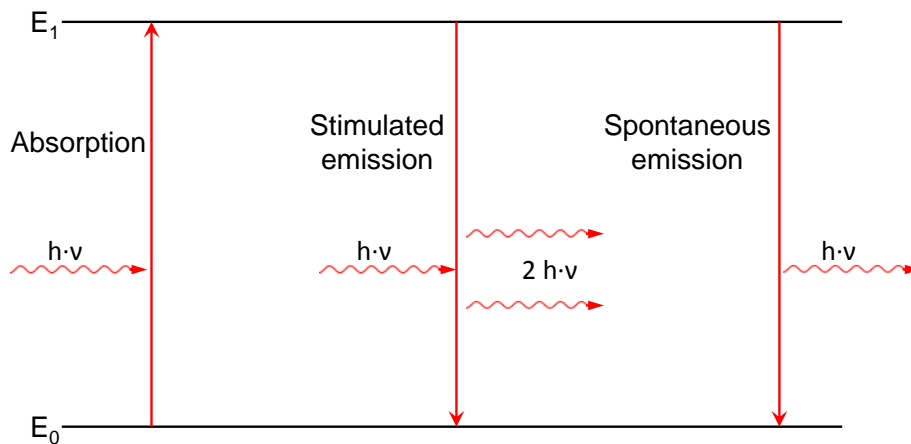


Figure 2.3: Schematic representation of the possible optical transitions between two discrete electronic states of an atom. In the first two cases, the transitions between state E_0 and E_1 are stimulated by an incoming photon (red wavy arrow). The third case shows the spontaneous emission of a photon without any stimulation.

2.2.2 Laser

LASER is the abbreviation for "Light amplification by stimulated emission of radiation". The laser process uses a chain of stimulated emission processes for the production of intense coherent light. The initial radiation is efficiently amplified if the stimulated emission processes overcome the losses by absorption of photons. This requires a larger amount of atoms in the energetically higher state than the lower state. In thermal equilibrium, it is impossible to fulfill this condition, which is known as population inversion, in a 2-level system. All existing lasers are therefore based on 3-level or 4-level systems. Those systems use a parallel process, called pumping, for an excitation of atoms from an energetically lower state to an higher state. In 3-level systems the higher or the lower state of the pumping process is identical to the higher or the lower state of the stimulated emission. In 4-level systems, as shown in Fig. 2.4, the processes of pumping and stimulated emission are decoupled and therefore most efficient. A transition is driven with highest efficiency, if the initial state in a medium is fully populated and the final state is empty. That is almost realizable in the illustrated 4-level system for pumping and stimulated emission, if the states $|1\rangle$ and $|3\rangle$ are highly populated and the states $|2\rangle$ and $|4\rangle$ are continuously depopulated by fast decay transitions.

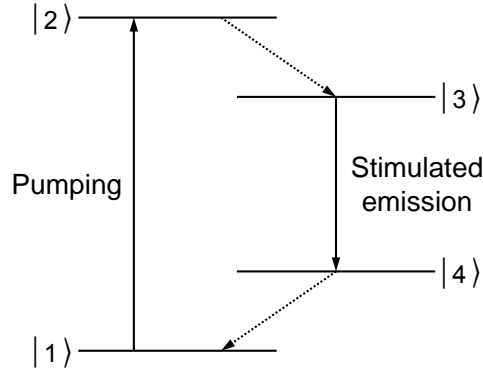


Figure 2.4: Schematic representation of a four-level laser system including a pumping process to enable efficient stimulated emission. The dotted arrows depict fast non-radiative decay transitions.

Besides a laser medium exhibiting a 3-level or 4-level system and an applicable pumping mechanism, efficient amplification of stimulated emission requires multiple pathways of the emitted radiation through the medium, which is realized by an optical resonator. The latter is set up by at least two mirrors and might include further optical elements. As consequence for a positive amplification, the stimulated emission needs to compensate unintentional occurring reflection losses as well as the decoupled laser light. This defines the threshold value condition for laser operation as:

$$\Delta N = N_u \left(\frac{g_l}{g_u} \right) - N_l \geq \frac{\gamma}{2 \sigma(\nu) L} = \Delta N_{threshold} \quad (2.8)$$

N_u, N_l : population density of the upper and lower state

g_u, g_l : statistical weight of the upper and lower state

γ : overall loss coefficient per pass through the resonator

$\sigma(\nu)$: cross section of the stimulated emission

L : resonator length

The steady state population inversion ΔN matches exactly the threshold inversion $\Delta N_{threshold}$ as soon as the laser operation reaches an equilibrium between pumping gain and losses due to stimulated emission. A second requirement for laser operation of a standing wave system is set by the resonator cavity which only allows buildup of a stable mode of oscillation of a light wave, if the full round trip resonator length matches a multiple of its wavelength. This condition limits laser emission to a finite number of discrete longitudinal modes. Further limitations and shifts by the shape of the cavity mirror, the refraction index of the laser medium, further optical elements in the laser cavity and the frequency and number of participating resonant transitions determine the final mode structure of a laser cavity.

Ti:sapphire laser

Despite a large variety of different laser media, only a limited number of these offer a wide range of tunability of the emission wavelength, which is necessary for laser spectroscopy in general as well as the specified application of resonance ionization. A perfectly suitable laser medium for widely tunable solid-state lasers has been created by formation of titanium-doped sapphire crystals ($\text{Ti}^{3+}:\text{Al}_2\text{O}_3$). The strong coupling of the Ti^{3+} ions to the crystal lattice causes a broadening of the electronic states by vibronic degrees of freedom.

Additionally, the single d electron in the outermost shell of the titanium ion is influenced by the electrostatic field of the neighboring oxygen. This interaction removes the fivefold degeneracy of the ground state of the free ion to a triplet ground state 2T_2 and a doublet excited state 2E . The combination of both effects leads to two electronic band structures, which provide the basis for a 4-level laser scheme, as schematically shown in Fig. 2.5. The electronic band structure enables fast relaxations to the lowest levels of both vibrational bands, which is the reason for the broad wavelength ranges of 420 nm - 600 nm for pumping and 650 nm - 1100 nm for stimulated emission. Both transitions address a continuous band as final state, which is rapidly depopulated. The pump transition commonly is generated by frequency-doubled Nd:YAG (532 nm) or Nd:YLF (527 nm) lasers. The corundum host crystal offers high transparency and thermal conductivity and is therefore suitable for high pump power. The first Ti:sapphire laser was developed by Moulten 1982 and was completely characterized in respective literature [35–38].

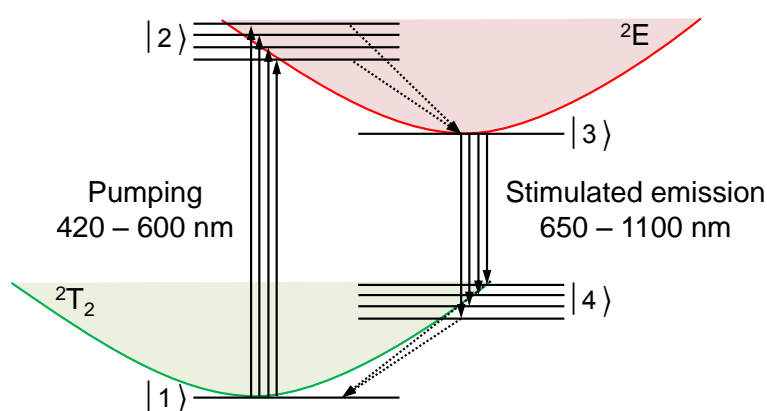


Figure 2.5: Four-level scheme of a Ti:sapphire laser: The red and the green parable represent the vibrationally broadened doublet and triplet band structure of the Ti^{3+} ion in an Al_2O_3 crystal.

2.2.3 Non-resonant laser ionization

In resonance ionization different types of laser ionization processes are possible depending on the number of lasers and the transitions. All of them provide sufficient energy to an atom or molecule to excite an electron above the ionization potential (IP). Single photon ionization (SPI) uses only one high energetic photon for a direct excitation from the ground state above the IP, as shown in Fig. 2.6. This technique requires lasers in the vacuum ultraviolet (VUV) range. SPI offers only a limited selectivity for the analyte, because every sample material with lower ionization energy than the photon energy will be ionized. The selectivity of a SPI analysis is correspondingly provided by subsequent mass spectrometry. A better suited laser ionization technique implies stepwise excitation with more than one photon by using intermediate excited states of the atom or molecule of interest. This process, which is called resonance-enhanced multiphoton ionization (REMPI), always involves a resonant or partially resonant excitation via m photons and a non-resonant ionization step via n photons. The classification for different combinations of excitation and ionization is $(m+n)$ -REMPI. For example, the $(1+1)$ -REMPI uses one photon for resonant excitation and a second photon of the same wavelength for ionization. Further combinations use additional virtual states in between or use supplementary lasers for inducing other transitions. An example of combinations and their designation is shown in Fig. 2.6. The use of intermediate states increases the selectivity of the ionization process tremendously, because the energy of these states is characteristic for the ionized atom or molecule. Remaining parallel laser ionized

background is easily separated by additional mass spectrometry. However, the application of the REMPI technique requires extensive laser spectroscopy on the excited states of the species of interest to identify the intermediate states. The term REMPI is mostly used for laser ionization of molecules. The same technique is applied to atoms simply as non-resonant laser ionization or resonant laser ionization with a non-resonant ionization step.

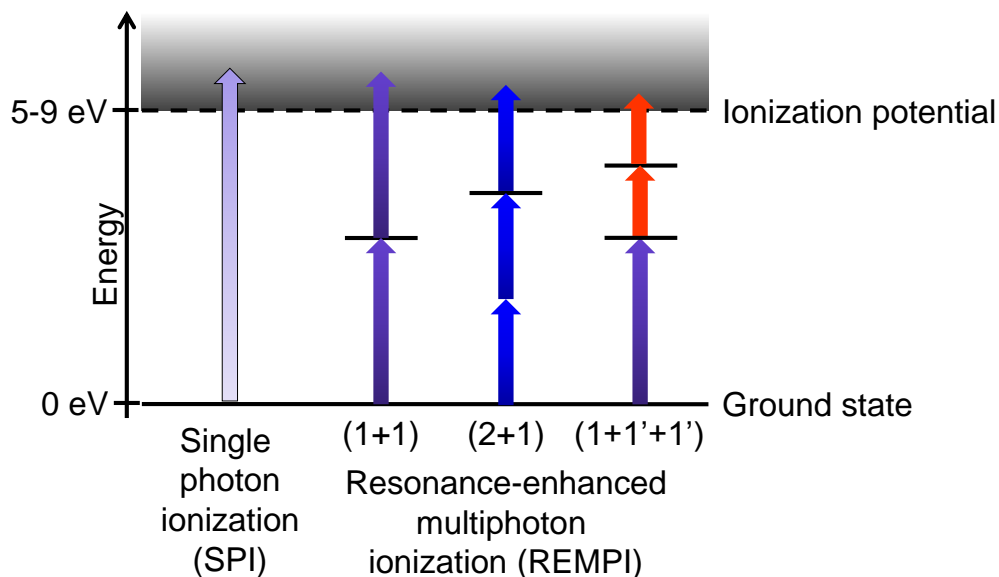


Figure 2.6: Comparative scheme of single photon ionization and different possibilities of resonance-enhanced multiphoton ionization.

2.2.4 Resonant laser ionization on atoms

The resonant laser ionization of atoms similarly relies on stepwise excitation via characteristic intermediate states like REMPI. This technique was developed in the 1970s for atomic laser spectroscopy [39–42]. Due to the high ionization efficiency and unsurpassed isobaric selectivity, it is nowadays used as a unique tool for selective and sensitive ultra-trace analysis [43, 44] and for efficient production of rare isotope beams at on-line facilities [45, 46]. Resonant laser ionization uses 2 - 4 powerful lasers, operating on strong atomic transitions, which allows for an ionization efficiency of more than 50 % [47] and by application of narrow-band lasers even isotopic selectivities of more than 10^{-12} [48]. The highest efficiency is only achievable with dedicated lasers and optimized excitation schemes. The most suitable lasers must be precisely tunable to the resonant transitions, must offer a high photon density to saturate the transitions and support a well adapted spatial and temporal behavior and control to optimize the overlap with the atom source. The efficiency of an ionization scheme is most often governed by the final ionization transition. The non-resonant excitation of an electron into the continuum above the IP, as for REMPI, provides in most cases rather low ionization efficiency, as the cross section for non-resonant ionization is typically in the order of 10^{-17} cm². Another option is the resonant ionization via excitation into Rydberg states. For increasing principle quantum number n these excited states converges to the IP. Therefore, they are located closely below the IP. The required energy for ionization of an Rydberg atom is very low and can be provided by different processes, i.e. collisions with other particles, black body radiation or strong electric fields. These non-radiative ionization mechanisms certainly result in an device-related dependence of the ionization efficiency, which varies strongly for different conditions in the ionization volume. However, the use

of a fully resonant excitation, the combination of various ionization mechanisms and the long lifetime of Rydberg states lead to a significantly enhanced overall ionization efficiency. The third possibility for resonant ionization uses a resonant last transition into a so called autoionizing state located above the IP. This state represents an excitation of two or more electrons, which results in an excitation energy of the atom located well above the IP. In case the total energy of all excited electrons is transferred to the weakest bound valence electron by internal coupling mechanisms, this leads to an detachment of this electron and therefore to autoionization of the atom. Autoionizing states have short lifetime due to a strong internal coupling. The resonant excitation to a spectrally broad autoionizing state with its high ionization probability consequently results in an ionization cross section that is about 10^3 to 10^4 times larger than for a non-resonant transition into the continuum.

As a drawback, the process of highly efficient resonant ionization is often accompanied by non-resonant effects induced by the laser light. As schematically shown in Fig. 2.7, the applied laser wavelengths for resonant ionization can also drive non-resonant transitions of the same species and furthermore, lead to non-resonant laser ionization of other atoms and molecules. Most of these unintentionally ionized species are separated in the subsequent mass spectrometry, while efficient suppression of isobaric contaminating ions might require a thorough choice and adaption of the resonant ionization scheme in use.

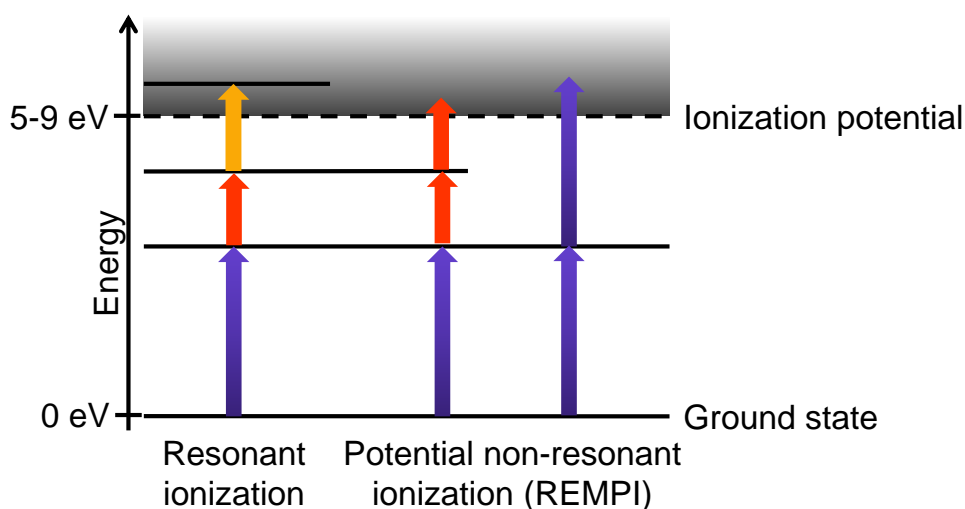


Figure 2.7: Scheme of resonant laser ionization by three excitation steps using an autoionizing state together with potential non-resonant processes for the same species.

2.3 Mass Spectrometry

The experimental procedure of mass spectrometry in general implies three specific parts. The substance, which is analyzed, needs to be ionized by an appropriate process. After that, the ions are separated by their mass-to-charge ratio and finally detected for qualitative and quantitative analysis. Since the development of first mass spectrometry instruments in the 1910s [49, 50] a permanent development and optimization of ionization, separation and detection techniques enlarged the field of application tremendously. The herein presented work also focuses on the development of a very specific application of mass spectrometry. The commercial TOF-SIMS instrument, involving different primary ion guns (described in detail in section 3.2) combines several methods for ionization and separation. Basic understanding of the various processes is essential to prevent possible disturbing interferences in the primary mass spectrometric operation. Therefore, besides an application-oriented description of SIMS, RIMS and Laser-SNMS, the following section also elucidates different basic processes of ionization and separation. A comprehensive description of mass spectrometry appears in the specialized literature [51, 52] on which this overview is based upon.

2.3.1 Ion sources and methods for mass separation

The former sections already described the theoretical basis of sputter and laser ionization, on top of which the conventional techniques of thermal, electron impact and field ionization are also applied in the experimental setup.

Thermal ionization

For thermal or surface ionization the analyte is brought into contact to a hot filament, which consists of a material with a high work function W . This contact leads to possible ionization of the sample material. The probability and therefore the efficiency for ionization depends on the ionization energy E_i of the species according to the Saha-Langmuir equation (2.9). Consequently, thermal ionization is only efficient for alkali and some alkaline earth metals. A modified geometry with multiple surface contacts increases the efficiency for providing reasonable ionization of further elements at highest temperatures.

$$\frac{n_i}{n_n} = \frac{g_i}{g_n} \exp \frac{W - E_i}{kT} \quad (2.9)$$

n_i, n_n : number of ions and neutrals

g_i, g_n : statistical weight of ions and neutrals

k : Boltzmann constant

T : surface temperature

Electron impact ionization

The ionization by collision with energetic electrons is called electron impact ionization. The electrons are produced by a hot cathode via thermionic emission. A static electric field is applied to accelerate the electrons to a defined kinetic energy. The atoms or molecules, which are analyzed, have to be transferred into the gaseous phase. The collision of an energetic electron with a free neutral particle results in an energy transfer ΔE from the electron. The neutral particle is ionized, if this transferred energy exceeds the specific ionization energy (mechanism shown in (2.10)). The ionization efficiency as well as fragmentation processes

of ionized molecules are strongly dependent on the kinetic energy of the electrons and the spatial overlap between the electron beam and the neutral particle gas volume.



Field ionization and field desorption

Field ionization is an autoionizing process, which is enhanced by a strong electric field. This electric field distorts the potential of the neutral particle, shrinks the potential barrier and intensifies the probability for quantum mechanical electron tunneling. Efficient ionization from low lying atomic levels requires strong electric fields ($10^{10} \frac{\text{V}}{\text{m}}$), which are formed at metallic tips and edges on high electric potential. The small radii present in the acceleration geometries cause an increased field strength according to:

$$E = \frac{Q}{4 \pi \epsilon_0 r^2} \quad (2.11)$$

$$= \frac{U}{r} \quad \text{for small radius } r \quad (2.12)$$

An analyte present in the gaseous phase, which experiences an sufficient high field is ionized and accelerated to the closest lower potential. In contrary, field desorption deals with liquid or solid sample material. It is an advancement of field ionization, because the ionization technique is identical. The difference is a direct absorption of the sample material on the tip or edge. As a result the neutral analyte species are positioned at the strongest region of the field and are desorped directly after ionization. Field ionization and field desorption are both "soft" ionization methods, because the fragmentation rate is much lower than for alternative processes like electron impact ionization.

Sector field mass separation

Mass separation within a magnetic sector fields was already used for the first mass spectrometric instruments [53]. The trajectory of an accelerated ion moving perpendicular to a magnetic field is given by the equilibrium between Lorentz force F_L and centripetal force F_C (2.13).

$$F_L = q v B = \frac{m v^2}{r} = F_C \quad (2.13)$$

$$r = \frac{m v}{q B} \quad (2.14)$$

As consequence, the radius r of the ions resulting circular path depends on the velocity v , charge q and mass m of the ion and on the magnetic field B . The insertion of monoenergetic, equally charged ions in a constant magnetic field reduces the dependency of the radius and the exit point only to the mass of the ion. Adjustable slits and a variable magnetic field complete the basis for a magnetic mass spectrometer using one ion detector placed at a fixed location. The modern magnetic sector field mass spectrometers use advanced magnet geometries and an additional electrostatic sector field to reduce the energy distribution of the ion source. This allows for a mass resolution R of 2000 - 15 000 depending on the application.

Quadrupole mass filter

An alternative technique of mass analysis is the quadrupole mass filter, which was developed by Paul 1953 [54], who was awarded a Nobel prize in 1989 for this task [55]. The linear quadrupole mass filter consists of four hyperbolically or cylindrically shaped rod electrodes. Two opposing electrodes are supplied with the same voltage, which comprises a DC component U and an AC component V . The quadrupole potential perpendicular to the quadrupole axis z is oscillating between attraction and repulsion in x - and y -direction. Certain voltages U and V and a specific oscillation frequency ω results in a stable trajectory for ions with a defined $\frac{m}{z}$ -value or within a defined $\frac{m}{z}$ -range. All other ions follow an unstable trajectory, that at some point leads to a collision with one of the electrodes. Therefore, the linear quadrupole is a mass filter and not a separator like the magnetic sector field. The advantages of a quadrupole mass spectrometer (QMS) are the small dimensions of the setup, the high transmission at low kinetic energy of the ions and the possibility of faster mass scans. The mass resolution R of a QMS in the region of 200 - 2000 is significantly lower than that of a sector field MS.

Time-of-flight mass spectrometry

The basic principle of a time-of-flight mass spectrometer (TOF-MS) is very simple. Ions with different $\frac{m}{z}$ -ratios are accelerated in an electrical field, which results in a $\frac{m}{z}$ dependent velocity (2.16). During a flight through a field free drift path, the ions experience a temporal dispersion. This results in a $\frac{m}{z}$ dependent time of detection (2.17).

$$E_{el} = e \cdot z \cdot U = \frac{1}{2} m_{ion} \cdot v^2 = E_{kin} \quad (2.15)$$

$$v = \sqrt{\frac{2 e z U}{m_{ion}}} \quad (2.16)$$

$$t = \frac{s}{\sqrt{\frac{2 e z U}{m_{ion}}}} = \frac{s}{\sqrt{2 e U}} \sqrt{\frac{m_{ion}}{z}} \quad (2.17)$$

The mass resolution of a TOF-MS is therefore limited by the measured flight time and its achievable precision (2.18). This flight time includes the time for the ionization process t_i , the time for acceleration t_a , the actual drift time in the field free region t_D and the response time of the detector t_d , which all got their own uncertainties.

$$R = \frac{m}{\Delta m} = \frac{1}{2} \frac{t}{\Delta t} \quad (2.18)$$

$$= \frac{1}{2} \frac{t_i + t_a + t_D + t_d}{\Delta t_i + \Delta t_a + \Delta t_D + \Delta t_d} \quad (2.19)$$

The contribution of the ionization process can be minimized by a two-step extraction, where the ions are produced in a field-free region and the accelerating electric field is applied after the ionization. It is not possible to accelerate the ions instantaneously to reduce the uncertainty of the acceleration time t_a . Some of the major effects, which increase the uncertainty, can be compensated. In theory, all produced ions start at the same position with no kinetic energy. But in reality the ions are distributed in a volume and with varying kinetic energies and directions. One optional improvement is the reduction of volume by a modified ionization mechanism or geometry. A further improvement can be achieved, if the

ions are accelerated perpendicular to the axis with broadest energy distribution. An active energy focusing to compensate the dispersion or different start positions can be realized by a reflectron. This device, as shown in Fig. 2.8, reflects the ions towards the detector by an electric field by almost 180° . The penetration depth into the reflection field and therefore the reflection time depends on the kinetic energy of the ion. The energy dispersion can be compensated by precise adjustment of the reflectron position and voltage. The drift time t_D is longer than any of the other contributions mentioned above, but for achieving increased resolution it can be extended further. This is the approach of a multi-reflectron time-of-flight mass spectrometer (MR-TOF-MS). A MR-TOF-MS traps the ions between two electrostatic mirrors, which fold the ion trajectory into a small volume and enables longest drift paths. The limitation for MR-TOF-MS is caused by the same effect, that is responsible for the uncertainty of t_D . Collisions with the residual gas molecules lead to further energy dissipation and are only reduced by improved vacuum conditions. The last part of the total flight time, which is constantly improved, is defined by the detection system. High-speed analog-to-digital converter (ADC) or even faster time-to-digital converter (TDC) for single-ion counting are applied to ensure the mass resolution of a TOF-MS at this part. All these enhancements for different applications lead to achievable mass resolutions of up to 4000 for linear systems, $>10^4$ for reflectron TOF-MS and $>10^5$ for MR-TOF-MS.

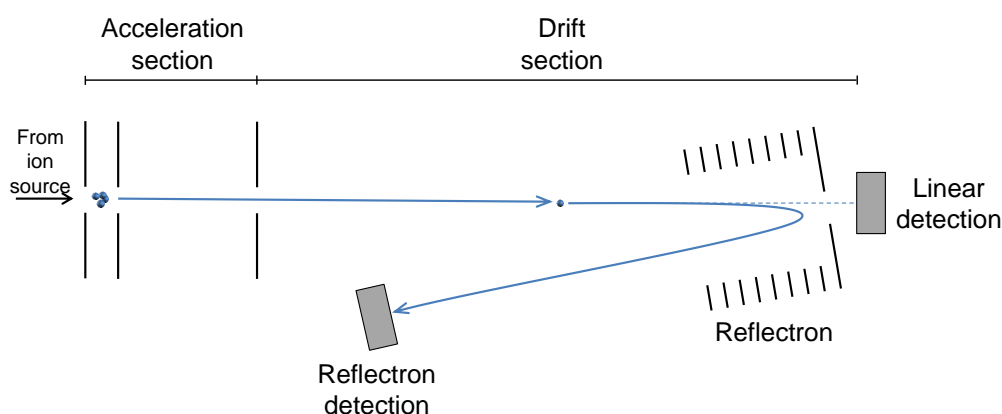


Figure 2.8: Scheme and ion trajectories of a Time-of-Flight mass spectrometer, including detectors for linear or reflectron operation

2.3.2 RIMS, SIMS and Laser-SNMS

As mentioned before, the combination of ionization process and mass spectrometric technique has to match the envisaged application. Different arrangements and special adjustments of ion sources and mass spectrometers can enhance or reduce the divers characteristics of the complete mass spectrometric system. That is the reason why this application-oriented specifications are of major importance and are described hereinafter for the techniques of RIMS, SIMS and Laser-SNMS, which were applied in this work.

Resonance ionization mass spectrometry

Resonance ionization mass spectrometry is a combination of resonant laser ionization and conventional mass spectrometry. The element selective ionization process together with the mass selective properties of mass spectrometry lead to a high isotopic selectivity, as shown in Fig. 2.9. This particular feature is used for production of isotopic pure ion beams for spectroscopic or analytical applications applied e.g. at on-line isotope separators for the

study of short-lived exotic nuclides with lowest production rates. Depending on the final application, the systems can be optimized for highest efficiency, highest selectivity or highest ion beam quality and density. For example, the best isotopic selectivity is achieved by narrow band laser ionization, which uses the isotope shift of the electronic structure for isotope selective ionization. Narrowest laser bandwidth is provided by cw-lasers with low power to prevent saturation broadening of the transitions. This ionization could be complemented by a dedicated TOF mass analyzer, which is optimized for high mass selectivity. Unfortunately, the combination of these two processes would be severely limited in efficiency and would require large amounts of sample material and measurement time. On the other hand, high efficient systems applying pulsed, broad band, high power lasers and a high transmission sector field MS deliver only reduced selectivity. In addition there are also continuous technical improvements to overcome those limitations [56–58].

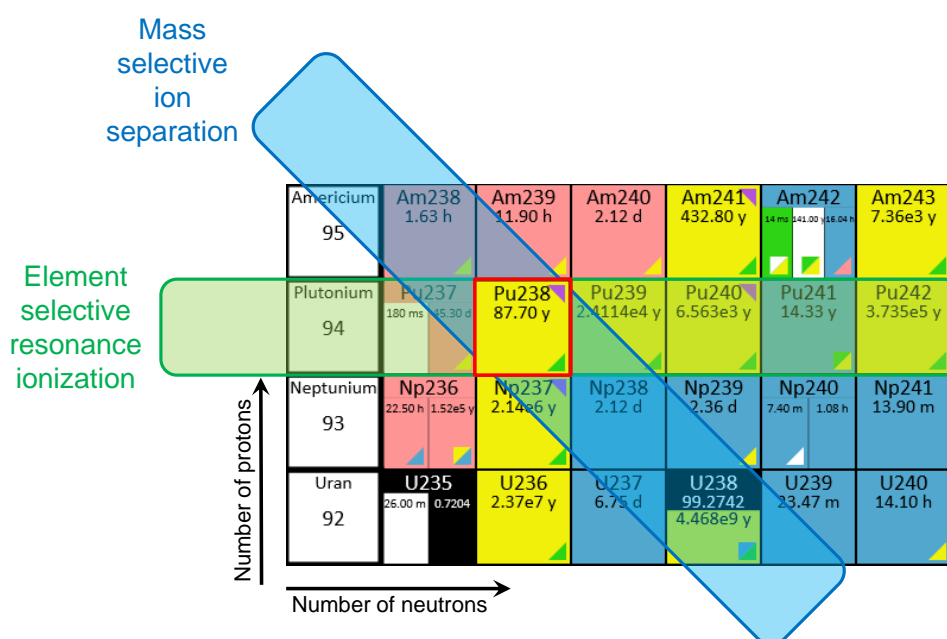


Figure 2.9: Exemplary presentation of the combined elemental and mass selectivity of RIMS on a section of the chart of nuclei. In this case, the resonant laser ionization of plutonium is combined with the separation of mass 238, which results in the isotopic selection of ^{238}Pu .

Secondary ion mass spectrometry

As briefly described in section 2.1, the sputtering of particles by impact of accelerated ions also ionizes a certain fraction of those particles. The combination of this sputter ionization and conventional mass spectrometry is the basis of secondary ion mass spectrometry (SIMS). The unique features of this technique are mainly determined by the characteristic of the primary ion beam applied for sputtering. Besides the mass resolution, SIMS offers the possibility of a spatially resolved analysis of the sample surface. For this purpose a primary ion beam for SIMS application is focused onto the sample surface and can be scanned two-dimensionally over a certain area of the surface layer. In this way, SIMS enables a structural analysis of the sample and not only a bulk analysis like most other mass spectrometric techniques. Additionally, the application of different primary ion species with different sputter energies allows an outstanding adaption of the SIMS technique to specific analytical

requirements. The selected primary ion species and its kinetic energy influence the polarity, the energy and spatial distribution, the sputter yield and the level of fragmentation of the secondary ions. As a result, SIMS is split into two distinguished methods, the static and the dynamic SIMS.

- Static SIMS uses very low ion dose to analyze the top surface layer without modifying it. Therefore, less than 1 % of the target area constituents receive an ion impact. It is applied for atomic and molecular analysis of the undisturbed top monolayer. Typically, static SIMS uses a pulsed primary ion beam and a TOF mass analyzer.
- Dynamic SIMS, conversely, uses a high primary ion dose and is mainly applied for bulk analysis and depth profiling. The high sputter rates of dynamic SIMS results in high sensitivity for atomic analysis, but the increased fragmentation prevents conclusive chemical speciation. Dynamic SIMS uses continuous primary ion beams and is usually equipped with a magnetic sector field or a quadrupole mass analyzer.

Secondary neutral mass spectrometry

Secondary neutral mass spectrometry (SNMS) is an advancement of the former described SIMS technique. In SIMS only 0.001 % - 1 % of the sputtered particles are ionized by the sputtering process. This low ionization efficiency strongly limits the overall efficiency and thus the sensitivity of SIMS analysis. The approach of SNMS is to improve this efficiency by specific post-ionization of the sputtered neutral particles. The most applicable techniques for post-ionization are resonant or non-resonant laser ionization (Laser-SNMS) [59] and plasma-induced electron impact ionization [60]. Those ionization methods are applied to the sputtered neutral particle cloud shortly after it is emitted from the sample surface, as schematically shown for Laser-SNMS in Fig. 2.10. The non-resonant Laser-SNMS by single photon ionization and the SNMS by an electron cyclotron wave resonance (ECWR) plasma are both non-selective techniques. They increase the ionization efficiency for every sputtered particle species by intensive bombardment with energetic photons or electrons. Nevertheless, this processes lead to fragmentation of different molecules and add further complexity to the speciation analysis of surface layers. In contrary, resonant Laser-SNMS ionizes element selective and can therefore increase the ionization efficiency and the signal-to-background ratio for one specific element of interest. For reduction of background, complete suppression of initially sputtered ions must be achieved. Still, all post-ionization methods lead to an increased ionization volume and a more complex instrumentation, which has to be accepted. The sensitivity enhancement by Laser-SNMS relies on several other important parameters of this advanced analysis technique. Besides the spectral and power conditions of the laser system itself, the spatial and temporal overlap between lasers and the neutral particle cloud has to be sufficiently adjusted.

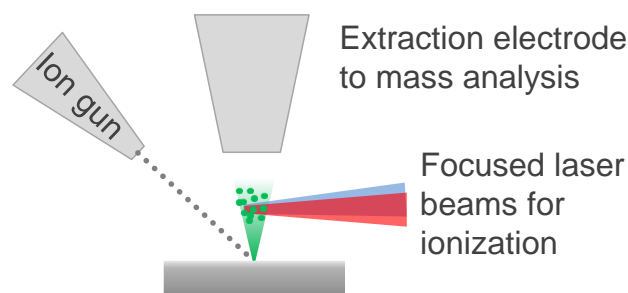


Figure 2.10: Schematic representation of the post-ionization process by resonant Laser-SNMS.

EXPERIMENTAL SETUP

Primary aspect and major part of the herein presented work was the development, installation and commissioning of the new system for resonant Laser-SNMS at the Institute for Radioecology and Radiation Protection (IRS) of the Leibniz Universität Hannover. This system combines a commercial TOF-SIMS instrument (TOF.SIMS 5 by IONTOF GmbH) with a dedicated, high repetition rate and high-power Ti:sapphire laser system. The TOF-SIMS instrument is a complex system optimized for surface analysis and incorporates several primary ion guns and further tools with a broad range of configuration options to fit different applications. The adaption of this instrument for resonant Laser-SNMS implies the thorough understanding of all technical and physical interactions as well as a general familiarity with the control software. The Ti:sapphire lasers itself and the complete laser system was designed to meet the special requirements of ultra-trace analysis with resonant laser ionization. Therefore, a complete description of the modifications and the individual characteristics of the laser system is given. The following chapter explains construction, important modifications and technical details of the specialized Ti:sapphire laser system, the conventional TOF-SIMS instrument and their coupling to a dedicated Laser-SNMS setup for ultra-trace analysis on environmental samples.

3.1 Ti:sapphire Laser System

The design of the Ti:sapphire laser for the IRS Hannover was entirely developed in the LARISSA group at the Institute of Physics of the Johannes Gutenberg-Universität Mainz. The first version of this compact design type with the characteristic z-shaped cavity was developed 2003 especially for ultra-trace analysis and atomic spectroscopy via resonance ionization mass spectrometry by R. Horn [61]. In the following years, the design was revised and advanced in several iterations, whereby further highly specialized designs for various applications were set up. On one side injection-locked narrow band operation for high resolution spectroscopy has been driven to maturity. Alternatively, grating-based versions for wide range scanning were developed [62–64]. The recent version of the standard Ti:sapphire laser design in use at the start of this work was developed explicitly for on-line production of isotopic pure ion beams at the Resonance Ionization Laser Ion Source (RILIS) for the radioactive ion beam facility ISOLDE at CERN in Geneva, Switzerland [65].

Besides the specialized versions, all iterations of the LARISSA standard Ti:sapphire laser are based upon of the same main components in a widely similar arrangement, as schematically shown in Fig. 3.1. A middle section, with high focusing of the laser radiation for efficient operation of the Ti:sapphire crystal, is enclosed quasi-symmetrical by sections of parallel

beam trajectory, for installation of frequency selective elements. Generally, the LARISSA Ti:sapphire lasers are pumped by frequency-doubled Nd:YAG or Nd:YLF lasers (532 nm or 527 nm) with a repetition rate of 7 kHz - 10 kHz. The end faces of the Ti:sapphire crystal are cut in Brewster's angle for the reduction of reflection losses of the p-polarized radiation of the laser mode and the pump laser. The Brewster geometry causes an astigmatism of the tangential and sagittal plane, which would influence the formation of stable resonator modes negatively. This astigmatism is compensated by a suitable tilt of the curved mirrors (CM) whereby also the characteristic z-shaped cavity is defined. Application of different mirror sets with specific coatings, together covering the whole Ti:sapphire emission wavelength range, provides high reflectivity for the Ti:sapphire laser wavelengths and high transmittance for the focused beam of the pump laser. Focusing of the pump laser at the rear of the crystal rod reduces the power density at the front possibly causing damage to the entrance facet. For prevention of heating effects in the crystal it is installed into a water cooled copper mount. The basic laser cavity is completed by a high reflective mirror (HR) at one end and a partially reflective outcoupling mirror (OC) at the other end.

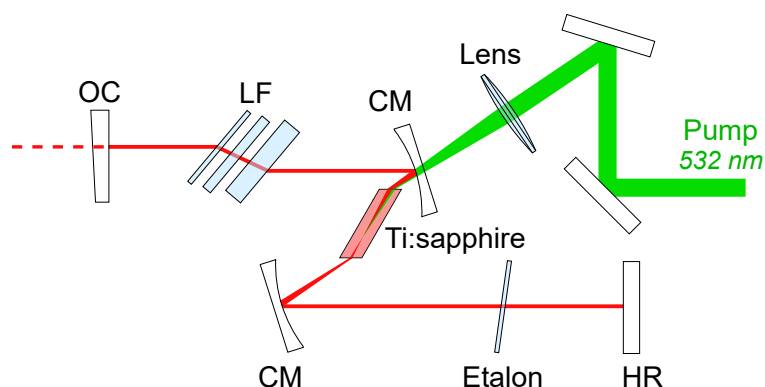


Figure 3.1: This schematic design of the z-shaped Ti:sapphire cavity shows the main components and their arrangement. For further explanations see text. (figure taken from [64])

The accessible range of emission wavelengths of the Ti:sapphire laser is determined by the broad emission range of the Ti:sapphire crystal. Further selection of the emission range by the mirror sets reduces the possible laser wavelength range and is necessary to ensure highest reflectivity over the emission range due to manufacturing limitations. The required precise wavelength is achieved by further frequency selective elements. The first such element is a Lyot filter (LF), which consists of three birefringent crystal plates. The three plates are mounted precisely parallel and with successive doubled thickness, which leads to a spectral filter system with spectral width of the thickest plate and free spectral range of the thinnest plate. Orientation of the Lyot filter in Brewster's angle results additionally in a linear polarization of the laser beam. All s-polarized fractions of emitted laser radiation suffer huge reflective losses in the Lyot filter. The spectral width of the range of possible longitudinal laser modes is determined by the Lyot filter to several hundred GHz and requires further reduction, which is achieved by a Fabry Perot etalon. The applied etalon consists of a glass substrate of width of 0.3 mm with a partially reflective coating ($R = 40\%$) on both surfaces. The tunable mounting of the Lyot filter and the etalon for compatible adjustment enables the laser operation on the whole Ti:sapphire emission range with a spectral width of 4 GHz - 10 GHz.

3.1.1 IRS Ti:sapphire laser

The IRS Ti:sapphire laser, shown in Fig. 3.2, was developed to fulfill all state-of-the-art and specialized requirements for the resonant Laser-SNMS system. The layout was based on the before mentioned laser cavity design for ISOLDE/RILIS at CERN. However, there were a few reasons for modifications of this already well-established concept. Most of the former Ti:sapphire lasers were used in combination with hot cavities or other atom sources delivering a steady atom flux. The combination with a pulsed atom source like the applied system for sputtering by accelerated ions required an advanced timing control with low jitter. All laser pulses must temporally overlap each other and the occurrence of the sputtered neutral particle cloud. The temporal adjustment of formerly developed systems with multiple Ti:sapphire lasers was controlled by Pockels cells as fast Q-switches inside the cavity. The application of Pockels cells includes some disadvantages like a reduced laser power due to reflection losses at the additional surfaces. Furthermore, the compensation of temporal delays with Pockels cells is limited and might not work well especially regarding the synchronization of Ti:sapphire lasers tuned to the center and edge of the available Ti:sapphire emission range. Hence, the Q-switch-based timing control was replaced in the new system by individual pump lasers for every Ti:sapphire laser, which can very easily be externally triggered (further description in section 3.1.2). The space-consuming recess for the Q-switch mount was excluded from the design and replaced by four threaded holes besides the beam axis. They are aligned in the necessary angle for a Q-switch, if future changes in the laser configuration would again require such a device. The accompanying beam displacement was also considered in the laser design.

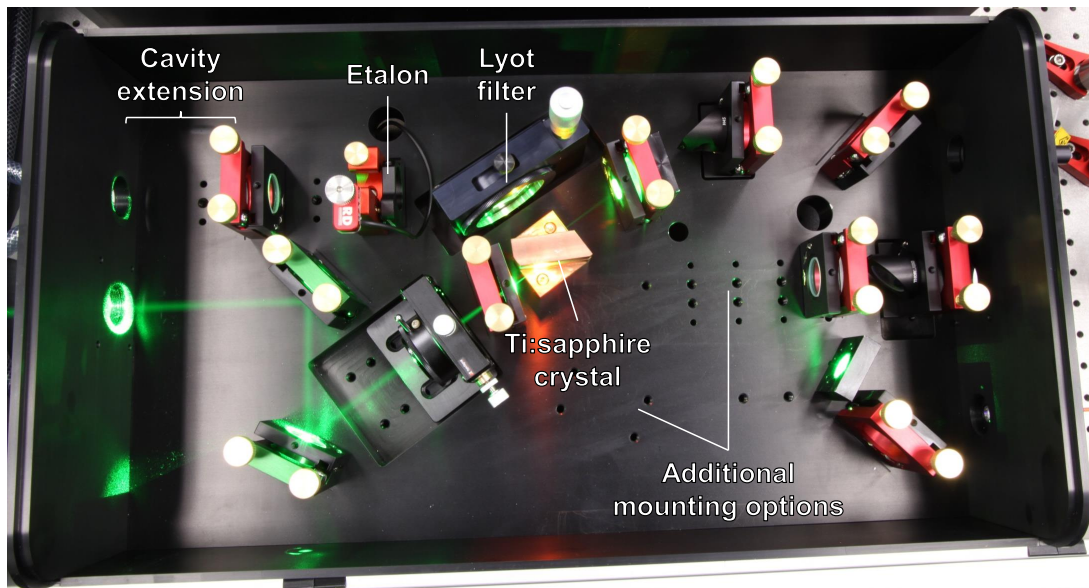


Figure 3.2: Photo of the IRS Ti:sapphire laser cavity during operation. The main components and modifications are marked. For further explanations see text.

The support of additional mounting options for mounts of different manufacturers provides a high flexibility for additional laser advancements. Therefore, all mounting positions offer different combinations of threaded and through holes according to the designs of the preferred optomechanics manufacturers. Primarily these additional mounting options consider two preceding developments for specialized laser operation:

1. A supplementary etalon with higher thickness could provide further reduction of the Ti:sapphire laser band width. This can be used to reduce the influence of unintended laser excitations.
2. Another recent development, which influenced the design, was the application of intra-cavity frequency doubling [66].

The possible utilization of both of these options as well as future ones is ensured by an optional cavity extension for gaining further space in the Ti:sapphire laser cavity. The final modification of the laser design concerns the mounting of the focusing lens for the incoming pump laser. An increased recess for the lens mount allows the installation of different lenses for further variation and optimization of the pump laser focus.

Characterization of the new Ti:sapphire laser

The modifications of the design as well as the variations between different batches of the main optical elements led to the necessity of a full characterization of the new Ti:sapphire laser. After installation and commissioning, the laser output power, the temporal pulse width and the beam profile was measured and evaluated for the whole spectral emission range. This was achieved by testing of every mirror set and also all reasonable combinations of one mirror set with the outcoupling mirror of another mirror set. The Ti:sapphire laser was constantly pumped with 15 W of pump laser power at a repetition rate of 10 kHz and only minor resonator adjustments were made to assure comparable results.

The Ti:sapphire laser need to fulfill several specification limits, which were set by the Laser-SNMS process and the TOF-SIMS instrument. The volume for interaction of the sputtered neutral particle cloud and the overlapped laser foci is limited by the distance between the sample surface and the extraction electrode of only 1.5 mm. An extension of this distance would negatively affect the analytical specifications of the SIMS instrument. Therefore and because an extended ionization volume would reduce the mass resolution (see section 2.3.1), the limit for the focused laser beam diameter was set below 300 μm at the end of the beam transport. The necessary temporal overlap between laser pulse and sputtered neutral particle cloud determined another specification limit for the laser pulse distribution. The width of the primary ion pulse can be varied between 1 ns - 50 ns depending on the specific settings of the ion gun. A laser pulse width above 50 ns would result in an increased temporal distribution of the ionization process. Correspondingly, the mass resolution of the applied TOF-MS would be further reduced, what should be prevented. The third specification limit concerns the wavelength range of the Ti:sapphire laser. A sufficient laser output power of more than 2 W should be supplied for the range of 730 nm - 920 nm to ensure the application of known excitation schemes for the elements of main interest.

The laser output power, pulse width and wavelength was measured directly at the Ti:sapphire laser exit, whereas the measurement of the focused beam profile required the 6.5 m long reference beam path as analogue of the later used beam transport path. The spatial limitation and the vacuum conditions in the SIMS instrument prevented the application of a beam profiler at the end of the main setup. The measured laser output power showed the expected dependence from the Ti:sapphire emission range, but stayed above 2 W for at least one mirror set in the range of 710 nm - 930 nm. As a result, it was also possible to identify the best mirror set combinations for every part of the emitted wavelength range (shown in the appendix as Fig. B.1). The laser pulse width was determined by the FWHM of

the measured pulse distribution via a fast photo diode to remain well below 50 ns. Besides the laser pulse width, also the response time between trigger signal at the pump laser and Ti:sapphire laser pulse was evaluated from the laser pulse data. The laser pulse width and the response time showed the expected correlation with the laser output power. A more efficient laser operation in the gain maximum results in higher laser power with shorter pulses, which appear earlier and vice versa at the edges. The measured beam diameter did also fulfill the requested specification and a best value even below $250\ \mu\text{m}$ was observed (shown in the appendix as Fig. B.3). The diameter was determined by the $D4\sigma$ -method from the measured beam profile. All required specifications including their reasons and the measured parameters of the Ti:sapphire laser are listed in Table 3.1.

Requirements	Reason	Measured
pulse length < 50 ns	matching of sputter pulse and laser pulse length	25 ns - 50 ns
wavelength range 730 nm - 920 nm	direct access of excitation schemes for U, Pu, Np, Tc, Sr, Gd and others	710 nm - 930 nm with 2 W - 3.5 W @ 10 kHz
focus ($D4\sigma$) < $300\ \mu\text{m}$	efficient overlap with sputtered particles	$262 \pm 62\ \mu\text{m}$

Table 3.1: Required and tested specifications of the IRS Ti:sapphire laser for Laser-SNMS application

3.1.2 Complete laser system for resonance ionization

The complete laser system consists of three Ti:sapphire lasers and several support, control and measurement systems, that are necessary for stable and adjustable operation. All those devices were installed on, below and above a $3\ \text{m} \times 1.5\ \text{m}$ optical table to generate a compact and easy accessible setup (picture in the appendix as Fig. A.1). This systems as well as the installation on the table can be separated into three sections, as shown in Fig. 3.3.

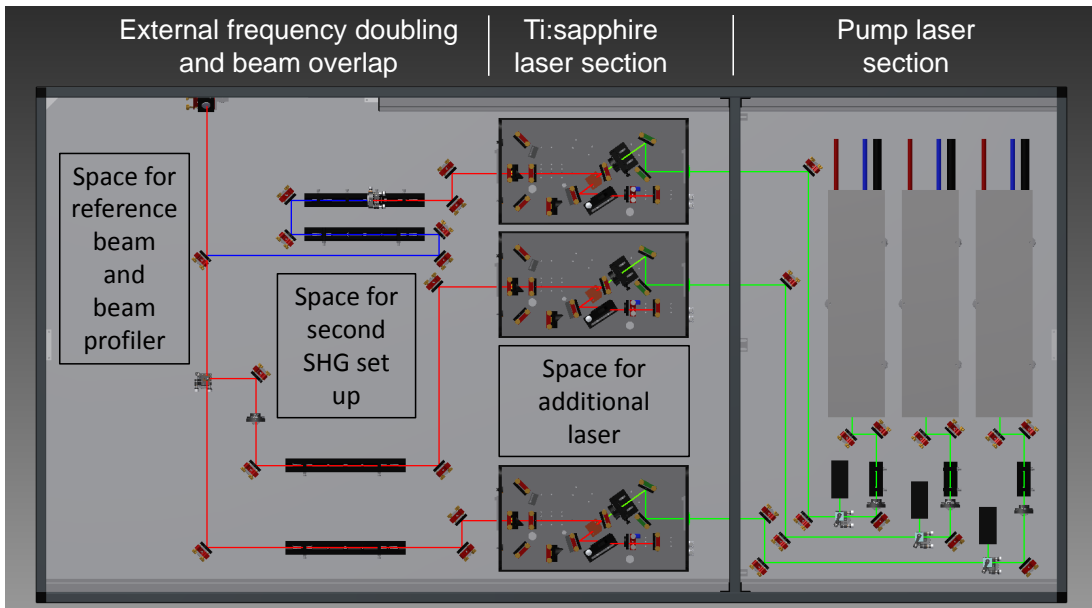


Figure 3.3: CAD scheme of the laser setup with three different sections of instrumentation. For further explanations see text.

Pump laser system

The first section involves the complete pump laser system, which provides the Ti:sapphire lasers with precisely timed and properly focused laser beams of appropriate power. The main part of this section are three commercial Nd:YAG lasers (DM60-532 by Photonics Industries). They produce intense pulsed laser radiation with a wavelength of 532 nm by internal frequency doubling. The repetition rate of the pump lasers is in principle variable between 1 kHz - 30 kHz, but was set to 10 kHz for all herein presented applications. Each laser can deliver up to 60 W output power with a pulse width of below 200 ns at full power. Although, one of the applied Ti:sapphire lasers requires only 12 W - 20 W for operation, each pump laser addresses only one Ti:sapphire laser for ensuring the individual timing control. The respective control units and water chillers were installed below the optical table. The optical setup in front of the pump lasers is identical for all three devices (picture in the appendix as Fig. A.2). The slightly divergent pump laser beam is at first shaped and focused by a telescope to achieve a beam diameter of 10 mm - 15 mm near the entrance of the Ti:sapphire laser cavity. Afterwards, the surplus pump laser power is separated by the combination of a rotatable $\lambda/2$ -plate and polarizing beam splitter cube, which additionally leads to the required p-polarized pump laser beam.

Ti:sapphire laser system and control

Three Ti:sapphire lasers and the supplementary control and measurement systems form the second section of the laser setup (picture in the appendix as Fig. A.3). The already described Ti:sapphire lasers (see section 3.1.1) require only sufficient pump laser radiation and active water cooling for operation. Generation of a precise temporal overlap between the three lasers and a longtime wavelength stability made further instrumentation necessary. Every laser cavity includes a beam sampler, which reflects 0.5 % - 1.5 % of the emitted laser light into a fiber coupling unit. The attached optical fibers transport the laser radiation to two different laser measurement systems.

The first system is a commercial wavemeter (HighFinesse WS6-600), which measures the wavelength of all three Ti:sapphire lasers using a 4-to-1 fiber optics switch. Besides the visual presentation of the spectral mode structure with the commercial software, the measured data is further evaluated by a dedicated LabVIEW program (picture in the appendix as Fig. A.5). This program uses PID controls for active wavelength stabilization via piezo motors, which are attached to the etalon mounts inside the Ti:sapphire laser cavity. Further options of the LabVIEW program enable continuous wavelength scans and indicate major deviations from preselected transition wavelengths for resonance ionization. The schematic setup for this wavelength control is shown in Fig. 3.4.

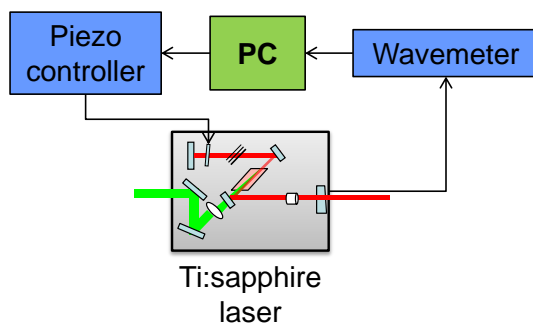


Figure 3.4: Schematic representation of the main components of the Ti:sapphire laser wavelength stabilization system

The second system, which is attached to the optical fiber, measures the temporal distribution of the Ti:sapphire pulses with fast photo diodes and a 350 MHz 4-channel oscilloscope. The oscilloscope is attached to a computer and permanently read out by a dedicated LabVIEW program (picture in the appendix as Fig. A.4). This program evaluates peak height, area, width and center of the laser pulses. Temporal shifts between the three Ti:sapphire lasers are therefore identified, measured and can be corrected by an appropriate shift in the trigger delay at the pulse generator for the affected pump laser. The pulse generator controls the trigger pulses for all three controllers of the pump lasers, which are set individually for a perfect temporal overlap of the Ti:sapphire lasers. The whole laser timing measurement and control system is shown schematically in Fig. 3.5. The automated shift correction by a software control of the pulse generator was prepared, but was not put into operation during this work as a major pulse drifting throughout operation was never observed. The connection between control PC and pulse generator is therefore only manually.

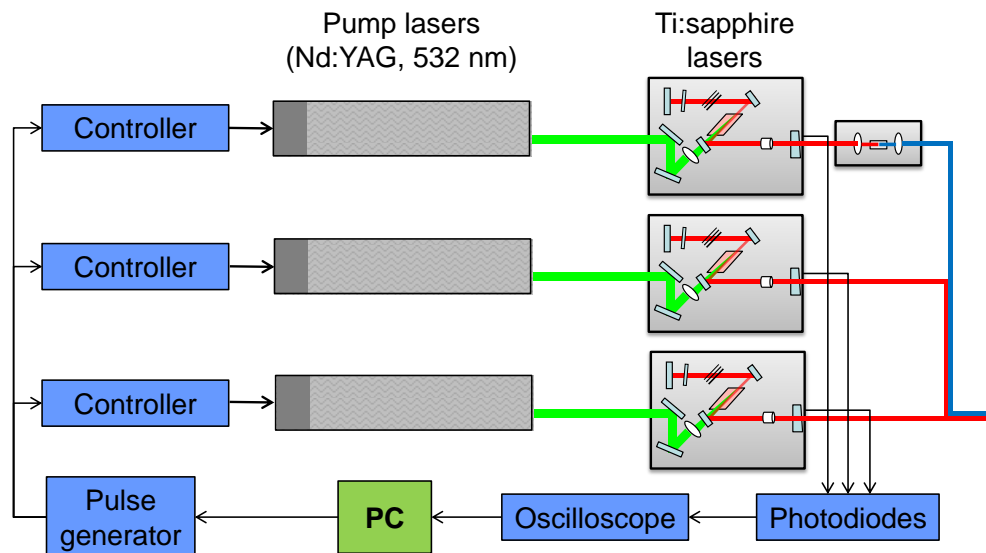


Figure 3.5: Scheme of the laser timing control system

Focusing, beam overlap and frequency doubling

The third section of the complete laser system involves all further treatment of the three fundamental Ti:sapphire laser beams.

All schemes for resonant laser ionization, which were applied in the first measurements, comprise one or two transitions well below the Ti:sapphire emission wavelength range. The wavelengths for those transitions are achieved by frequency doubling of the fundamental Ti:sapphire laser radiation. This second harmonic generation is a non-linear process and a special application of sum frequency generation in a crystal without inversion symmetry. The interaction between photons of the fundamental Ti:sapphire laser and the crystal material generates secondary photons with doubled frequency and therefore half wavelength. Efficient application of the frequency doubling can be ensured by high laser intensity and the non-linear characteristic of the process, which is realized by strong focusing on the fundamental laser beam in the crystal. The setup for external frequency doubling involves a beta barium borate crystal (BBO), enclosed by two convex lenses for focusing of the fundamental and parallelizing of the frequency doubled laser beam and an additional cylindrical lens for

compensation of the elliptical shape of the frequency doubled output beam. The different divergence angle for the horizontal and vertical axis is caused by the different refractive indices for the the horizontal and vertical crystal axis.

Instrumentation for intra-cavity frequency doubling is also applicable. This setup performs the second harmonic generation directly inside the Ti:sapphire laser cavity. Due to the high laser intensity inside the cavity, focusing lenses are unnecessary in this configuration, which is further increased with the replacement of the output coupling mirror by a specific dichroic mirror. This dichroic output mirror reflects the fundamental and transmits only the frequency doubled laser radiation. A second dichroic mirror with reverse reflection characteristics is added inside the cavity to reflect the produced frequency doubled laser radiation with opposed output direction. The complete optical setup is shown in Fig. 3.6. Omission of the convex lenses and the high photon density inside the cavity lead to an enhanced beam profile and increased efficiency for the frequency doubling process, that results in a higher output laser power [66]. Otherwise, additional optical elements in the laser cavity are also possible sources for negative influences and interference in the laser behavior.

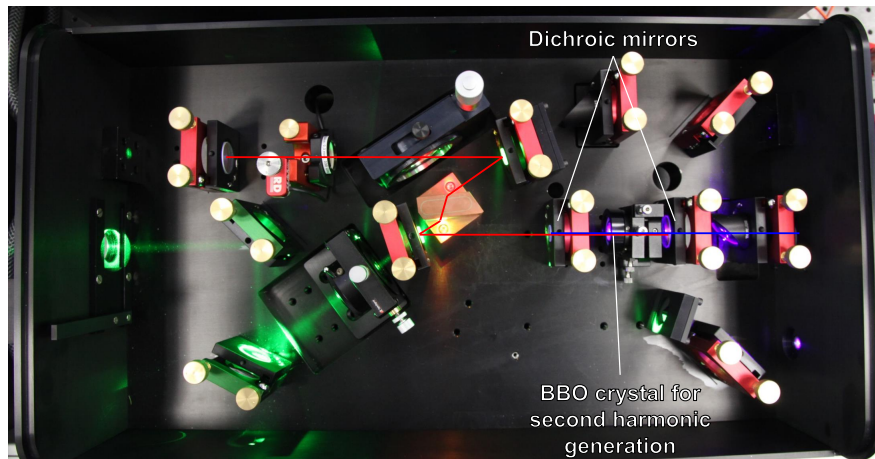


Figure 3.6: Photo of the intra cavity doubling with marked fundamental and frequency doubled beam path.

All three beams are focused and aligned by individual telescope and aperture setups. Afterwards the beams are overlapped by polarizing beam splitter cubes or dichroic mirrors. Focus and overlap are measured by a commercial beam profiler (Ophir SP620U) at the end of the reference beam path, that is of identical length than the main optical beam path and includes the same focusing lens at the end (further described in section 3.3.1). Switching between main path and reference path is enabled by a magnetic mirror mount.

3.2 TOF-SIMS

The utilized TOF-SIMS instrument is a commercial TOFSIMS 5 model manufactured by the company IONTOF GmbH that was installed at the IRS Hannover in January 2014. This setup combines the non-destructive analysis method of static SIMS with the fast removal of sample material by dynamic sputtering both carried out in a high performance time-of-flight mass spectrometer. The considerable complexity of this measurement system with different adjustable ion sources, a reflectron TOF mass analyzer for high mass resolution and a variety of instrumental measurement options allows mass spectrometric surface analysis, high laterally resolved surface imaging and low energy depth profiling on any kind of samples. The following section gives a short overview about the major components and their functionality. Detailed descriptions can be obtained from the company IONTOF directly or taken from their Internet homepage¹.

3.2.1 Components

The configuration of the TOF-SIMS instrument at the IRS Hannover, as shown in Fig. 3.7, includes a bismuth cluster primary ion gun, two different sputter guns for individual depth profiling, a gridless reflectron TOF mass analyzer with extended dynamic range, a 5-axis sample stage with heating and cooling systems, an active charge compensation for insulating material and a highly automated vacuum system and control.

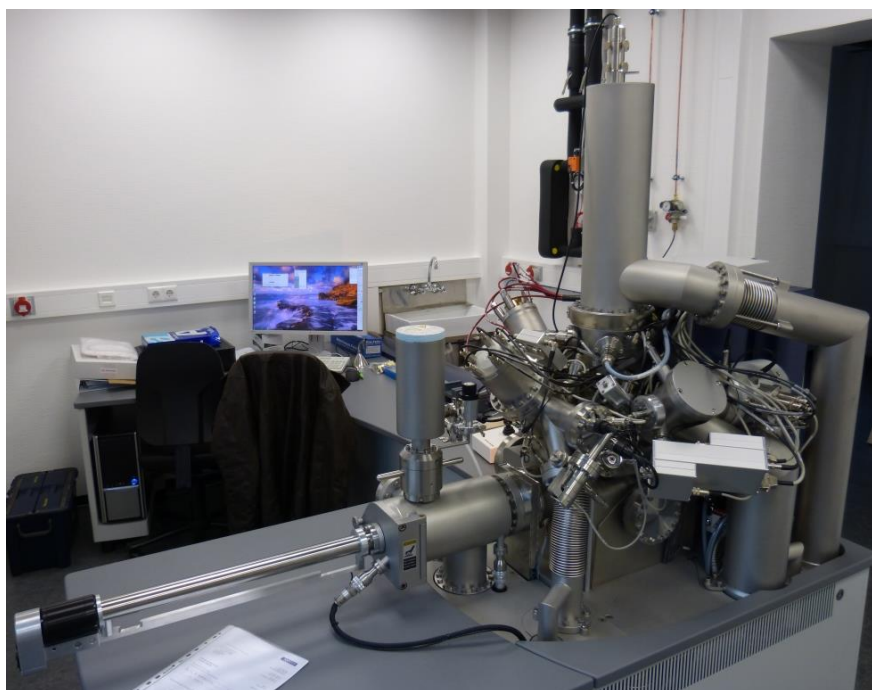


Figure 3.7: Photo of the IONTOF TOFSIMS 5 after installation at the IRS Hannover without additional extensions for Laser-SNMS.

Bi cluster ion gun / LMIG

The primary ion source of the TOF-SIMS instrument is a pulsed liquid metal ion gun (LMIG), which uses spatial and temporal focused ion bunches with a kinetic energy of up to 30 keV for non-destructive surface sputtering and is therefore perfectly suited for static SIMS analysis

¹<https://www.iontof.com/> (status at 02.06.2017)

(picture in the appendix as Fig. A.6). The primary ions are produced via field desorption of an bismuth-manganese emitter (see section 2.3.1). The following setup of several ion optical lenses, apertures and deflection electrodes allows a controlled beam alignment and shaping, either for high ion beam current or for high lateral resolution with a small focus. Additionally, two combinations of apertures and deflection electrodes are applied for stepwise, flight-time dependent chopping of the continuous ion beam. As a result, the pulse-length and the species of the primary ion bunches is fully adjustable. The available primary ion species are Bi_1^+ , Bi_3^+ , Bi_1^{2+} , Bi_3^{2+} and Mn_1^+ . Depending on the adjustment, the bismuth ion gun is able to provide 20 - 1000 ions per shot, with a pulse length between 1 ns - 50 ns and a lateral resolution of 80 nm - 2 μm . For special samples and under optimized operation conditions even 20 nm of lateral resolution was achieved with this primary ion source [67].

TOF mass analyzer

The applied time-of-flight mass analyzer offers a high mass resolution of up to 12.000 at high transmission (picture in the appendix as Fig. A.9). The small conical extraction electrode at the entrance of the mass analyzer is positioned in a distance of only 1.5 mm above the sample surface, specifically at the point of origin of the sputtered ions. The position ensures efficient extraction, the small size reduces the initial spatial distribution and the shape provides a minimum of surfaces for deposition, which reduces memory effects. The subsequent ion optics consists of a lens and a X- and Y-deflection for focusing and beam alignment. The occurring energy diversion during the acceleration is compensated by the installed gridless non-linear reflectron. The detection is realized by a single channelplate-scintillator-photomultiplier combination, which offers high sensitivity and long lifetime. The detected signals are processed by a fast time-to-digital converter (TDC). The TOF mass analyzer is switchable for analysis of positive or negative ions, which are both generated by sputter ionization. An additional extension of the dynamic range (EDR) is provided by a system that separates the ions of a chosen mass interval from the rest, directs those ions through defined reduction grids with an ion signal reduction of 10 or 100 and directs them back to the same ion beam trajectory of the non-separated ions. This complex EDR instrument inside the TOF mass analyzer enables the well defined reduction of a certain mass interval.

Sputter guns for depth profiling

A standard static SIMS instrument is not able to perform depth profiling, due to the low ion beam current and the related almost negligible erosion rate. The dual beam depth profiling is a technical extension of a static SIMS to achieve the fast surface erosion of a dynamic SIMS in combination with optimum lateral resolution. As the name suggests, the dual beam depth profiling includes an additional ion beam source, which provides a high ion current for surface erosion. At first, the low energy sputter beam is applied to remove a significant amount of sample material, then the surface of the sputtered crater is analyzed by the high energy but low current ion beam of the static SIMS. Steady alternation and individual adjustment of both ion beams enables the generation of depth profiles for structures of several micrometer thickness with a depth resolution of a few nanometer [68, 69]. The TOF-SIMS instrument at IRS Hannover offers different sputter sources for surface erosion to fulfill the requirements for efficient surface analysis of different samples.

The installed dual source column (DSC) combines two ion sources for sputtered depth profiling (picture in the appendix as Fig. A.7), which share the same ion-optical configuration for spatial and temporal focusing, a mass separating pulsing system as well as deflection

electrodes for beam alignment. The cesium ion source, which uses thermal ionization (see section 2.3.1), is installed in axial orientation. The perpendicularly oriented electron impact ion source (see section 2.3.1) generates an oxygen ion beam, which is guided on the axial beam path by an electrostatic 90°-deflector. Sputtering with either Cs⁺ or O₂⁺ ions enhances the emission of negatively or positively charged ions, respectively, during subsequent sputter ionization with the analysis ion gun.

For reduced fragmentation during the sputtered erosion of organic material or weakly bound molecules, the TOF-SIMS is equipped with another ion source (picture in the appendix as Fig. A.8) for production of a gas cluster ion beam (GCIB). The applied argon gas forms clusters via adiabatic expansion through a thin nozzle by a strong pressure gradient (30 bar to 10⁻³ mbar). The argon clusters are ionized by electron impact ionization and then separated depending on cluster size by a Wien filter. The following ion-optical combinations of lenses, apertures and deflection electrodes provide a pulsed, focused and aligned ion beam similar to the other equipped ion sources. The argon cluster ion sources offers cluster sizes from 250 - 10 000 atoms/cluster at an energy range from 2.5 keV - 20 keV. The large amount of atoms per cluster leads to a very low energy per atom, which prevents fragmentation. A technical modification of this ion gun would even allow the direct surface analysis with an argon cluster ion beam [70].

In-situ sample handling: sample stage, camera system, SE detector and charge compensation

The analysis with high spatial resolution as well as precisely adjusted and overlapped foci of the ion guns and the mass analyzer requires a highly stable and complete orientable sample holder. As shown in Fig. 3.8, the sample holder is mounted on a sample stage, which allows the precise positioning of the sample in the sputter and analysis focus slightly below the instruments. With the 5-axis sample stage the sample may be positioned tilted and rotated to achieve the ideal orientation. One of the switchable sample holder mounts even offer the possibility to heat the sample up to 600 °C or to cool it down to -150 °C.

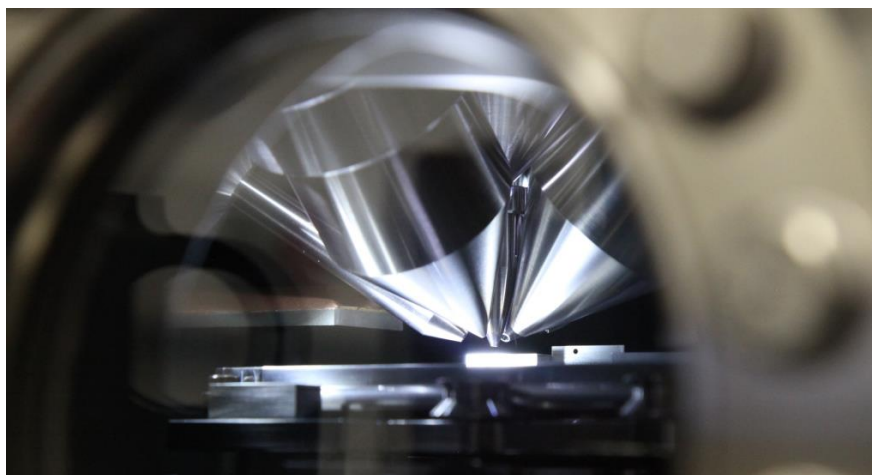


Figure 3.8: Photo of the sample region in the TOFSIMS 5: The small aluminium sample holder, which is fixed on the top mount, is positioned directly under the tips of the mass analyzer and the ion guns. The narrow tip in the middle belongs to the vertical mounted TOF mass analyzer. The larger cone-shaped structure in the front is the tip of the Bi cluster ion gun.

The precise orientation of the sample also requires a reliable monitoring of the sample and its surface. Besides the ion images, which are generated with the SIMS setup, the instrument is equipped with two optical cameras. Both are installed in the back of the instrument and generate a macroscopic image for rough sample observation and a microscopic image for sample surface observation. Additionally, the TOF-SIMS instrument includes a secondary electron detector, which enables to receive electron images of the surface during the sputter process.

A further component, which supports the handling of every kind of sample, refers to the analysis of non-conducting samples. The positive charge, which is transported by the primary sputter ions, increases the surface potential of insulating samples. The resulting variations of the electric field configuration above the sample lead to shifted and blurred ion images. An installed electron flood gun compensates the applied positive charge by provision of negatively charged electrons.

Vacuum system

The utilized TOF-SIMS instrument is housed in a very complex vacuum system to provide the high vacuum conditions, which are required for sputter ionization and time-of-flight mass analysis. Constant preservation of the vacuum in the main chamber is ensured by a load lock system, which enables to introduce the samples under vacuum conditions. The main chamber, the load lock chamber, every sputter ion gun and the TOF mass analyzer are equipped with an individual turbo pump and can be separated from the rest of the system with a number of valves. The prevacuum conditions for all turbo pumps are generated by a combination of a turbo-molecular drag pump, a buffer system and a rotary vane pump. Additionally, the vacuum conditions in the main chamber and the load lock chamber can be optimized by an internal bakeout system. Due to its complexity the vacuum system is fully computer controlled by an embedded system, known as vacuum control unit (VCU).

3.2.2 Analysis methods and programs

The control of the TOF-SIMS instrument including all installed power supplies is managed via the software package "SurfaceLab" programmed by IONTOF (version 6.5 was used for this work). It provides different programs for system control, sample navigation and measurement specification during the surface analysis, but also programs for measurement evaluation and data reconstruction after the analysis.

- The "Spectra program" displays the measured mass spectra, offers the functionality of mass calibration by known mass peaks or mass peak structures and allows the selection and automatic evaluation of individual mass peaks and peak lists. In addition, the software corrects the measured mass spectra in a fully automated manner for dead time effects of the detection system by a Poisson correction.
- The "Images program" displays the measured ion images of marked mass peaks. Further options, which are included, are different operations for analysis and manipulation of images or chosen regions of interest, like overlays, histograms, filters, addition and subtraction of other ion images and many more. The program also offers a 3D reconstruction of the sample composition by using the measured depth profile.
- The "Profiles program" displays and processes the mass spectrometric data of a depth profile analysis. This program allows to calibrate the recorded depth profile via further

information of sample composition or erosion rate to achieve reliable structural information.

3.3 Combined Laser-SNMS System

As already mentioned, the resonant Laser-SNMS system at the IRS Hannover is a combination of the former described pulsed Ti:sapphire laser system (section 3.1) and the commercial TOF.SIMS 5 by IONTOF (section 3.2), as schematically shown in Fig. 3.9. The system is specifically tailored element selective and spatially resolved ultra-trace analysis of radionuclides directly on environmental samples, but should also be used as a conventional SIMS for chemical speciation and sample characterization. The development of this system is based on a former test installation at the Institute for nuclear chemistry of the Johannes Gutenberg-Universität in Mainz, which used a very early development stage of the Ti:sapphire laser and a modified TOF.SIMS 3 by IONTOF [71]. The herein described resonant Laser-SNMS system was also influenced by other experimental approaches, like the similarly IONTOF-based setups at the Universität Münster [72] or the completely self-developed setups at three institutes in the United States under supervision of M. Pellin [73–76]. Most of these systems were geometrically and technically optimized exclusively for Laser-SNMS analysis and are incapable of parallel, highly resolved SIMS measurements.

The resonant Laser-SNMS process (theory in section 2.3.2) requires a stable spatial and temporal overlap of the sputtered neutral particle cloud and the laser pulses as well as a sufficient suppression of the sputtered secondary ions. Control, monitoring and testing of these parameters made modifications of the TOF-SIMS instrument inevitable. The technical extensions and the characterization of combined sputtered atomization and resonant laser ionization is described in this section.

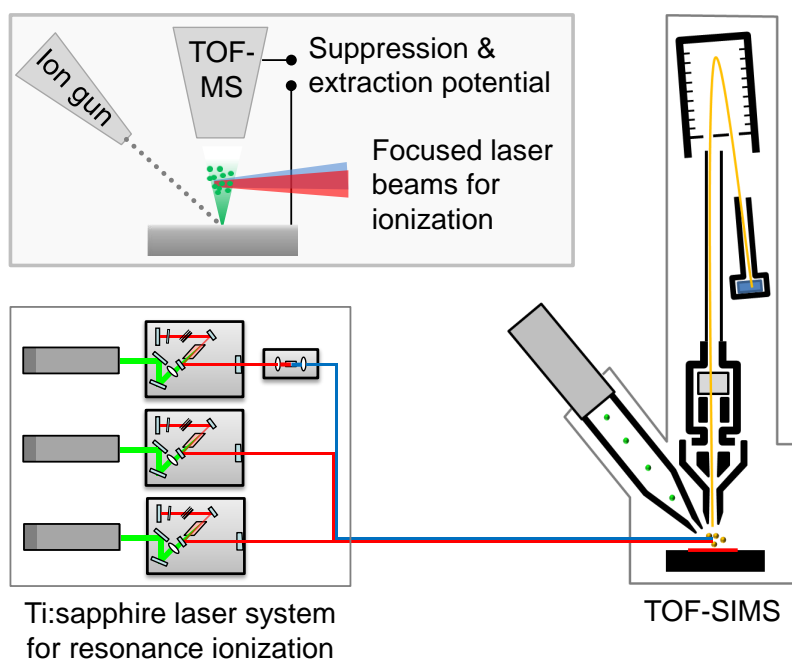


Figure 3.9: Schematic representation of the two main parts of the combined Laser-SNMS system. The upper inset shows a magnification of the sputter and ionization region.

3.3.1 Beam transport, coupling and monitoring

The overlapped laser beam of the Ti:sapphire laser system needs to be transported from the laser lab to the SIMS lab in the neighboring room. The beam transport was imple-

mented with broadband high reflective mirrors to reduce losses of any of the applicable wavelengths. The whole beam path and the mirror mounts were installed into aluminium tubes and housings for laser safety (picture in the appendix as Fig. A.10). The elevated beam guidance at 2 m height allows undisturbed access to all technical systems in both labs. The predecessor Laser-SNMS system at the university of Mainz used a fiber-based beam transport. This would deteriorate the beam profile of the transported laser and therefore increase the minimum diameter of the focused laser beams. The very strict limitation for the laser focus mention before (see section 3.1.1) were the reason for refraining from an easier maintainable fiber-based transport.

The TOF-SIMS instrument was equipped with an optical breadboard for mounting of the beam coupling setup. A wedged vacuum window made of fused silica to reduce any kind of interference with the laser beam was installed at the sidewise flange connection at the main chamber of the TOF-SIMS. Besides two high reflective mirrors for beam guiding, the coupling system consists of two iris diaphragms for fixed pre-alignment of the laser beam and a convex focusing lens ($f = 400 \text{ mm}$) on a 5-axis mount in front of the window to ensure precise adjustment of the laser focus in the TOF-SIMS instrument (picture in the appendix as Fig. A.11). The coupling setup and the beam transport is mechanically decoupled, because the TOF-SIMS instrument is floating on an air buffer system for vibration reduction. Compensation of possible drifts and the overall laser beam position optimization in the TOF-SIMS required a very sensitive beam control system. Therefore, the mirror mounts for overlapping of the three individual laser beams and the last mirror mount before coupling of the combined laser beam are equipped with additional piezo actuators. This allows central control of laser beam overlap and position as well as a future possibility for automated stabilization. Fig. 3.10 and Fig. 3.11 show the influence of the horizontal and vertical laser beam position on the Laser-SNMS ion signal. As expected, the horizontal scan shows a nearly symmetric behavior with an maximum at a piezo voltage between 40 V and 50 V for the resonant laser ion signal of U and the non-resonant laser ion signals of UO and UO₂. Small deviations from the symmetry can be explained by asymmetric laser beam profiles and the resulting asymmetric overlapped laser focus.

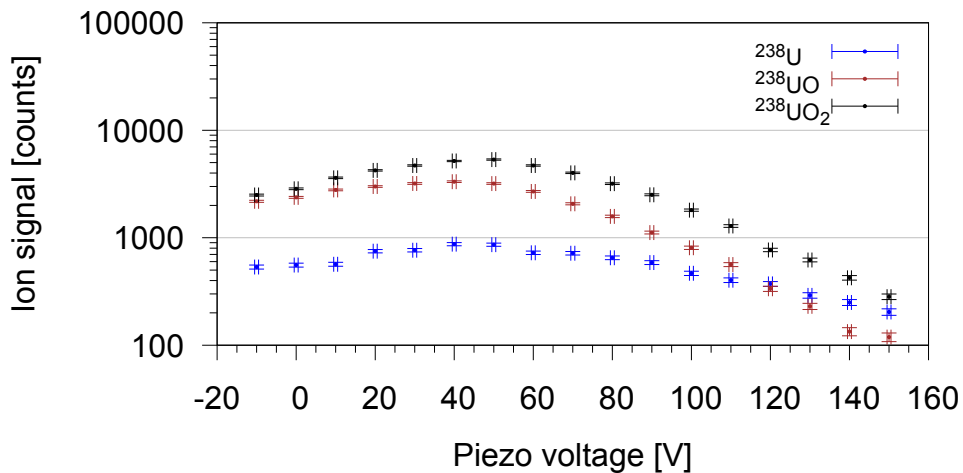


Figure 3.10: Spatial scan of the lasers in x-direction: The three scans show the dependence of the resonant laser ion signal of U and the non-resonant laser ion signal of UO and UO₂ on the horizontal position of the overlapped laser foci. (approx. $2 \frac{\mu\text{m}}{\text{V}}$)

The vertical scan of the laser beam position also shows an expected behavior. The sputtered neutral particle cloud spreads in all directions after the impact of the primary ion bunch. As a result, the highest amount of neutral atoms are in the small laser focus, if the focus position is as close to the sample surface as possible. The presented vertical scan in Fig. 3.11 does not cover the full piezo voltage range up to 150V, because the outer parts of the gaussian distributed laser foci hit the sample at 130V. Despite the lower ion signal for larger distance, the decrease of the resonant laser ion signal of U is smaller than for the non-resonant laser ion signals of UO and UO₂, due to increased ionization efficiency. The variation of the piezo voltage from 110V to 30V resulted in an ion signal decrease of 35.4% for the resonant U signal and 50.7% or 70.4% for the non-resonant laser ion signals of UO or UO₂. The actual distance of the laser focus above the sample can only be approximated by the expansion of the piezo actuator and geometrical configuration, because the system was not yet equipped with a device for direct beam position measurement in the vacuum chamber.

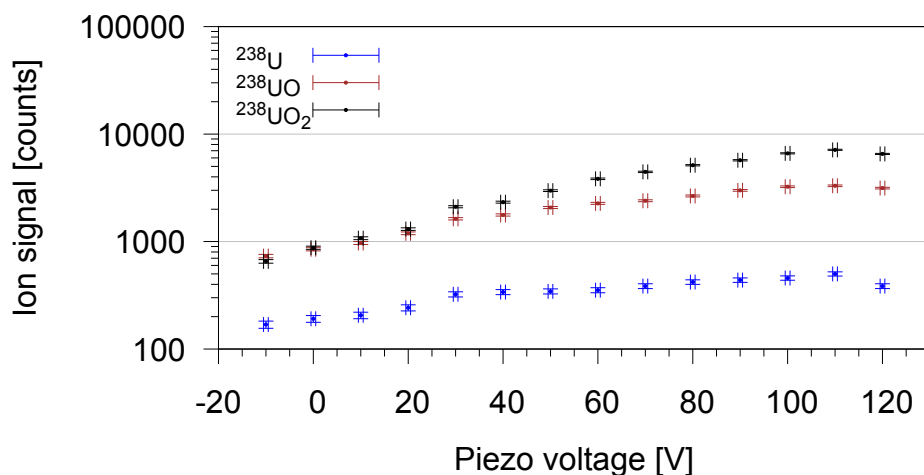


Figure 3.11: Spatial scan of the lasers in y-direction: The three scans show the dependence of the resonant laser ion signal of U and the non-resonant laser ion signal of UO and UO₂ on the vertical position of the overlapped laser foci. The higher the piezo voltage, the lower is the laser beam position above the sample surface. (approx. $2 \frac{\mu\text{m}}{\text{V}}$)

The precise control of the spatial laser beam position inside the main chamber of the TOF-SIMS instrument requires a laser monitoring system. Therefore, an additional optical breadboard was installed behind the main chamber and two cameras were mounted before and behind the TOF-SIMS instrument, as schematically illustrated in Fig. 3.12. The front camera was installed for rough laser beam position adjustment and for visual control of the sample interaction region, as reflections from the entrance and outlet windows and the laser itself prevent direct visual inspection (picture in the appendix as Fig. A.11). Besides a telescope and an iris diaphragm for sharp and clearly resolved pictures, the front camera is provided with a colored glass bandpass filter, as the laser reflections would easily destroy the camera chip. The filter suppresses the intensity of the fundamental and the SHG wavelength emission range of the Ti:sapphire laser by more than two orders of magnitude. The front camera pictures (Fig. A.13 in the appendix) show the tip of the TOF mass analyzer, the sample holder and weak or strong laser reflections, depending on the beam height.

The back camera was installed for direct beam position monitoring of the escaping laser beam behind the main chamber of the TOF-SIMS (picture in the appendix as Fig. A.12). Due to the high sensitivity of the camera sensor, only the small reflection of a beam sampler (R

$\approx 1\%$) is used, while the major part of the laser radiation hits a beam dump device. The reflected laser beam is further attenuated by four orders of magnitude in intensity via two neutral density filters before focusing on the camera sensor. The camera signal is evaluated by a LABVIEW program to determine the laser beam position relative to a fixed set position, which are both marked in the camera picture (Fig. A.14 in the appendix).

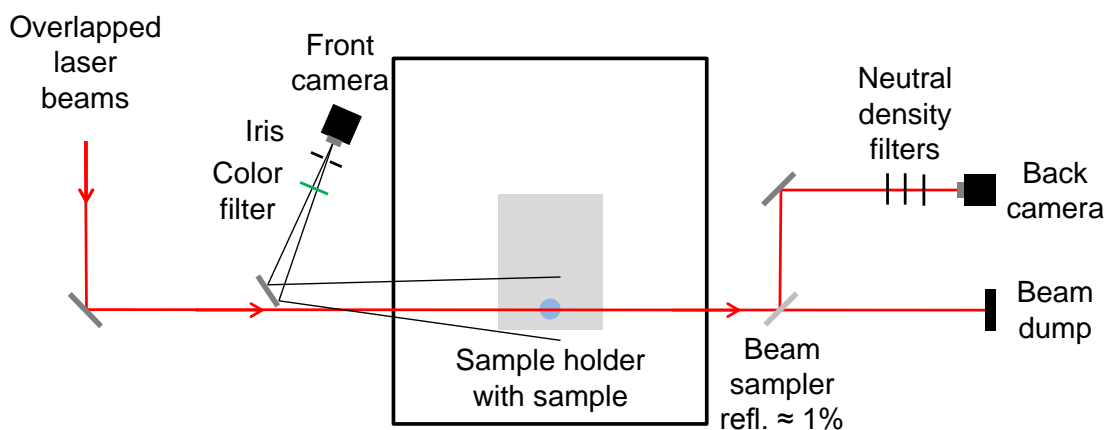


Figure 3.12: Scheme of the camera based monitoring system in top view: The scheme shows the schematic arrangement of cameras, filters and mirrors for a reliable laser beam monitoring.

3.3.2 Synchronization of all pulsed processes

The TOF-SIMS instrument with all its components as well as the laser system apply several pulsed processes, which require accurately adjusted temporal overlap for stable and efficient resonant Laser-SNMS operation. The master clock of the Laser-SNMS system is the USB-TDC unit of the TOF-SIMS instrument. This device included already the TDC detection system of the mass analyzer and the thereupon based timing system for all pulsed components. The start of every sputtering and analysis cycle is initiated by a 100 ns - 200 ns long trigger pulse of the USB-TDC. Less than 1 μ s after this initial pulse starts the generation of the primary ion pulse via a sputter species dependent sequence of the chopping, pulsing and bunching parts of the primary ion gun. The main reference point for the Laser-SNMS timing is the impact of the primary ion bunch on the sample surface. The suppression of sputtered ions, the laser ionization and the extraction to the mass analyzer must be temporally adjusted relative to this reference point. For conventional SIMS there is no laser ionization or ion suppression and the extraction potential is already applied before the impact of the primary ion bunch. Therefore, the timing and suppression sequence had to be developed, tested and optimized from scratch.

The repetition rates of both systems is basically variable but limited by different correlations. The detectable mass range of the TOF mass analyzer is defined by the maximum flight time of the sputtered ions in the system. At the maximum repetition rate of 50 kHz the detectable mass is only about 30 masses wide, but enables fast secondary ion data acquisition. The minimum repetition rate of 2.5 kHz results in a mass range of 1 u - 13760 u but with 20 times lower data acquisition. The pump lasers of the laser system can in principle be used with a repetition rate between 1 kHz - 30 kHz, although any significant change requires a readjustment for stable operation. The Ti:sapphire lasers and resonant ionization processes in particular are certainly not applicable for this entire range. A lower repetition rate than the specified 10 kHz would require reduced laser power, due to energy limitations of the mirror coatings, and would therefore constitute no advantage. A higher repetition rate reduces

the laser energy per pulse, which results in less efficient frequency doubling and requires higher power to saturate the transitions of resonant laser ionization. Consequentially, the repetition rate for the Laser-SNMS system was set to the typical value of 10 kHz, where extensive experience is existing and which allows a reliable operation of the laser system. For the TOF-MS this value gives access to a mass range of 1 u - 860 u.

Delayed extraction

Delayed application of the extraction potential is necessary for the Laser-SNMS process to acquire a temporal gap for the suppression of the sputtered ions. But the delayed extraction mode is also utilized for SIMS analysis, because it decouples the mass resolution from any influence of the primary ion pulse length [77]. For instance high lateral resolution requires smallest primary ion beam focus, which goes along with an increased pulse length. Using direct extraction, this would result in an increased uncertainty of the ionization time and therefore in a decreased mass resolution (see theory section 2.3.1). A further advantage of delayed extraction is the disappearance of shadows and shifts on ion images caused by field distortion on samples with strong topology [78]. The extraction field and the related distorted field at the surface is in that case best applied after the ions already left the surface. Nevertheless, delayed extraction reduces the amount of extracted and analyzed ions depending on the duration of the temporal delay. As essential part of the Laser-SNMS process this influence of the extraction delay on the detected ion signal was analyzed before regular application of delayed extraction for SIMS measurements on rough environmental samples. Fig. 3.13 shows the behavior of the ion signal for different extraction delays obtained on a synthetic test sample of uranium (description of the sample, see section 5.1). The five chosen ion species represent different materials of interest in the sample. Atomic uranium and its oxides are of main interest for radionuclide analysis. Copper represents light atomic species and is always present in all sample solutions. Organic species are represented by the fragment ion $\text{Si}_2\text{C}_5\text{H}_{15}\text{O}$ of polydimethylsiloxane (PDSM) at mass 147 u, which is a very mobile surface contaminant emerging from silicon oil.

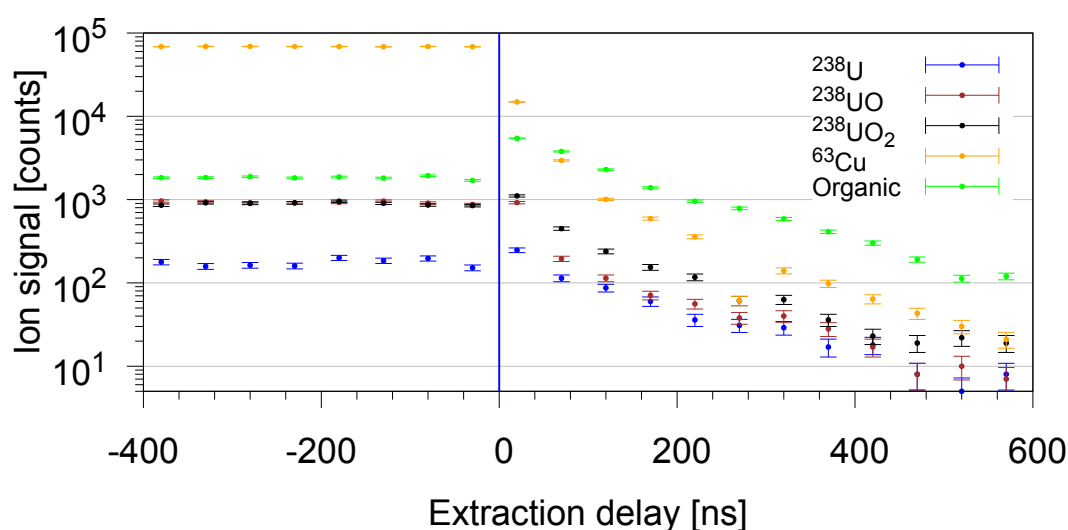


Figure 3.13: Influence of the extraction delay on the direct sputter ion signal: The graph shows the ion signal of five sputtered species as function of the applied extraction delay. The blue line marks the impact of the sputter pulse.

As expected the measured secondary ion signal decreases for larger extraction delays, but the effect is not identical for all species during the first 200 ns. The ion signal of ^{63}Cu declines faster due to its lower mass and the resulting higher escape velocity. For the other test species, the ion signal is reduced by up to one order of magnitude per 200 ns extraction delay. The short but significant increase in the ion signal of the organic species at an extraction delay of 20 ns is caused by another effect of the delayed extraction. As the alignment of the primary ion beam is adjusted for direct extraction, it compensates for a deflection by the extraction field. Stepwise delay of the pulsed extraction potential leads to a reduced deflection of the primary ion beam. As a result, the focus position of the primary ion beam is shifted on the sample surface and must be corrected for optimum alignment to the TOF mass analyzer. The surface area for the measurement, which is shown in Fig. 3.13, was sputter cleaned before by argon clusters to remove organic contamination from the surface. For delayed extraction the shift of the primary ion beam was not completely compensated. Therefore, the primary ion beam partially hits the untreated surface area with significantly higher organic contamination. The size of the shift of the primary ion beam caused by an absent extraction field without active readjustment is shown in Fig. 3.14.

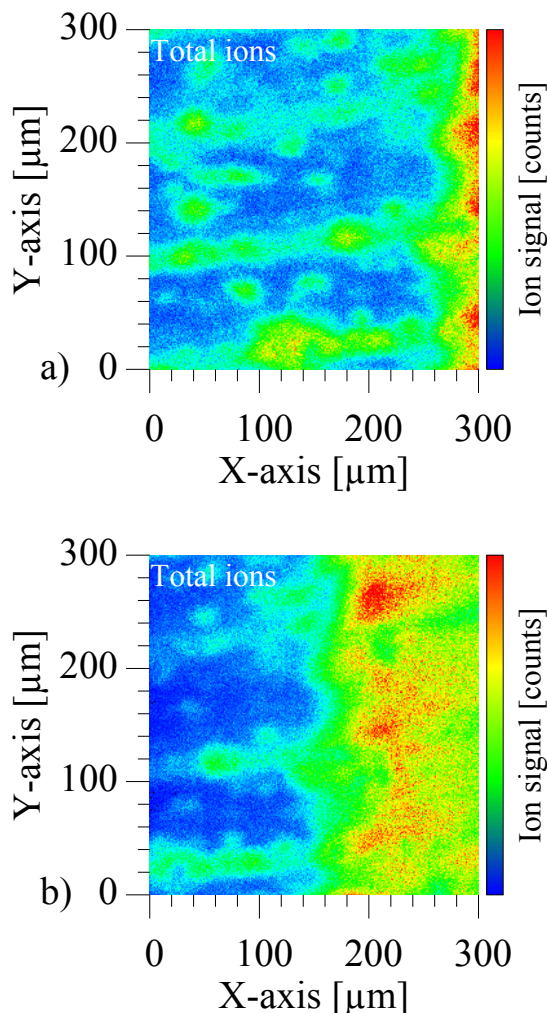


Figure 3.14: Shift of the primary ion beam position due to the absent extraction field: Ion image a) was taken with an extraction delay of -25 ns and ion image b) was taken with an extraction delay of +25 ns. The ion image is shifted by approx. 100 μm - 120 μm, if the primary ion beam is not deflected by the extraction field and no compensation is applied.

Suppression of the sputtered ions

The non-selective sputter ionized signal acts as a strong background for the element selective laser ion signal of resonant Laser-SNMS. Increased selectivity and separation of isobaric contaminations is only achieved by active suppression of all sputtered ions before resonant laser ionization of the sputtered neutrals is applied. The interaction region above the sample surface is already packed with electrodes of the different ion guns and the mass analyzer, which prevented a simple installation of a dedicated suppression electrode. Consequently, the potentials of the extraction electrode at the mass analyzer were modified to generate a suppression field for the sputtered ions and to be switched afterwards to a suitable extraction field for the laser ions. This modification did not require a complex technical arrangement, because a weak suppression field is routinely applied to repel electrons of the charge compensation process. The standard power supply delivers voltages from -500 V to $+500\text{ V}$, which allowed to investigate the influence of either a strong repelling field or a strong attractive field on the removal of sputtered ions from the laser ionization volume. The measurement, as presented in Fig. 3.15, shows the comparison of the ion signal of ^{238}U at various extraction delays for three different suppression potentials obtain with conventional SIMS. As expected, the suppression with -500 V or $+500\text{ V}$ leads to a faster decline of the ion signal after the sputtering. The most significant effect on the sputtered ion signal was achieved by an repelling potential of $+500\text{ V}$. The measured SIMS data for different ion species with negative or positive suppression is shown in Fig. B.4 and Fig. B.5 in the appendix.

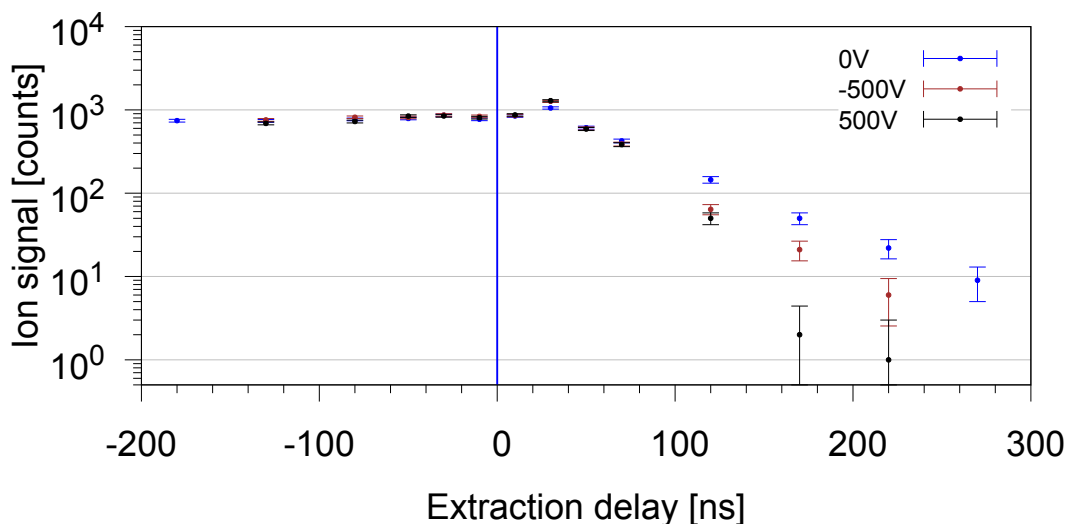


Figure 3.15: Influence of the suppression potential on the sputter ion signal: The graph shows the ion signal of sputtered ^{238}U for different applied extraction delays and different suppression potentials. The blue line marks the impact of the sputter pulse.

The graph, which is presented in Fig. 3.16, shows the influence of the extraction delay on the laser ion signal and on the residual background signal of initially sputtered ions obtained by a Laser-SNMS measurement of an uranium sample .

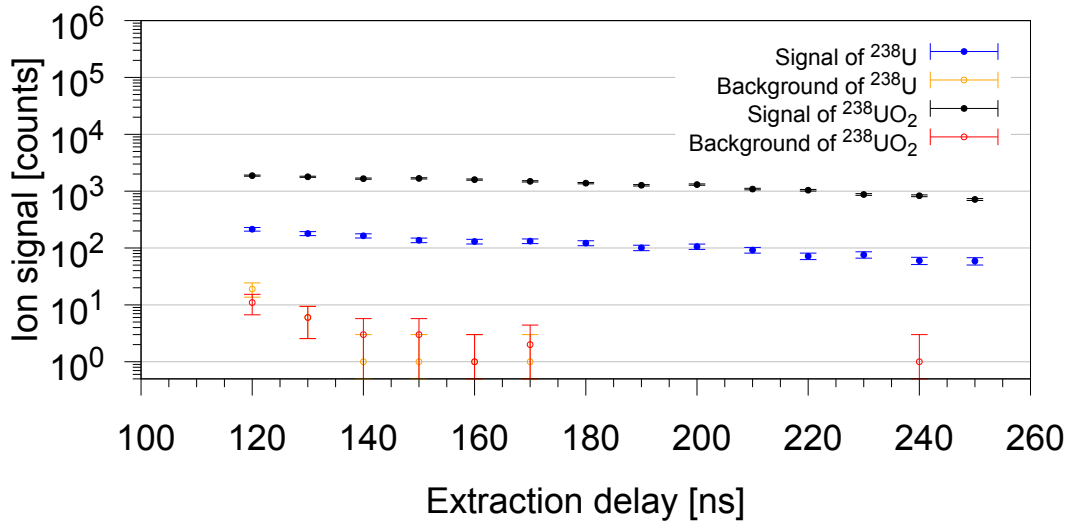


Figure 3.16: Influence of the extraction delay on the laser ion signal and the residual background: The graph shows the ion signal of laser ionized ^{238}U and $^{238}\text{UO}_2$ and the sputter ionized background on the masses of ^{238}U and $^{238}\text{UO}_2$ for different applied extraction delays. The applied suppression potential is +500 V.

This measurement with a suppression potential of +500 V demonstrates, that an extraction delay of at least 180 ns - 200 ns is required for reliable background suppression (a graph of the same measurement with neg. suppression is given in the appendix as Fig. B.6). Those test measurements were made with relatively clean synthetic samples. The expectable organic background could even lead to a larger extraction delay. As the measurements in Fig. 3.13 and Fig. 3.15 indicate, a extraction delay of 200 ns results in a loss of approximately one order of magnitude in ion signal and therefore also in available sputtered neutrals for laser ionization. A shorter extraction delay can be achieved with an increased suppression field. The necessary change of the fully embedded power supply, could not be realized in this work.

A further problem is the influence of the suppression potential on other processes of the SIMS instrument. The potential of +500 V is also applied during the charge compensation via an electron flood gun, due to the invariable sequence in the control software. The attraction of the strong potential prevents application of the electrons ($E_{kin} = 20\text{ eV}$) to the sample surface. Consequently, the charge compensation of non-conductive samples is not applicable for Laser-SNMS measurements without modification of the IONTOF control software.

Synchronized laser ionization

The temporal adjustment of the individual lasers via a precise pulse generator and a fast oscilloscope was already described in section 3.1.2. This system was extended for synchronization of the laser system to the TOF-SIMS instrument. The initial pulse of the USB-TDC unit in the TOF-SIMS is used as trigger pulse of the pulse generator of the laser system. Both, the primary ion gun as well as the laser system involve more than $3\ \mu\text{s}$ reaction time after the initial trigger pulses, which have to be synchronized with a precision of few ns. A further signal of a temporally closer lying reference point was required from the TOF-SIMS for monitoring relative to the Ti:sapphire laser pulses on the fast oscilloscope. This was generated by an inductive probe as signals from the timing of the ion impact on the sample surface or alternatively the pulsed extraction potential were not accessible. The extraction electrode of the TOF mass analyzer is connected to a pulsing device, that switches between

the suppression voltage of +500 V and the extraction voltage of -1000 V to -3000 V with a short gap of 50 ns - 70 ns at 0 V ground potential in between. The fast shift of high voltage potential in a few ns leads to a measurable magnetic field pulse on the connection cable. The inductive probe, which was attached to the cable, delivered a reliable signal for the extraction timing (photo of the measured oscilloscope signals in the appendix as Fig. B.7).

The temporal shift between the pulsed extraction and the laser pulse, referred to as laser delay, was analyzed for optimization of the timing of the Laser-SNMS process. The influence of the laser delay on the resonantly ionized signal of ^{238}U and the non-resonantly ionized signal of $^{238}\text{UO}_2$ is presented in Fig. 3.17. The highest amount of detected ions referring to the optimum laser delay was measured at -30 ns in respect to the application of the extraction voltage. The high signal decline below a laser delay of -60 ns is caused by the suppression potential. The slightly decreasing ion signal for higher laser delay results from the increasing amount of sputtered neutrals, which already have left the laser ionization volume. Depending on application it could be necessary to shift the laser delay towards a value of -60 ns, because this offers higher mass resolution (picture of the measured mass resolution in the appendix as Fig. B.8).

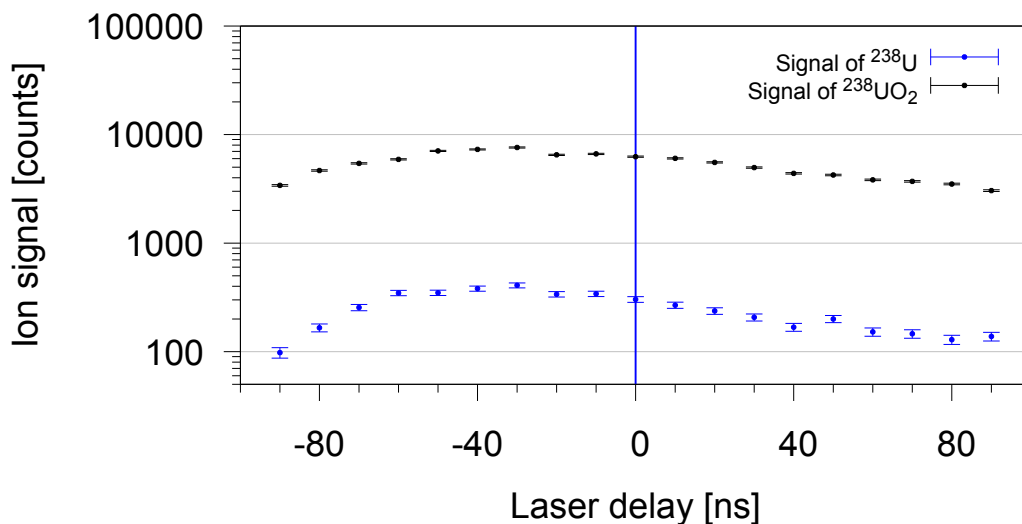


Figure 3.17: Influence of the laser delay on the resonant and non-resonant laser ion signal: The graph shows the ion signal of laser ionized ^{238}U and $^{238}\text{UO}_2$ for different applied laser delays. The blue line marks the activation of the extraction potential.

The analysis of the extraction delay at different suppression voltages and for different laser delays resulted in an optimized temporal sequence for the Laser-SNMS process, as shown in Fig. 3.18. The chosen extraction delay of 200 ns after the primary ion impact leads to a sufficient suppression of sputtered ions with a potential of +500 V followed by a resonant laser ionization 30 ns before the extraction of the laser ions to the TOF mass analyzer.

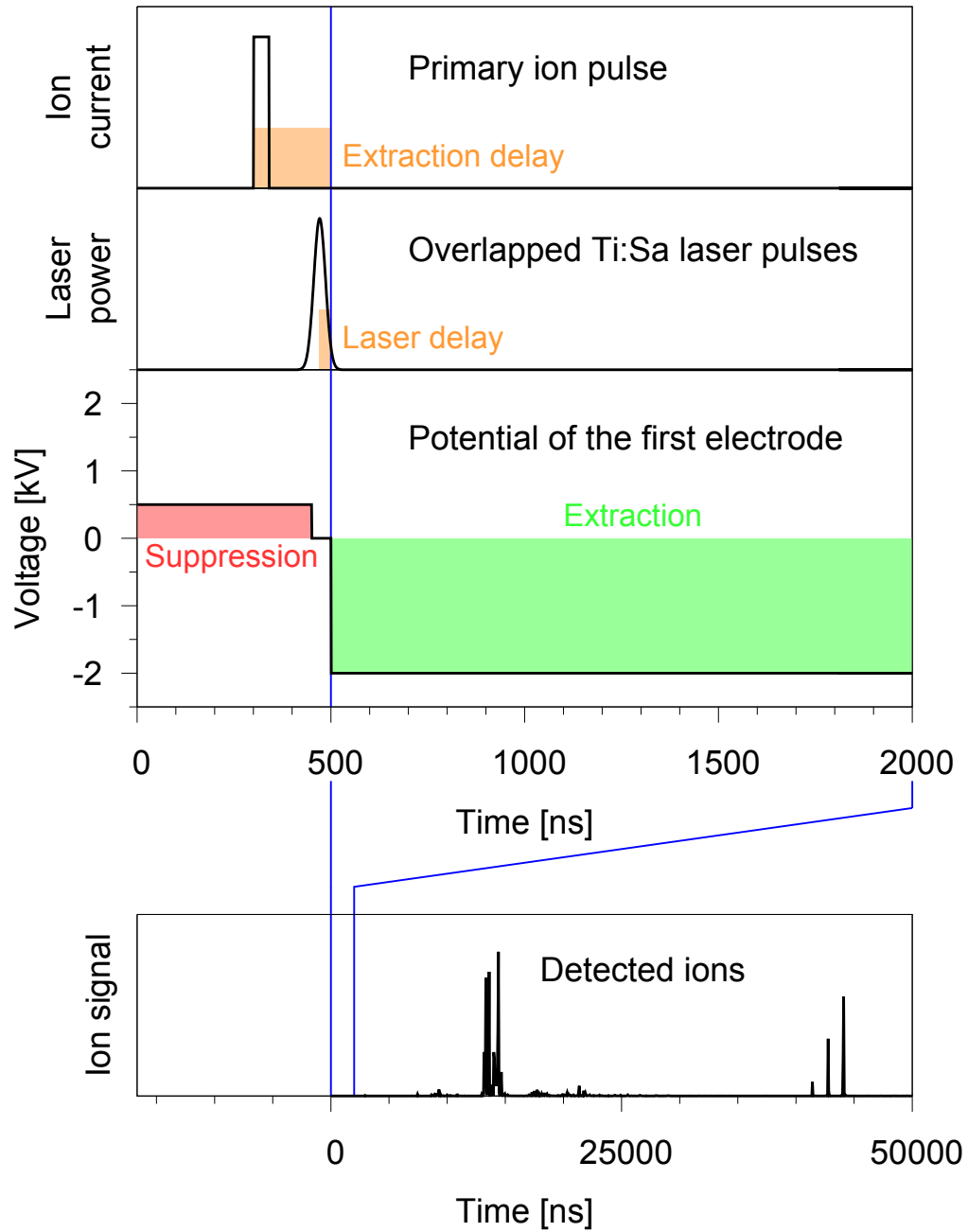


Figure 3.18: Relative temporal sequence of the pulsed processes for Laser-SNMS: The graph shows the optimized timing of the primary ion pulse, the temporally overlapped laser pulses, the potential of the first electrode and the detected ion signals relative to the point of extraction. This sequence is repeated with a rate of 10 kHz.

SIMULATION BASED OPTIMIZATION

The Time-of-flight mass analyzer, which is installed in the TOF-SIMS instrument, was designed and tuned for conventional SIMS with high mass resolution. The main difference between SIMS and Laser-SNMS is the size and the position of the ionization volume. The secondary ions, which are produced by sputter bombardment, originate from a small spot on the sample surface. Generation of the laser ions takes place above the sample surface in a much larger volume. Expansion and repositioning of the acceptable ionization volume requires extensive correction of the mass analyzer configuration for adaption. For ultra-trace analysis, the highest transport efficiency is of primary concern to reach the envisaged sensitivity. The transport characteristic of the TOF mass analyzer is defined by a multidimensional system of six parameters. Coupling of those parameters by strong interrelations inhibits a stepwise manual adjustment for ion signal enhancement. Consequently, the adaption of the TOF mass analyzer for efficient resonant Laser-SNMS requires an simulation-based analysis and optimization of the multidimensional parameter space.

Realization of the simulation-based optimization was achieved with a Monte Carlo approach by sending a large number of simulated ions through a simulated mass analyzer. The development of the optimization process was separated into three parts. Ion trajectories in the mass analyzer are mainly influenced by the starting conditions. Initial simulation of the development and behavior of a sputtered neutral particle cloud for the subsequent resonant laser ionization process was therefore necessary. Manipulation and analysis of the ion trajectories were provided by a precise simulation model of the TOF mass analyzer. The combination of the simulation of laser ions and the model of the ion optical configuration of the mass analyzer formed the basis for the iterative optimization program. These three steps of the simulation process are described in detail in the following chapter.

4.1 Simulated Sputtered Particle Cloud

Besides providing the start parameter for the optimization, the simulation of a sputtered and laser ionized particle cloud enabled the determination of its spatial and temporal expansion behavior after the impact of the primary ion bunch. The simulation program is based on the theoretical standard concept for a linear cascade regime (see theory section 2.1). The kinetic energy of the primary ions forms collision cascades, that result in characteristic angular and energy distributions of the sputtered neutral particles, as specified in Eq. 2.3 and 2.4 in the theory chapter. The sputtered ionization and the suppression process was neglected to reduce the complexity of the simulation program. Interactions inside the laser ionized particle cloud and the analysis of the ion behavior for all timing configurations required addition of the temporal distribution for simulating the point of ionization. A measurement

of the intensity distribution of a Ti:sapphire laser pulse was used for consideration of the temporal behavior instead of a theoretical concept. For the Monte Carlo simulation, the measured distribution was reproduced qualitatively on the basis of a squared hyperbolic secant distribution, which matches a laser pulse better than a Gaussian distribution:

$$P(t) = P_{peak} \cdot \operatorname{sech}^2\left(\frac{t}{\tau}\right) \quad (\tau: \text{pulse duration}) \quad (4.1)$$

However, the temporal distribution of the real laser pulse is asymmetrically deformed by the steady imbalance of gain and losses in the gain-switched laser resonator. Addition of an asymmetric term in the simulated distribution led to matching of the pulse distribution with the pulse duration factor τ ($\tau = 0.57 \cdot \text{FWHM}$):

$$P(t) = P_{peak} \cdot \frac{1}{\sqrt{1 - \tanh\left(\frac{t}{\tau}\right)}} \operatorname{sech}^2\left(\frac{t}{\tau}\right) \quad (4.2)$$

The implementation of the distributions with a Monte Carlo approach to generate the sputter cloud simulation was done on the basis of programs of other groups in the field [79][72].

4.1.1 Simulation program "Ionengenerator"

In this work the simulation program "Ionengenerator" was developed. It provides specific and simple control of the simulation environment and is applicable for future simulations without the necessity of programming skills. "Ionengenerator" (German for ion generator) was written in the platform independent programming language Java on the popular editor "Eclipse". Fig. 4.1 shows the simple graphical user interface (GUI) of the simulation program. Before the simulation starts, the program requires several parameters for definition of the process. The laser ionization region is simplified by a cylindrical volume, with a certain length, diameter and height above the sample surface. Further configurable parameters are the species of the generated ion cloud with natural isotopic abundance, the related surface binding energy, the drift time of the sputtered neutrals till laser ionization, the primary ion pulse length, the charge state (only modified for SIMS simulations) and the number of sputtered neutral particles. After the input of all required parameters, the program is started and goes through three individual parts of the simulation. At first, the entered parameters are read in and verified for correctness. Generation of sample ions for the Monte Carlo simulation is the second process of the program. Therefore, every generated neutral particle is randomly assigned with a mass, a kinetic energy, a direction and the moment of sputtering, which is calculated by the quantile functions of the different distributions. Additionally, the program calculates if the sputtered neutral particle overlaps spatially and temporally with laser pulse and is consequently ionized. The last part of the program writes all informations in four different files. The info file includes the start parameters of the simulation. Lists of the generated neutrals and ions with all parameters are written in two ASCII files. The last file consists of the list of generated ions formatted for direct application in the ion trajectory simulation software SIMION.

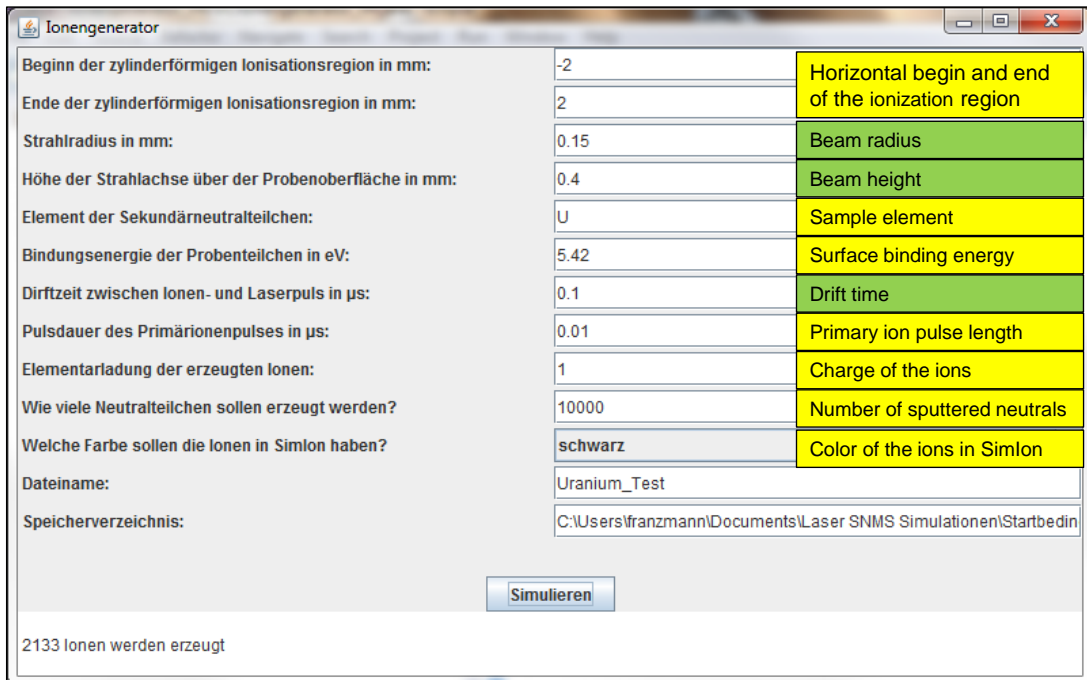


Figure 4.1: GUI of the "Ionengenerator" software: The graphical user interface (GUI) allows to adjust different parameters of the simulated particle cloud. The green marked parameters were most frequently adjusted, while the yellow marked parameters were almost always kept. After input of all required parameters, the simulation is started by clicking the "Simulieren"-button. Afterwards, the bottom text field shows the number of generated ions.

For verification of the simulation program, the generated ion clouds were analyzed for their energy, angular and temporal distribution. The comparison of the theoretical Sigmund-Thompson energy distribution with the binned simulated energy distribution of the sputtered neutrals demonstrates the expected matching behavior, as shown in Fig. 4.2.

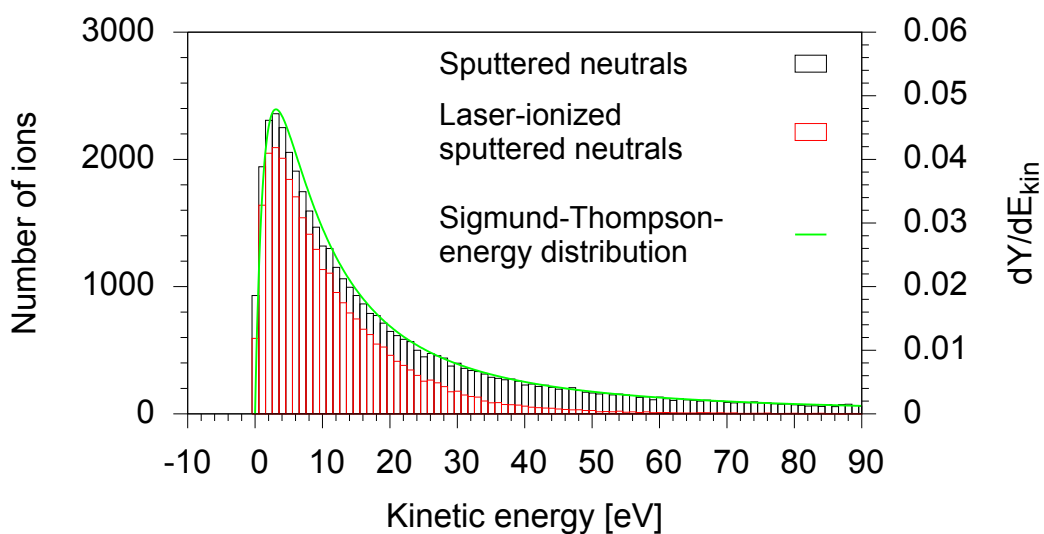


Figure 4.2: Comparison of the theoretical and simulated energy distributions: The graph shows the simulated kinetic energy distribution of all sputtered neutrals and the laser-ionized fraction of the sputtered neutrals in comparison with the Sigmund-Thompson energy distribution.

A comparison with the simulated energy distribution of the generated laser ions at optimized parameters revealed, that only the low energy part of the sputtered neutrals gets ionized, because the high energy part already left the laser interaction volume before the laser pulse arrives. The compared angular distributions (shown in the appendix as Fig. B.9) on one side confirm the expected cosine behavior of the simulated sputtered neutrals but on the other side reveals a deviation from the cosine distribution of the laser ions, due to the influence of the cylindrical ionization volume. The simulated temporal distribution of the ionization point (shown in the appendix as Fig. B.10) matches the measured intensity distribution of a Ti:sapphire laser pulse sufficiently.

4.1.2 Expansion behavior and overlap

Analysis of the simulated expansion behavior of the sputtered neutral particle cloud as well as the test of different overlap configurations with the laser focus supported the development of optimized operational coupling parameters. As the simulated energy distribution indicated, the important part of the sputtered ion cloud are the low energy ions in the lower center, which also show the largest particle density, as apparent from the 3-dimensional representation of the simulated cloud in Fig. 4.3.

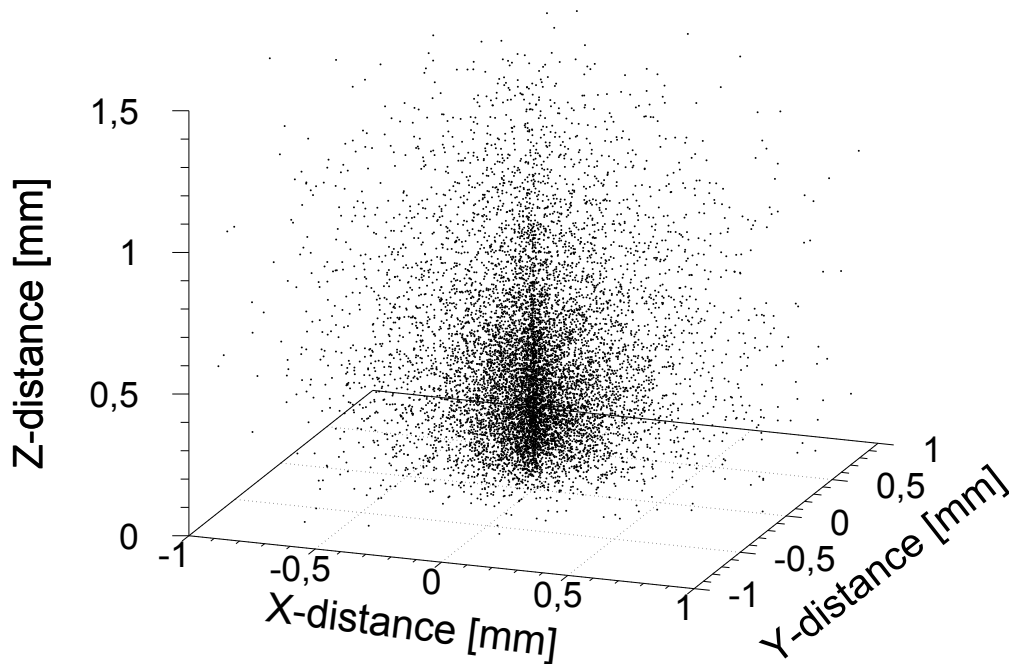


Figure 4.3: 3D representation of the expanded ion cloud from the simulation after an expansion time of 100 ns.

The analysis of the expansion behavior focused on the drift time of this dense center towards the extraction electrode. The main difference in comparison with other Laser-SNMS setups is the short distance of 1.5 mm between the sample surface and the first electrode of the mass analyzer for high resolution SIMS. After passing this distance, the sputtered neutrals are lost for ionization or analysis. As shown in Fig. 4.4, the outer parts of the sputtered

neutral particle cloud reach the extraction electrode after approximately 250 ns. The dense center follows after approximately 500 ns, but is already too far expanded for a sufficient overlap with the focused laser beam.

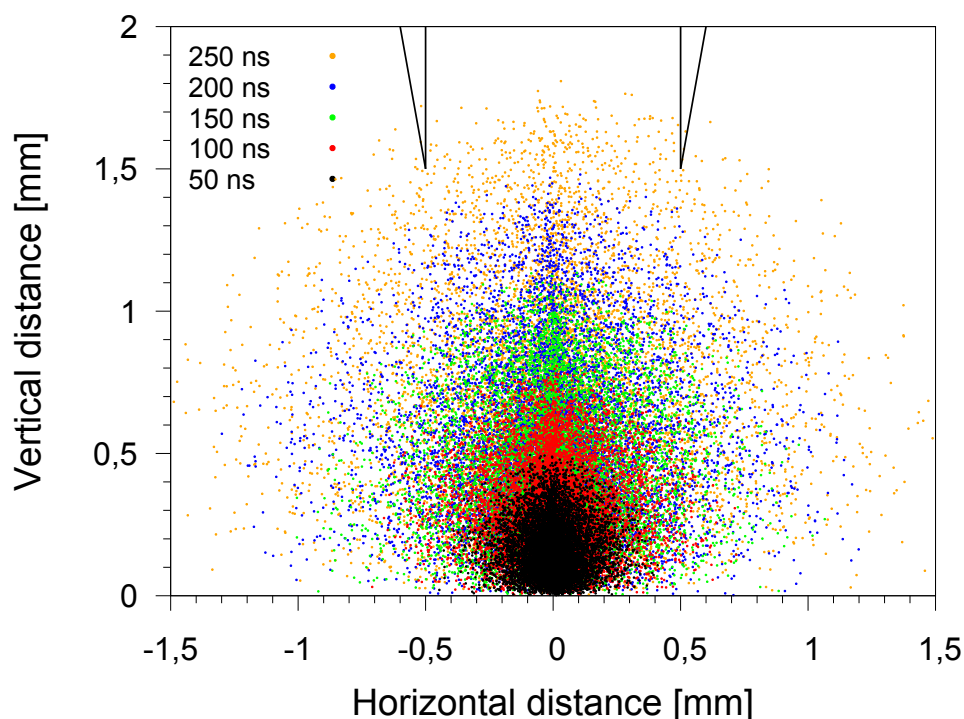


Figure 4.4: Expansion behavior of the simulated cloud: The plot shows a comparison of the simulated spatial distribution of a sputtered neutral particle cloud for different expansion times. The black structure above the cloud is a sectional view of the tip of the extraction electrode.

The operational parameters are limited by technical specification. In section 3.3.2 is described, that a sufficient suppression of the background by sputtered ions and the switching to the extraction potential takes at least 200 ns. The focus of the laser beam for resonance ionization is required to be $\leq 300 \mu\text{m}$. The small interaction region between ionization lasers and the neutral particles reduce the spatial distribution of the generated ions, which is strongly related to the mass resolution of the TOF mass analyzer. Furthermore, the envisaged ultra-trace analysis requires saturated optical transitions for highly efficient ionization. An increased diameter of the laser beam focus leads to a reduction of the photon density in the interaction region, which decreases the ionization efficiency. An additional limit is set by the imperfection of the overlap of the laser beams. The laser focus is always surrounded by an low energy halo generated by scatter and distortion effects of imperfect optical elements. Preventing of surface interaction via heating is achieved by a minimum distance of the laser beam of approximately $100 \mu\text{m}$. Nevertheless, the determination for optimized operational parameters slightly exceeded those limitations for a complete overview and understanding of the involved processes. Therefore, Fig. 4.5 shows the simulated ionization yield for a drift time of 20 ns - 400 ns at different laser beam heights of $200 \mu\text{m}$ - $500 \mu\text{m}$ with a laser focus diameter of $300 \mu\text{m}$. The ionization yield is at the same level of 15 % for the beam height of $300 \mu\text{m}$, $400 \mu\text{m}$ and $500 \mu\text{m}$ at the minimum drift time of 200 ns. The same simulations with extended laser focus diameter (shown in the appendix as Fig. B.11 and B.12) show a slightly improved yield for $400 \mu\text{m}$ beam height, which also leaves enough space for any kind of possible topology of environmental samples. The significant increase

in the ionization yield for the extended laser focus diameter is unfortunately not realistic, because the simulation excludes the reduced photon density.

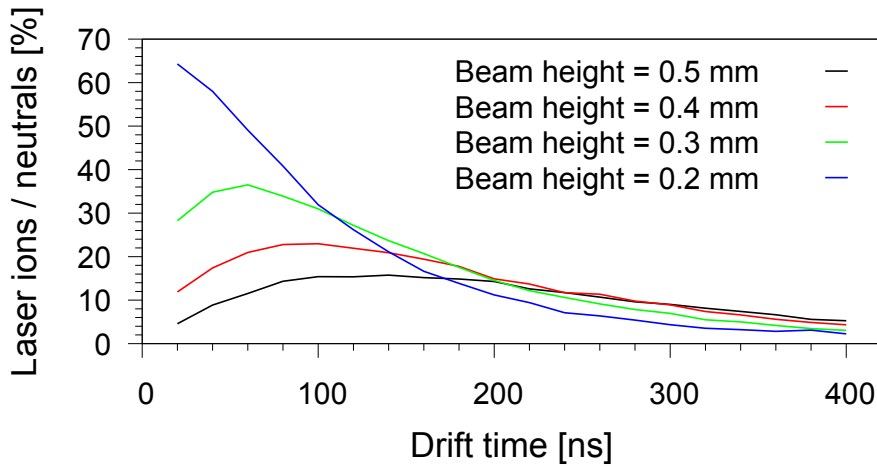


Figure 4.5: Ionization yield for different beam heights: The graph shows the dependence of the ionization yield from the drift time of the neutral particle cloud at different laser beam heights for a laser focus diameter of $300\ \mu\text{m}$.

The final configuration of operational parameters for the overlap are shown in Fig. 4.6. The achieved insufficient overlap, that only includes 15 % of the sputtered neutral particles, could be enhanced by a shorter drift time, which requires a stronger suppression of sputter ions, or by an increased laser focus with analysis of the influence on ionization efficiency and mass resolution.

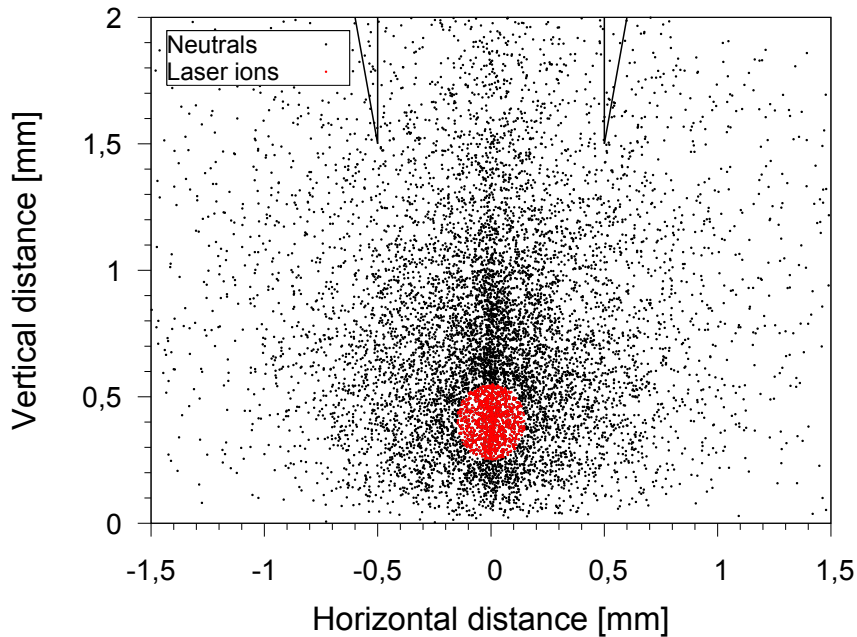


Figure 4.6: Overlap of the ionization lasers and the sputtered particle cloud: The plot shows the sputtered neutral particle cloud (black) with the fraction of laser ionized particles (red) with the chosen operational parameters of a drift time of 200 ns, a beam height of 0.4 mm and a beam diameter of $300\ \mu\text{m}$.

4.2 Mass Analyzer Simulation Model

Development of the simulation model, which covers the main components of the TOF mass analyzer, was based on technical drawings of the real instrument. The technical drawings and other specifications were provided by the IONTOF GmbH for this work and are not described in detail, due to industrial confidentiality. Transfer of the drawings into a simplified 3-dimensional CAD model in "Autodesk Inventor", shown in Fig. 4.7, reduced the complexity of the system and enabled to expose the important ion optical structures, which guides the extracted ions through the mass analyzer.



Figure 4.7: 3D representation of the TOF mass analyzer (simplified) including the main ion optical components based on the technical drawings and created by "Autodesk Inventor 2014".

The next part of the model development for the simulation included the transformation of the CAD model to a grid structure model for the ion optics simulation software SIMION. The grid based potential arrays for SIMION were programmed manually via geometry files for a number of reasons. The automatic import of CAD models with SIMION 8.1 was insufficient for the required high precision, because rounding errors during the transformation led to distorted structures like unsymmetrical apertures (pictures shown in the appendix as Fig. B.13). Another reason was the limited storage capacity of 16 GB RAM. The TOF mass analyzer is nearly 1 m long but includes structures of only 1 mm size. The necessary resolution of this structures requires an even smaller grid size, which results in a model size that exceeds the storage capacity. Therefore, the simulation model was split into four parts with different grid sizes relative to the smallest included structures:

1. Front part till the flight tube aperture
2. Reflectron
3. Post-accelerator with detection
4. Middle part, that connects the other three parts

This was possible, because the connecting regions are each on a fixed potential. On top of this approach, the major influence on a reduced memory requirement was achieved by the programmed model generation. The geometry files allow to add symmetries to the generated potential arrays. Consequently, the modeling and calculation of all rotational symmetric structures, like the first electrodes, the reflectron and the post-accelerator, is reduced to a section of the structures and extrapolated for the rest by the simulation software. The automatic import function for CAD models does not identify symmetries and was therefore not used. Additionally, the manually programmed model was further simplified by removing unsymmetrical structures on the outside of the mass analyzer model. At the end only the

important inner structures, which define the electric fields, identically represented the real mass analyzer. The resulting simulation model is shown in Fig. 4.8.

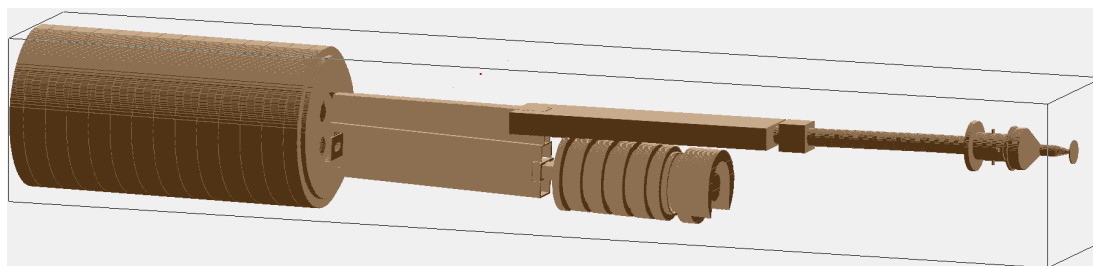


Figure 4.8: 3D simulation model of the mass analyzer: The drawing shows a three-dimensional view of the simulation model in SIMION 8.1. The model of the mass analyzer is defined by a geometry file, which was written according to the informations extracted from the technical drawings provided by IONTOF.

After the generation of the simulation model, SIMION determines the potentials between the different electrodes by solving the Laplace equation with finite difference methods. The resulting model with all potential fields of the mass analyzer is fast adjustable by addition and variation of the real electric potentials and calculates the trajectories of 10 000 ions in a few seconds. In Fig. 4.9 a cross section through the mass analyzer model is presented including 10 000 calculated ion trajectories.



Figure 4.9: Simulated ion trajectories through the mass analyzer: The drawing shows a cross section of the mass analyzer in SIMION 8.1 with trajectories of 10.000 sample ions.

4.3 Optimization Procedure

For laser ions only 6.7% overall transport efficiency through the simulated mass analyzer was determined with conventional SIMS parameters. Therefore, a variation and increase of the acceptance region to include the laser ionization volume was essential. Optimization of the TOF mass analyzer was achieved by stepwise analysis of the relations between the six potentials, which are of highest importance for the ion trajectory. The first three potentials define the shape of the overall ion trajectory by forming an ion optical Einzel lens. The first part is the suppression/extraction electrode, which also defines the start energy of the ions as well as their energy distribution. The middle part of the Einzel lens structure is a ring electrode, which determines the focus of the transported ion ensemble. The drift tube potential specifies the kinetic energy of the ions during the flight through the rest of the instrument and acts as final part of the Einzel lens structure. Additional deflection plates allow to manipulate the flight direction of the ions in X- and Y-direction. The X-deflection is irrelevant for the perfectly adjusted simulation model, but necessary in the real instrument for corrections. The Y-deflection guides the ions in the correct angle through the flight tube and into the reflectron. An additional option of mass analyzer adjustment is given by the potential between the flight tube and the entrance plate of the reflectron. This so called virtual drift path (VDP) decelerates the ions for a slower movement through the residual

part of the system. The reflectron redirects the ion trajectories and reduces the energy dispersion of the transported ions to increase the mass resolution, as described in section 2.3.1. Although it consists of several ring electrodes, its adjustment is defined only by the potential of the back plate at the end. The other potentials are determined by the fixed resistor chain, which is attached to all ring electrodes up to the entrance plate and which leads to equal potential differences between neighboring electrodes. After passing of the reflectron the ions fly through another drift passage until they enter the post-accelerator. Acceleration of the ions to 11 keV ensures the detection of every ion, that reaches the channelplate at the end of the mass analyzer. The potentials of the post-accelerator and detection were indirectly adjusted, because the first electrode of this structure is always on the same potential as the drift tube, while the others are adjusted relative to the first electrode and the fixed end potential. The potentials of extraction, ring lens, drift tube, Y-deflection, virtual drift path and reflectron back plate are the six strongly correlated parameters, which define the ion trajectory. A schematic representation of the TOF mass analyzer with all described structures is shown in Fig. 4.10 and Fig. 4.12.

4.3.1 Optimization program

Detailed iterative optimization within the six-dimensional parameter space required a control program for the simulation process. The SIMION software offers control, verification and evaluation of the simulation data via fully embedding of the LUA programming language. The LUA code enables a free programmable adjustment of the simulation model with all necessary program structures for the iterative process, providing functions, loops and conditional statements. After execution of the TOF-SIMS.lua program, the potentials of all electrodes are calculated based on default values for the six central parameters and the simulation starts to calculate the trajectories of the 10 000 arbitrarily chosen laser ions. At the end of the simulation, all ions that passed specified interrogation points are counted separately by the evaluation function. The subsequent routine exports the results of the evaluation and optionally gives a list of all ions in a text file. In the last part of the sequence, one of the central parameters is changed and the control program starts again. Therefore, this program allows for automatic coverage of a large parameter space. Nevertheless, the automatic processing of the whole parameter space at once would require an enormous computing capacity or a calculation duration of several years. Reduction to investigation of three specific parameters at once decreased the calculation time to several days, but required a stepwise correlation analysis.

4.3.2 Correlation analysis

Simultaneous variation of three main parameters in a dedicated parameter space including 10 000 - 20 000 simulation runs resulted in sufficient amount of data for statistical analysis of the parameter correlations. The first processed parameter space included the three einzel lens components: extraction potential, ring lens and drift tube. The achieved simulation results of this parameter scans were analyzed regarding extraction efficiency, transmission through test point 1 and a small ion beam focus at the limiting aperture. The test points for different requirements are shown in Fig. 4.10. The highest extraction efficiency of 60.6 % was obviously achieved with the strongest extraction potential of -2 kV. Further evaluation showed, that the highest transmission up to test point 1 is not connected to the highest extraction efficiency. Optimum operation of the first three electrodes should result in a high transmission to test point 1 and a small focus at the limiting aperture inside the drift tube. The evaluation of operational parameters for a transmission above 30 % and a focus diameter below 2 mm resulted in different parameter spaces with only a small overlap

(shown in the appendix as Fig. B.14). Correlated behavior was found for the potentials of extraction electrode and ring lens without a distinct optimum point of operation. Separate evaluation of the drift tube potential instead resulted in a clear maximum combining high transmission and small focus diameter at -3 kV (shown in the appendix as Fig. B.15).

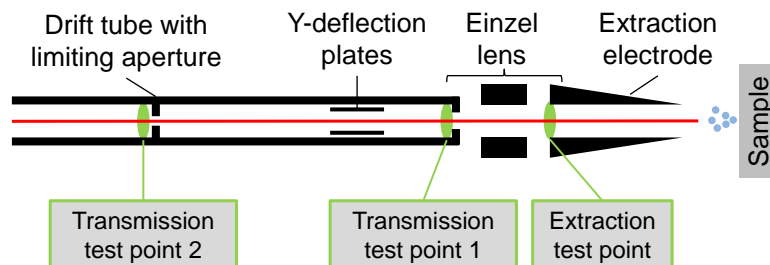


Figure 4.10: Electrodes (black) and test points (green) in the first half of the TOF mass analyzer used in the optimization process.

The second simulation run involved a scan through the parameter space of extraction potential, ring lens and Y-deflection on a fixed drift tube potential. At first, the evaluation of the simulation data aimed for highest transmission up to test point 2, which was determined to 40 %. Analysis of the overall efficiency for this simulation demonstrated, that the highest efficiency once again is not achieved at highest transmission through the aperture, but a small focus is explicitly required. The dependence of focus, transmission and efficiency is presented in Fig. 4.11.

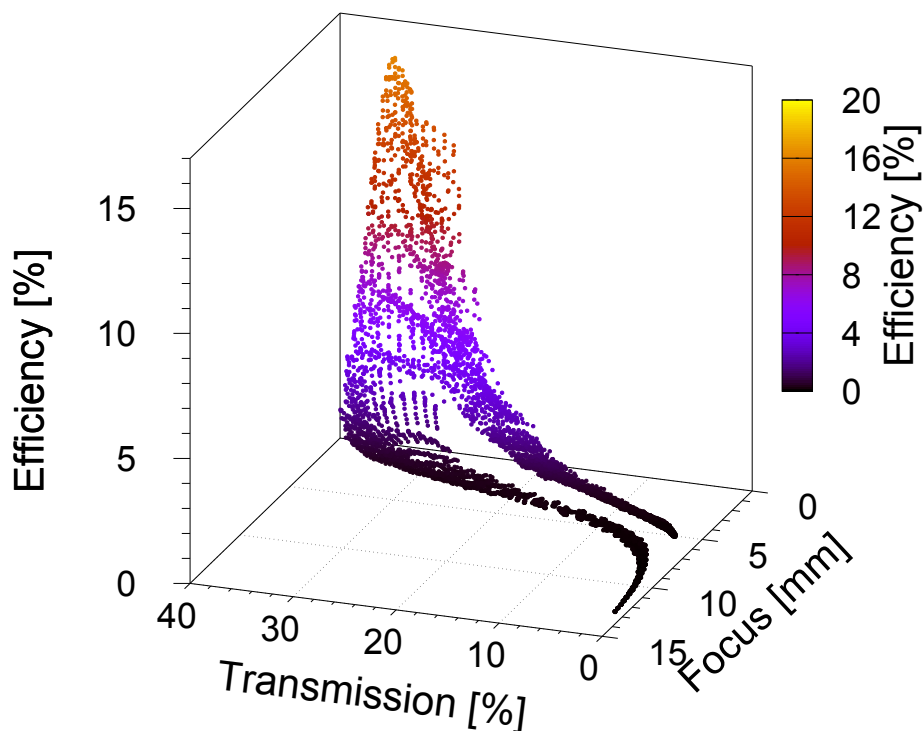


Figure 4.11: 3D plot of the dependence of the ion beam focus at the limiting aperture, the transmission to test point 2 and the overall transport efficiency as function of the potentials of extraction, ring lens and Y-deflection.

The modified evaluation for sufficient transmission and highest efficiency revealed a strong correlation between the extraction potential and the ring lens potential (shown in the appendix as Fig. B.16). The Y-deflection showed only a lower influence in the defined parameter space instead. Application of an exponential fit function to the most efficient parameter combinations led to Eq. (4.3) for the correlation of the first two electrodes (shown in the appendix as Fig. B.17).

$$U_{Einzellens} = 9028 \text{ V} \cdot e^{\left(\frac{U_{Extraction}}{1129 \text{ V}}\right)} - 7118 \text{ V} \quad (4.3)$$

Determination of the extraction potential for highest efficiency was the aim of the third simulation run. Besides the extraction electrode, the parameter space was defined by the potentials of the Y-deflection and the reflectron, because those two potentials have the strongest influence on the trajectory. The evaluation of the simulation data resulted in an maximum efficiency at an extraction potential of -1450 V (shown in the appendix as Fig. B.18). Determination of the optimized potentials for the Einzel lens structure reduced the overall parameter space of the mass analyzer to three potentials. This prepared the final determination of the optimized parameters for Y-deflection, virtual drift path and reflectron back plate in a fourth simulation run. The resulting potentials of all reflectron electrodes define the ion trajectory through the rear part of the mass analyzer as shown in Fig. 4.12. Data evaluation of these final simulations resulted in optimized potentials of -400 V for the virtual drift path, 300 V for the reflectron back plate and a Y-deflection of 15.40 % (shown in the appendix as Fig. B.19 and B.20). The specification in % for the Y-deflection refers to the SIMS control program and corresponds to a maximum of $\pm 125 \text{ V}$ potential difference on the deflection plates towards the drift tube potential. All resulting parameters of the six main potentials and the achieved overall efficiency are summarized in Tab. 4.1.

	Conventional parameters for SIMS	Optimized parameters for Laser-SNMS
Extraction potential	-2000 V	-1450 V
Lens potential	-4870 V	-4619 V
Acceleration potential/ drift tube potential	-2000 V	-3000 V
Y-deflection	16.05 % ($\pm 20.06 \text{ V}$)	15.40 % ($\pm 19.25 \text{ V}$)
Virtual drift path (VDP)	-153.6 V	-400 V
Reflectron back plate	20 V	300 V
Efficiency (simulated)	6.7 %	16.6 %

Table 4.1: Comparison of conventional and optimized parameters for the TOF mass analyzer: The values of the main parameters are listed for the conventional SIMS settings and in comparison for the optimized Laser-SNMS settings determined by simulations. An increase of a factor 2.5 was achieved.

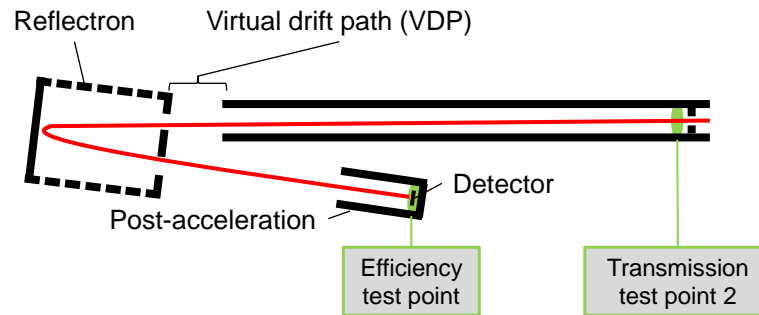


Figure 4.12: Electrodes (black) and test points (green) in the second half of the TOF mass analyzer used in the optimization process. The red line indicates the trajectory of the transported ions in the instrument until their detection at the end.

4.4 Verification of Optimized Parameters

All assumptions and simplifications made in the simulation of the sputtered ion cloud as well as limited resolution of the SIMION model necessitate the verification of the optimized parameter set of the TOF mass analyzer by experimental measurements. Comparison of the conventional parameters and the parameters optimized for Laser-SNMS were performed for the isotopes ^{238}U , ^{99}Tc and ^{239}Pu (specifications of the samples are described in sections 5.1, 5.3 and 6.1). The fast software supported change of previously defined parameter sets allows a direct comparison during the same measurement with a switchover time of a few seconds. Therefore, all comparison measurements were made on the identical spot of the respective sample with the same measurement configuration for conventional and optimized parameters. Fig. 4.13 shows the Laser-SNMS mass spectra of an uranium sample in comparison of both operation modes.

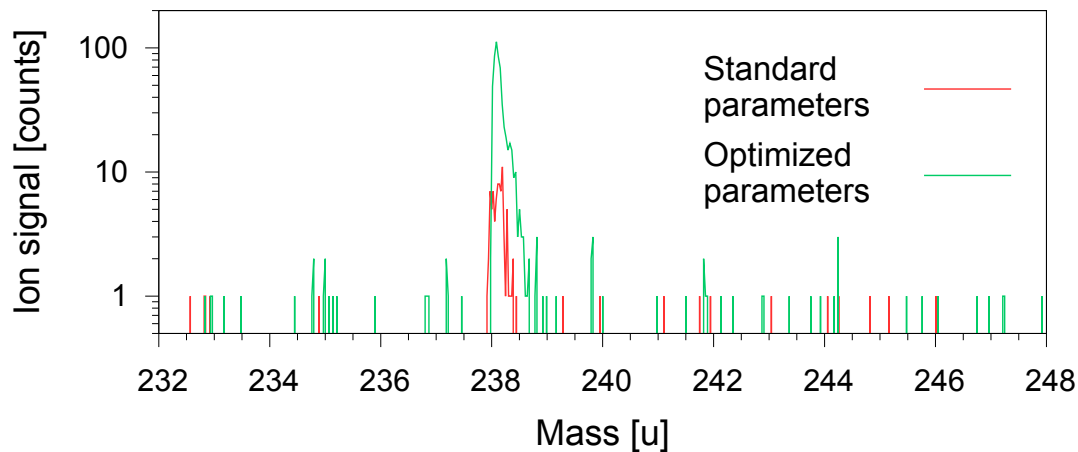


Figure 4.13: Comparison of two Laser-SNMS spectra of a synthetic ^{238}U sample for different parameter sets: red spectrum measured with the standard parameter set, green spectrum measured with the optimized parameter set. In this specific measurement, the ion signal of ^{238}U was increased by a factor of 7 from 81 counts to 570 counts.

The measured increase of the detected ion signal of about a factor of 7 significantly surpassed the expectation of 2.5 based on the simulations. In this particular measurement, the background was also slightly increased, as expected by the extended acceptance region, which led to a factor 1.8 higher signal-to-background ratio. The increase in mass resolution

amounts to a factor of 1.3. Further measurements of the uranium sample and the measurement series for technetium and plutonium resulted in small variations of those factors due to slightly different instrumental performance and sample conditions (mass spectra of Tc and Pu shown in the appendix as Fig. B.21 and B.22). Nevertheless, in all cases the simulation-based, optimized parameter set leads to an enhanced detected ion signal, in some cases even a higher signal-to-background ratio while the expected reduction in mass resolution was barely observable.

	^{238}U	^{99}Tc	^{239}Pu
Ion signal gain	5.2 ± 1.7	2.7 ± 0.4	6.3 ± 2.6
Signal-to-background ratio gain	3.4 ± 1.6	1.0 ± 0.1	4.4 ± 3.4
Mass resolution gain	1.2 ± 0.7	1.4 ± 0.6	3.3 ± 1.5

Table 4.2: Gain in conditions for mass spectrometric analysis, achieved by the simulated-based, optimized parameter set. Errors correspond to the standard deviation of all comparison measurements for the respective isotope.

CHARACTERIZATION WITH RADIONUCLIDES

Development, installation and optimization of the resonant Laser-SNMS system for the IRS Hannover focused on its application for direct, spatially resolved ultra-trace analysis of different radionuclides on environmental samples without involving any chemical preparation. The analysis of unknown samples requires a well-founded understanding of all main and side processes of the applied technique. Additionally, the basis for identification of unexpected results is formed by characterization measurements of precisely specified sample material. Repetition of those measurements is necessary for every individual element and resonant ionization scheme applied, because they might lead to characteristic differences in the resonant Laser-SNMS spectra. The various cross sections and lifetimes of energy levels and transitions involved in all laser ionization schemes result in different and most often unpredictable laser ionization efficiencies. Also the laser output power and the pulse length of the Ti:sapphire lasers is varying dependent on the specific wavelength, according to the laser medium gain and properties of the installed optical elements. Furthermore, the different wavelengths may contribute to the occurrence of non-resonant laser ionization for the analyzed element, its molecular forms or other included species in the sample, respectively. A full characterization of the Laser-SNMS system is therefore essential for every element of interest. The following chapter comprises characterization measurements performed on the elements uranium, plutonium and technetium, which all are of high interest for radioecology.

Identical proceeding within the sample preparation for all produced test samples of the three elements guaranteed well comparable results of the characterization. 0.2 μL - 1 μL of every measured sample solution was pipetted onto an aluminium sample holder. Heating of the sample holder led to vaporisation of the solution and deposition of the precipitated element on the sample surface in an area with 1 mm - 3 mm diameter (photos in the appendix as Fig. A.16 and Fig. A.15). Besides accurate cleaning of the sample holder and proper sample treatment, the sample surface is always covered with thin layers of organic contaminations. The contamination originates at least partially from silicone oil of adhesive tape, that was used during other conventional SIMS measurements. Even a frequent application of the internal bakeout system and a test with an empty sample holder, that was cleaned with concentrated nitric acid, showed nearly no effect towards reduction of these surface contaminations. Therefore, complete prevention of the surface contamination was not achievable with simple methods, while the in-situ sample surface cleaning with the installed Ar cluster ion gun at least resulted in a strong reduction of the organic contamination (shown in the appendix as Fig. B.23 and Fig. B.24). Although, further investigation or installation of a glove box could have identified or even eliminated the contamination source, it must be noted, that the system was developed for analysis of environmental sample, which unavoidably introduce of

organic material. Consequently, the sputter cleaning by argon clusters was added as a part of the standard sample preparation and applied to all samples analyzed for the characterization measurements. Surface cleaning was required once per day before a measurement even for samples which were stored in the vacuum chamber, due to unavoidable deposition of silicone oil.

5.1 Uranium

Characterization of the Laser-SNMS system for analytical uranium measurements used a synthetic uranium standard solution¹. The original concentration of 999 ppm uranium in a 1.1 % solution of nitric acid was further diluted to produce sample solutions with different concentrations between 100 ppm and 1 ppb. The isotopic composition of the dissolved depleted uranium is shown in Tab. 5.1.

	²³⁵ U	²³⁸ U
Isotopic fraction	0.25 %	99.75 %

Table 5.1: Isotopic composition of the synthetic depleted uranium sample, which was used for the characterization measurements

The applied 3-step excitation scheme for resonant laser ionization of uranium is shown in Fig. 5.1. This scheme was developed for isotope selective resonance ionization of uranium with narrow spectral bandwidth by use of a diode laser system [80].

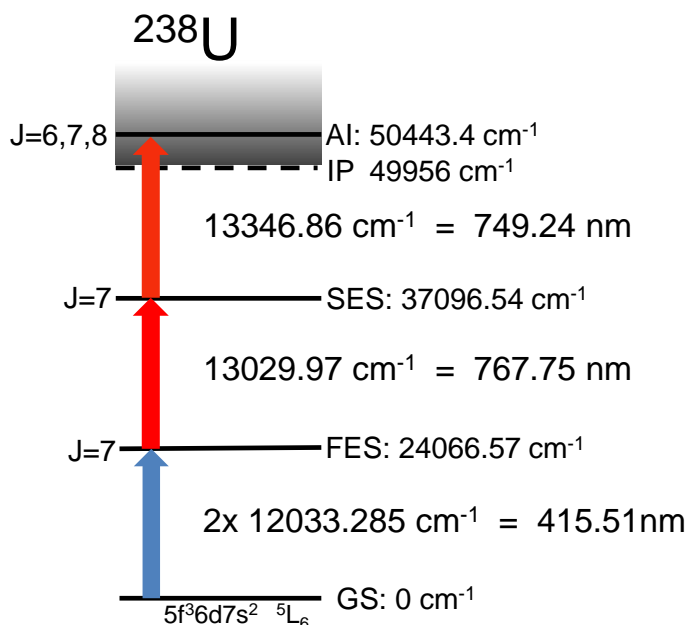


Figure 5.1: Resonant 3-step excitation scheme for ²³⁸U: The shown excitation scheme for uranium requires a frequency doubled Ti:sapphire laser for the FES and two fundamental Ti:sapphire lasers for the SES and the AI excitation.

¹SIGMA-ALDRICH uranium atomic absorption standard solution, PN:207624

Further application for ultra-trace analysis using Ti:sapphire lasers in combination with a hot cavity atom source demonstrated superior ionization efficiency in comparison to other excitation schemes [81]. Due to previous application for high efficient RIMS analytic, the 3-step scheme was applied without additional scheme development. The different population behavior of thermal and sputter process could also result in changed ionization efficiencies for known and unknown excitation schemes.

5.1.1 Characteristic spectrum, laser influence and saturation behavior

Based on former analytical uranium measurements in a hot cavity laser ion source at Mainz [82], the expected resonant Laser-SNMS mass spectra should primarily contain the ion signal produced by resonantly ionized, sputtered uranium atoms at mass 235 u and 238 u and a strongly suppressed ion background originating from various sputtered ions. The SNMS mass spectrum of the synthetic uranium sample, presented in Fig. 5.2, showed laser dependent ion signals, that were identified as uranium oxide, dioxide and carbide molecules. Additionally, the ion signals of a few light elements, like sodium, aluminium, potassium and the aluminium dimer were observed.

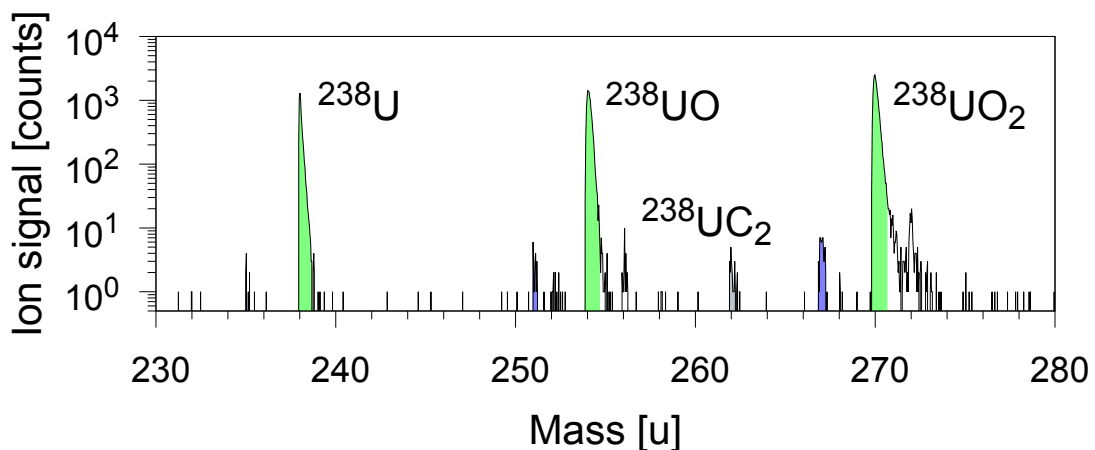


Figure 5.2: Characteristic Laser-SNMS spectrum of the synthetic uranium sample: The mass peaks of the dominant isotope ^{238}U and its oxide molecules are marked in green. The smaller mass peaks of the minor isotope ^{235}U and its oxide molecules are marked in blue. The mass peak of the non-resonant ionized $^{238}\text{UC}_2$ is marked in gray.

Generation of these unexpected ion signals is caused by non-resonant laser ionization processes. The applied laser wavelengths for resonant ionization in combination with sputtering induced population of higher lying atomic states lead to ion signals of other elements and molecules. This behavior was also observed during earlier comparable experiments [83, 84] and varies according to the applied excitation scheme and the energy per laser pulse. Prevention of disturbing non-resonant signals, that interfere with the resonant laser ion signal, is therefore possible by reduction of the laser power or change of the excitation scheme. On the other hand, the ion signals of uranium oxides and dioxides provide additional data without interference with the atomic uranium ion signal. The combined signal of atomic and molecular uranium ion increases the sensitivity for detection of small amounts of sample material. Furthermore, the analysis of the ratios between atomic uranium and its oxide and dioxide provides information about the chemical composition of the sample material.

An important part of the characterization is the analysis of the influence of every individual laser and combination of lasers for identification of disturbing non-resonant laser ionization processes and for validation of the resonant behavior of the laser ion signal of atomic uranium. The resulting ion signals for ^{238}U , ^{238}UO and $^{238}\text{UO}_2$ with different applied laser combinations is presented in Fig. 5.3.

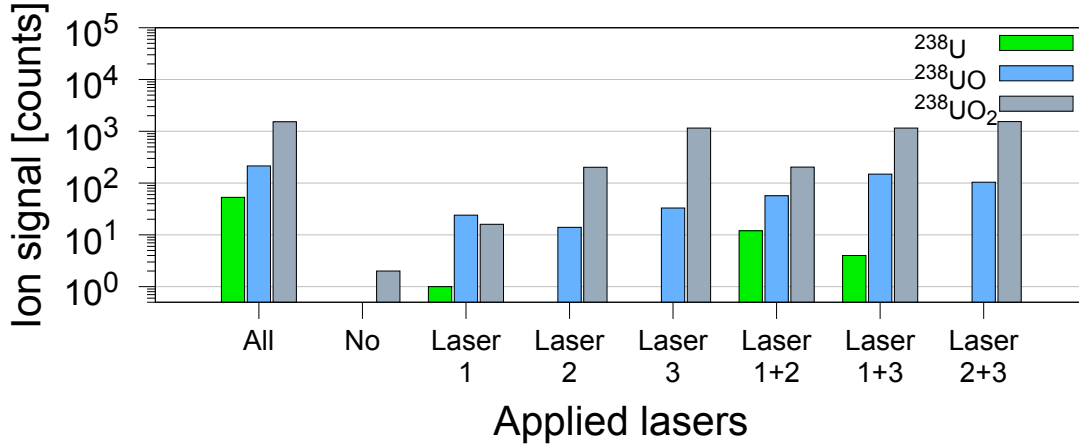


Figure 5.3: Influence of the three individual lasers and every possible combination on the resonant ion signal of ^{238}U and the non-resonant ion signal of ^{238}UO and $^{238}\text{UO}_2$.

Without any applied laser only a small background ion signal on the mass of $^{238}\text{UO}_2$ was detected, which leads to a full dependency on lasers for all three ion signals. The ^{238}U ion signal is mainly based on resonant ionization only. Application of the first and second laser causes non-resonant ionization of ^{238}U , probably by an excitation from the second excited state with an additional photon by one of the two lasers. The small non-resonant ^{238}U ion signal for the combination of the first and third laser is not understood. The clearly non-resonant ion signal of ^{238}UO depends mostly on laser power and not on a specific combination of laser wavelengths. The ion signal of $^{238}\text{UO}_2$ is influenced to a large degree solely by the third laser, which underlines the non-resonant origin of the signal. Additionally, the $^{238}\text{UO}_2$ ion signal is even slightly increased without the application of the first ionization laser. The higher energy of the first laser, which is frequency-doubled, might break some of the molecular bonds of the UO_2 converting it to UO .

Besides the influence of the individual lasers, the laser excitation and ionization process depends also strongly on the pulse energy of the three lasers. Measurement of the laser power at constant repetition rate of 10 kHz provides an equivalent parameter for the averaged pulse energy. The atomic transitions for laser ionization of the entire amount of atoms in the laser focus are saturated, if the laser output surpasses a defined amount of laser power. This saturation behavior results in a saturation curve for the dependence of the generated laser ion signal $I(P)$ from the laser power, that is described by Eq. 5.1.

$$I(P) = I_0 + \frac{A \cdot \frac{P}{P_{Sat}}}{1 + \frac{P}{P_{Sat}}} + m \cdot P \quad (P_{Sat}: \text{saturation power}) \quad (5.1)$$

The saturation behavior was analyzed for the three excitation steps of uranium for determination of their saturation power. The saturation curve and power indicate the efficiency of every transition used and of the whole ionization process. The diagrams of the measured

power dependence for ^{238}U including the fitted saturation function appear in the appendix as Fig. B.25, while the resulting saturation power of the three steps is listed in Tab. 5.2.

	FES	SES	AI
Saturation power [mW]	2.0(7)	32(10)	>2300, not saturated

Table 5.2: Saturation powers of the first excitation step (FES), the second excitation step (SES) and the autoionizing step (AI) for resonant Laser-SNMS on ^{238}U . The related saturation scans appear in the appendix in Fig. B.25.

The first two transitions were already saturated with a fraction of the available laser power, while the third transition could not be saturated at all. The third transition leads to an autoionizing state, which is rapidly depopulated, due to internal coupling processes (see theory section 2.2.4). Therefore, an approximately linear increase was expected instead of saturation. The measured power dependence for ^{238}U showed this linear increase starting at 1800 W. Below this power level the third laser had only a minor influence. The process, that leads to this behavior, is not understood, but spatial or spectral misalignment was excluded by repeated measurements and the observation of the same behavior for other tested radionuclides.

5.1.2 Decision threshold and efficiency

The decision threshold (DT), is one of the main parameters, that defines the suitability of an analytical system for the detection of ultra-trace amounts of sample material. The lowest detectable and quantifiable amount of a specified trace species defines the decision threshold. It is often mixed-up with the detection limit, which is slightly lower and does not allow quantification. Determination of the decision threshold for characterization of the system was realized by two different methods.

Indirect determination by efficiency measurements

For valid detection and quantification the ion signal must clearly exceed the detected background signal by more than three times of the standard deviation σ_{bg} of this background. Furthermore, the ratio of the lowest detectable and quantifiable amount of sample material to the lowest validated ion signal is defined by the overall efficiency of the mass spectrometric system. As a result, calculation of the decision threshold, as shown in Eq. (5.2), requires a measurement of the efficiency and the background signal.

$$\text{DT} = \frac{3 \cdot \sigma_{bg}}{\varepsilon} \quad (\varepsilon: \text{overall efficiency}) \quad (5.2)$$

The Laser-SNMS system at the IRS Hannover is based on a static SIMS setup, which operates on low primary ion sputter rates to ensure mostly unaffected sample surfaces. Measurement of the overall efficiency requires the complete consumption of a well specified amount of sample material for comparison with the simultaneously detected ion signal. Achievement of a reliable value for the efficiency by a measurement, which is limited to a few hours by ion gun instabilities, required very small and highly concentrated samples. First tests with conventional SIMS and the smallest quantifiable amount of sample solution of only 100 nL showed no decreasing ion signal as sign of complete consumption even after more

than 12 h (shown in the appendix as Fig. B.28). One reason for this could be the remaining surface roughness of the polished sample holder, that allows deposition of sample material in deepenings and scratches, or additional matrix material, which precipitates during sample deposition. Another option of applicable uranium sample material for the efficiency measurement was provided by the Research Center Jülich. They produced synthetic uranium particles with a well defined diameter of $1.3 \mu\text{m} - 1.4 \mu\text{m}$ based on the standard material IRMM-183 [85, 86]. The particles consist of triuranium octoxide (U_3O_8) and contain $5.43 \pm 0.20 \text{ pg}$ uranium per particle. The main parameters of the particles are summarized in Tab. 5.3.

^{235}U	^{238}U	Diameter	Mass of U per particle	^{238}U atoms per particle
0.32 %	99.66 %	$1.35 \pm 0.05 \mu\text{m}$	$5.43 \pm 0.20 \text{ pg}$	$(1.37 \pm 0.04) \cdot 10^{10}$

Table 5.3: Composition and size of the synthetic uranium particles

Several uranium particles were deposited on a silicon waver by the development team in Jülich with sufficient space in between for individual Laser-SNMS analysis (shown in the appendix as Fig. A.17). The small diameter of the particles enabled a very well localized analysis in a reduced measurement area, as shown in Fig. 5.4.

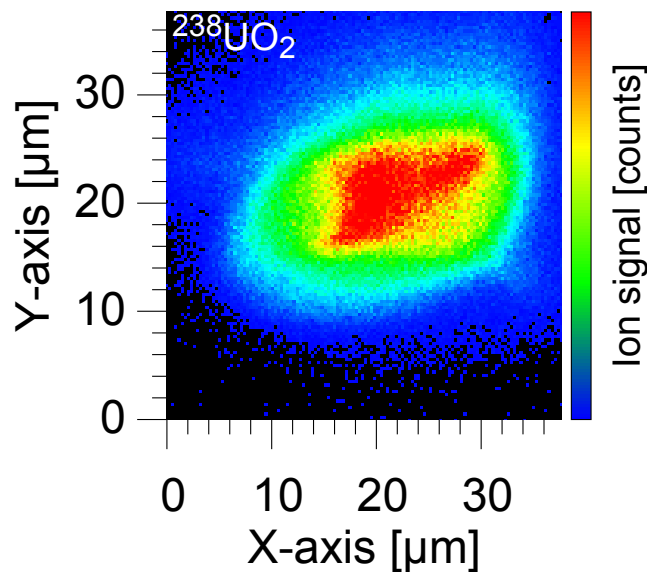


Figure 5.4: $^{238}\text{UO}_2$ -ion image of a U_3O_8 particle obtained during the efficiency measurement: The size of the particle image is roughly $30 \mu\text{m} \times 20 \mu\text{m}$ for a particle size of $1.35 \pm 0.05 \mu\text{m}$. The reason for this enlarged ion image is the size of the primary ion focus, which is several μm in the applied more efficient spectrometry mode.

Efficiency measurements with the synthetic uranium particles demonstrated the expected decreasing ion signal due to complete consumption, as shown in Fig. 5.5. The obtained Laser-SNMS mass spectra for the uranium particles showed a higher concentration of ^{238}UO and $^{238}\text{UO}_2$ at the surface than in the self-produced samples and also showed further fragment uranium molecules like U_2O_4 and U_3O_6 . Additionally, the laser ion signals of atomic uranium, uranium oxide and dioxide show different behavior in the presented temporal

development. This behavior indicates that the degree of oxidation is higher in the shell than in the core of the analyzed particle. Another possible explanation is an enhancement of the impact induced break-up of the molecular bonds towards the surface erosion. This could lead to a pile-up effect for the light fragments until a saturation level is reached.

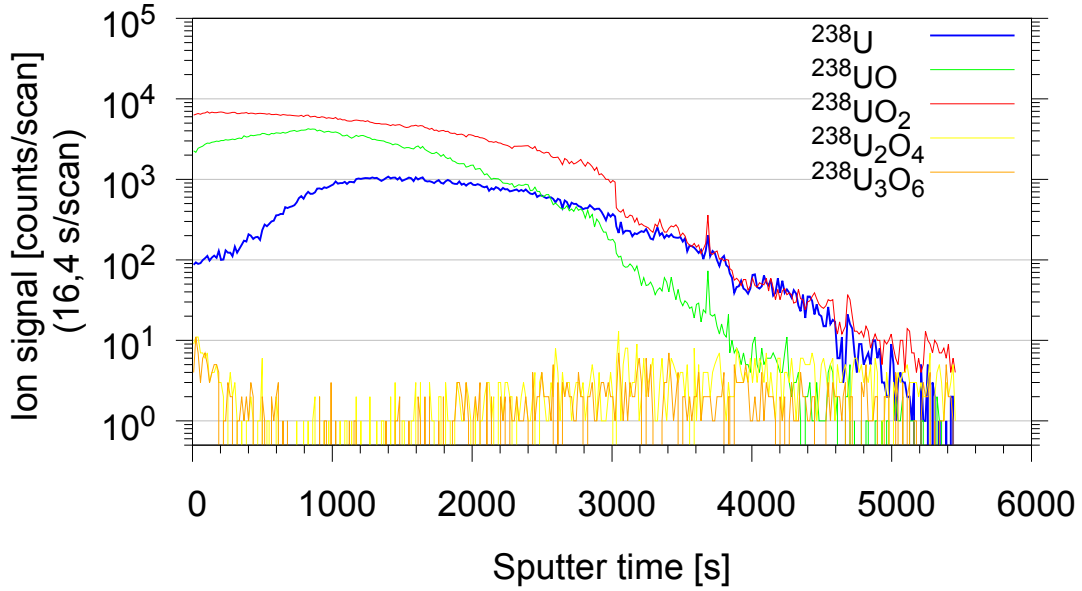


Figure 5.5: Efficiency measurement of a synthetic U_3O_8 particle showing the temporal development of the ion signal for resonantly ionized ^{238}U and for four non-resonantly ionized molecular uranium species during the Laser-SNMS analysis.

Because of the large fraction of detected oxidized uranium, the determination of the overall efficiency was extended from the resonantly ionized ^{238}U ion signal to all laser dependent ion signals of uranium containing species. As the non-resonantly ionized uranium molecules are applicable for sample detection and identification of ultra-trace amounts, they should also be considered in the decision threshold. Three independent measurements led to the values for overall efficiency and decision threshold, that are presented in Tab. 5.4.

	Efficiency	Decision threshold
^{238}U	$(2.63 \pm 0.07) \cdot 10^{-5}$	$(2.12 \pm 0.08) \cdot 10^6$ atoms
All U species	$(2.05 \pm 0.05) \cdot 10^{-4}$	$(3.58 \pm 0.09) \cdot 10^5$ atoms

Table 5.4: Decision threshold based on efficiency measurements

Based on the simulation of the ion trajectories through the mass analyzer, the transport efficiency is approx. $1.6 \cdot 10^{-1}$. The additional losses of three orders of magnitude for resonant ionization of ^{238}U originate from two effects. First, the well-known excitation scheme for resonant laser ionization of uranium provided, despite higher efficiency than other schemes, overall efficiencies of only 10^{-3} in former hot cavity ion source measurements in combination with a QMS system (approx. 10^{-1} transport efficiency) [81]. The second effect is caused by the large amount of uranium molecules. Non-resonant laser ionization of the

high fraction of uranium oxides is significantly less efficient than the resonant ionization process. Nevertheless, the achieved efficiency is only a factor 2 lower than the one of a comparable measurement at the CHARISMA instrument at Argonne National Laboratory (USA) [87].

Direct determination by small sample amounts

Another method for determination of the decision threshold is an approximation of the lowest value by small, well defined sample amounts. This approach delivers a more meaningful DT than the calculation based on efficiency measurements. The indirect determination provides the best achievable decision threshold of the system, if the sample material is completely consumed. High purity samples like the synthetic U_3O_8 particles used are subject for this maximum sensitivity, but the field of application for this specialized Laser-SNMS system, i.e. the ultra-trace analysis on nearly unprepared environmental samples could react differently. Temporal limitations reduce the realistic achievable decision threshold, because the complete consumption of an environmental sample with the surplus of enclosing organic and inorganic matrix material requires unrealistically long measurement time. Therefore, the direct determination method searches for the smallest amount of sample material, which produces a detectable and quantifiable laser ion signal during a reasonable measurement time. The lowest applied sample for uranium was 200 nL of a 1 ppb sample solution corresponding to $(5.2 \pm 1.6) \cdot 10^8$ uranium atoms. After a Laser-SNMS measurement of 1 h the mass spectrum, which is presented in Fig. 5.6 was achieved.

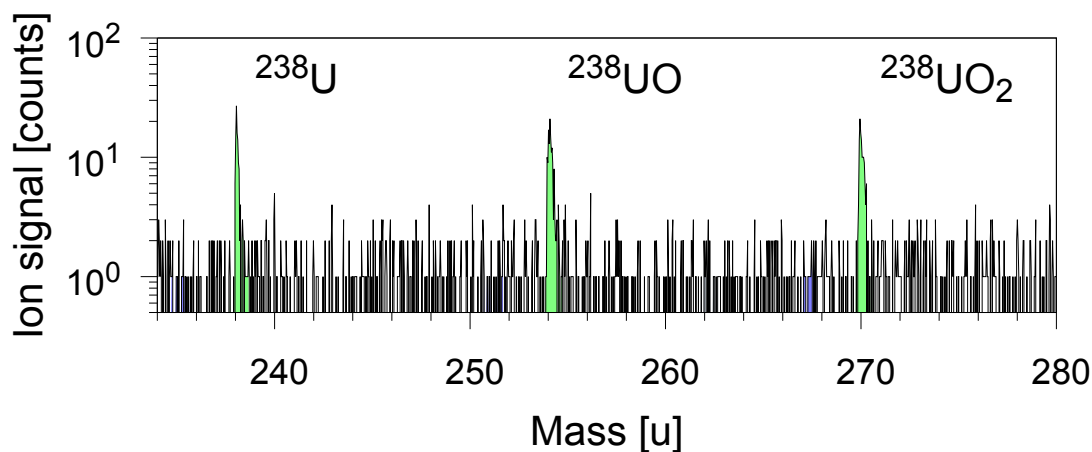


Figure 5.6: Laser-SNMS mass spectrum of the 1ppb uranium sample: The mass peaks of the resonantly ionized ^{238}U and its non-resonantly ionized oxides are marked in green. The positions of ^{235}U and its oxides are marked blue, although their signal is below the background level.

The detected resonant laser ion signal of ^{238}U contained 112 counts, which results in a detection rate of 1 count per 32.8 s. The parallel detected ion background was measured with only 15 counts for an equally sized mass range. Therefore, the ion signal of this ultra-trace amount of uranium was definitely detected and quantified and sets the upper limit for the realistic decision threshold to $(5.2 \pm 1.6) \cdot 10^8$ atoms. The achieved signal-to-background ratio and inclusion of the non-resonantly ionized oxides enables an approximation for the decision threshold of a value of $1 \cdot 10^8$ atoms. This is about two orders of magnitude higher,

means worse, than the indirect determined decision threshold, which is the inevitable influence of surrounding matrix material. All important values for the direct determination of the decision threshold are summarized in Tab. 5.5.

Concentration	Uranium amount	Signal-to-background ratio	Decision threshold
1 ppb	0.21 pg	7.5 ± 0.5	$< (5.2 \pm 1.6) \cdot 10^8$ atoms

Table 5.5: Decision threshold based on the lowest measured quantity

5.2 Plutonium

The synthetic sample for Laser-SNMS characterization as basis for analytical plutonium measurements was a nearly mono-isotopic certified reference standard solution ². The isotope ratios of the sample material used are shown in Tab. 5.6. Application of a mono-isotopic plutonium sample prevented coverage of possible unexpected background on neighboring masses. Additionally, the long half-life of the chosen ²⁴²Pu enabled a higher sample concentration. Nevertheless, the applicable amount of radiation was limited by the fraction of 0.0075 % ²⁴¹Pu in the sample material. The chemical composition of the plutonium is Pu(NO₃)₄ dissolved in 0.1 M nitric acid.

	²⁴⁰ Pu	²⁴² Pu	Other Pu isotopes	²⁴¹ Am	²⁴³ Am
Isotopic fraction	0.02 %	99.96 %	< 0.01 %	0.97 %	0.05 %

Table 5.6: Isotopic composition of the synthetic plutonium sample

The 3-step excitation scheme for resonant laser ionization, presented in Fig. 5.7, was applied for the plutonium Laser-SNMS characterization. A predecessor scheme, which used a rydberg state for ionization, was developed to determine plutonium isotope ratios in ultra-trace sample amounts for a conventional TOF-MS system [88, 89]. The continuing scheme development revealed a more efficient ionization for field free ionization volumes via the shown autoionizing state [56]. It was chosen for the Laser-SNMS system, because tests with uranium showed an increased ion signal for an temporal adjustment of the lasers before the activation of the strong extraction field.

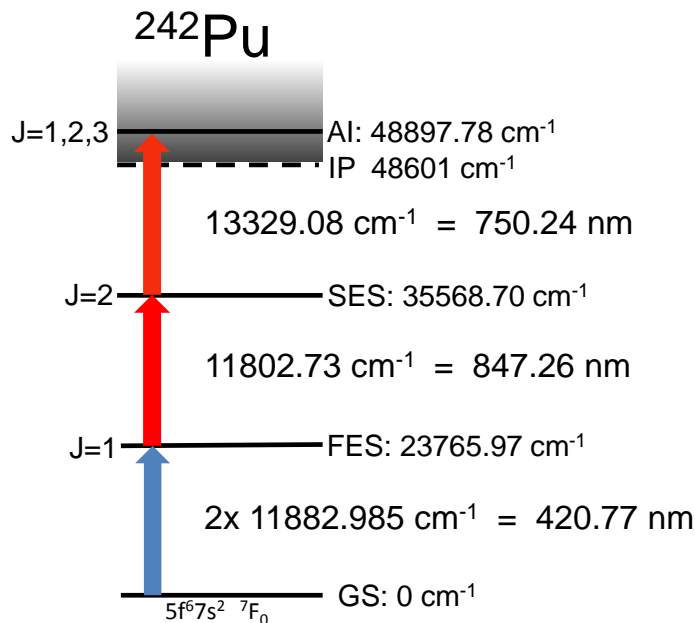


Figure 5.7: Resonant 3-step excitation scheme for ²⁴²Pu: The shown excitation scheme for plutonium requires a frequency doubled Ti:sapphire laser for the FES and two fundamental Ti:sapphire lasers for the SES and the AI excitation.

²Eckert & Ziegler, Catalog No.: 6242

5.2.1 Characteristic spectrum, laser influence and saturation behavior

Similarly to the U spectrum, the characteristic Laser-SNMS mass spectrum of the synthetic plutonium sample, presented in Fig. 5.8, showed also non-resonantly ionized signals of some light elements as well as molecular oxides. Unlike in the uranium spectra, there was no Laser-SNMS ion signal of plutonium dioxide observed at mass 274 u, although it was measured by SIMS analysis. Besides, the resonant ^{242}Pu laser ion signal and the non-resonant ^{242}PuO laser ion signal, two very small signals appeared on mass 254 u and 270 u. Those masses would fit to ^{238}UO and $^{238}\text{UO}_2$, which could be remains from the plutonium production in the standard sample.

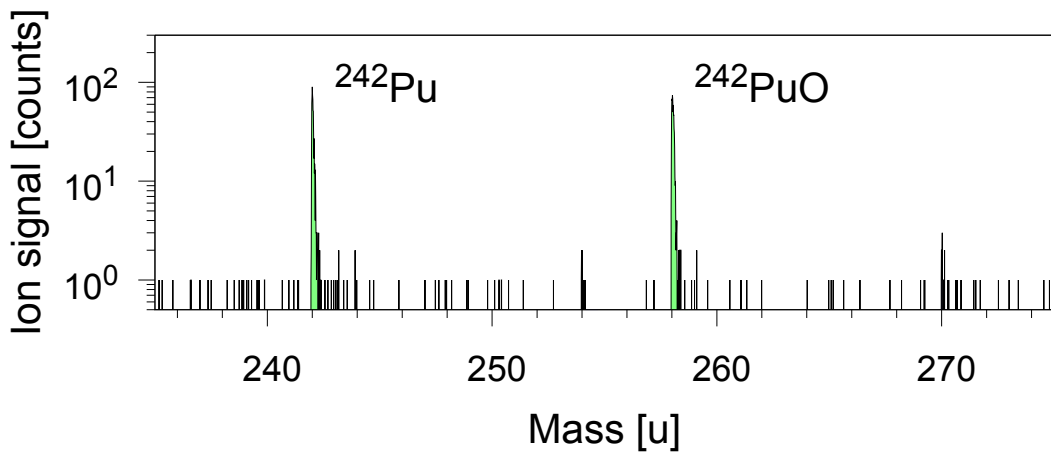


Figure 5.8: Characteristic Laser-SNMS spectrum of the synthetic plutonium sample: The mass peaks of the dominant isotope ^{242}Pu and of the ^{242}PuO molecule are marked in green.

The analysis of the influence of every single laser and all combinations on the ion signal, as presented in Fig. 5.9, identified parallel non-resonant processes and verified the resonant generation of the ^{242}Pu laser ion signal. The ion signals of ^{242}Pu and ^{242}PuO are both laser dependent. Once again the dominant part of the ^{242}Pu ion signal is produced by resonant laser ionization using all three lasers. However, there are significant non-resonant ionization processes involved, that are induced by the first laser.

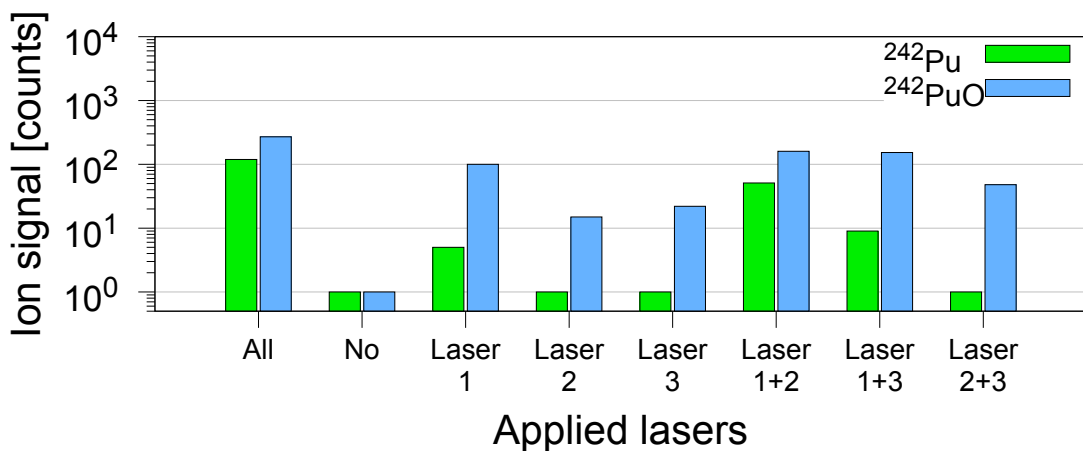


Figure 5.9: Influence of the three individual lasers and every combination on the resonant ion signal of ^{242}Pu and the non-resonant ion signal of ^{242}PuO .

During former experiments with a hot cavity laser ion source and a QMS only the non-resonant ionization by combination of the first and second laser was measured as a 20 % effect [82]. Therefore, the additional ionization processes induced e.g. by the combination of lasers 1 and 3 could be a result of states populated by sputtered ablation of the sample material. Understanding of all observed laser ionization processes of ^{242}Pu would require further spectroscopic analysis at a Laser-SNMS instrument. The laser ion signal of ^{242}PuO showed the expected non-resonant behavior. In general, every sole laser and every combination generates a sizable laser ion signal of ^{242}PuO .

The saturation behavior of the three resonant excitation steps for ionization of ^{242}Pu was equal to the behavior for uranium. The first and second excitation step were saturable with laser powers below 100 mW. The third excitation step, that leads to the final autoionizing state, required more than 1300 mW for an increasing laser ion signal. Below this power level it showed no influence on the signal. A spectral misalignment of the third laser would explain this unexpected dependence, but was excluded by the broad spectral width of the autoionizing state and the constant monitoring of the laser wavelength. The diagrams of the measured power dependence for ^{242}Pu including the fitted saturation functions appear in the appendix as Fig. B.26, while the resulting saturation power of the three steps is listed in Tab. 5.7.

	FES	SES	AI
Saturation power [mW]	10(5)	25(18)	>1800, not saturated

Table 5.7: Saturation powers of the first excitation step (FES), the second excitation step (SES) and the autoionizing step (AI) for resonant Laser-SNMS on ^{242}Pu . The related saturation scan appears in the appendix in Fig. B.26.

5.2.2 Decision threshold

The decision threshold for analytical plutonium measurements was only determined directly using a small sample. Appropriate plutonium sample material for efficiency measurements and indirect determination of the decision threshold was not available. The measurement with the lowest detectable and quantifiable laser ion signal of ^{242}Pu used a 200 nL sample of a 1 ppb sample solution containing $(5.1 \pm 1.5) \cdot 10^9$ plutonium atoms.

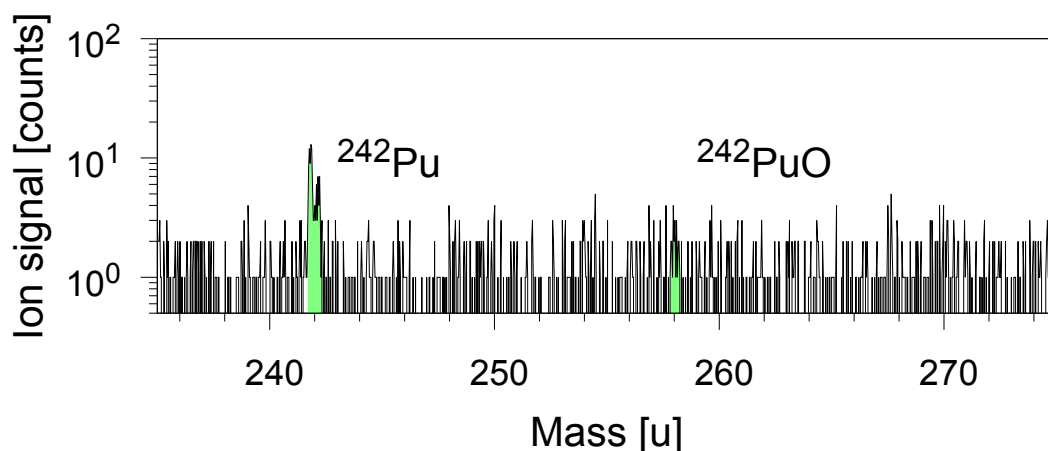


Figure 5.10: Laser-SNMS spectrum of the 10ppb plutonium sample: The mass peaks of the resonantly ionized ^{242}Pu and the non-resonantly ionized ^{242}PuO are marked in green.

The Laser-SNMS analysis of this sample with a measurement duration of 44 min resulted in the mass spectra presented in Fig. 5.10. The clearly identifiable mass peak of the resonant laser ion signal of ^{242}Pu contained 112 counts, while the parallel detected ion background on an equally sized mass range was only 19 counts. The non-resonant laser ion signal of ^{242}PuO is with 28 counts only slightly larger than its background signal of 22 counts. The upper limit for the decision threshold of $(5.1 \pm 1.5) \cdot 10^9$ atoms for plutonium is 10 times higher than for uranium. A possible explanation for this could be a lower fragmentation yield during the sputtering process. If significantly less plutonium is available in its reduced, i.e. non-oxidized atomic form, the overall ionization efficiency is strongly reduced. Another explanation is based on the unexpected influence and saturation behavior of the applied excitation scheme. If the combination with the sputtered ablation leads to a reduce ionization efficiency via unidentified effects, the application of an alternative 3-step scheme or a recently tested 2-step scheme for plutonium should be tested [88, 90].

Concentration	Plutonium amount	Signal-to-background ratio	Decision threshold
10 ppb	2.1 pg	5.9 ± 0.5	$< (5.1 \pm 1.5) \cdot 10^9$ atoms

Table 5.8: Decision threshold for plutonium based on the lowest measured quantity

5.3 Technetium

Characterization of the Laser-SNMS system for analytical technetium measurements was made using a certified, mono-isotopic ^{99}Tc reference standard solution³. The original standard solution contained ammonium pertechnetate (NH_4TcO_4) dissolved in water, but for the subsequent dilution 0.1 M nitric acid was added.

The applied 3-step excitation scheme for resonant Laser-SNMS, presented in Fig. 5.11, also uses a highly efficient autoionizing state for ionization similar to the schemes for uranium and plutonium. It was developed for laser spectroscopic determination of the ionization potential of technetium and later successfully used for ultra-trace analysis experiments [43, 91]. It requires two frequency doubled Ti:sapphire lasers instead only one like the two other schemes, which leads to more photons in the higher energy range. Therefore, more non-resonantly laser ionized species were expected to appear on the mass spectra.

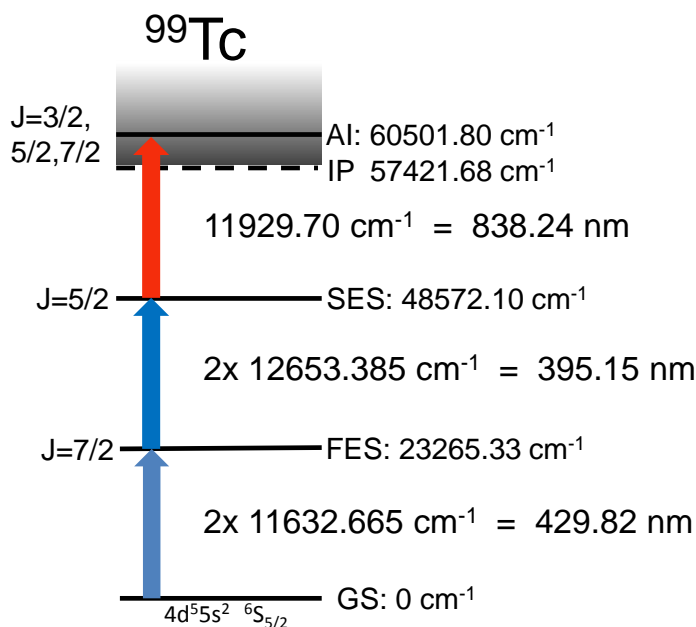


Figure 5.11: Resonant 3-step excitation scheme for ^{99}Tc : The shown excitation scheme for technetium requires two frequency doubled Ti:sapphire lasers for the FES and the SES and a fundamental Ti:sapphire laser for the AI excitation.

5.3.1 Characteristic spectrum, laser influence and saturation behavior

The characteristic Laser-SNMS mass spectrum of technetium, as present in Fig. 5.12 exhibits exclusively the resonantly ionized ^{99}Tc signal, although strong peaks on the masses of TcH_9 and TcO were measured with conventional SIMS on the same sample. The complete absence of non-resonant ionization of molecular technetium species even led to a problem for the mass calibration of the spectra. A sufficiently well calibrated mass spectra requires at least two identified mass peaks. Therefore, the non-resonantly ionized light elements sodium, aluminum, potassium and the aluminum dimer, which provide wavelength independent laser ion signals, were utilized. The ion signal of the aluminum dimer ($^{27}\text{Al}_2$) on mass 54 u showed a narrow mass peak and the highest signal to background ratio of the light elements.

³Eckert & Ziegler, Catalog No.: 6099

Consequently, it was used for the mass calibration and for comparison of resonant and non-resonant ionization behavior. To the knowledge of all involved collaborative partners, this measurement was the first ever resonant Laser-SNMS analysis on technetium.

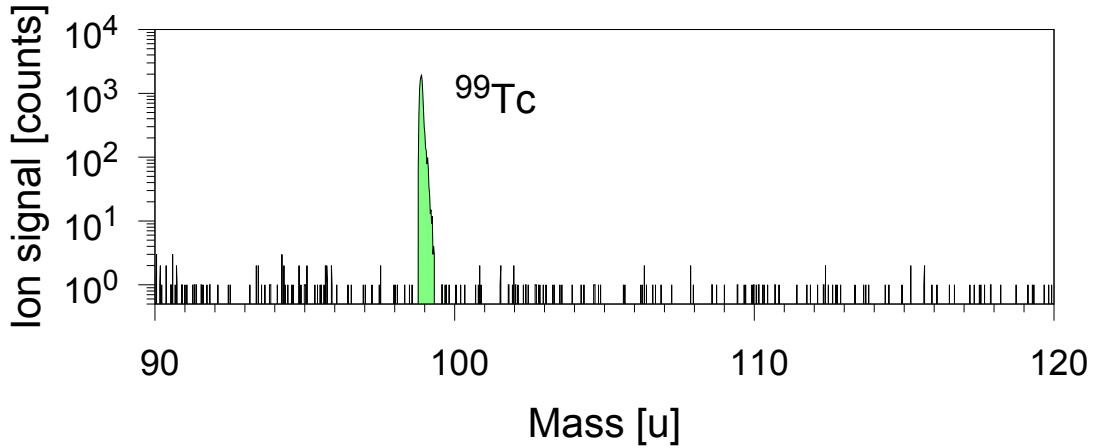


Figure 5.12: Characteristic Laser-SNMS spectrum of the synthetic technetium sample: The mass peak of the main isotope ^{99}Tc is marked in green.

The influence of every individual laser and all combinations on the ion signals are presented in Fig. 5.13. The histogram shows, that the ^{99}Tc laser ion signal originates predominantly from resonant ionization by all three lasers. Most other combinations lead to negligible ion signals, which are more than three orders of magnitude lower. Only the combination of first and second laser induces a non-resonant laser ionization by another blue photon from the second excited state. Nevertheless, this process contributes only well below 10% to the ^{99}Tc laser ion signal. The ion signal of $^{27}\text{Al}_2$ showed a clearly non-resonant behavior, that relates to irradiation of the first and second laser individually. Furthermore, the laser ion signal of $^{27}\text{Al}_2$ is reduced, if the third laser is added. This indicates an optical pumping process to a dark state, which is rather untypical for the majority of ionization schemes.

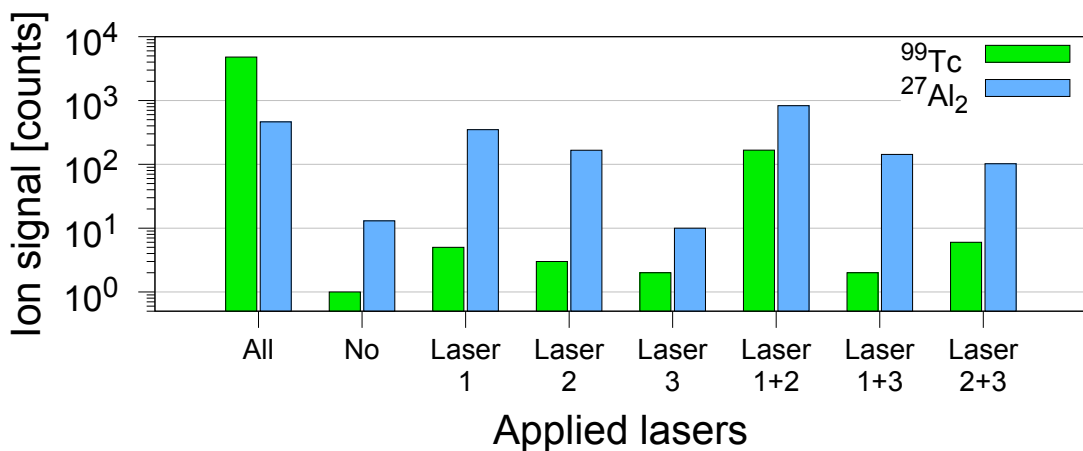


Figure 5.13: Influence of the three individual lasers and of every combination on the resonant ion signal of ^{99}Tc and the non-resonant ion signal of $^{27}\text{Al}_2$.

The saturation behavior of the first two excitation steps exhibited very low saturation powers. A weakly increasing signal above the saturation limit proves the completely saturated, resonant excitation up to the SES. The last excitation step to the autoionizing state shows no saturation. As mentioned before, the fast depopulation of autoionizing states leads to a linear power dependence of the ion signal. Besides this linear increase of the ion signal with raised laser power, there is also a sudden increase of ion signal above 1500 mW laser power. A partially similar power dependence, was identified for uranium and plutonium and is therefore a not fully understood effect of Laser-SNMS. The described diagrams of the measured power dependence for ^{99}Tc including the fitted saturation functions are given in the appendix as Fig. B.27, while the resulting saturation power values of the three steps are listed in Tab. 5.9.

	FES	SES	AI
Saturation power [mW]	0.3(1)	3.5(8)	>2400, not saturated

Table 5.9: Saturation powers for resonant Laser-SNMS on ^{99}Tc . The related saturation scan appears in the appendix in Fig. B.27.

5.3.2 Decision threshold

In the case of technetium, similar as for plutonium, there were no appropriate sample materials available for efficiency measurements and indirect determination of the decision threshold. The decision threshold was therefore directly determined by the smallest detectable and quantifiable sample. This 200 nL sample was made with a 2 ppb sample solution containing $(2.2 \pm 1.6) \cdot 10^9$ atoms of technetium. The resulting Laser-SNMS mass spectra after a measurement time of 5 min is presented in Fig. 5.14.

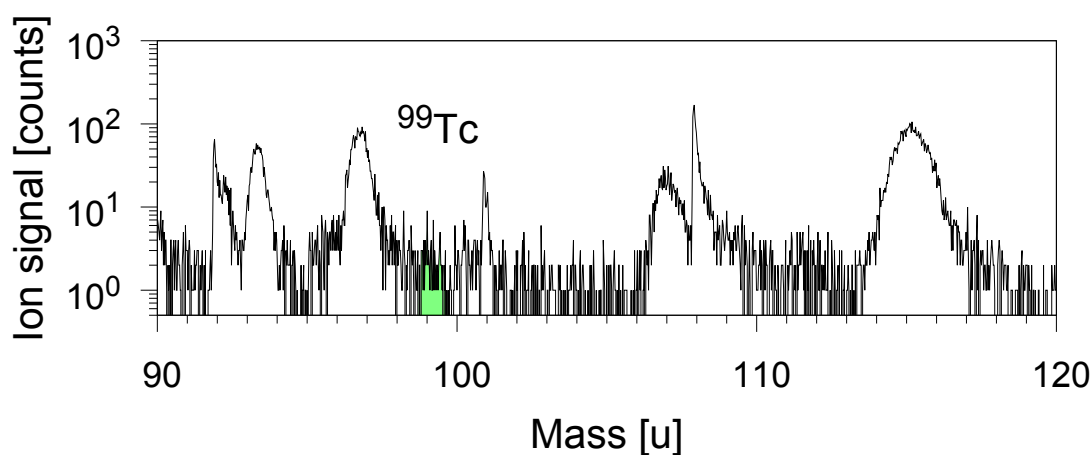


Figure 5.14: Laser-SNMS spectrum of the 2ppb plutonium sample: The mass peak of the isotope ^{99}Tc is marked in green.

The measured background level for technetium was much stronger than for the actinide samples, due to the mass range. The fragmentation during sputtered ablation leads to a comparably strong background signal for lower masses. The detected signal of ^{99}Tc appeared at a gap in the mass spectra with relatively low background. Nevertheless, the measured laser ion signal was only 86 counts at a background level of 41 counts. Neighboring isotopes would

have been covered by the unidentified background signal, preventing isotope ratio determinations without further sample treatment and purification. Nevertheless, this measurement gave a decision threshold for Laser-SNMS analysis on technetium of $(2.2 \pm 1.6) \cdot 10^9$ atoms.

Concentration	Signal-to-background ratio	Decision threshold
2 ppb	2.0 ± 0.5	$\approx (2.2 \pm 1.6) \cdot 10^9$ atoms

Table 5.10: Decision threshold for technetium based on the lowest measured quantity

5.4 Laser-SNMS in Comparison to Conventional SIMS

One of the main tasks of the work presented herein was the demonstration of the sensitivity gain for mass spectrometric ultra-trace analysis by extension of a conventional SIMS system with a dedicated laser system for resonant Laser-SNMS. Verification of the improvement in sensitivity requires a direct comparison of SIMS and Laser-SNMS measurements on identical samples. This is possible, because the software assisted modification of operation parameters allows to switch rapidly between both methods within a few seconds. Fig. 5.15 presents the resulting mass spectra in comparison for SIMS and Laser-SNMS on the same synthetic technetium sample. Similar comparison spectra for measurements on synthetic plutonium and uranium samples are given in the appendix as Fig. B.29 and Fig. B.30.

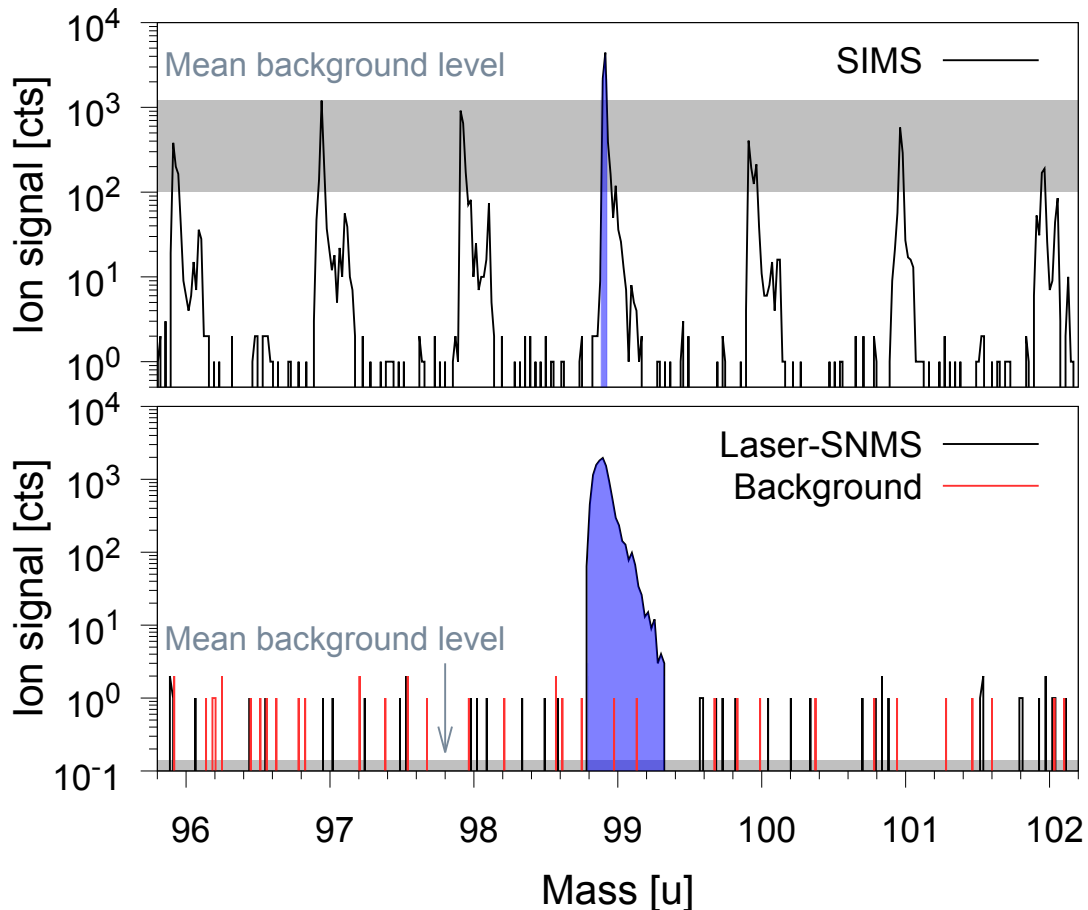


Figure 5.15: Comparison of SIMS and Laser-SNMS mass spectra for a synthetic technetium sample ($0.6 \text{ ng} \sim 4 \cdot 10^{12}$ atoms of ^{99}Tc): Both diagrams are generated with identical binning and show the same mass range. The detected ion signal for both methods is plotted by black lines. The individually detectable background signal by spectral laser detuning for Laser-SNMS is indicated by red lines. The grey bars show the mean background level at the blue marked mass peaks of ^{99}Tc . For the SIMS measurement, the background level was estimated from the neighboring mass peaks.

5.4.1 Ion signal

The intensity of the detected ion signal for both methods depends on combination of the specific ionization efficiency ε_{Ion} and the transport efficiency ε_{Trans} through the mass spectrometer. Because the TOF mass analyzer was designed specifically focusing on SIMS, the transport efficiency might be higher for SIMS measurements. The known significant efficiency losses of sputter ionization led to the motivation for the Laser-SNMS extension. As described in the theory section, only 0.001 % - 1 % of the sputtered particles are ionized directly during the sputter ablation process. The remaining fraction of 99 % or more of neutrals is available for the resonant laser ionization, which could lead to an increase of measured ion signal by several orders of magnitude, as repeatedly proven [92, 93].

The measured laser ion signal at the IRS Laser-SNMS system did not surpass the level of the sputtered ion signal, as exemplary shown in the presented mass spectra. The transport efficiencies $\varepsilon_{transSIMS}$ and $\varepsilon_{transSNMS}$ of both methods are not varying by orders of magnitude. Therefore, the nearly equal ion signal intensities I_{SIMS} and I_{SNMS} imply a relatively low laser ionization efficiency $\varepsilon_{laserIon}$ for the sputtered neutrals:

$$I_{SIMS} = \varepsilon_{sputterIon} \cdot \varepsilon_{transSIMS} \cdot I_{sputter} \quad (5.3)$$

$$I_{SNMS} = \varepsilon_{laserIon} \cdot \varepsilon_{transSNMS} \cdot I_{sputter} \quad (5.4)$$

The laser ionization efficiency itself comprises the spatial and temporal overlap factor of particle cloud and laser focus $f_{overlap}$, the efficiency of the applied ionization scheme ε_{scheme} and the saturation factor of each individual optical transition of the multi-step excitation scheme $f_{saturation}$:

$$\varepsilon_{laserIon} = \varepsilon_{scheme} \cdot f_{overlap} \cdot f_{saturation} \quad (5.5)$$

First, the sputter ionization efficiency $\varepsilon_{sputterIon}$ can be significantly higher in some cases. The ratio of sputtered ions to sputtered neutrals is severely affected by the specific sample material via matrix effects. For example, determination of the sputtered ionization efficiency of uranium in other experiments demonstrated a neutral-to-ion ratio of ~ 3000 for metallic uranium but only ~ 60 for a UO_2 sample [94]. Furthermore, the simulation of the overlap conditions (see section 4.1.2) already imply an overlap factor of only 15 %, due to the long expansion time for suppression of the sputtered ions. Developments of the applied excitation schemes at different RIMS instruments resulted in overall efficiencies of approximately 4 % for technetium, 2 % for plutonium and 0.1 % for uranium [81, 82, 95]. Consideration of the individual transport efficiencies of the systems leads to an estimated laser ionization efficiency of 1 % - 10 %. Additionally, it was assumed that a saturation factor is possibly below 1, due to the unexplained saturation behavior of all third excitation steps. The combination of these operational conditions prevents a gain in ion signal with Laser-SNMS towards conventional SIMS (summarized in Tab. 5.11) for the three radionuclides, which were analyzed. Nevertheless, further analysis of the laser ionization process of sputtered particles including a check of efficient extraction schemes could result in the same gain, that was verified by other Laser-SNMS systems for other elements.

5.4.2 Signal-to-background ratio

The main enhancement for ultra-trace analysis with resonant Laser-SNMS of the three radionuclides analyzed is achieved by the resulting signal-to background ratio. As listed in Tab. 5.11 the gain of signal-to-background ratio is found somewhere between one up to

nearly three orders of magnitude (gain of 930 in Fig. 5.15). Therefore, the suppression of all sputtered ions and element selectivity of resonant laser ionization leads to the necessary increase in sensitivity for ultra-trace analysis on environmental samples. Additionally, the individual determination of the background signal by spectral detuning of the first laser enables reliable identification of the ion signal of interest, which is impossible with conventional SIMS.

5.4.3 Mass resolution

The mass resolution is reduced by application of resonant Laser-SNMS by a factor of 5 - 10. This decrease was expected, due to the enlarged ionization volume. The resulting energy dispersion, which broadens the peaks of the detected mass spectra, can be reduced by a pulsed 2-step extraction. This requires a modification of the extraction electrode configuration, which could not be realized during the setup of the Laser-SNMS instrument, but is planned as advancement in the next development stage.

	^{238}U	^{99}Tc	^{242}Pu
Ion signal gain	1.0 ± 0.4	1.1 ± 0.7	0.56 ± 0.32
Signal-to-background ratio gain	30 ± 14	700 ± 330	54 ± 50
Mass resolution gain	0.16 ± 0.04	0.098 ± 0.005	0.22 ± 0.12

Table 5.11: Comparison of gains and losses of the essential mass spectrometric parameters by application of Laser-SNMS instead of conventional SIMS for three analyzed radioisotopes.

5.5 Influence of Argon Cluster Sputtering

As shortly mentioned before, the efficiency and sensitivity of resonant Laser-SNMS is significantly reduced by the high degree of oxidized sample material. Although the non-resonant laser ionization of oxides is very inefficient compared to the specific resonant laser ionization of atoms, the detected mass peaks of plutonium and uranium oxides were approximately on the same level or even higher than the atomic mass peak. Consequently, the fragmentation during the sputter analysis is only a minor process and a large surplus of sample material reaches the ionization volume as molecular species. SIMS measurements of the synthetic radionuclides resulted in a surplus of at least one order of magnitude for UO, PuO and TcH₉ towards atomic U, Pu and Tc. The future application of the Laser-SNMS system on even higher oxidized environmental samples forced the development of sample processing for reduction of the molecular species without destruction of structural information.

There are different possible methods for reduction of molecules before or during the Laser-SNMS analysis. The interaction of a reductive material with the sample either by pulsed laser deposition of nanolayers on the surface, low energy sputtered implantation via the existing Cs gun or the application of a reductive sample holder surface are approaches for future developments. Other methods were already tested by the predecessor experiment at the Johannes-Gutenberg Universität Mainz [96]. The reduction of oxides by a combination of previous sample heating at 800 °C in an auxiliary vacuum chamber and intensive sputtering of the surface layer led to a gain of atomic uranium laser ion signal of about one order of magnitude. The application of prior heating is another approach for future developments, while the influence of an intensive sputter treatment was already analyzed within the work presented herein. The TOF-SIMS instrument is equipped with different sputter guns, which were applied for reductive sputtering. Previous tests showed a reduced structural destruction of the sample surface by application of the argon cluster gun compared to the other guns. Additionally, the argon cluster gun is already used for sputter cleaning of organic contamination and therefore anyway aligned and configured for every measurement. The enhancement of the atomic to molecular ion signal achieved for synthetic uranium samples is shown in Fig. 5.16.

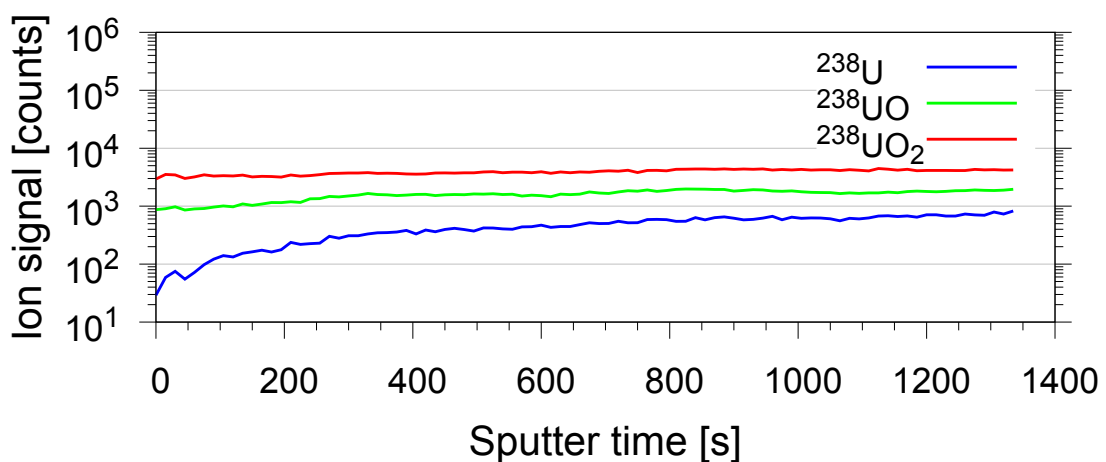


Figure 5.16: Development of the ion signals of resonantly ionized ²³⁸U and non-resonantly ionized ²³⁸UO and ²³⁸UO₂ during continuous argon cluster sputtering.

20 min of continues sputtering by argon clusters led to an ion signal gain of resonantly ionized ^{238}U of more than one order of magnitude. If this would be a result by sputter reduction of oxides, the non-resonant ion signals of ^{238}UO or $^{238}\text{UO}_2$ should be reduced. But the ion signal of ^{238}UO is increased, too, and the ion signal of $^{238}\text{UO}_2$ stays at the same level. A possible explanation would be a higher degree of oxidation in the upper layers of the synthetic uranium samples. Therefore, the presented ion signal development is interpreted to show only the resulting depth profile. Another explanation could be the fragmentation of other uranium molecules in the sample material, that are not ionized by the laser radiation.

Although no conclusive result was achieved for the approach for sputter reduction on uranium, the increased laser ion signal of ^{238}U led to further sputter treatment of the other two analyzed radionuclides. The laser ion signal during sputtering of the synthetic plutonium sample after all showed the expected behavior for reduction (diagram appears in the appendix as Fig. B.31). The increase of the atomic ^{242}Pu ion signal proceeds parallel to the decrease of the ion signal of ^{242}PuO . Sputter treatment of the synthetic technetium sample showed no influence on the ^{99}Tc laser ion signal (diagram appears in the appendix as Fig. B.32).

ANALYTICAL MEASUREMENTS

The characterization of the Laser-SNMS system formed the basis for future analytical measurements. Additionally, it verified the increased sensitivity of resonant Laser-SNMS in comparison to conventional SIMS for ultra-trace analysis. Another reason for the extension of the SIMS instrument by a laser system for resonant ionization is the elemental selectivity of this ionization process. The combination with active suppression of sputtered ions during the analysis prevents the influence of isobaric contaminants on the analyzed ion signal. Consequently, this setup enables ultra-trace analysis of different elements on environmental samples without previous chemical preparation. The verification of the intended isobaric suppression and of the direct application on environmental samples were the first analytical tasks for the newly developed system and are described in the following chapter.

6.1 MOX Fuel Pellet

One main application goal of this system is the ultra-trace analysis of released plutonium in environmental samples. The isotopic composition of analyzed plutonium samples provides insight into the irradiation history of the material, including release process, reactor type and initial fuel. Other techniques with ultra-trace sensitivity require a chemical separation from isobaric contaminants of elements like uranium and americium. The first analytical measurement of the Laser-SNMS system was therefore the analysis of a dissolved fragment of a Mixed-Oxide (MOX) pellet. The isotopic composition of the MOX material, which is presented in Tab. 6.1, was very well known, because this information is of high significance for the general purpose of the MOX pellet as future fuel for nuclear reactors.

	²³⁵ U	²³⁸ U	²³⁸ Pu	²³⁹ Pu	²⁴⁰ Pu	²⁴¹ Pu	²⁴² Pu	²⁴¹ Am
Actinide fraction	0.23 %	89.98 %	0.24 %	5.39 %	2.54 %	0.70 %	0.74 %	0.19 %
Uranium fraction	0.25 %	99.75 %						
Plutonium fraction			2.52 %	56.14 %	26.42 %	7.25 %	7.67 %	

Table 6.1: Isotopic composition of the MOX sample (decay corrected for March 2016)

6.1.1 Verification of element selectivity

The mixture of uranium dioxide and plutonium dioxide in this material is an ideal test sample for verification of the element selection of resonant laser ionization. The main problem of many analytical techniques is the parallel determination of the content of ^{238}Pu , ^{239}Pu and ^{240}Pu in environmental samples. The always present surplus of ^{238}U and ^{238}UH prevents the ultra-trace analysis of ^{238}Pu and ^{239}Pu for most mass spectrometric approaches. Radiometric techniques are limited instead by the long half-lives and nearly identical alpha energies of ^{239}Pu and ^{240}Pu . The applied MOX sample includes a high uranium surplus on mass 238 u utilized to prove elemental selectivity. Additionally, the contained ^{241}Am , which is constantly produced by the decay of ^{241}Pu , provides a separate test case for isobaric contamination. The relative amounts of known isobaric contaminations on mass 238 u and 241 u is presented in Tab. 6.2.

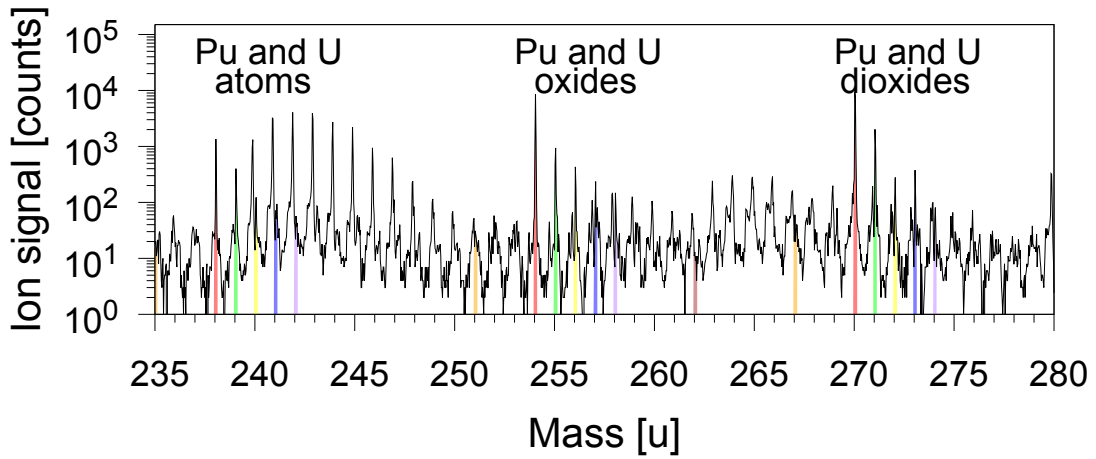
	$^{238}\text{U} / ^{238}\text{Pu}$	$^{241}\text{Am} / ^{241}\text{Pu}$
Isotope ratio	37 200 %	27.6 %

Table 6.2: Isotope ratios of isobaric contaminations

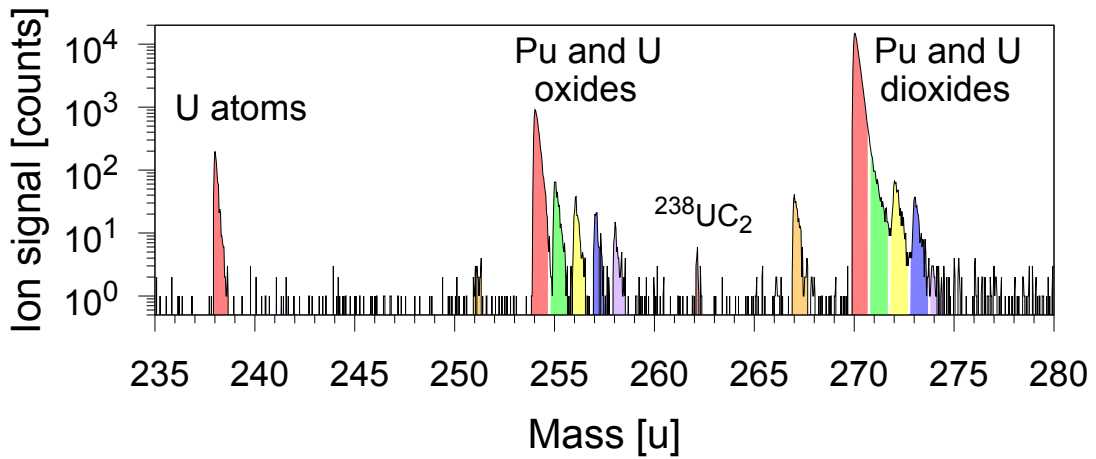
The matrix material of the MOX fuel pellet as well as the present organic contamination, which resulted from parallel SIMS measurements on adhesive tape, provided an additional background for realistic representation of plutonium containing environmental samples.

The first analysis of the MOX sample was performed with conventional SIMS for determination of the contamination on all involved masses, which visualizes the limitations for most mass spectrometric methods. The SIMS mass spectrum, which is presented in Fig. 6.1a, shows different background ion signals, that actually cover parts of the spectrum. There are two kinds of unidentified background signal apparent. A continuous background on the basis of every mass peak, which was also present in former SIMS measurements during characterization and is therefore assigned to unavoidable organic contamination. Additionally, the spectrum is influenced by two series of intensive unidentified mass peaks with their center at mass 243 u and at mass 265 u. The signals of ^{238}U (red) and its oxide and dioxide species are identifiable in the SIMS mass spectra, but the ion signals of all other isotopes are disturbed by further unidentifiable ion signals.

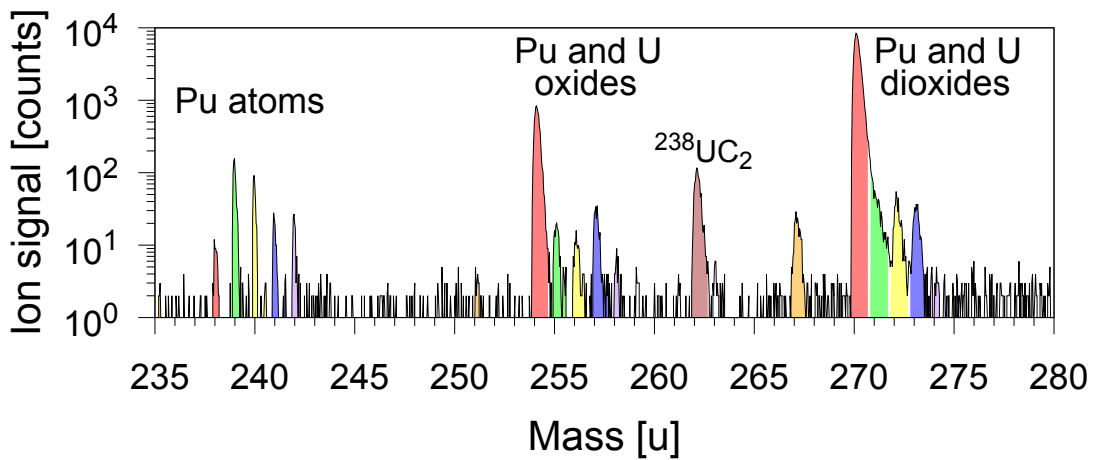
The Laser-SNMS mass spectrum, that is presented in Fig. 6.1b, was measured by application of laser ionization for uranium. The same excitation scheme as used for characterization (Fig. 5.1) was applied for the analysis of the MOX sample. As expected, the unidentified ion background was nearly completely suppressed. The whole mass spectrum consists of the resonantly ionized ^{238}U mass peak and the non-resonantly ionized oxide and dioxide mass peaks of uranium and plutonium. Additionally, a small amount of uranium carbide was detected. The element selectivity for resonant ionization of uranium is verified by the absent ion signals on the masses 239 u - 242 u. A resonantly ionized signal of ^{235}U was not detected for two reasons. Due to its small fraction of the sample, it would be only slightly higher than the background ion signal. Additionally, the lasers were precisely adjusted for resonant laser ionization of ^{238}U . The isotope shift between ^{238}U and ^{235}U for the first and second excitation step is larger than the bandwidth of the applied Ti:sapphire lasers (isotope shifts listed in the appendix as Tab. C.1), which leads to a further significant reduction of the ^{235}U ion signal.



(a) SIMS mass spectrum of the MOX sample, a higher resolved mass spectrum is given in the appendix as Fig. B.33a



(b) Laser-SNMS mass spectrum of the MOX sample with resonant ionization of uranium, a higher resolved mass spectrum is given in the appendix as Fig. B.33b



(c) Laser-SNMS mass spectrum of the MOX sample with resonant ionization of plutonium, a higher resolved mass spectrum is given in the appendix as Fig. B.33c

Figure 6.1: Comparison of the MOX mass spectra: The positions of expected ion signals were marked with different colors, whereas the atomic, oxide and dioxide peak of the same isotope are marked generally with the same color.

The non-resonant laser ionization of uranium oxides is apparently unaffected by the isotope shift, resulting in a small mass peak of ^{235}UO at mass 251 u and a clearly identifiable mass peak of $^{235}\text{UO}_2$ at mass 267 u. The detected non-resonantly ionized plutonium oxides appear on the expected masses, but show an incorrect isotope ratio. Without well-founded knowledge of the non-resonant laser ionization process, it is impossible to determine the reason for this deviation.

The resulting mass spectra of the Laser-SNMS analysis with resonant laser ionization of plutonium is shown in Fig. 6.1c. The applied excitation scheme was identical to the one used for characterization, with small shifts of the wavelengths for ionization of ^{240}Pu instead of ^{242}Pu (Fig. 5.7). The well known isotope shifts relative to ^{240}Pu are smaller than the bandwidth of the Ti:sapphire laser, which should result in equal ionization behavior for all plutonium isotopes (isotope shifts listed in the appendix as Tab. C.2). The achieved mass spectrum consist of the resonantly ionized atomic plutonium mass peaks and the non-resonantly ionized oxide and dioxide mass peaks of uranium and plutonium. The resulting isotope ratios for plutonium, based on the resonant laser ion signal, match the specified values within the errors given as presented in Tab. 6.3. This correct determination verifies the high element selectivity of resonant laser ionization, because even a surplus of more than two orders of magnitude on mass 238 u was suppressed. The same conclusion applies for the influence of ^{241}Am .

	^{238}Pu	^{239}Pu	^{240}Pu	^{241}Pu	^{242}Pu
Specified	2.52 %	56.14 %	26.42 %	7.25 %	7.67 %
Measured	2.8 ± 0.8 %	58 ± 3 %	25 ± 2 %	6.7 ± 1.0 %	7.1 ± 1.0 %

Table 6.3: Comparison of specified and measured isotope ratios of plutonium in the MOX sample. The measurement was performed with resonant Laser-SNMS.

The different laser wavelengths lead to a modified spectra of the non-resonantly ionized molecules towards the Laser-SNMS measurement with ionization of uranium. Therefore, the non-resonantly ionized oxides, dioxides and the even stronger measured $^{238}\text{UC}_2$ are not reliable for determination of isotopic compositions. Nevertheless, they enlarge the sensitivity for identification of small amounts of radionuclides and can at least be applied for approximations of isotopic compositions. The Laser-SNMS measurement of the MOX sample for resonant ionization of plutonium, which is shown in Fig. 6.1c was additionally evaluated to approximate the uranium composition based on oxides and dioxides. The results are listed in Tab. 6.4.

	^{235}U	^{238}U
Specified	0.25 %	99.75 %
Approximated via oxides	0.22 ± 0.07 %	99.8 ± 1.8 %
Approximated via dioxides	0.27 ± 0.02 %	99.7 ± 0.5 %

Table 6.4: Comparison of specified and measured isotope ratios of uranium in the MOX sample. The approximation is based on the measured values of non-resonantly ionized oxides and dioxides.

The isotope ratios for uranium based on oxides and dioxides match the specified values of the sample material within their errors. Further analysis of the non-resonant laser ionization process could lead to reliable values, which offer a method for independent ultra-trace analysis on plutonium and uranium with one measurement on the same sample. The necessary modifications of the Ti:sapphire laser system for changing the excitation scheme between uranium and plutonium require only about two hours. An independent measurement with resonant Laser-SNMS on both elements is therefore generally possible, but will require more technical effort and time.

6.1.2 Influence of lasers and laser power

During analytical measurements on the MOX samples a different influence of the laser power on the resonant and non-resonant laser ionization processes was observed. Additional ion signals were detected by application of all lasers with their maximum power to the MOX sample. The Laser-SNMS mass spectra with resonant ionization of uranium showed a weak ion signal on mass 239 u, that could be generated by a non-resonant ionization of either ^{239}Pu or ^{238}U . The resonant Laser-SNMS measurement of plutonium showed an increased ion signal on mass 238 u relative to the other ion signals of plutonium isotopes. The high intensity in the laser focus led apparently to a non-resonant laser ionization of the atomic ^{238}U , which must be prevented for future analytical applications. For analysis of the influence of non-resonant laser ionization, the influence of all individual lasers and every combination were determined (shown in the appendix as Fig. B.34). Application of the maximum laser power far above the saturation level nearly saturated the non-resonant laser ionization path of ^{239}Pu based on the first and second lasers, which uses a non-resonant transition into the continuum above the ionization potential. This was further substantiated by a saturation measurement with a nearly negligible influence of the third excitation step (shown in the appendix as Fig. B.35). Additionally, the combination of the first and third laser generated an ion signal on mass 238 u, that is not related to ^{238}Pu , because it had no effect on ^{239}Pu . This signal indicates a non-resonant ionization process on ^{238}U . After identification of this process, the laser power for the first excitation step was significantly reduced. The comparison of the mass spectra in Fig. 6.2 for plutonium ionization and in Fig. B.36 in the appendix for uranium ionization show the influence of the reduced laser power.

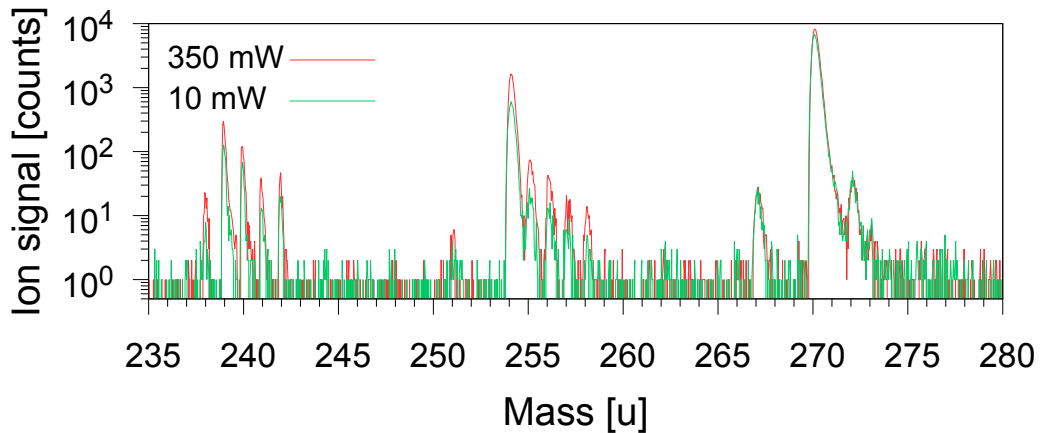


Figure 6.2: Laser power influence on the non-resonant background of the MOX sample: The comparative spectra show the influence of the laser power for the first resonant transition of the plutonium ionization scheme. The red spectrum was measured with a laser power of 350 mW and the green spectrum was measured with a laser power of 10 mW.

The stronger reduction on mass 238 u for lower laser power is clearly visible in Fig. 6.2 compared to the signal decrease of the other plutonium signals. The evaluated ion signal ratio of mass 238 u and 239 u, listed in Tab. 6.5, demonstrates the reduction of the non-resonantly ionized background. The signal ratio matched the specified isotope ratio only with reduced laser power in the first excitation step. The comparative measurement for resonant ionization of uranium showed also the disappearance of the additional ion signal on mass 239 u for reduced laser power. In both spectra, the lower laser power lead to a decreased ion signal of uranium and plutonium atoms and oxides but not of dioxides. The dioxide signals are apparently fully saturated even by the low laser power and depend primarily on the second and third laser.

	Signal on mass 238	Signal on mass 239	Mass ratio $\frac{238}{239}$
Specified for Pu			0.045
$P_{FES} = 350 \text{ mW}$	$129 \pm 12 \text{ counts}$	$1442 \pm 39 \text{ counts}$	0.089 ± 0.012
$P_{FES} = 10 \text{ mW}$	$38 \pm 7 \text{ counts}$	$641 \pm 26 \text{ counts}$	0.059 ± 0.014

Table 6.5: Comparison of specified and measured mass ratios for different laser powers

6.1.3 Sputtering behavior

After the effective application of argon cluster sputtering for reduction of oxides and increase of atomic ion signal, it was also tested during the analytical measurement on the MOX sample material. The resulting behavior during sputtering differentiates strongly from the influence of sputtering on the synthetic samples for characterization. The development of atomic and molecular laser ion signals measured during resonant Laser-SNMS of uranium on a MOX sample is presented in Fig. 6.3.

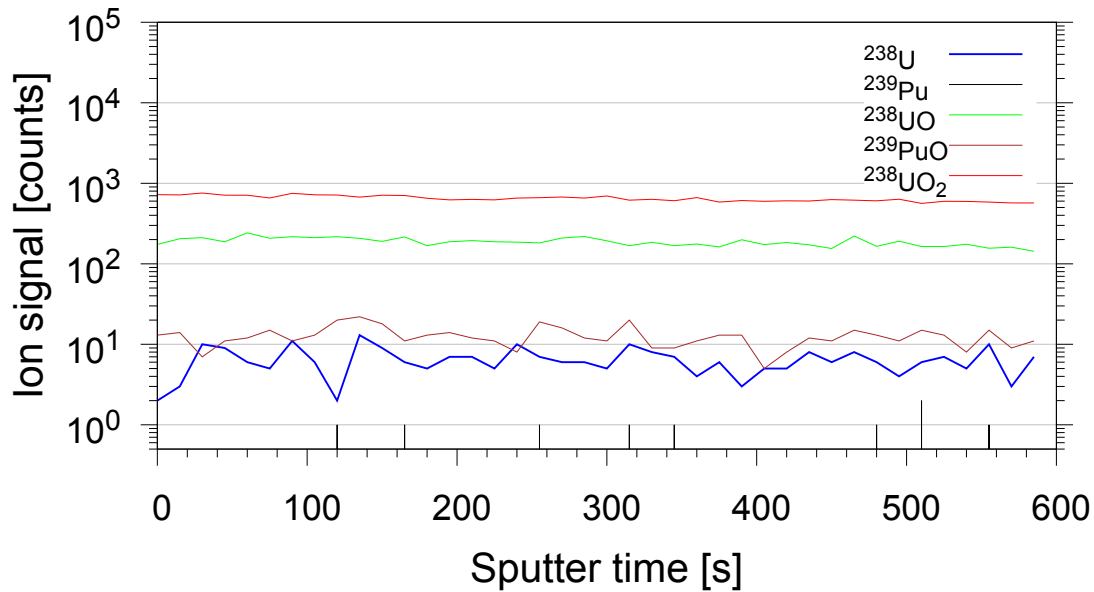


Figure 6.3: Development of the ion signals of resonant ionized ^{238}U and non-resonant ionized ^{238}UO , ^{239}PuO and $^{238}\text{UO}_2$ during continuous argon cluster sputtering.

In contrast to the characterization no apparent influence on the ion signal of ^{238}U , due to argon cluster sputtering, was found. This supports the former theory (see section 5.5), that the atomic uranium ion signal gained by sputtering is not related to a reduction process, but results from a higher degree of oxidation on the surface of the synthetic samples. For resonant Laser-SNMS of plutonium on a MOX sample the sputtering showed an influence and increased the ion signal of atomic plutonium by a factor of 5, presented for ^{239}Pu in the appendix as Fig. B.37. Therefore, the reduction by argon cluster sputtering is at least applicable for oxidized plutonium samples, as additionally shown in section 5.5.

6.1.4 Origin of oxides

The measurement of oxides and dioxides for uranium and plutonium containing samples led to speculations about the origin of those oxides. The absence of oxide laser ion signals in former measurements with hot cavity laser ion sources could indicate, that the oxidation occurred after the sputtering of even after the laser ionization, due to the density inside the sputtered particle cloud. This theory was disproved by an unexpected phenomenon during analysis of the MOX sample. The measured ion images, that show the origin of the detected ion signals, demonstrated a discrepancy in the areas of origin for laser ion signals of atoms and of oxides or dioxides. As presented in Fig. 6.4, the resonantly ionized plutonium and uranium ions were sputtered at different locations than their non-resonantly ionized molecular species.

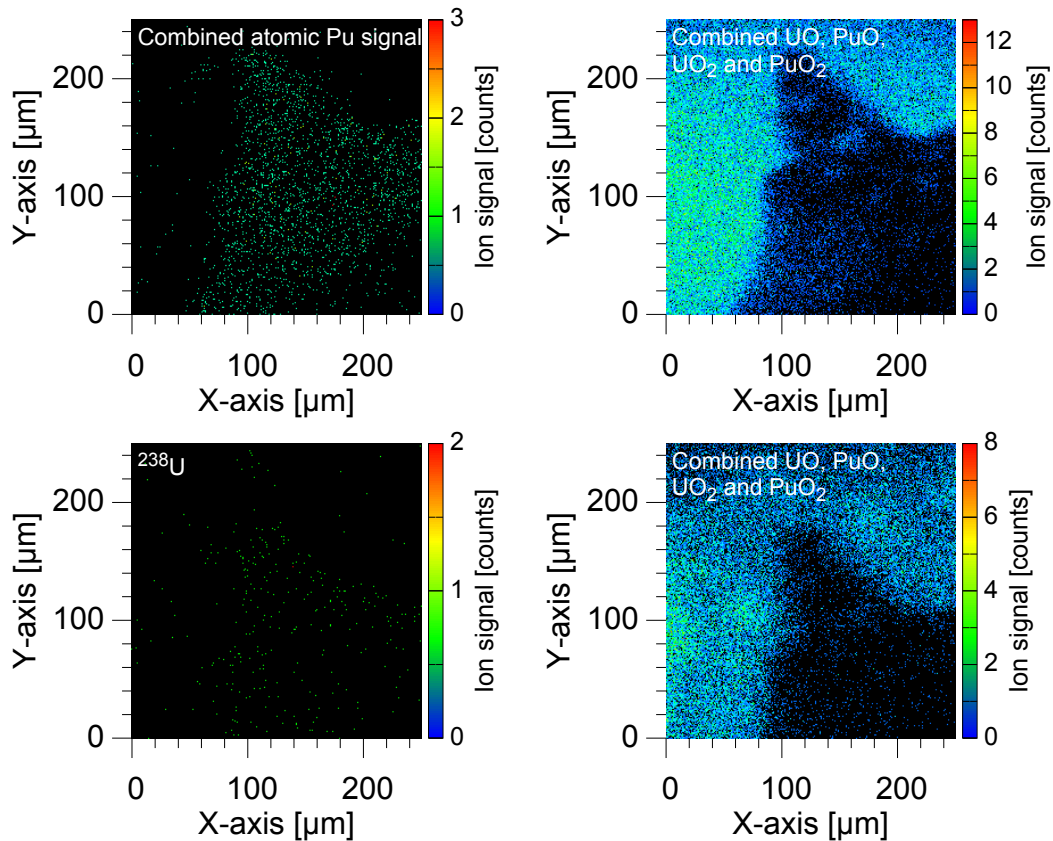


Figure 6.4: Ion image comparison of atoms and oxides: The ion images on the left side show the spatial origin of the combined atomic Pu signal and the ^{238}U signal with different Laser-SNMS measurements on the MOX sample. On the right side are the respectively related ion images of combined oxides and dioxides of U and Pu.

The different areas are caused by structural differences of the deposited MOX material on the sample holder. Therefore, the oxides of uranium and plutonium are already existing on the sample surface at the beginning of the analysis. A subsequent oxidation process could never distinguish between the sample locations. The structural differences are visible on the camera picture presented in Fig. 6.5 and could be a result of varying thickness of the deposited sample material. The aluminium sample holder applies a reductive effect on the bottom layers, which should be measurable for very thin layers, but not for thick layers. The same effect was measured at another location of the identical MOX sample and was compared with a conventional SIMS measurement. The ion images of Laser-SNMS on plutonium and of SIMS show the same separated areas for atomic and oxide ion signal, which was also visible with the installed camera (ion images and camera picture appear in the appendix as Fig. B.38, Fig. B.39 and Fig. B.40).

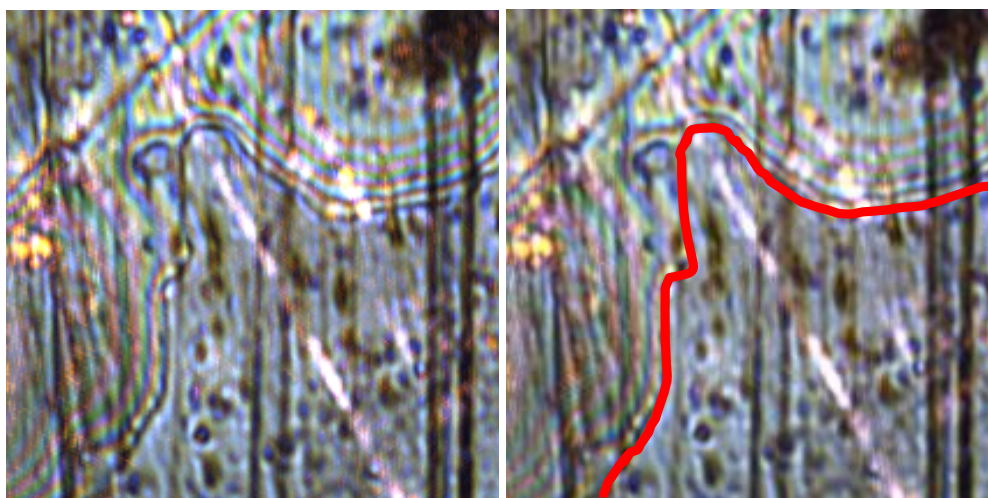


Figure 6.5: Camera image of the sample surface showing the inhomogeneous deposition of the MOX sample material. For better identification of the characteristic border between the oxidized and reduced areas in the left image it is marked in the right image.

6.2 Kabul Soil Sample

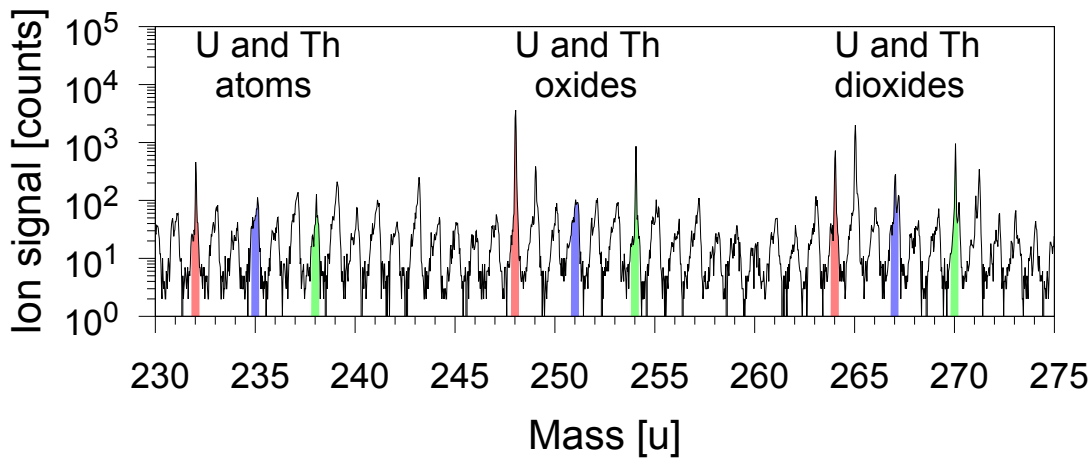
After several measurements on synthetic samples and prepared sample solutions, the newly developed system for resonant Laser-SNMS was applied on a real environmental sample for localization and analysis of radionuclide particles. The sample material is a soil sample from the city of Kabul in Afghanistan. A rocky terrain in Kabul close to inhabited areas showed elevated values of radioactivity with unknown origin. For identification of the radiation source, M. Tanha¹, a PhD student at the IRS Hannover, collected soil and rock samples at this location (photo of the sampling is given in the appendix as Fig. B.41) [97]. Although the technique of resonant Laser-SNMS dispenses with chemical preparation, the size of the rocks in the soil samples and the amount of sample material required additional treatment. First, the sample material was milled to reduce the size of the rock fragments. The produced sand-like material was pressed into an indium foil as sample mount. For rough localization of radioactive particles, a solid-state nuclear track detector (SSNTD) was placed above the sample material (picture appears in the appendix as Fig. B.42). The emitted alpha particles cause small defects in the detection film, which were visually inspected in a microscope after etching and development to provide coordinates of high radiation on the sample area. Those identified spots were cut out and placed on an aluminum sample holder for analysis with conventional SIMS and Laser-SNMS. This sample preparation was done by L. Hamann² as part of her PhD thesis and is described in detail therein [98].

6.2.1 Analysis with SIMS and Laser-SNMS

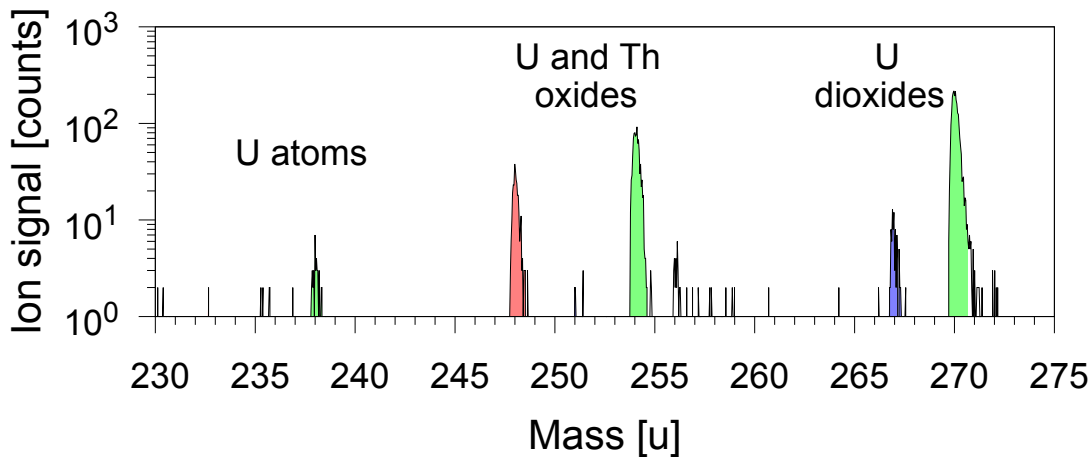
Before the analysis with conventional SIMS and Laser-SNMS the samples were already analyzed by alpha spectroscopy, which led to a well specified uranium content [99]. The mass spectrometric measurements should confirm those results and localize the hot particles of uranium. The resulting mass spectra measured with conventional SIMS and Laser-SNMS on uranium are presented in Fig. 6.6. The mass peaks of ^{235}U and ^{238}U in the SIMS spectrum were too low for reliable identification, but the peaks at the masses of ^{238}UO and $^{238}\text{UO}_2$ indicate the presence of uranium in the sample. Additionally, some other strong peaks appeared at masses 232 u, 248 u and 264 u, which matches the only natural occurring thorium isotope ^{232}Th and its oxides ^{232}ThO and $^{232}\text{ThO}_2$. Subsequent measurements of resonant Laser-SNMS clearly identified the uranium content in the sample material, due to the tested resonant behavior of the ^{238}U ion signal. The comparative measurement of laser ion signal and background signal identified the other laser dependent mass peaks (appears in the appendix as Fig. B.43). The mass peaks of ^{238}UO , $^{235}\text{UO}_2$ and $^{238}\text{UO}_2$ are much stronger relative to the resonantly ionized atomic ^{238}U ion signal than for the synthetic samples. This is explained by the fact that the sputtered ablation led to a lower degree of fragmentation during analysis of the environmental sample. This could be caused by the influence of the surrounding matrix material or an indication of a different uranium species as basic sample. The additional peak at mass 248 u was assigned as the non-resonantly ionized ^{232}ThO based on the previous SIMS measurement. A determination of the isotope ratio of ^{235}U to ^{238}U was prevented by the low signal of ^{235}U , which barely surpasses the measured background level.

¹M.Sc. Mohammad Rahmatullah Tanha, tanha@irs.uni-hannover.de

²Dipl. Phys. Linda Hamann, hamann@irs.uni-hannover.de



(a) SIMS mass spectrum of the Kabul sample



(b) Laser-SNMS mass spectrum of the Kabul sample with resonant ionization of uranium

Figure 6.6: Comparison of the Kabul mass spectra: The identified mass peaks of uranium and thorium isotopes and their oxides and dioxides were marked.

For the first tests of analytical measurements on the environmental sample from Kabul, the material was attached to adhesive tape instead of indium, which led to a better fixation but also to further problems. The adhesive tape is an isolating material, that results in charging effects during ion sputtering. The installed electron flood gun for charge compensation is not applicable in Laser-SNMS mode, because the strong electric potential for suppression of sputtered ions is also active during charge compensation and attracts all electrons before they hit the sample surface. A different potential during the charge compensation would require major technical modifications of the TOF-SIMS instrument. A further problem is the increased organic background by direct insertion of adhesive tape in the TOF-SIMS, which strongly reduced the sensitivity of the measurement system. Additionally, the adhesive tape is very sensitive even to application of small levels of laser radiation. Parts of an analyzed sample were burned by the low energy halo of the laser, although the main focus was still positioned well above the sample surface. These circumstances made a change of the fixation material necessary. Sufficient electrical and thermal conductivity as well as reduced organic contamination in the system, made indium foil to act as perfect carrier material.

6.2.2 Element selective ion images

Besides the mass spectra, the lateral distribution of the different detected ion signals provided further informations about the soil sample material from Kabul. The spatially resolved analysis showed isolated concentrations of uranium and thorium as origin of the measured signals instead of an equal distribution on the sample surface. Consequently, the radionuclides in the soil samples are agglomerated in small particles, which were further analyzed. The images received for different ion signals and signal combinations detected from one specific particle are presented in Fig. 6.7. The analyzed particle has a size of approximately $16\ \mu\text{m} \times 16\ \mu\text{m}$ determined by the origin of the resonantly ionized ^{238}U signal. All detected atomic and molecular signals of uranium and thorium are concentrated on such particles, which strongly indicates a natural occurrence of the uranium. The distribution on the surface of the analyzed particle is inhomogeneous for uranium and thorium ion signals. Additionally, the combined uranium ion signals showed a higher concentration on one spot of the surface sample without a higher concentration of thorium. As a result, the two elements show no constantly related occurrence or ratio on the particle surface, which is an important information for further analysis. The ion image of $^{115}\text{In}_2$ acts as reference of a non-resonantly ionized species, that is clearly part of the sample fixation. A camera picture of the analyzed sample region in Fig. 6.8 shows the milled sample material and uncovered areas of indium in between, which enabled the reference image.

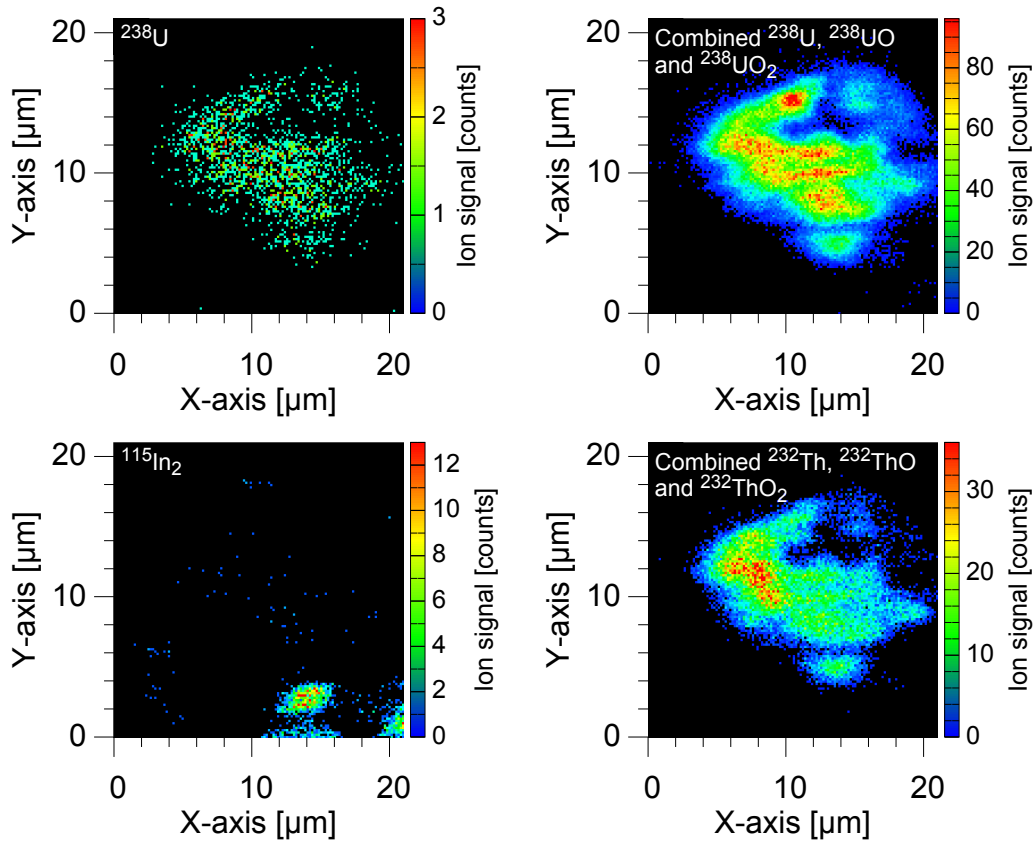


Figure 6.7: Ion image comparison of atoms and oxides: The ion images show the spatial origin of the ^{238}U signal, the $^{115}\text{In}_2$ signal and the combined atomic, oxide and dioxide signal of U and Th with Laser-SNMS.

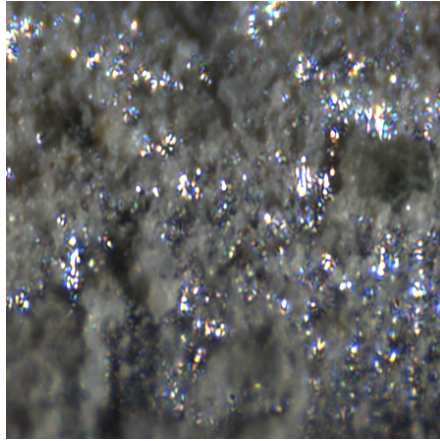


Figure 6.8: Camera image of the sample surface showing the milled soil sample on indium foil.

CONCLUSION AND OUTLOOK

The work presented herein focuses on the development, optimization and characterization of a resonant Laser-SNMS system dedicated to ultra-trace analysis of radionuclides. It demonstrates the scientific tasks for setting up a highly complex analytical system far beyond technical issues and provides the direction for future analysis of radionuclide nanoparticles. The detailed explanations about target-oriented modifications and adaptations based on extensive simulations in combination with well-elaborated characterization measurements create the solid foundation for environmental ultra-trace analysis. Furthermore, the first analytical measurements of the IRS resonant Laser-SNMS system delivered fundamental insights and results on the analysis of colloidal formations of radionuclides as well as on the capabilities of this new analytical instrument.

The development of the resonant Laser-SNMS system at the Institute for Radioecology and Radiation Protection in Hannover was performed together with the LARISSA group of the Institute of Physics in Mainz and was based on a successful test of such a system at the Institute for Nuclear Chemistry in Mainz. Besides the application of a new TOFSIMS 5 instrument from the company IONTOF, the pulsed, high-power Ti:sapphire laser system was designed and modified to fulfill all specifications for the resonant Laser-SNMS analysis. The first part of this work describes the modifications of the laser system as well as the development of control and monitoring systems to accomplish the required spacial and temporal overlap of the sputtered neutral particle cloud and the focused laser beams in the ionization region. Within the implementation of the combined Laser-SNMS instrument, the influence of delayed extraction and different applied suppression voltages on the sputtered ion background was analyzed. Laser-SNMS measurements on uranium standards provided first reliable settings for the interaction region and temporal synchronization of all processes.

The acceptance volume of the time-of-flight mass analyzer had to be changed due to the increased and displaced ionization region for resonant Laser-SNMS being located well above the sample surface. The strong correlation of the operational parameters of the mass analyzer required a simulation-based optimization, which is presented in the second part of this work. The computer simulations used a Monte Carlo approach for calculation of transmission probabilities and transport efficiencies by evaluation of 10.000 ion trajectories through the mass analyzer geometry. The 10.000 sample ions were provided by a second simulation program called "Ionengenerator", which was developed as part of this work and delivered additional information about the expansion behavior of the sputtered particle cloud and optimum overlap conditions for the laser focus. Generation of the simulation model in the simulation software SIMION was realized by the conversion of technical drawings of the real

mass analyzer. Extensive scans through the operational parameter space allowed stepwise analysis of the different correlations, which resulted in an optimized parameter set for application of resonant Laser-SNMS. The simulations yielded an enhancement of the overall transport efficiency for uranium ions by a factor of 2.5. After the Laser-SNMS system was fully operational, those optimized parameters were tested with measurements on synthetic samples of ^{238}U , ^{99}Tc and ^{239}Pu . The measured gain of transport efficiency surpassed the expectations of the simulation with values between 2.7 ± 0.4 for ^{99}Tc and 6.3 ± 2.6 for ^{239}Pu .

Characterization of the Laser-SNMS system is necessary to create the basis for every following radioanalytical measurement and was a major part of the presented PhD project. The mass spectra produced by an instrument for resonant Laser-SNMS can be strongly influenced by the composition of the sample, due to sputter ionized background and non-resonantly ionized species, and by the intensity and wavelength of the applied laser radiation. The characterization of the main elements of interest, i.e. uranium, plutonium and technetium, used clean synthetic test samples and included an analysis of the influence of every laser for resonance ionization. Besides the characteristic mass peaks of the atomic ions, the mass spectra of all three elements showed signals of parallel non-resonant laser ionization. Even the oxides of uranium and plutonium produced clearly detectable ion signals, that do not interfere with the atomic ion signals and are therefore applicable for speciation analysis. Additionally, the characterization focused on the determination of the sensitivity of the analytical measurements via the decision threshold for the three tested elements. Analysis of 200 nL of 1 ppb - 10 ppb sample solutions resulted in upper limits for the decision threshold between $(5.1 \pm 1.5) \cdot 10^9$ atoms for plutonium and $(5.2 \pm 1.6) \cdot 10^8$ atoms for uranium. The efficiency measurement of high-purity synthetic uranium particles provided an overall efficiency of $(2.63 \pm 0.07) \cdot 10^{-5}$, which leads to a calculated decision threshold of $(2.12 \pm 0.08) \cdot 10^6$ atoms. The characterization measurements were furthermore used to compare the results of resonant Laser-SNMS with similar measurements by conventional SIMS. The combination of element selective ionization and suppression of the sputtered background signal leads to a gain in the signal-to-background ratio of more than one to more than two orders of magnitude, depending on the element. A reduction of the mass resolution of about one order of magnitude was expected as a consequence of the increased ionization volume, but is well acceptable for element selective mass spectra. The expected increase of ion signal was prevented by the high degree of oxidation on the sample surface. Application of argon cluster sputtering for ablation of upper surface layers showed a strong influence for the analyzed uranium and plutonium samples, but the reduction of fully oxidized environmental sample material for future analytical tasks will require advanced procedures. To the knowledge of all involved collaborative partners, this characterization measurement included also the first ever resonant Laser-SNMS analysis on technetium.

Initial analytical measurements addressed the main fields for the development of this Laser-SNMS system to verify its capabilities. The extension by resonant laser ionization offers the possibility to suppress isobaric background, especially interfering isotopes from other elements, without chemical separation. This characteristic feature was verified by the analysis of a dissolved fragment of a MOX fuel pellet, consisting of a mixture of uranium oxide and plutonium oxide. The isotope ratios of the plutonium isotopes ^{238}Pu and ^{241}Pu would be heavily affected by the presence of ^{238}U and ^{241}Am without an element selective ionization in combination with suppression of all sputtered ions. The determination of the measured plutonium isotope ratios showed a sufficient suppression of a surplus of 37.2 times more ^{238}U than ^{238}Pu . Additionally it was possible to approximate the uranium isotope ratio of ^{235}U and ^{238}U by their non-resonantly ionized oxides and dioxides within the same

measurement. A comparison with the mass spectrum provided by conventional SIMS shows the enhancement for signal identification and undisturbed isotope ratio determination by resonant Laser-SNMS. Additional analytical measurements, which were performed during this PhD project, focused on the ability of spatially resolved analysis on radionuclide particles in chemically unprepared environmental samples. The origin of increased radioactive radiation in soil samples from Kabul (Afghanistan) was confirmed by Laser-SNMS. The combination of SIMS and Laser-SNMS analysis enabled the localization of particles in the milled sample material that consist of an inhomogeneous mixture of uranium and thorium as typical for specific natural sources. The inhomogeneous distribution was clearly visible on ion images of the approximately $16\ \mu\text{m} \times 16\ \mu\text{m}$ sized particle. Those analytical measurements completed the test operation of the new resonant Laser-SNMS system and verified its potential for ultra-trace analysis on hot particles.

The future field of activities for the Laser-SNMS system will be the analysis of radionuclide nanoparticles in environmental samples within the research project SIRIUS. The focus of this project is an advanced understanding of the transport mechanisms and geochemical behavior of trace amounts of plutonium and technetium under varying natural conditions for nuclear safeguard concerns. Besides the analytical applications, there are several interesting approaches for further increase of the sensitivity. As mentioned before, the efficiency of resonant laser ionization is mainly limited by the large degree of oxidation of the sample material. A reduction could be achieved by application of the different sputter species at high or low energies that are available in the Laser-SNMS system, either for implantation of reductive species or for increased fragmentation yield during the analysis. The influence of different sample holder materials could offer further reduction properties as well as the application of sample conditioning via preparatory heating, which was applied at the predecessor system at the Institute for Nuclear Chemistry in Mainz. Further increase of the sensitivity could also be achieved by the installation of a two-step extraction electrode setup, which would also enhance the mass resolution. The scientific applications of the Laser-SNMS system on top of the SIRIUS project could concern a wide range of activities like dedicated ionization scheme development for sputter sources, methodical development for analysis of environmental samples and, primarily, the radioecological ultra-trace analysis of further elements of interest. An expansion of the analytical possibilities was already introduced within the master thesis of H. Bosco, which focused on the detection of radioactive strontium with the IRS Laser-SNMS system [100]. In conclusion, the demonstrated capabilities of this analytical system offer a variety of future fields of application to enhance the understanding of radionuclide interactions in the environment and to improve the nuclear safeguard systems for a reliable protection against the health hazards from radioactivity.

PHOTOS OF THE LASER-SNMS SETUP

A.1 Lasersystem

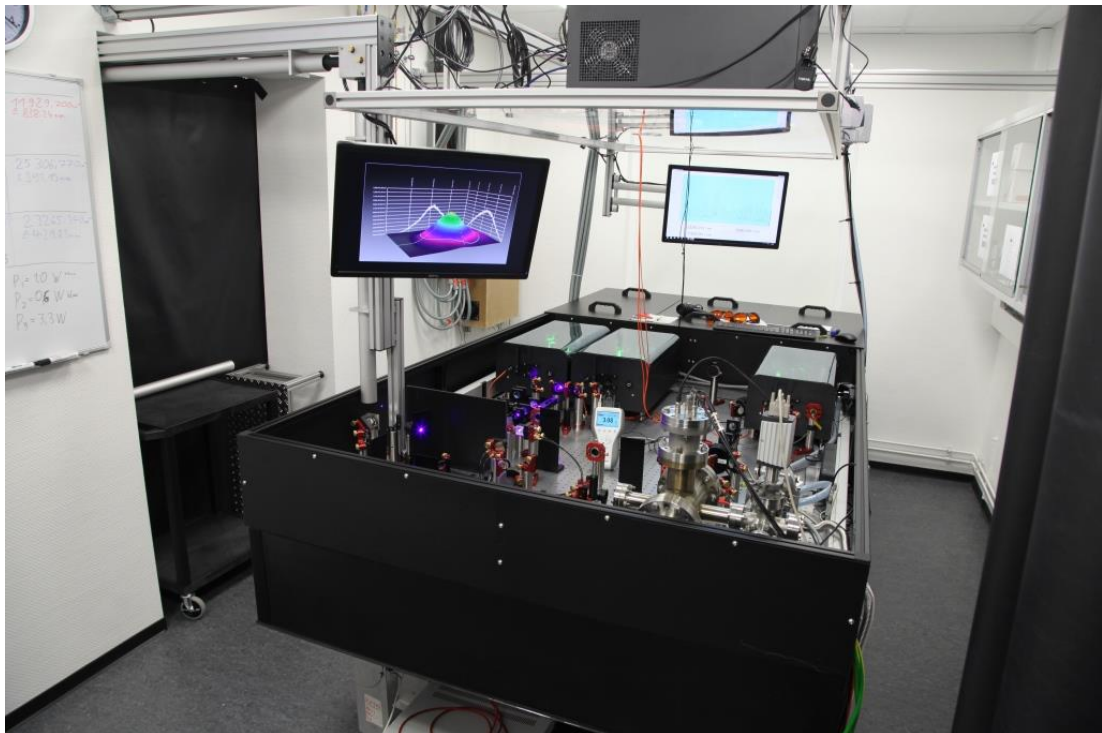


Figure A.1: Photo of the complete laser system

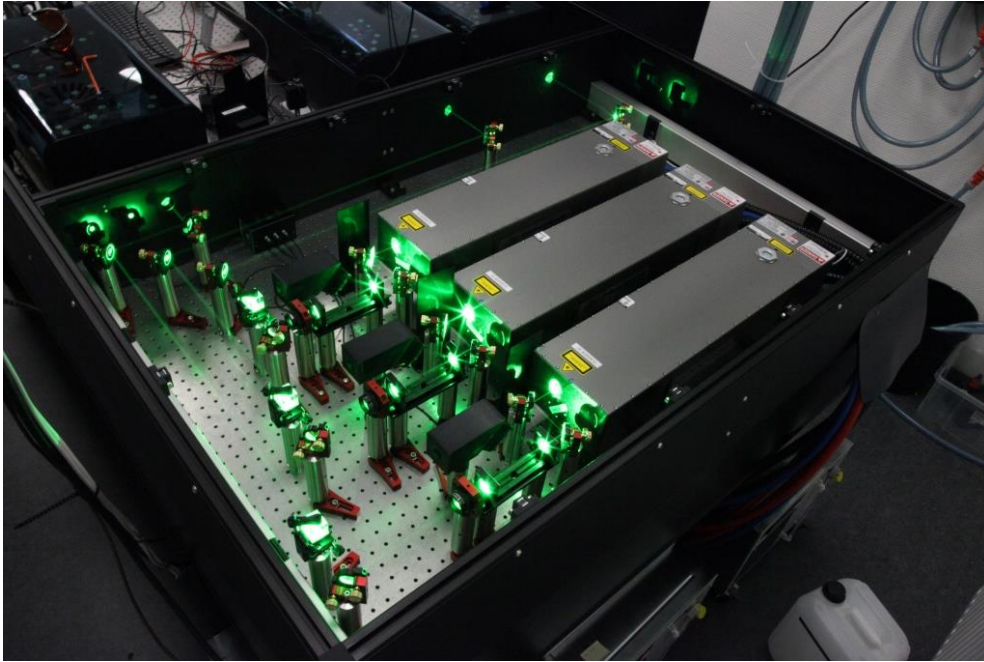


Figure A.2: Photo of the pump laser setup

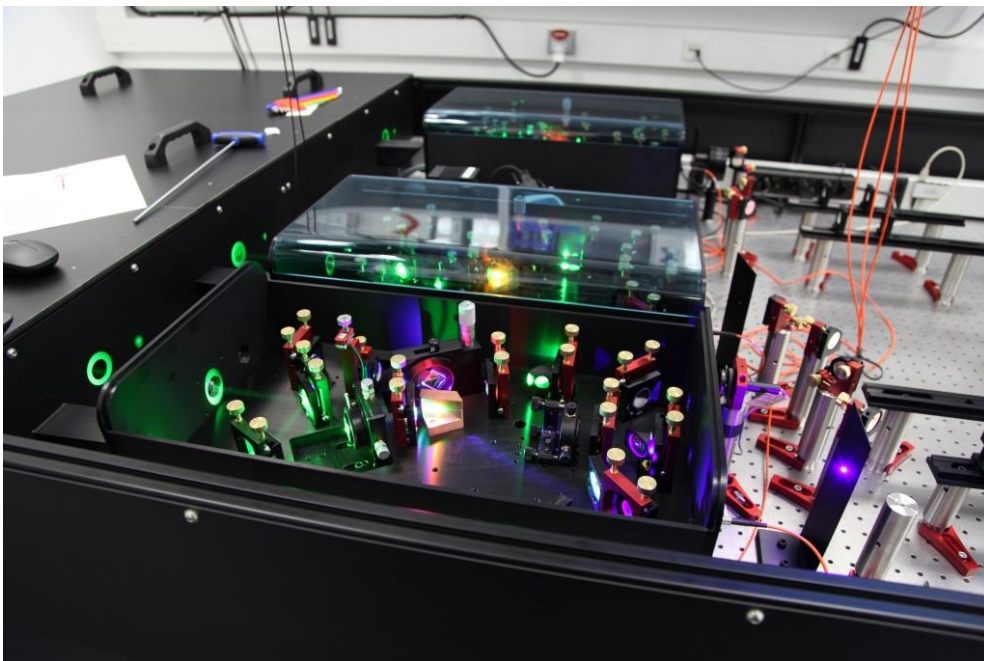


Figure A.3: Photo of the Ti:sapphire laser setup

A.2 LabVIEW program interfaces

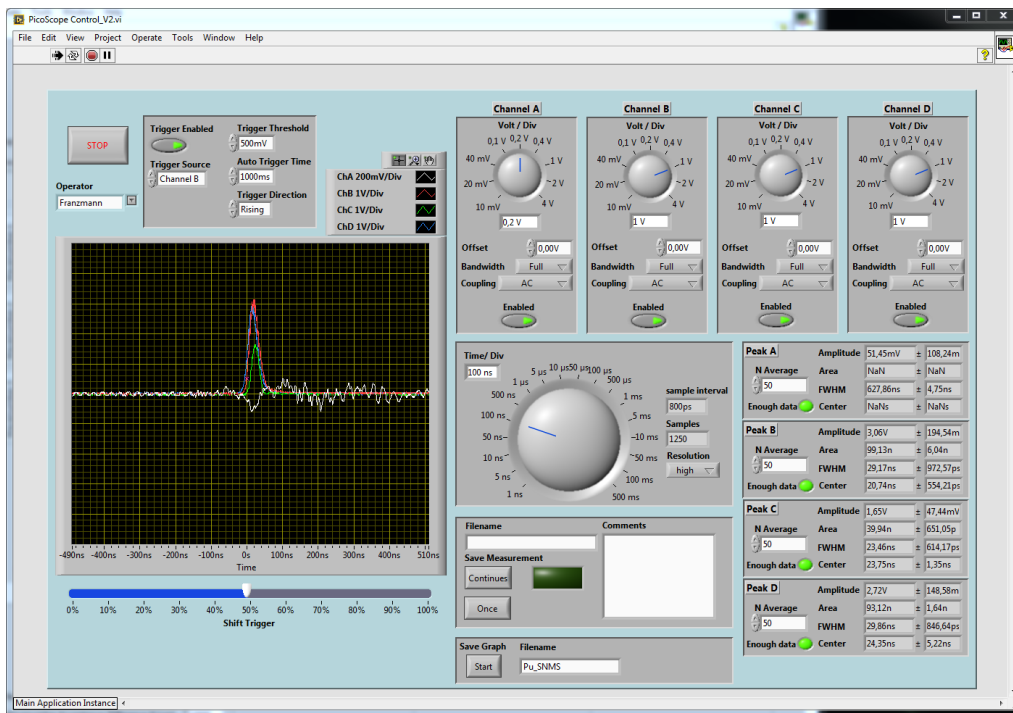


Figure A.4: Screenshot of the GUI of the timing measurement program

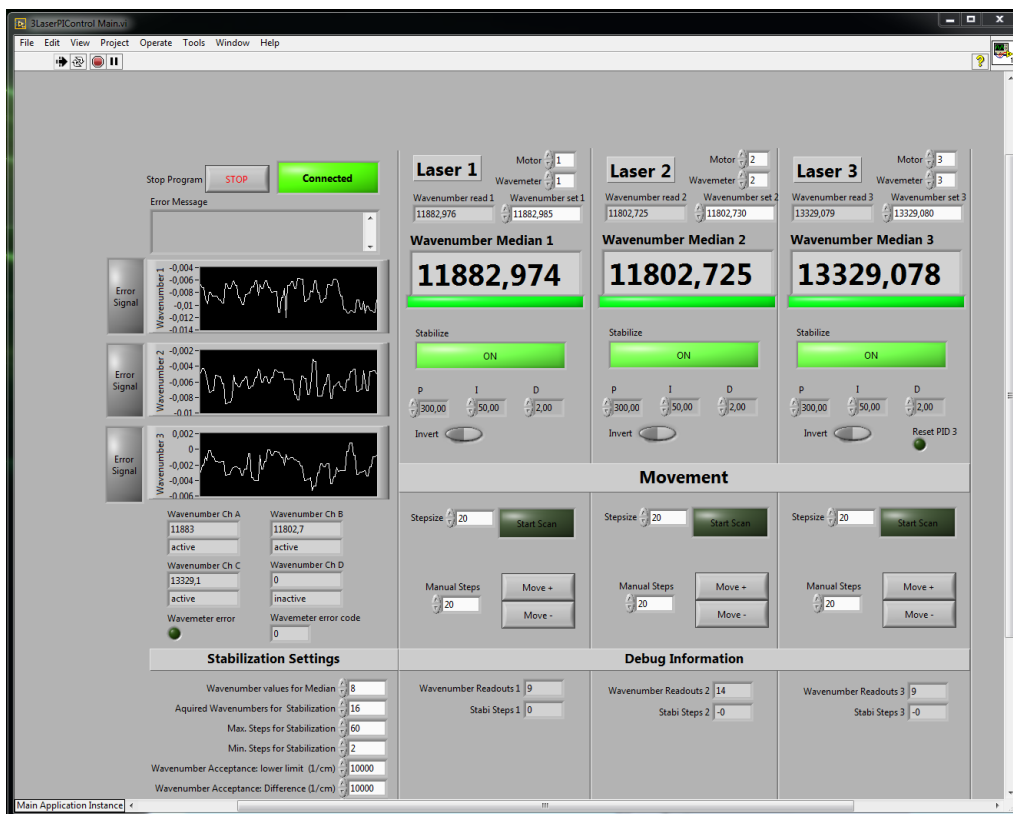


Figure A.5: Screenshot of the GUI of the wavelength stabilization program

A.3 TOF-SIMS instrument

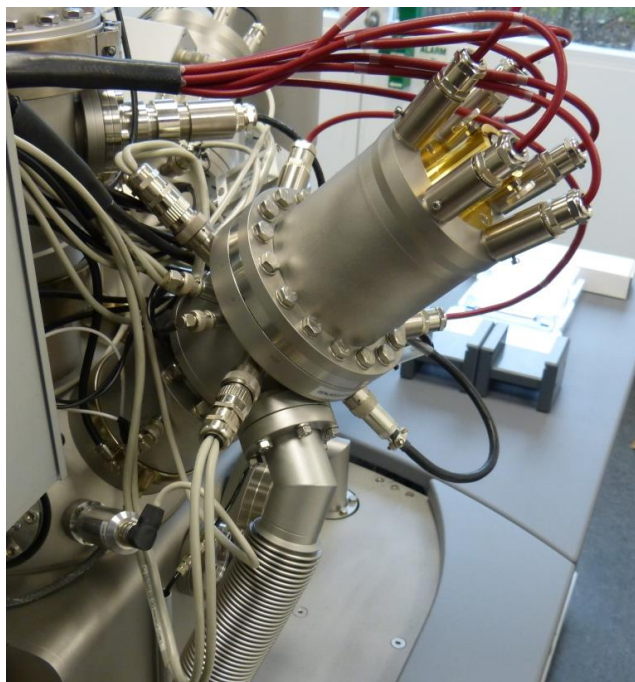


Figure A.6: Photo of the liquid metal ion gun (LMIG)

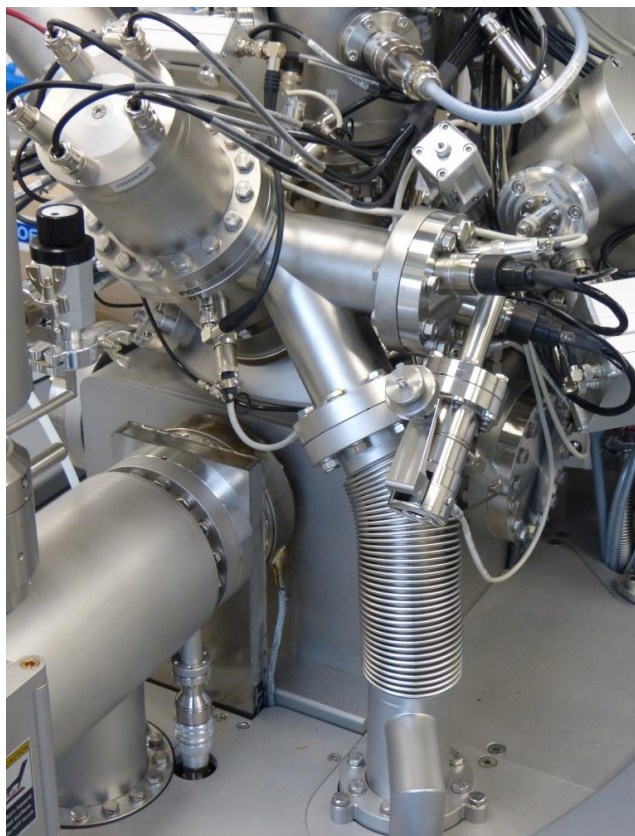


Figure A.7: Photo of the dual source column (DSC)

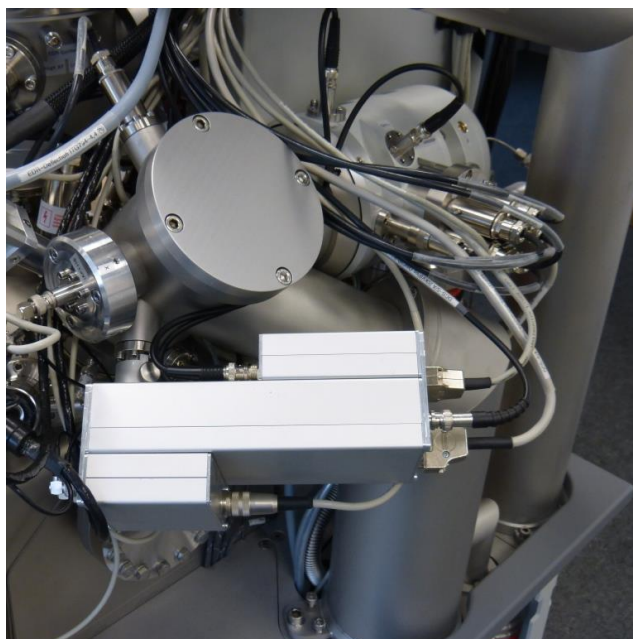


Figure A.8: Photo of the gas cluster ion beam (GCIB)



Figure A.9: Photo of the time-of-flight mass analyzer

A.4 Beam transport, coupling and monitoring

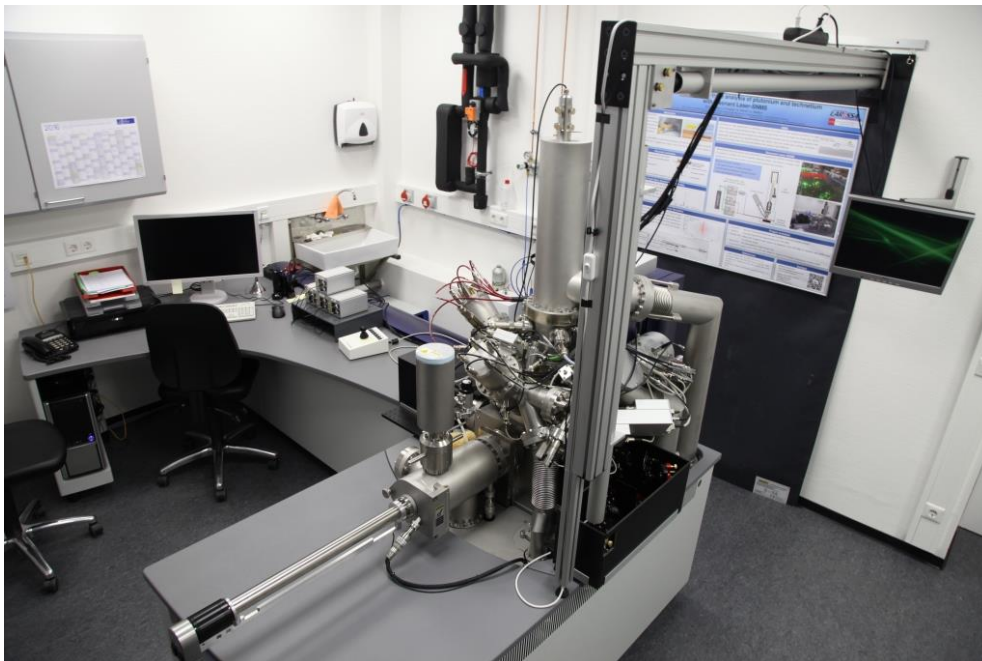


Figure A.10: Photo of the TOF-SIMS instrument including all modifications for resonant Laser-SNMS: The photo shows the beam transport to the TOF-SIMS instrument through aluminium tubes. The beam transport ends at the coupling and monitoring setup besides the main chamber.

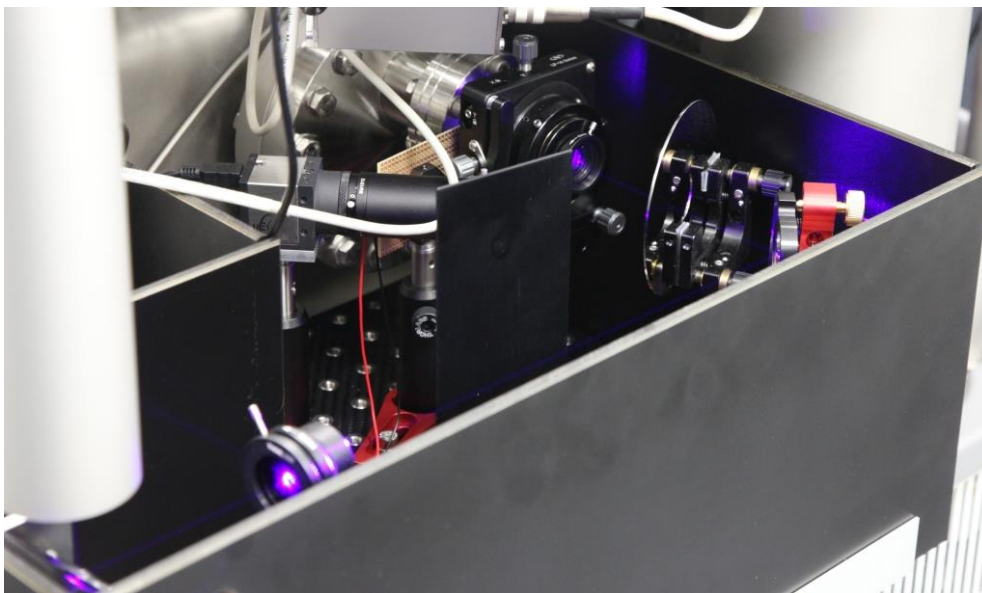


Figure A.11: Photo of the laser coupling and monitoring setup at the TOF-SIMS instrument: The laser beam is transported through the aluminium tube at the left side and is then horizontally reflected through the first iris diaphragm. The piezo mounted high reflective mirror in the right corner sends the laser beam through the ring mirror, the second iris diaphragm, the hidden focusing lens and vacuum window inside the TOF-SIMS. On the left side of the 5-axis lens mount is the front camera with telescope and filter installed.

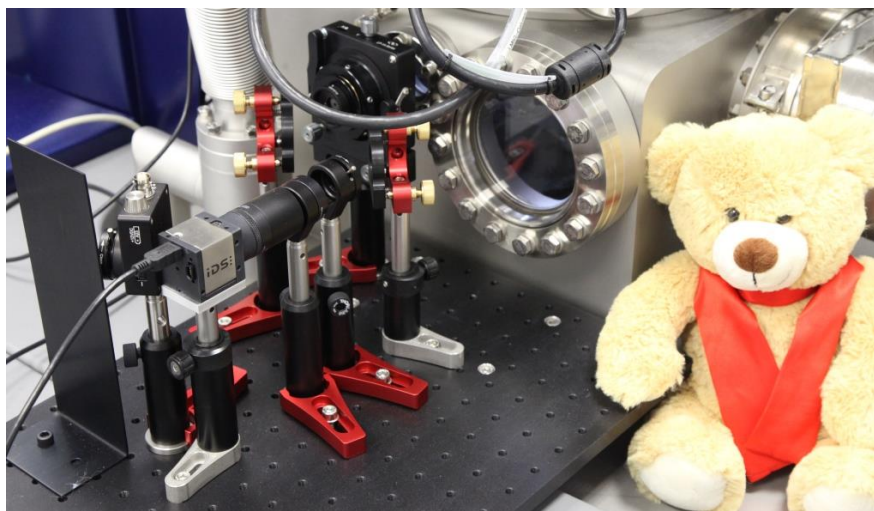


Figure A.12: Photo of the laser monitoring setup behind the TOF-SIMS: The laser beam escapes through the aperture in the 5-axis mount and hits the beam block at the left side of the picture. A small amount of laser radiation is separated before and directed through neutral density filters and lenses to the back camera. The applied teddy bear mascot was necessary to ensure proper operation of the whole Laser-SNMS instrument.

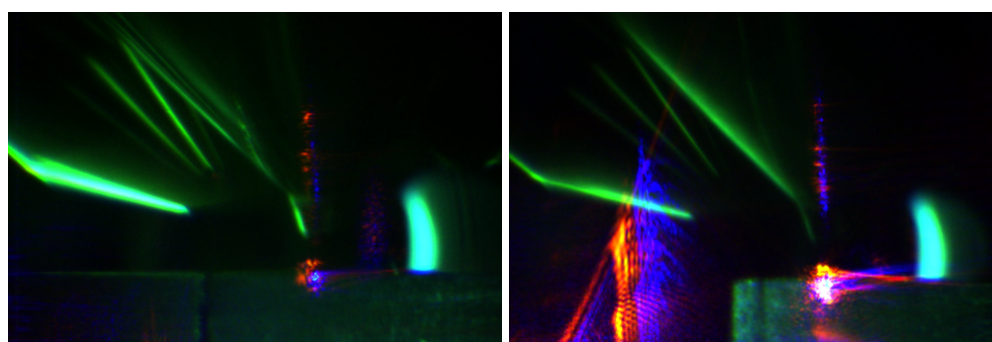


Figure A.13: Photo of the sample region seen by the front camera: Both photos show the ionization volume inside the TOF-SIMS. The laser is adjusted under the the mass analyzer tip and above the sample holder. At proper laser beam height only the weak halo around the laser focus is reflected (left photo). If the laser beam is adjusted to low, a part of the focus is also reflected (right photo).

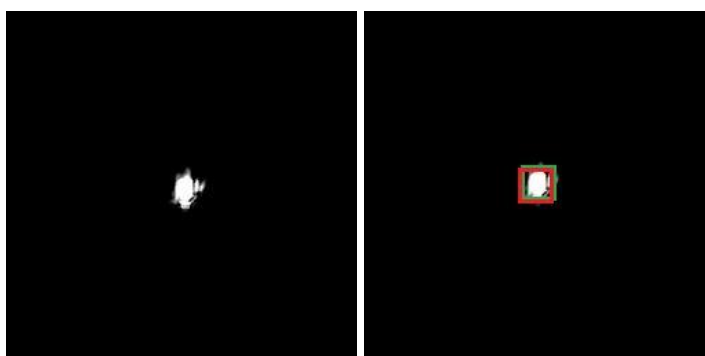


Figure A.14: Photo of the laser beam seen by the back camera: Both photos show the detected and strong attenuated laser beam behind the TOF-SIMS. The right photo shows additionally the determined beam position marker (green square) and the set position marker (red square).

A.5 Sample preparation

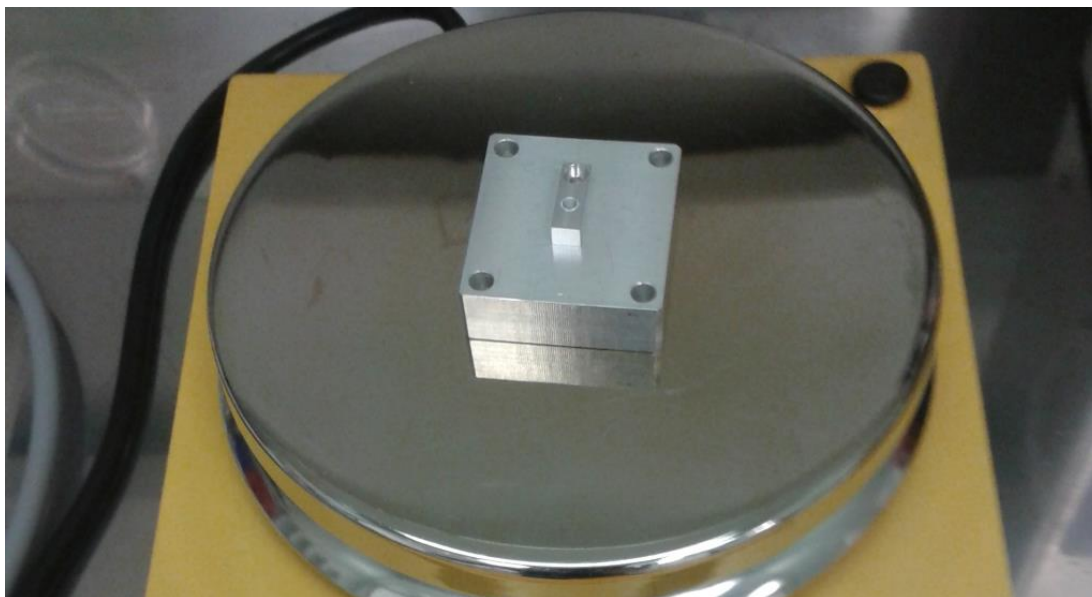


Figure A.15: Photo of the heated sample holder: The sample holder with a small amount of sample solution is placed on a heat plate until the solvent is vaporized.



Figure A.16: Photo of the prepared sample before analysis: The deposited sample material is visible as darker area in the middle of the four orientation marks on the sample holder.



Figure A.17: Photo of the uranium particle containing silicon waver: The brighter fields in the middle are the analyzed areas. The two areas of $500\ \mu\text{m} \times 500\ \mu\text{m}$ visible on the left side were used for test measurements. The four small areas on the right side mark the positions of the efficiency measurements. (one measurement was incomplete due to technical problems)

GRAPHS, PLOTS AND DIAGRAMS

B.1 Characterization of the IRS Ti:sapphire laser

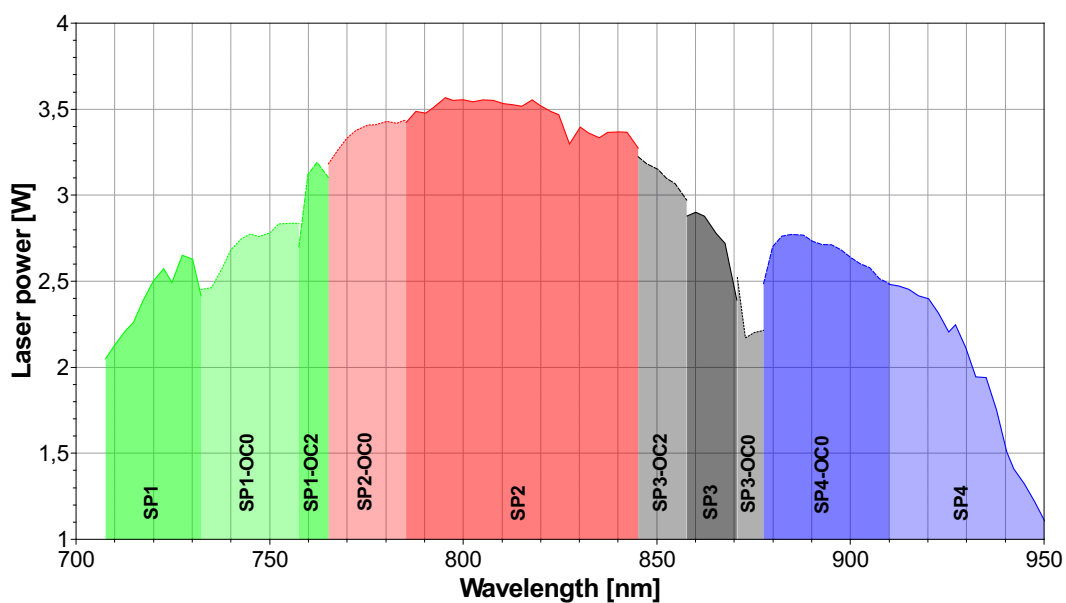


Figure B.1: Power of the IRS Ti:sapphire laser over the complete emission range: The bars under the graph shows the cavity mirror set (SPx) which led to the highest laser power in a certain wavelength range. Also combinations with an output coupler (OC) of a different mirror set were applied. Measured with an OPHIR Vega Powermeter and an OPHIR 12A thermal power sensor

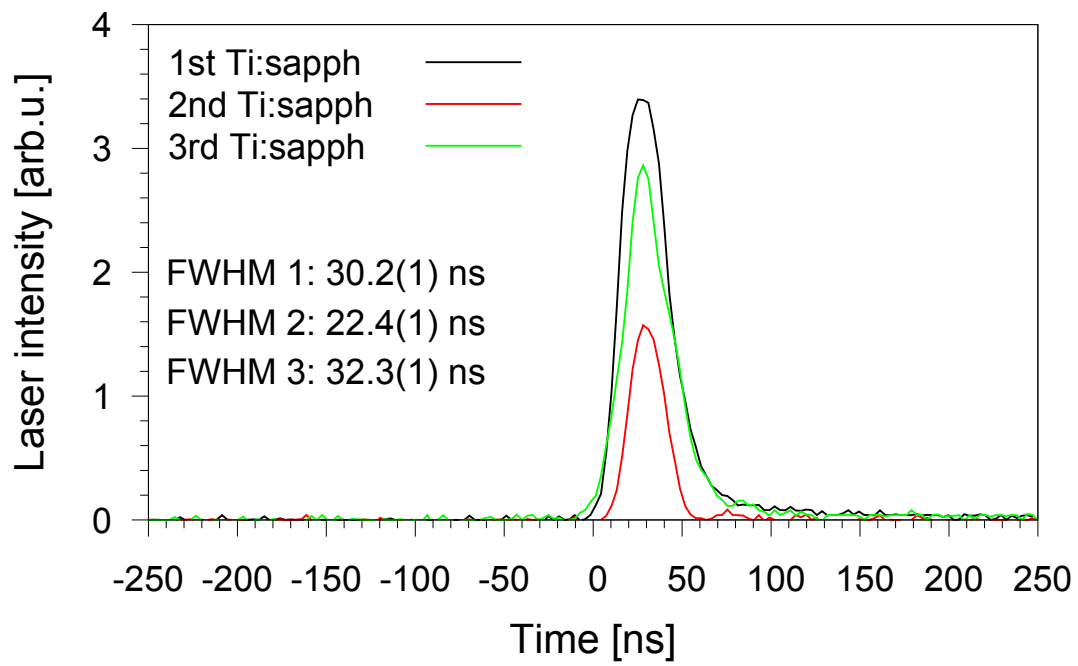


Figure B.2: Pulse width measurement of all three Ti:sapphire lasers

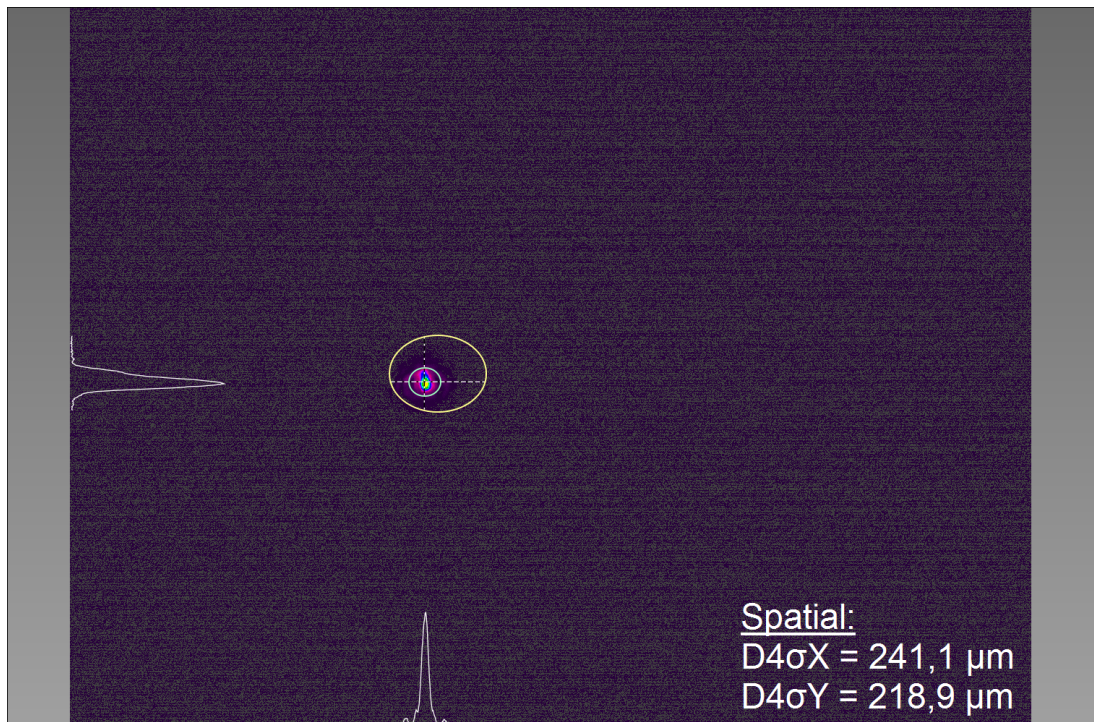


Figure B.3: Beam profile of the IRS Ti:sapphire laser with the smallest measured beam diameter

B.2 Parameter scans

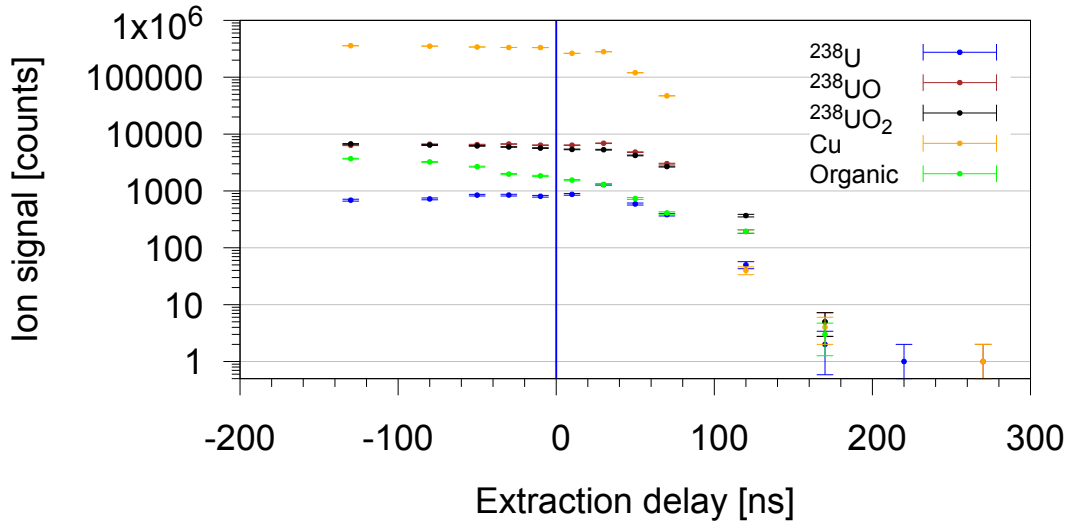


Figure B.4: Influence of the extraction delay on the suppressed sputter ion signal: The graph shows the ion signal of five different sputtered species for different applied extraction delays and a suppression potential of +500V. The blue line marks the impact of the sputter pulse.

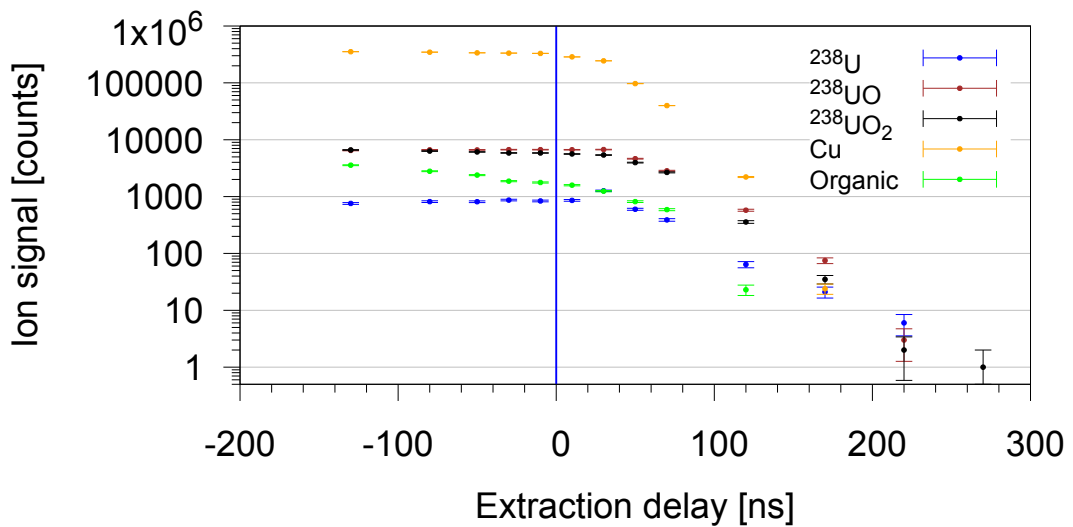


Figure B.5: Influence of the extraction delay on the suppressed sputter ion signal: The graph shows the ion signal of five different sputtered species for different applied extraction delays and a suppression potential of -500V. The blue line marks the impact of the sputter pulse.

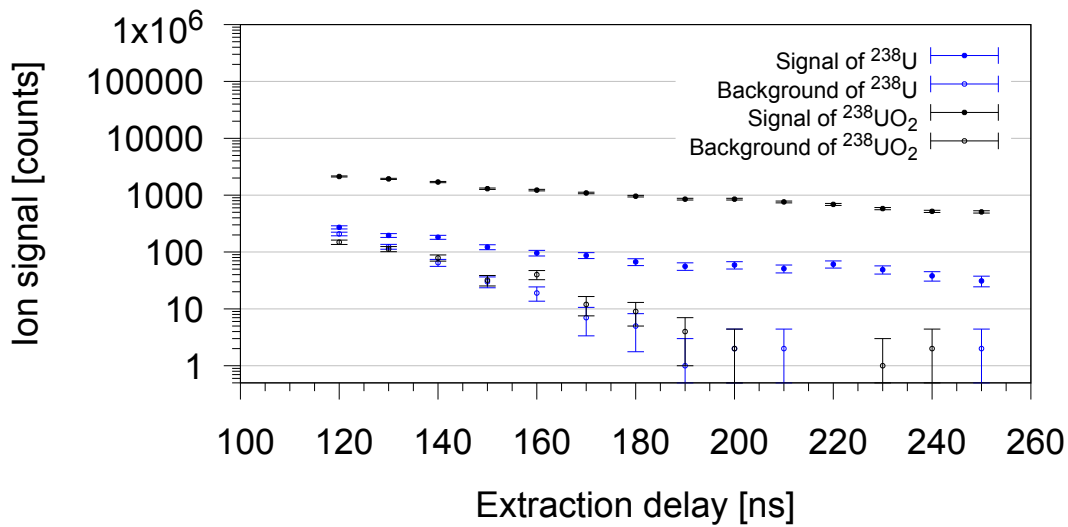


Figure B.6: Influence of the extraction delay on the laser ion signal and the suppressed background: The graph shows the ion signal of laser ionized ^{238}U and $^{238}\text{UO}_2$ and the suppressed, sputter ionized background of ^{238}U and $^{238}\text{UO}_2$ for different applied extraction delays. The applied suppression potential is -500 V .

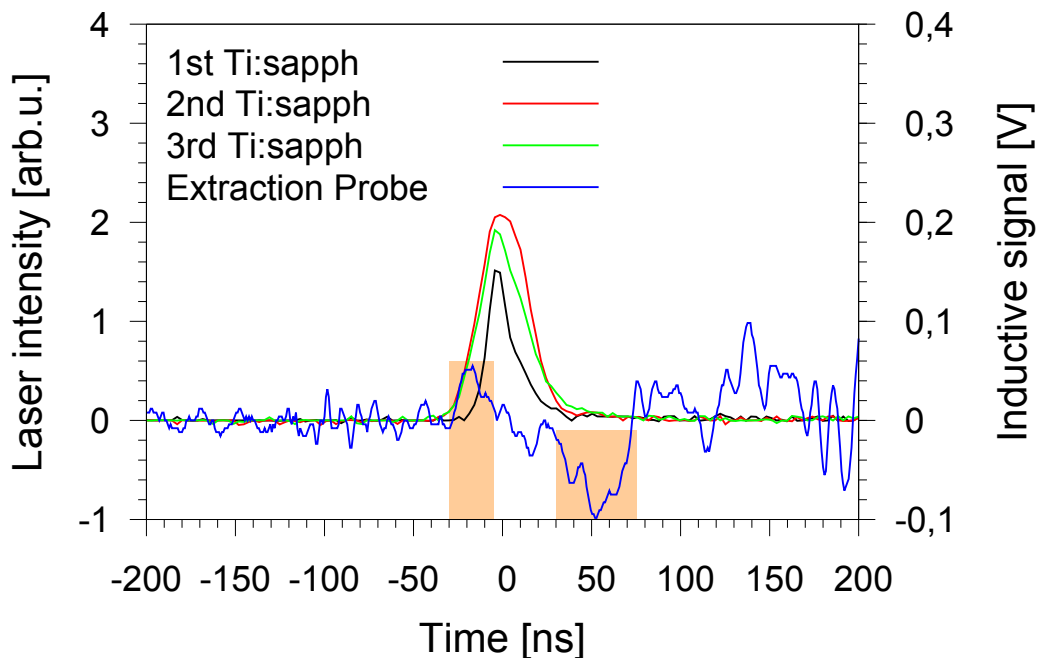


Figure B.7: Monitoring of the laser and extraction pulse timing: The graph shows the three pulses of the Ti:sapphire lasers and the signal of the inductive probe, which picks off the fast potential shifts of the extraction electrode. The orange boxes mark the two important pulses, when the suppression is switched off and the extraction is switched on 50 ns - 70 ns later. The following overshooting signal is the result of insufficient electronic damping.

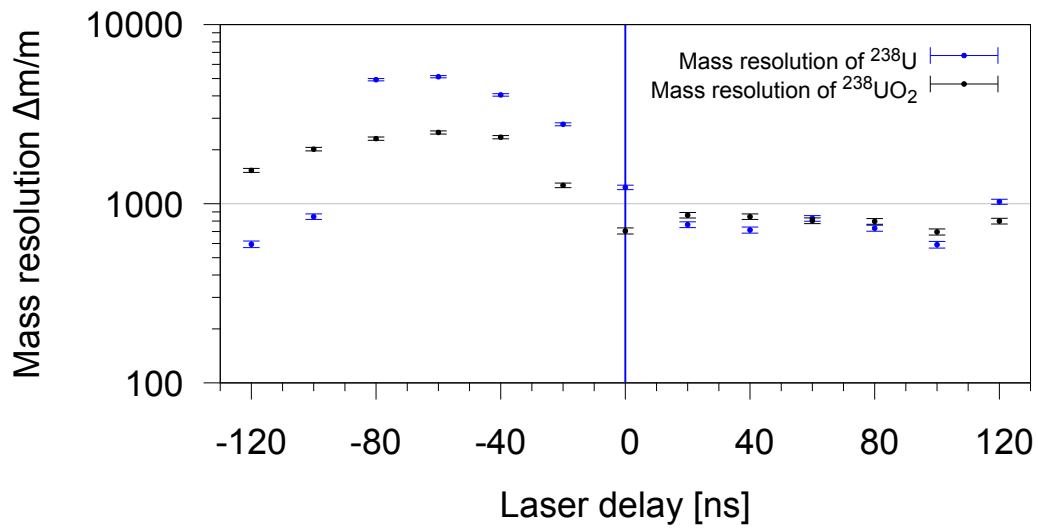


Figure B.8: Influence of the laser delay on the mass resolution of the resonant and non-resonant laser ion signal: The graph shows the mass resolution of laser ionized ^{238}U and $^{238}\text{UO}_2$ for different applied laser delays. The blue line marks the impact of the sputter pulse.

B.3 Sputter distributions and laser overlap

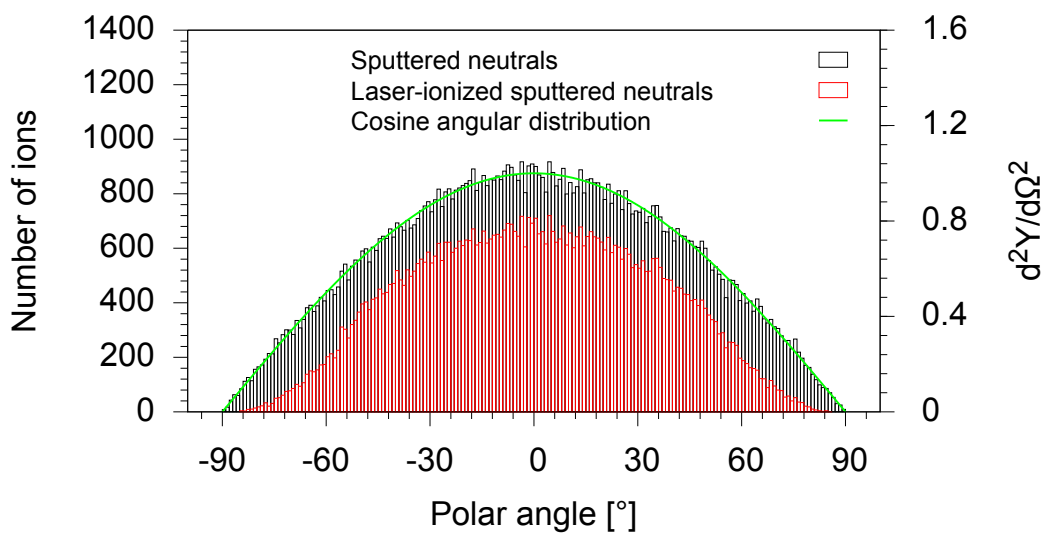


Figure B.9: Comparison of the theoretical and simulated angular distributions: The graph shows the simulated angular distribution of all sputtered neutrals and the laser-ionized fraction of the sputtered neutrals in comparison with the cosine angular distribution.

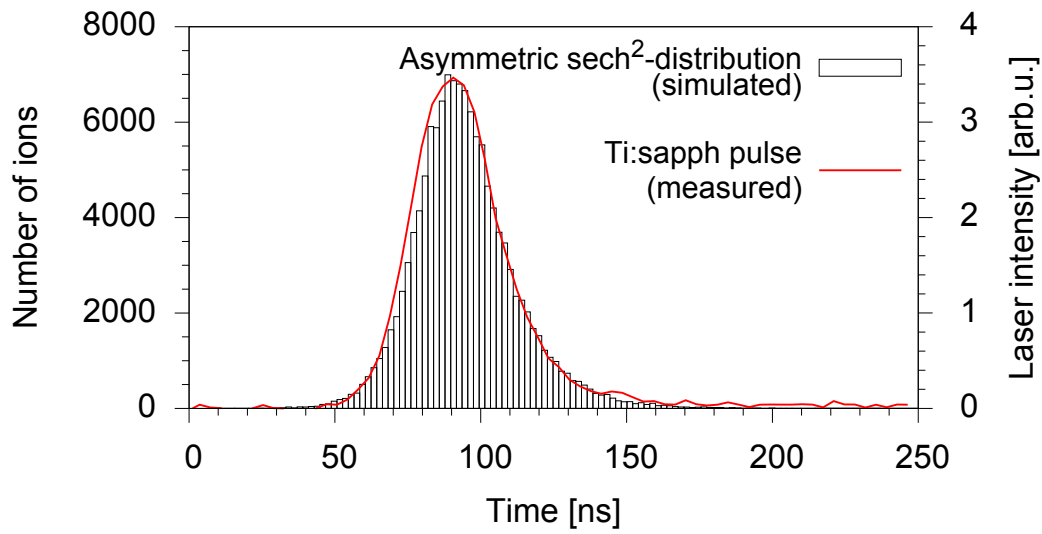


Figure B.10: Comparison of the measured and simulated temporal distribution: The graph shows the simulated temporal distribution of the time of origin of the laser-ionized sputtered particles in comparison with the measured temporal distribution of a Ti:sapphire laser pulse.

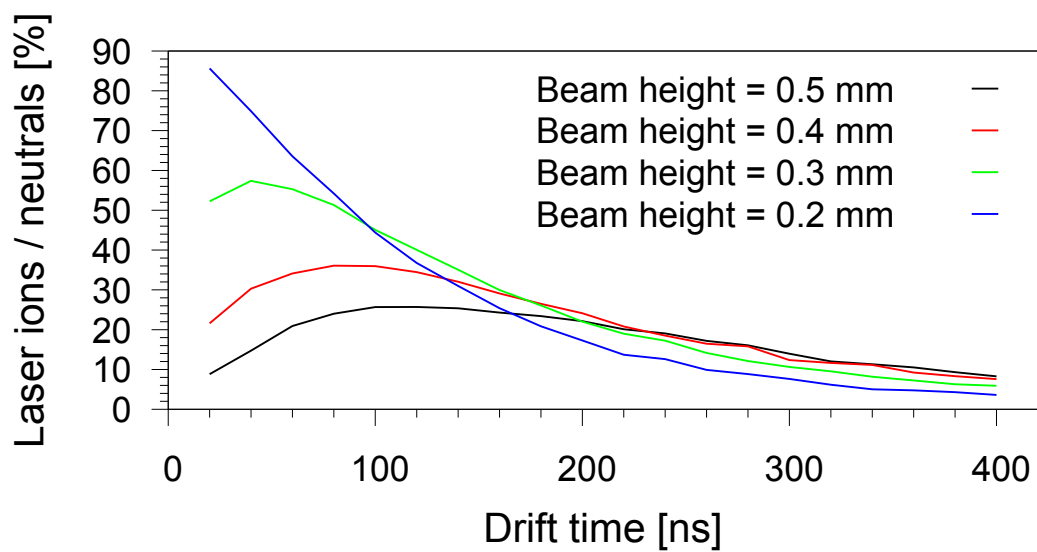


Figure B.11: Ionization yield for different beam heights: The graph shows the dependence of the ionization yield from the drift time of the neutral particle cloud at different laser beam heights for a laser focus diameter of $400\ \mu\text{m}$.

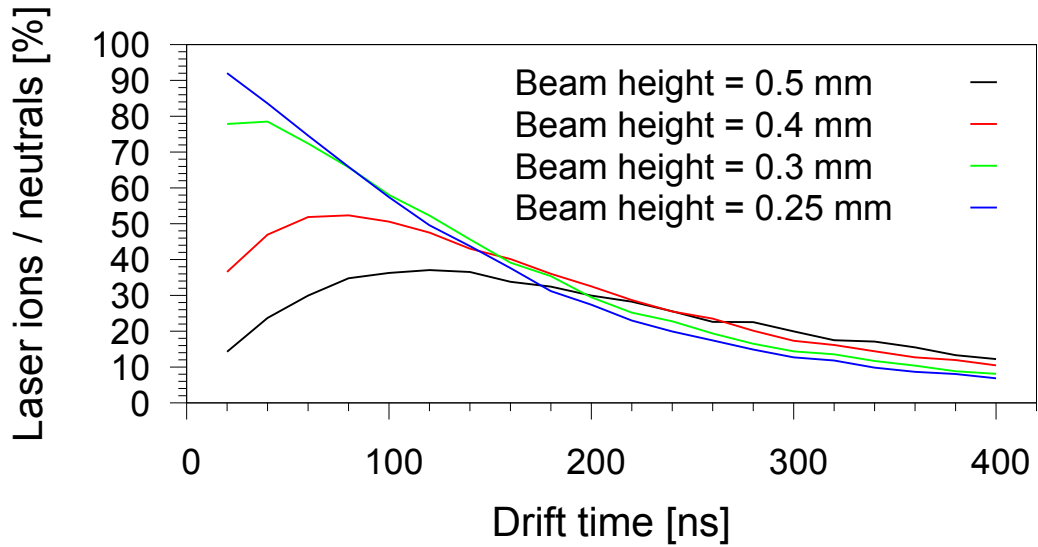


Figure B.12: Ionization yield for different beam heights: The graph shows the dependence of the ionization yield from the drift time of the neutral particle cloud at different laser beam heights for a laser focus diameter of $500\ \mu\text{m}$.

B.4 Simulation model

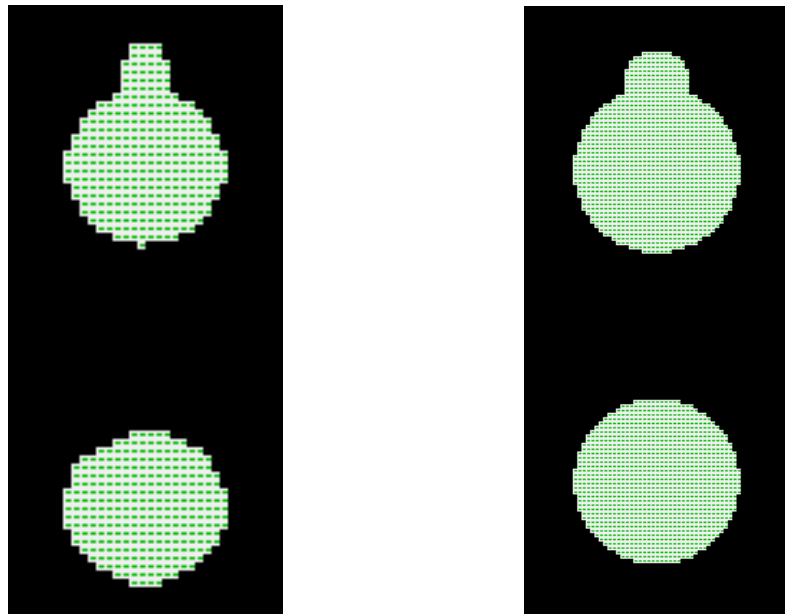
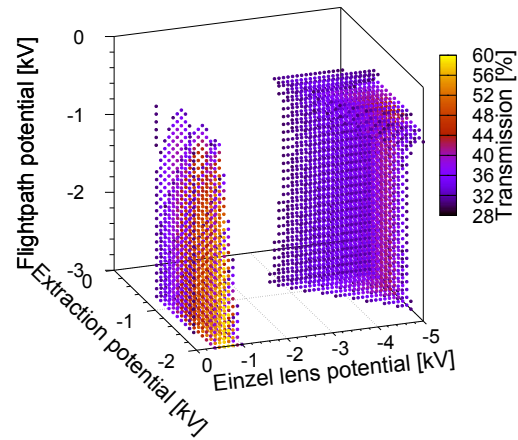
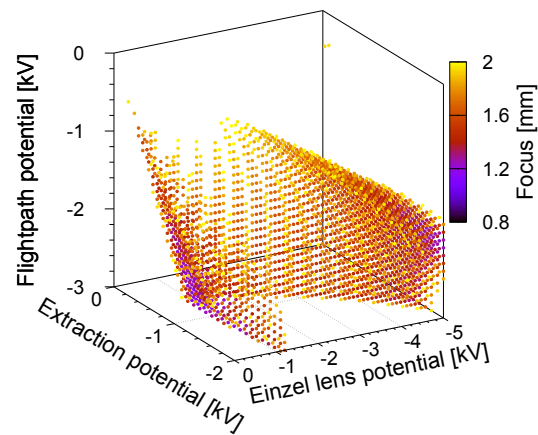


Figure B.13: Differences between automatic and programmed model generation: Both pictures show a part of a potential array (PA) with two apertures. The left PA was automatically generated and includes unsymmetrical apertures caused by rounding errors. The right PA was manually programmed, whereby the included apertures are defined as symmetrical objects independent from the higher resolution.

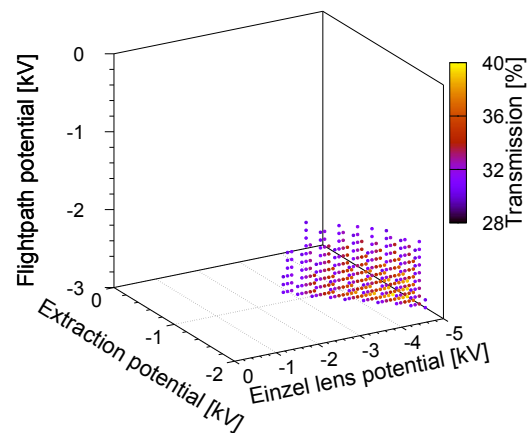
B.5 Optimization scans



(a) Operational parameters for a transmission above 30 %



(b) Operational parameters for a focus with below 2 mm diameter



(c) Operational parameters for a transmission above 30 % and a focus with below 2 mm diameter

Figure B.14: 3D plots of the parameter scans of the first three electrodes: The plots show the correlations of the operational parameters for different limitations.

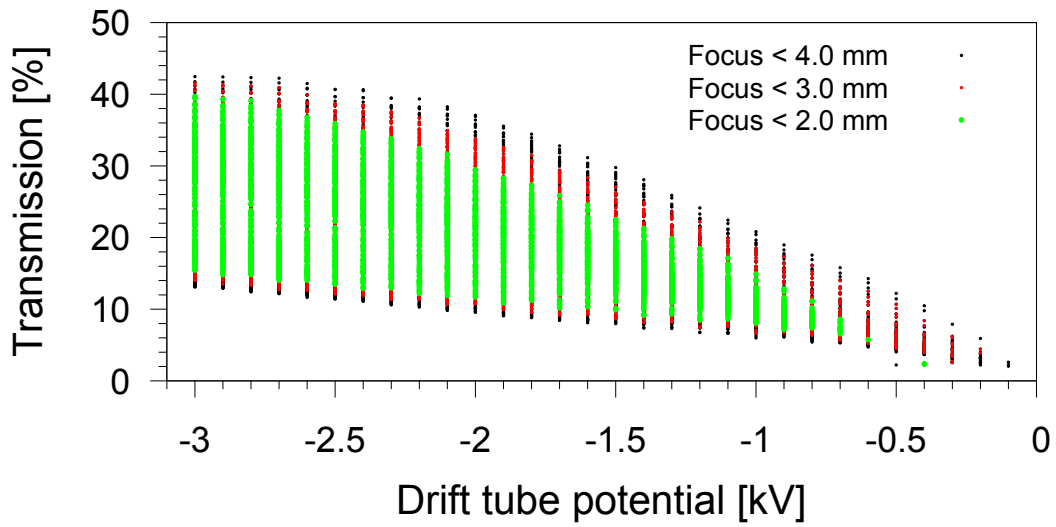
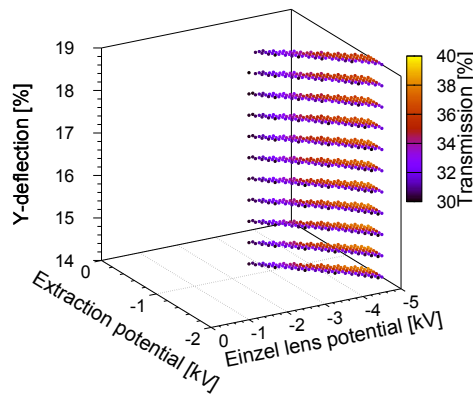
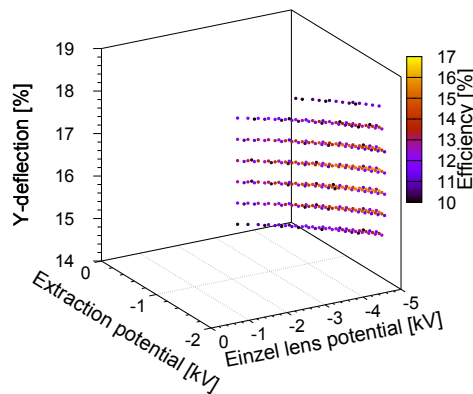


Figure B.15: Influence of the drift tube potential: The plot shows the achievable transmission at test point 1 and the focus diameter at the aperture for different drift tube potentials.



(a) Operational parameters for a transmission above 30%



(b) Operational parameters for an transport efficiency above 10%

Figure B.16: 3D plots of the second simulation run: The plots show the parameter space of extraction potential, lens potential and Y-deflection for different limitations. The resulting shape indicates possible correlations.

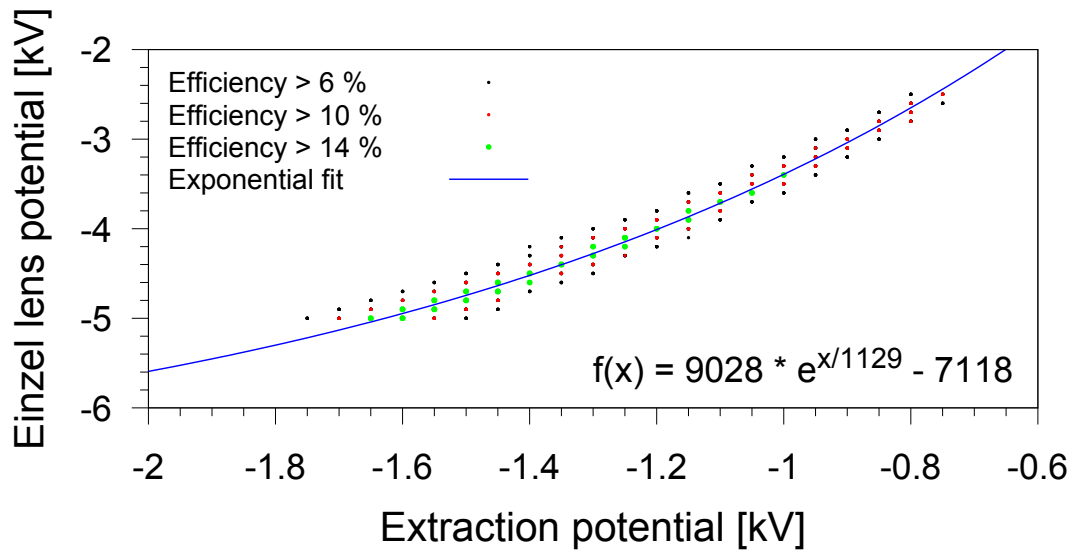


Figure B.17: The plot shows the most efficient combinations of the potentials for extraction and einzel lens. The identified correlation was fitted with an exponential function in the selected part of reasonable applicable potentials

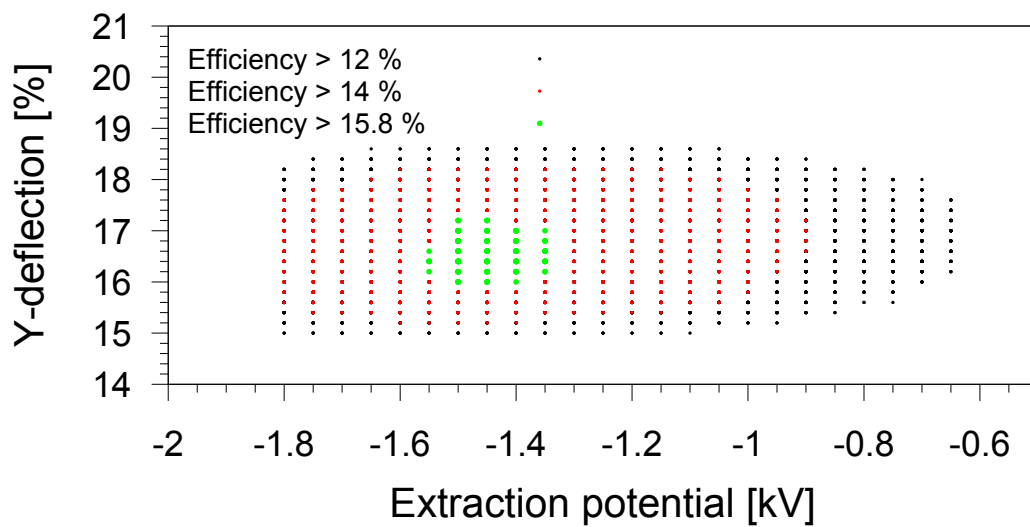


Figure B.18: The plot shows the dependence of Y-deflection and extraction potential for different transport efficiency limitations. The elliptical shape of the parameter area allows the determination of the most efficient extraction voltage at -1450 V.

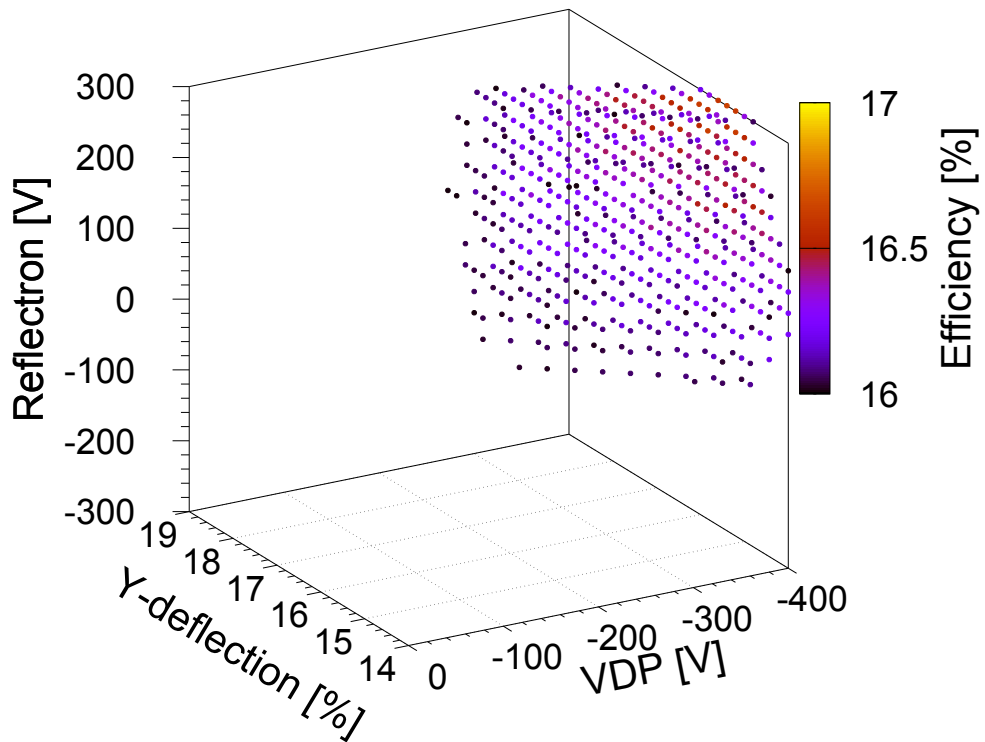


Figure B.19: 3D plots of the final simulation run: The plot shows the parameter space of Y-deflection, virtual drift path and the reflectron back plate for efficiencies above 16 %. The required potential for the VDP of -400V and for the reflectron back plate of 300V is directly identifiable by the highest efficiency at the upper right edge.

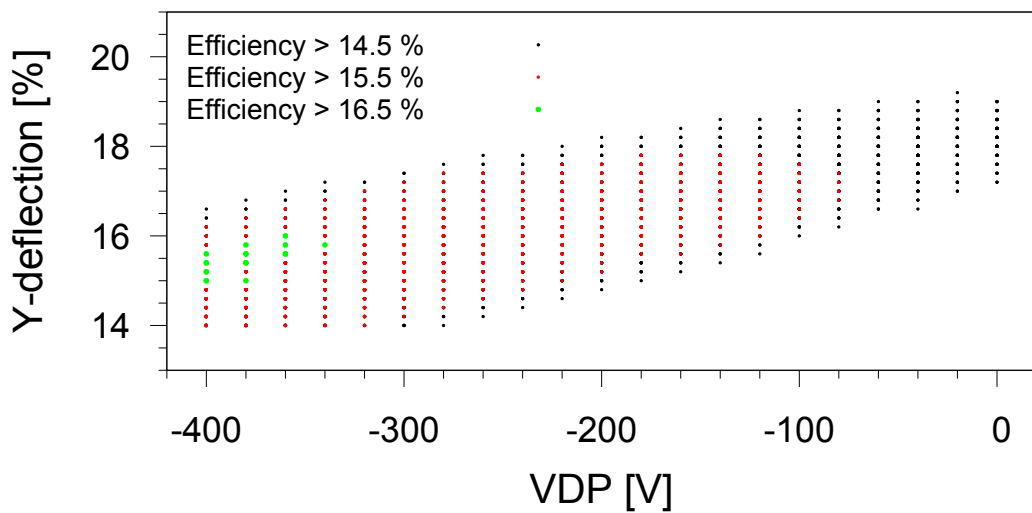


Figure B.20: The plot shows the dependence of Y-deflection and virtual drift path for different transport efficiency limitations. The limited parameter area for highest efficiency allows the determination of the Y-deflection potential to 15.4%.

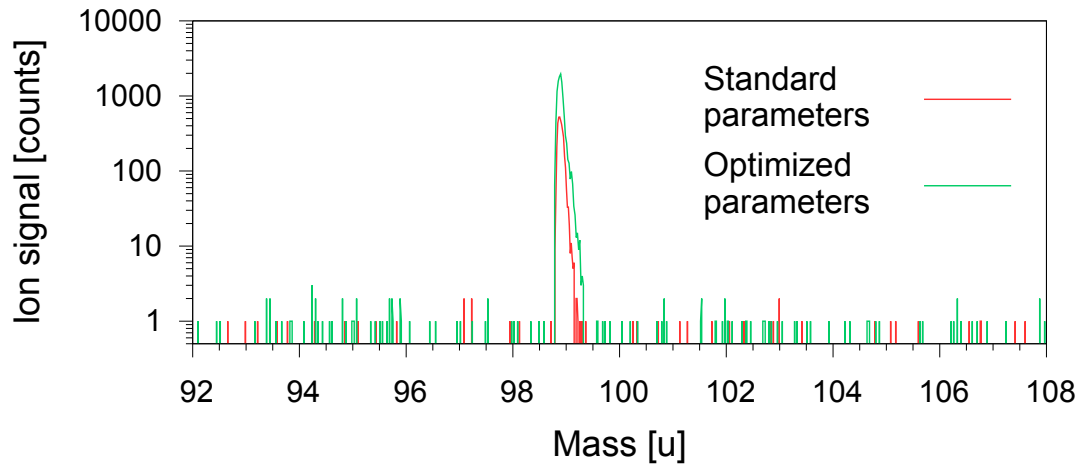


Figure B.21: Comparison of the Laser-SNMS spectra of a synthetic ^{99}Tc sample for different parameter sets: The red spectra was measured with the standard parameter set, while the green spectra was measured with the optimized parameter set. In this specific measurement, the ion signal of ^{99}Tc was increased by a factor of 3 from 3700 counts to 11 160 counts.

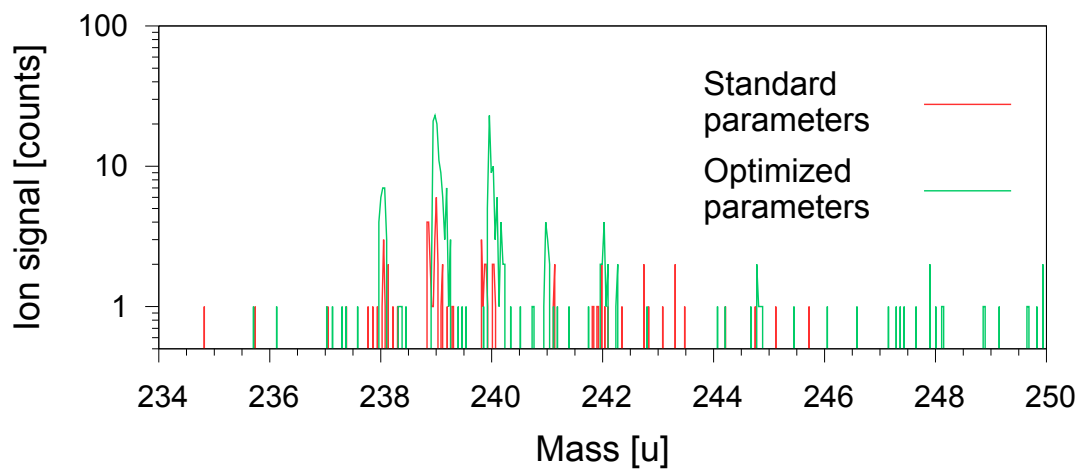


Figure B.22: Comparison of the Laser-SNMS spectra of a synthetic MOX sample for different parameter sets: The red spectra was measured with the standard parameter set, while the green spectra was measured with the optimized parameter set. In this specific measurement, the ion signal of ^{239}Pu was increased by a factor of 3.4 from 31 counts to 105 counts.

B.6 Sputter cleaning

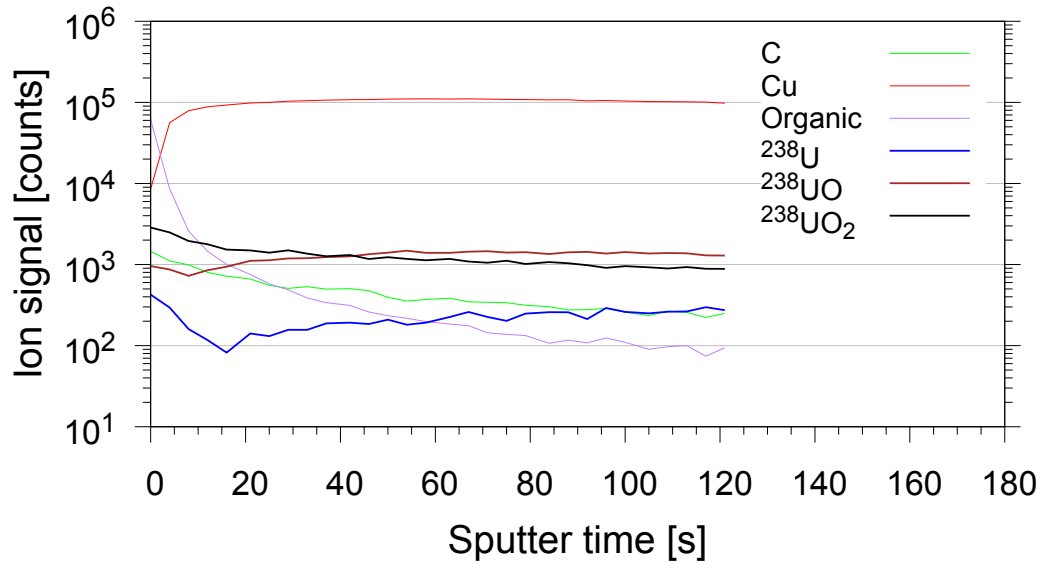


Figure B.23: Ion signal variation during sputtered surface cleaning: The plot shows the temporal behavior of different SIMS ion signals during sputter cleaning of a new sample. The signals of ^{238}U and its oxides show variations in the signal intensity, due to different organic background on the mass peaks and an covering layers above the real sample. The cover effect is strongly visible for the Cu ion signal, because copper is part of the aluminium alloy of the sample holder. The organic ion signal, by the fragment ion $\text{Si}_2\text{C}_5\text{H}_{15}\text{O}$ of polydimethylsiloxane (PDSM) at mass 147 u, as well as the carbon ion signal show a significant reduction.

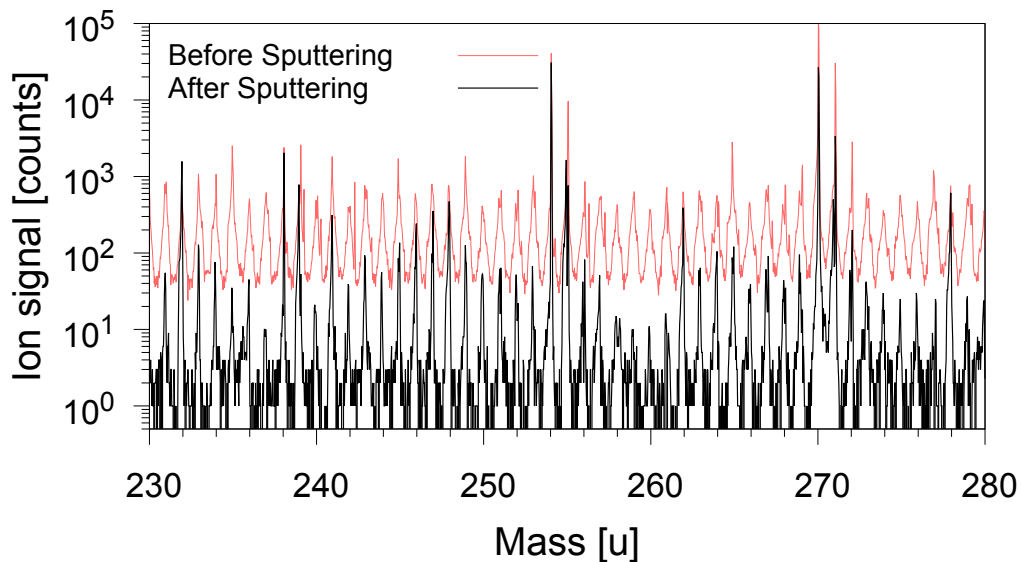


Figure B.24: Influence on the mass spectrum by sputtered surface cleaning: The plot shows the SIMS mass spectrum of a synthetic uranium sample before and after the sputtered surface cleaning procedure. In this measurement the ion signals of ^{238}U and its oxides is only slightly reduced, while the organic background, which is spread over the whole mass spectra, shows a reduction of 1 - 2 orders of magnitude.

B.7 Laser saturation scans

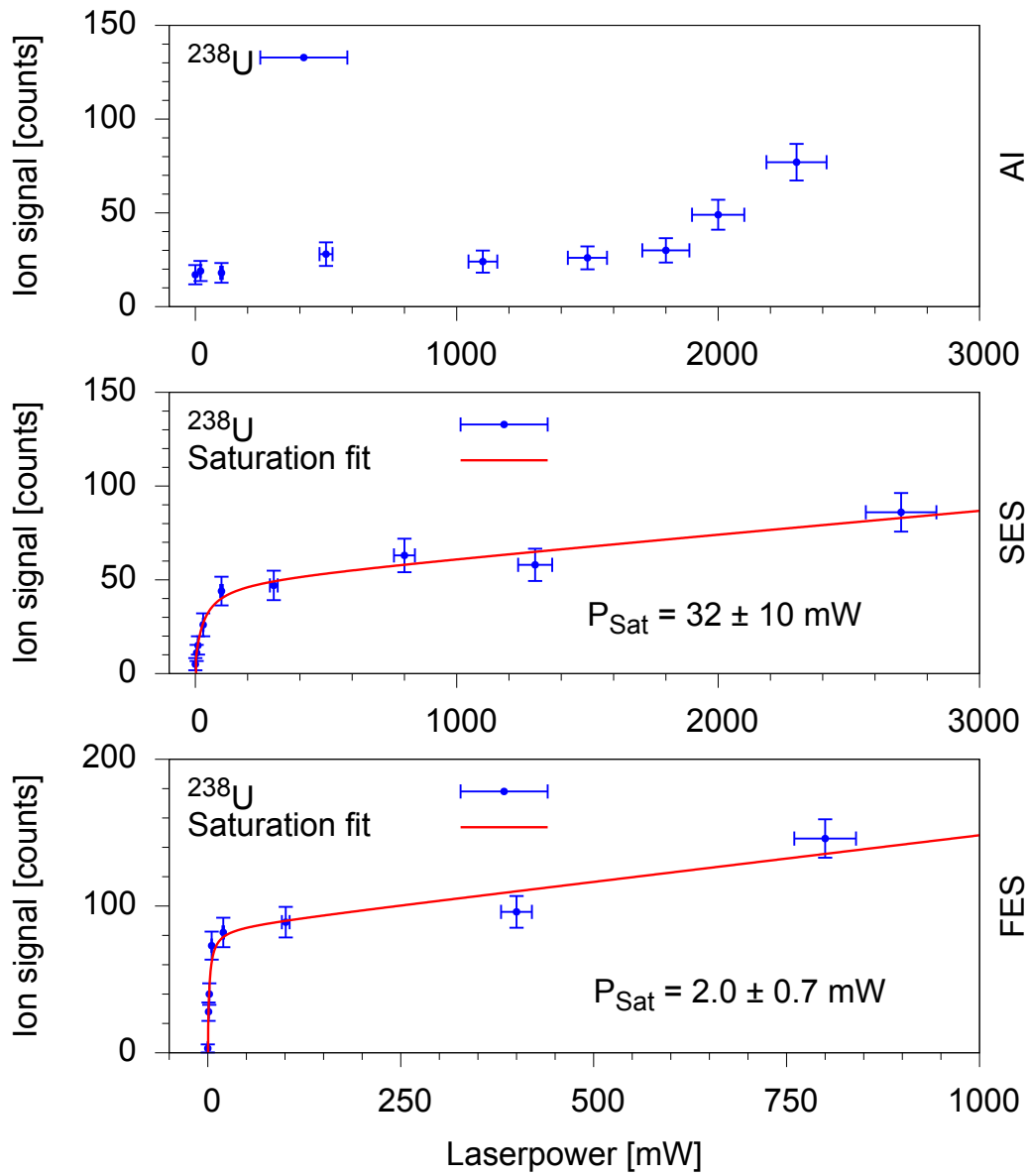


Figure B.25: Saturation scans for all three steps on ^{238}U : The plots show the dependence of the resonant laser ion signal of ^{238}U from the applied laser power of the three used excitation steps. The first and second transition showed saturation behavior and were fitted with a corresponding saturation function. For further description see section 5.1.

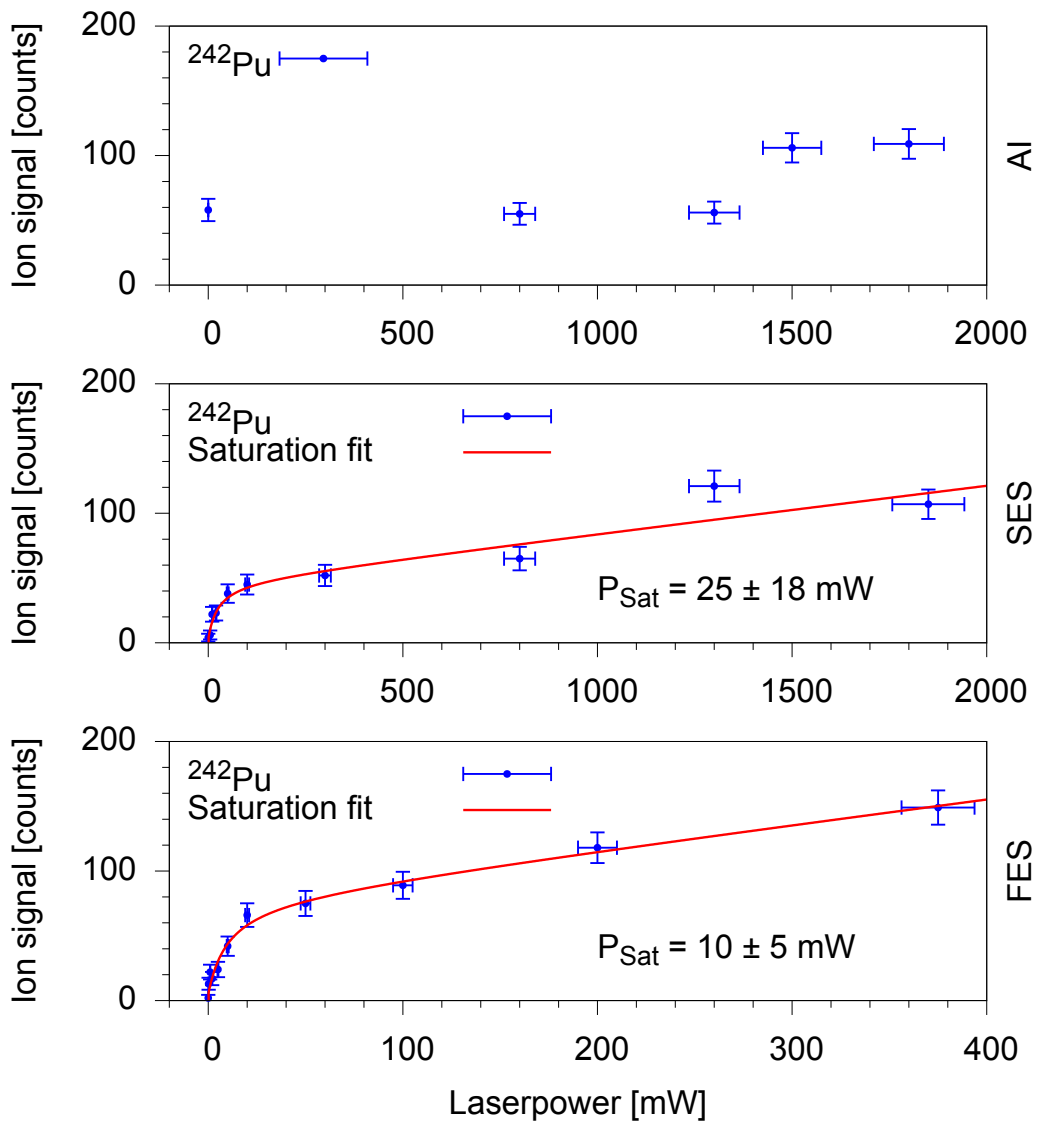


Figure B.26: Saturation scan of the laser power for all three steps on ^{242}Pu : .

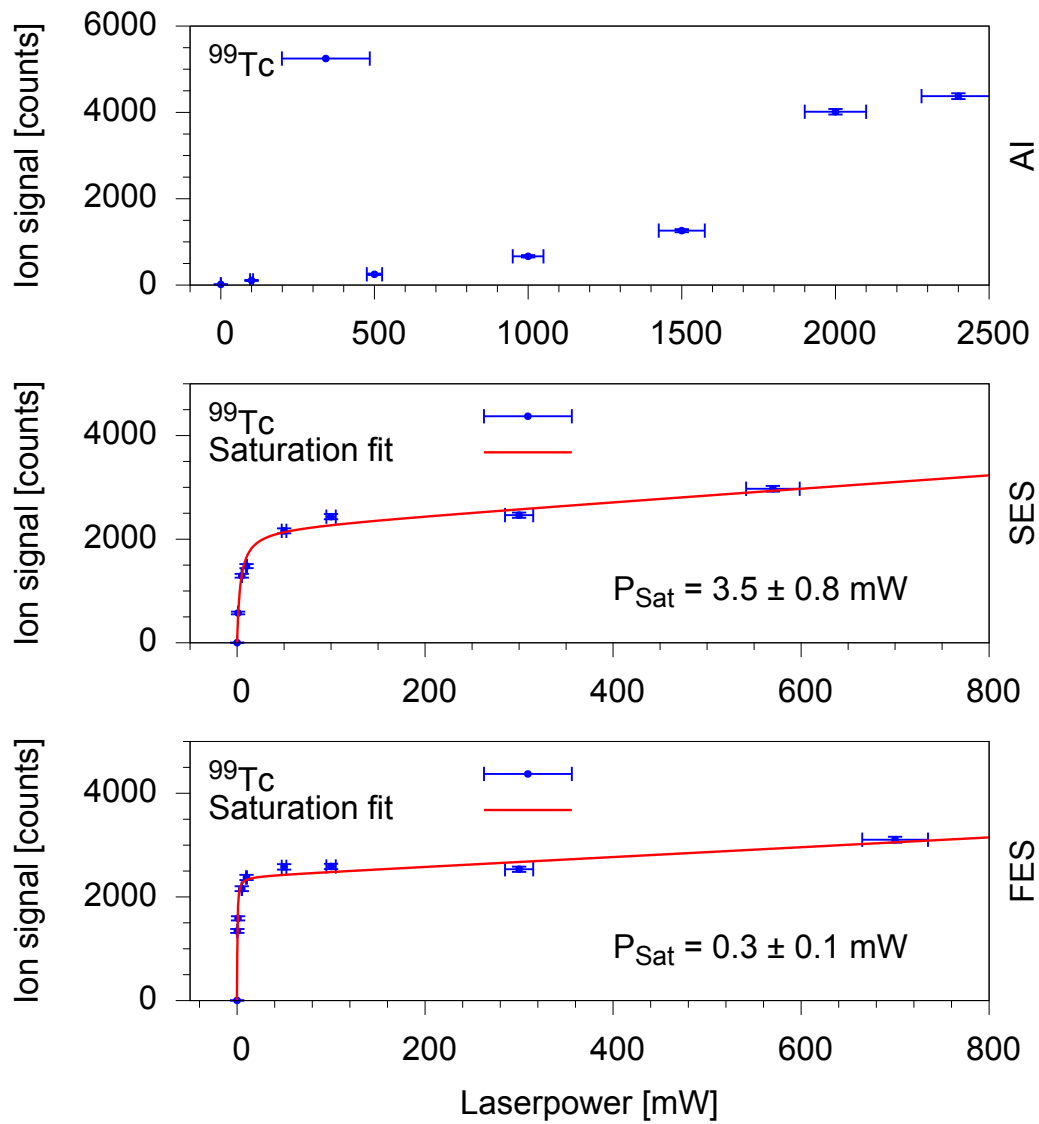


Figure B.27: Saturation scan of the laser power for all three steps on ^{99}Tc : .

B.8 Efficiency measurements

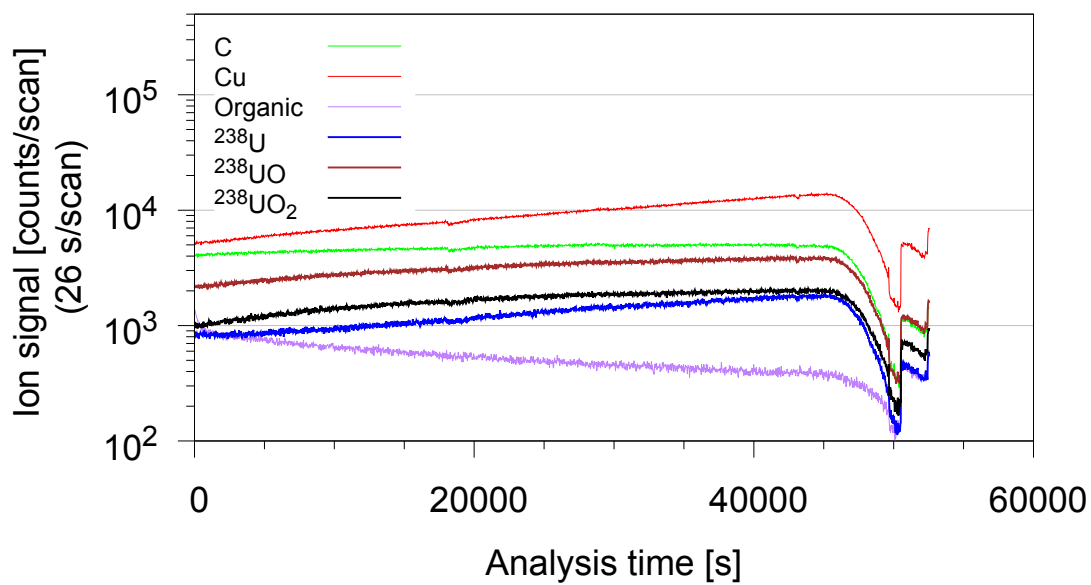


Figure B.28: Efficiency test measurement with SIMS

B.9 Comparison of Laser-SNMS and SIMS

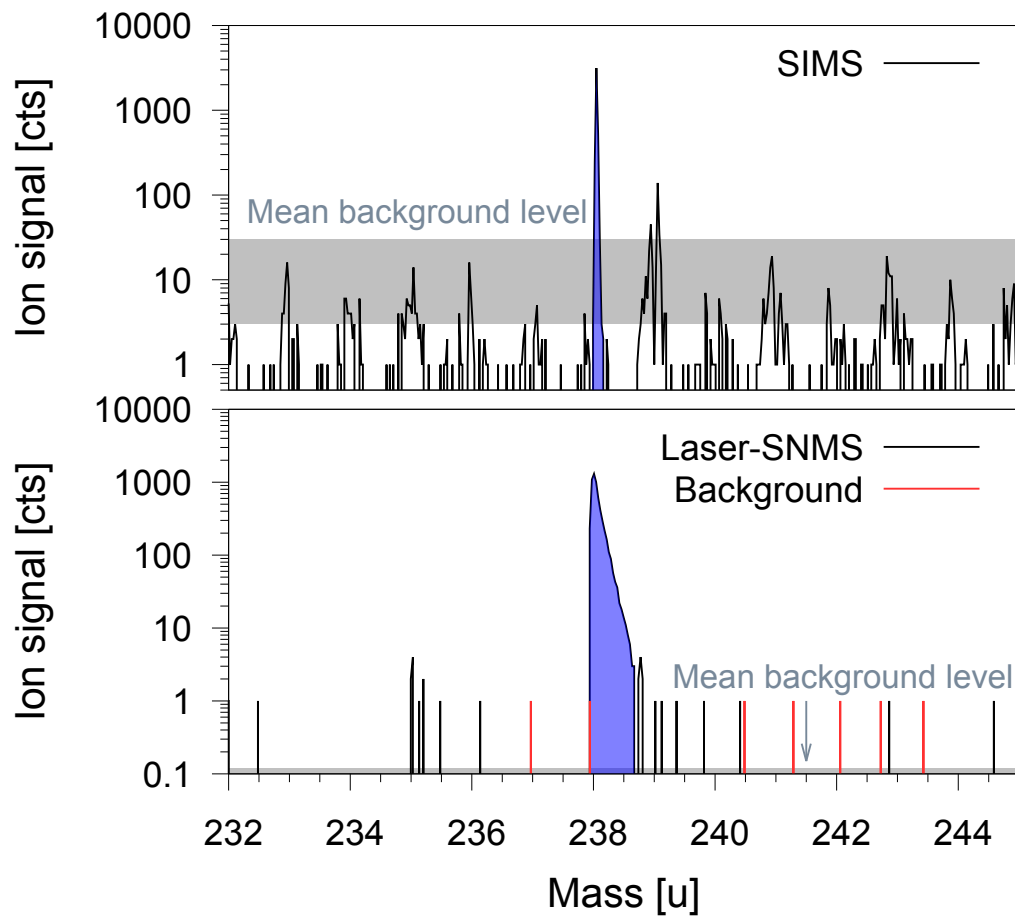


Figure B.29: Comparison of SIMS and Laser-SNMS spectra of a synthetic depleted uranium sample ($2.1 \text{ ng} \sim 5 \cdot 10^{12}$ atoms of ^{238}U).

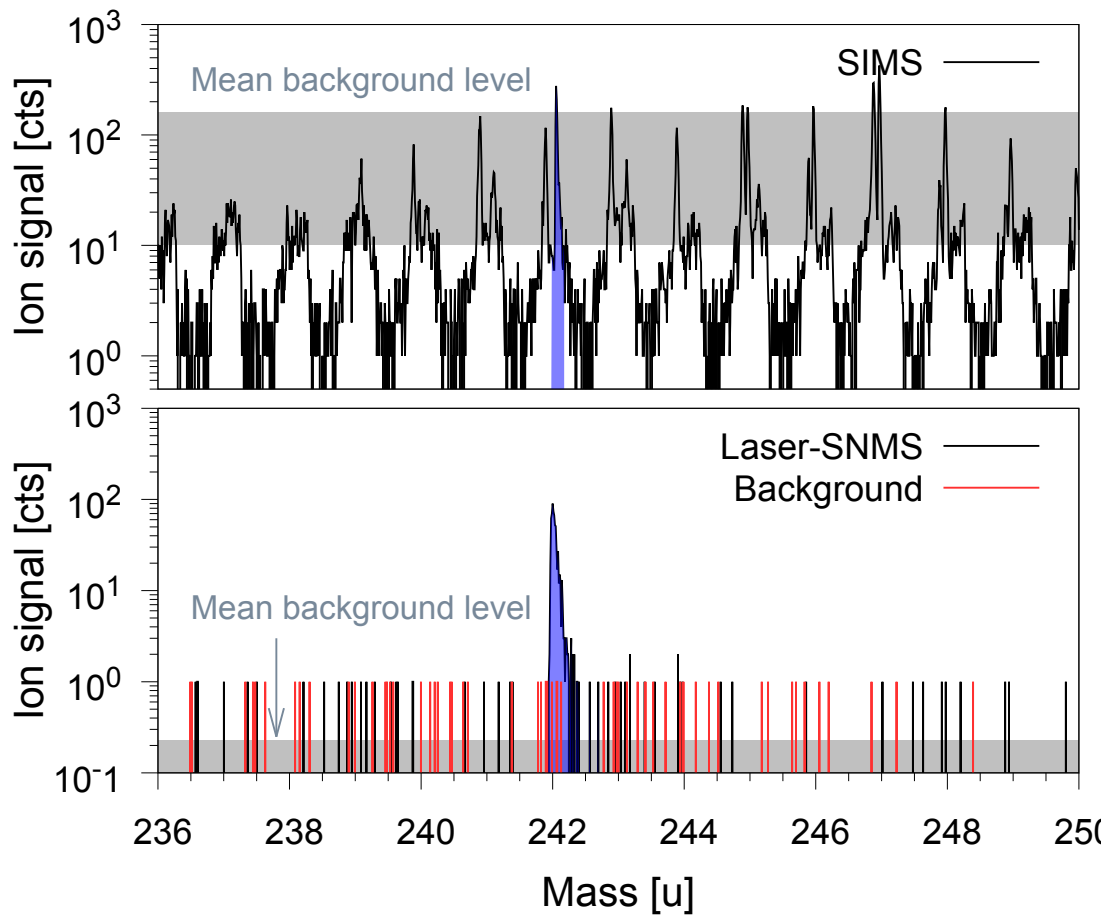


Figure B.30: Comparison of SIMS and Laser-SNMS spectra of a synthetic plutonium sample (30.6 pg $\sim 8 \cdot 10^{10}$ atoms of ^{242}Pu).

B.10 Argon cluster sputtering

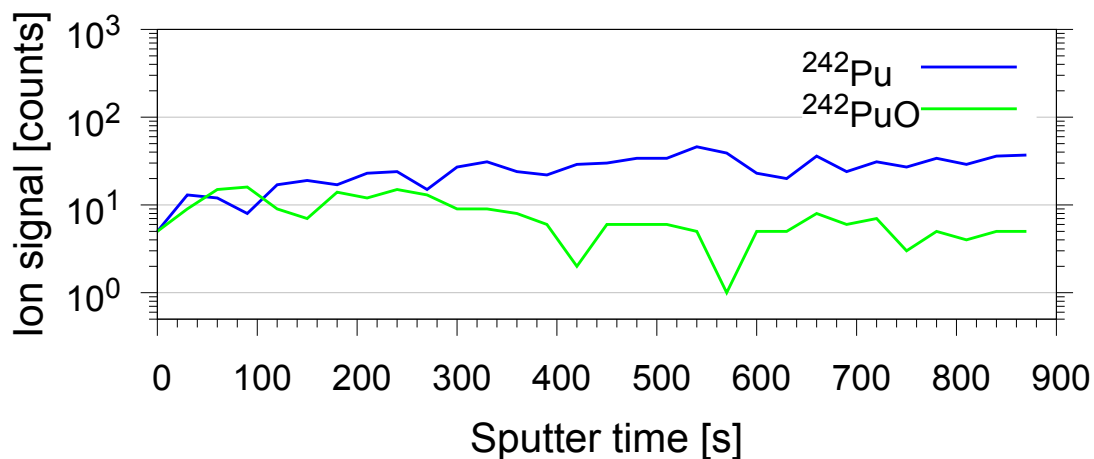


Figure B.31: Development of the ion signals of resonantly ionized ^{242}Pu and non-resonantly ionized ^{242}PuO during continuous argon cluster sputtering.

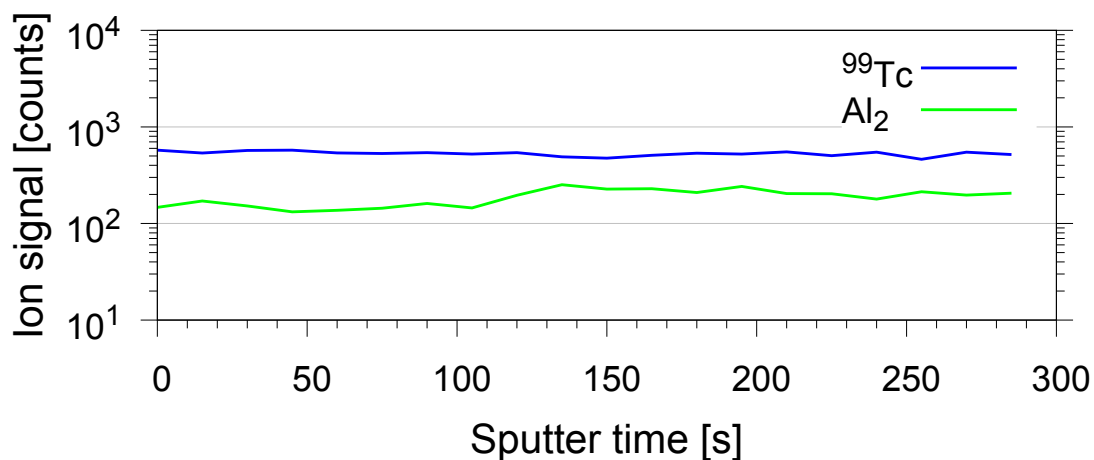
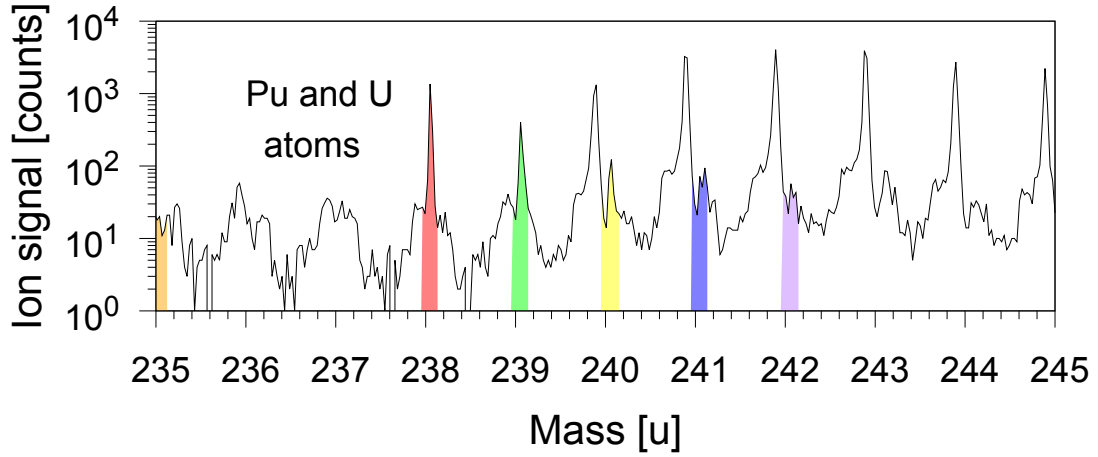
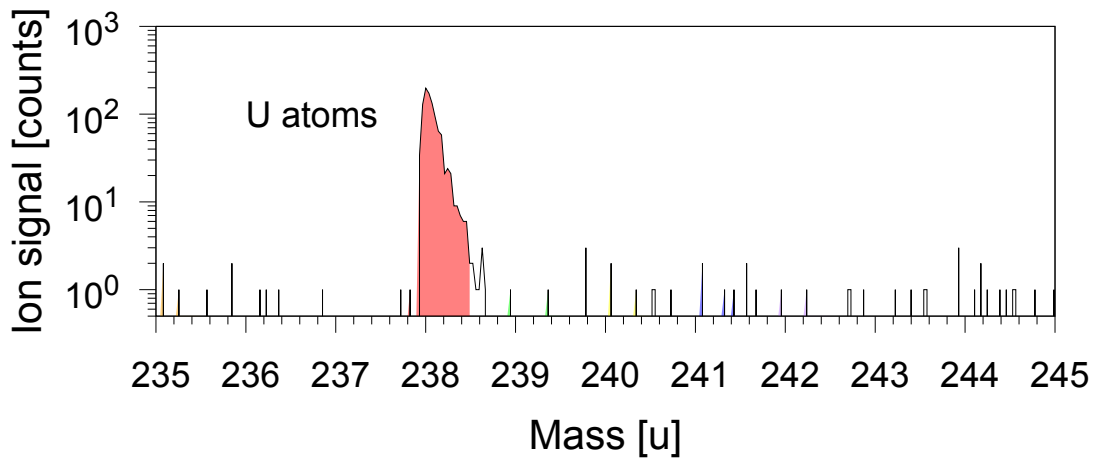


Figure B.32: Development of the ion signals of resonantly ionized ^{99}Tc and non-resonantly ionized $^{27}\text{Al}_2$ during continuous argon cluster sputtering.

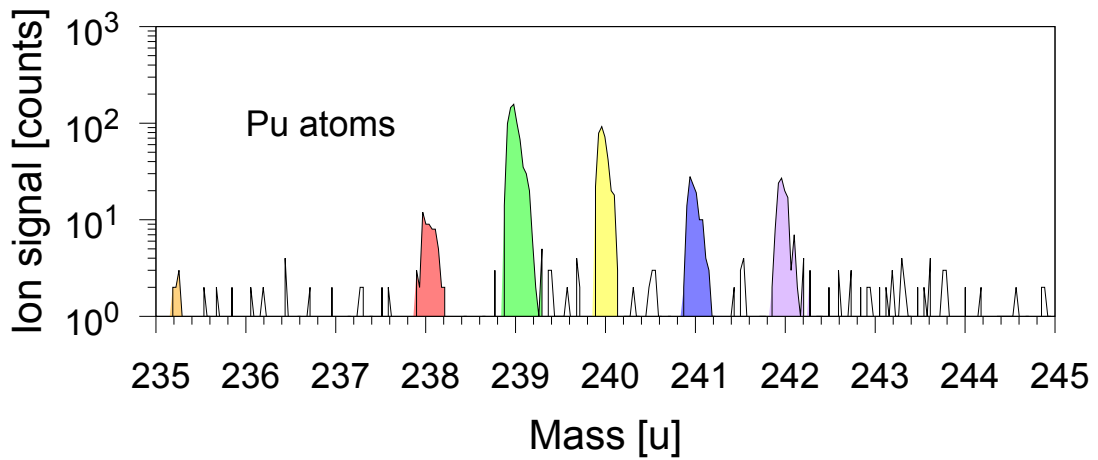
B.11 Analysis of a MOX fuel pellet



(a) SIMS mass spectrum of the MOX sample



(b) Laser-SNMS mass spectrum of the MOX sample with resonant ionization of uranium



(c) Laser-SNMS mass spectrum of the MOX sample with resonant ionization of plutonium

Figure B.33: Comparison of the MOX mass spectra: The three spectra show the mass range of atomic uranium and plutonium. The positions of expected ion signals were marked with different colors.

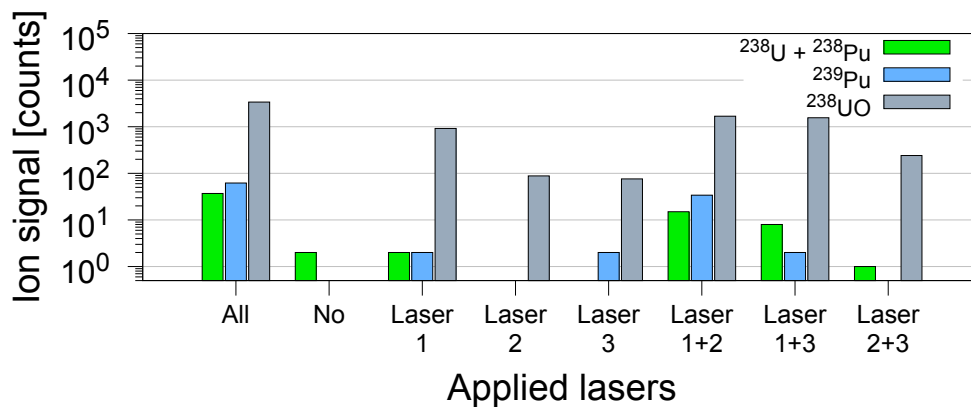


Figure B.34: Influence of the three lasers: The histogram shows the influence of the three lasers and every combination on the resonant ion signal of ^{239}Pu , the non-resonant ion signal of ^{238}UO and the resonant ion signal of ^{238}Pu with a non-resonant background of ^{238}U .

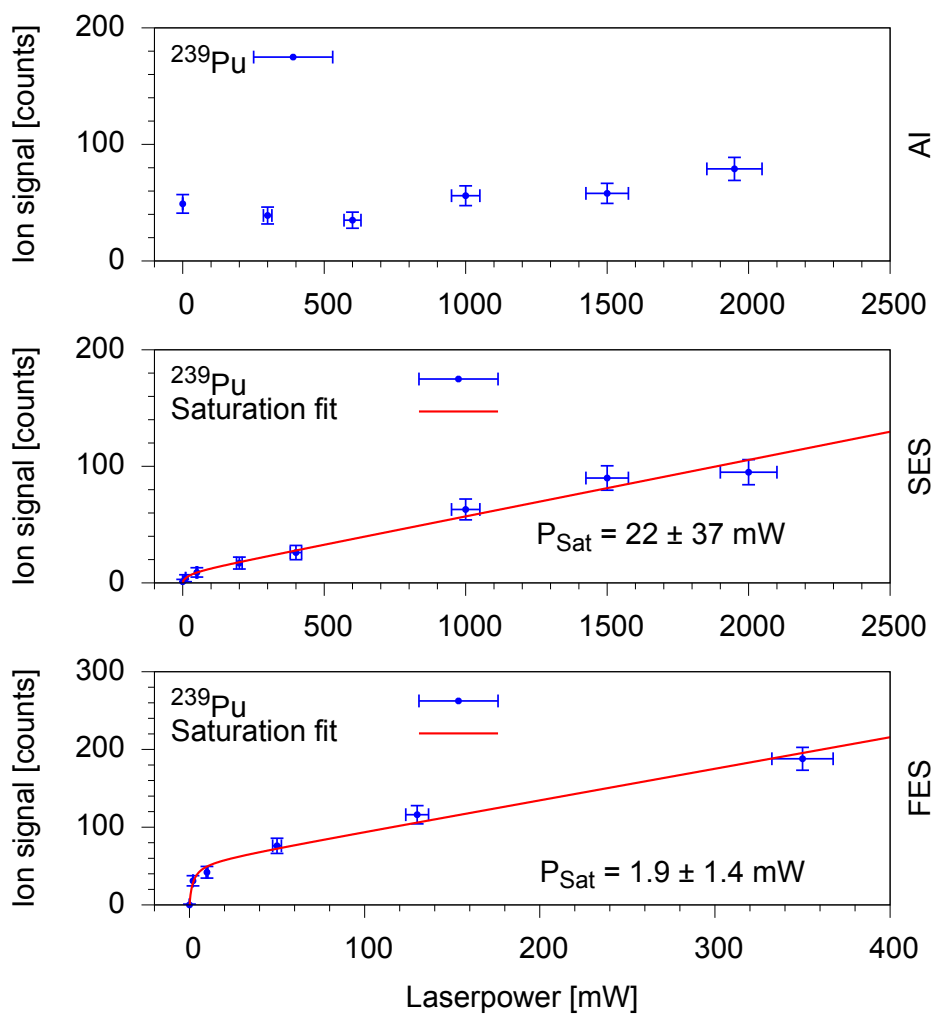


Figure B.35: Saturation scan of the laser power for all three steps on ^{239}Pu : .

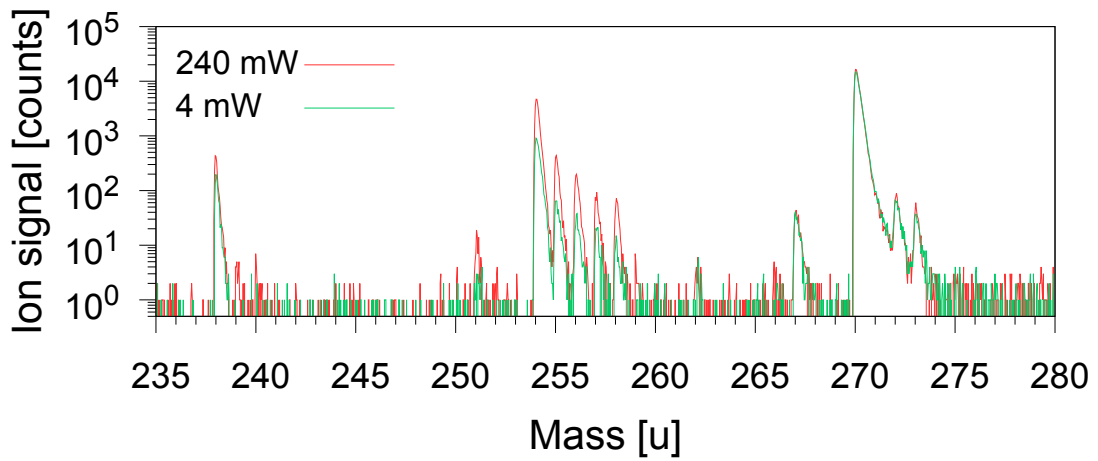


Figure B.36: Laser power influence on the non-resonant background of the MOX sample: The comparative spectra show the influence of the laser power for the first resonant transition of the uranium ionization scheme. The red spectrum was measured with a laser power of 240 mW and the green spectrum was measured with a laser power of 4 mW.

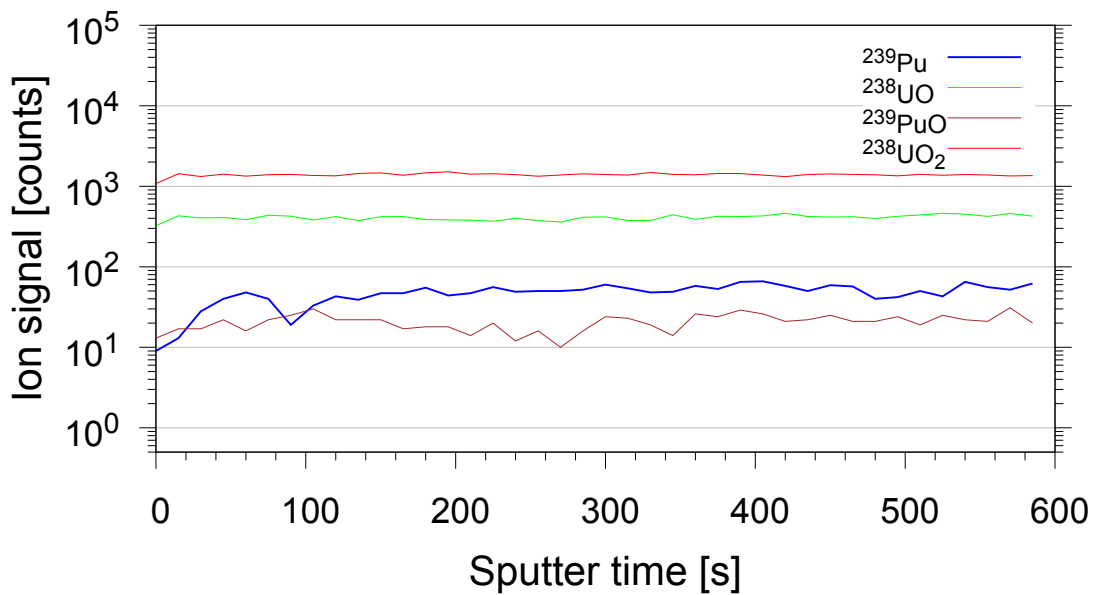


Figure B.37: Development of the ion signals of resonantly ionized ^{239}Pu and non-resonantly ionized ^{238}UO , ^{239}PuO and $^{238}\text{UO}_2$ during continuous argon cluster sputtering.

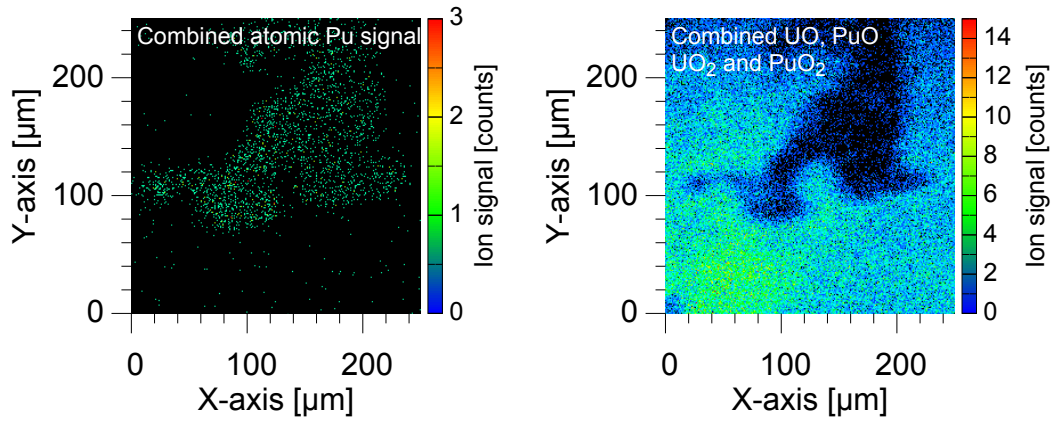


Figure B.38: Compared ion images of atoms and oxides: The ion images show the spatial origin of the combined atomic Pu signal and the combined oxides and dioxides of U and Pu with Laser-SNMS.

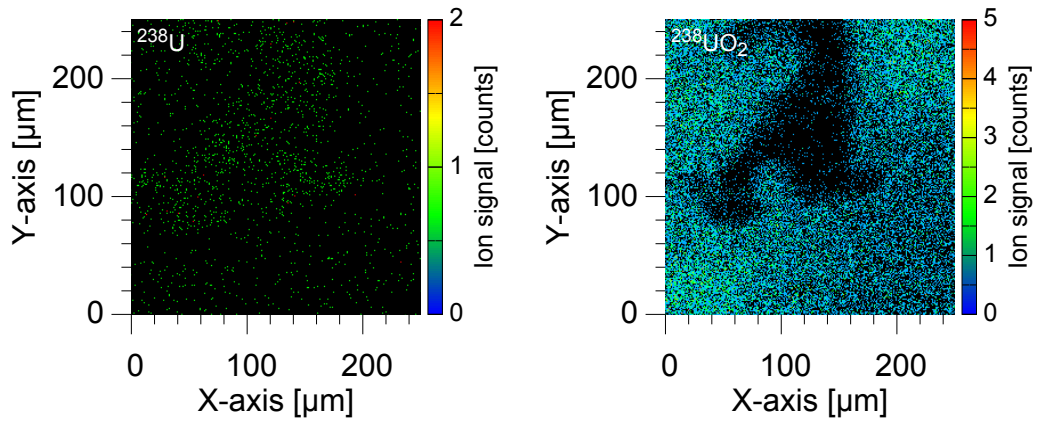


Figure B.39: Compared ion images of atoms and oxides: The ion images show the spatial origin of the ^{238}U signal and the $^{238}\text{UO}_2$ signal with SIMS.

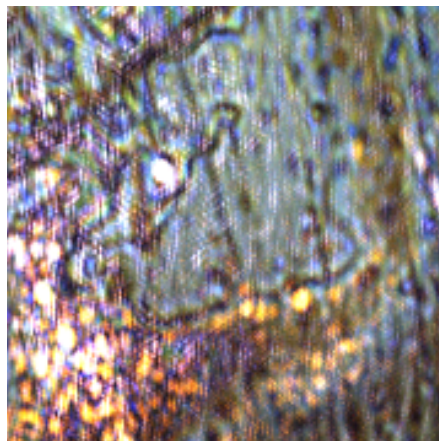


Figure B.40: Camera image of the sample surface showing the inhomogeneous deposition of the MOX sample material.

B.12 Analysis of a rock sample from Kabul



Figure B.41: Photo of M. Tanha during the sample collection in Kabul

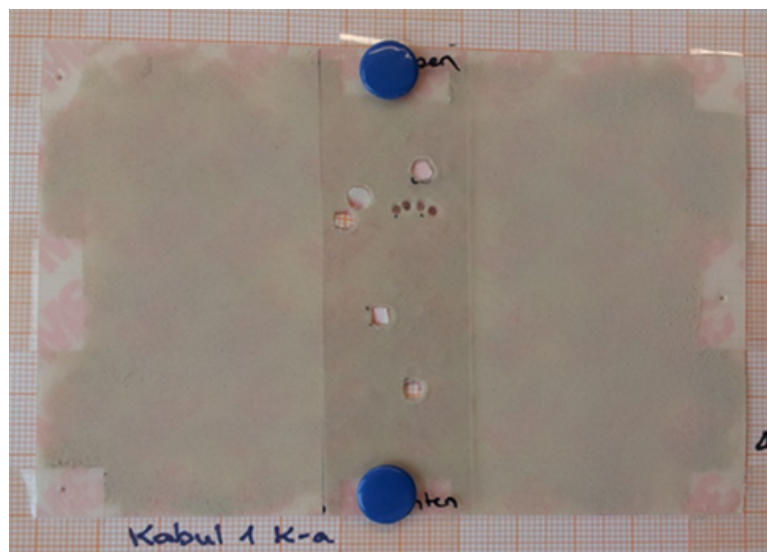


Figure B.42: Photo of the milled sample material

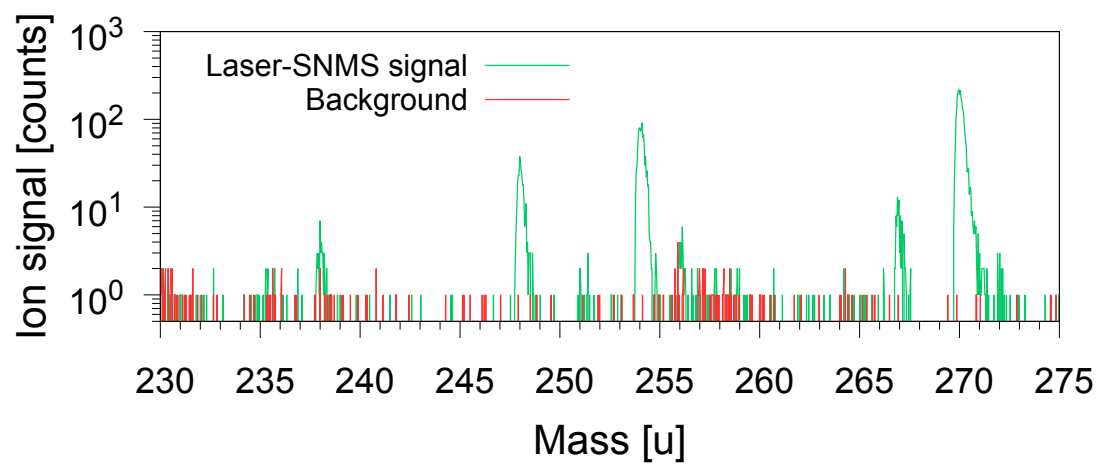


Figure B.43: Comparison of the signal and background spectrum of the Kabul sample

ISOTOPE SHIFTS OF THE APPLIED EXCITATION SCHEMES

	States used for ^{235}U	Isotope shift for ^{235}U (relative to ^{238}U)	
	cm^{-1}	10^{-3} cm^{-1}	GHz
FES	24067.10(3)	434 ± 40	13.0 ± 1.2
SES	37097.32(4)	361 ± 40	10.8 ± 1.2
AI	50443.99(5)	-126 ± 40	-3.8 ± 1.2

Table C.1: Isotopic shift of the resonant transitions for uranium

	States used for ^{238}Pu	Isotope shift for ^{238}Pu (relative to ^{240}Pu)	
	cm^{-1}	10^{-3} cm^{-1}	GHz
FES	23766.38(5)	215 ± 50	6.5 ± 1.5
SES	35568.85(7)	-118 ± 50	-4.4 ± 1.5
AI	48898.05(8)	70 ± 50	2.1 ± 1.5
	States used for ^{239}Pu	Isotope shift for ^{239}Pu (relative to ^{240}Pu)	
	cm^{-1}	10^{-3} cm^{-1}	GHz
FES	23766.31(3)	149 ± 20	4.5 ± 0.6
SES	35568.86(4)	-70 ± 20	-2.1 ± 0.6
AI	48898.03(3)	42 ± 20	1.3 ± 0.6
	States used for ^{240}Pu		
	cm^{-1}		
FES	23766.16(3)		
SES	35568.78(4)		
AI	48897.91(3)		
	States used for ^{241}Pu	Isotope shift for ^{241}Pu (relative to ^{240}Pu)	
	cm^{-1}	10^{-3} cm^{-1}	GHz
FES	23766.10(3)	-65 ± 20	-1.9 ± 0.6
SES	35568.74(4)	24 ± 20	0.7 ± 0.6
AI	48897.86(3)	-12 ± 20	-0.4 ± 0.6
	States used for ^{242}Pu	Isotope shift for ^{242}Pu (relative to ^{240}Pu)	
	cm^{-1}	10^{-3} cm^{-1}	GHz
FES	23765.97(3)	-188 ± 20	-5.6 ± 0.6
SES	35568.70(4)	107 ± 20	3.2 ± 0.6
AI	48897.78(3)	-49 ± 20	-1.5 ± 0.6

Table C.2: Isotopic shift of the resonant transitions for plutonium

BIBLIOGRAPHY

- [1] Henri Becquerel. “Emission des radiations nouvelles par l’uranium métallique”. In: *Comptes rendus* 122 (1896), pp. 1086–1088.
- [2] Marie Curie and Gabriel Lippmann. *Rayons émis par les composés de l’uranium et du thorium*. Gauthier-Villars, 1898.
- [3] Otto Hahn and Fritz Strassmann. “Nachweis der Entstehung aktiver Bariumisotope aus Uran und Thorium durch Neutronenbestrahlung; Nachweis weiterer aktiver Bruchstücke bei der Uranspaltung”. In: *Naturwissenschaften* 27.6 (1939), pp. 89–95.
- [4] Lise Meitner and Otto R Frisch. “Disintegration of Uranium by Neutrons: a New Type of Nuclear Reaction”. In: *Nature* 143.3615 (1939), pp. 239–240.
- [5] Xiaoping Yang et al. “Worldwide nuclear explosions”. In: *International Geophysics Series* 81.B (2003), pp. 1595–1600.
- [6] Wilfried Pfingsten, Jörg Hadermann, and Pierre Perrochet. “Radionuclide release and transport from nuclear underground tests performed at Mururoa and Fangataufa—predictions under uncertainty”. In: *Journal of contaminant hydrology* 47.2 (2001), pp. 349–363.
- [7] DK Smith, DL Finnegan, and SM Bowen. “An inventory of long-lived radionuclides residual from underground nuclear testing at the Nevada test site, 1951–1992”. In: *Journal of environmental radioactivity* 67.1 (2003), pp. 35–51.
- [8] Qin-Hong Hu, Jian-Qing Weng, and Jin-Sheng Wang. “Sources of anthropogenic radionuclides in the environment: a review”. In: *Journal of environmental radioactivity* 101.6 (2010), pp. 426–437.
- [9] Jim T Smith and Nicholas A Beresford. *Chernobyl: catastrophe and consequences*. Springer, 2005.
- [10] Georg Steinhauser, Alexander Brandl, and Thomas E Johnson. “Comparison of the Chernobyl and Fukushima nuclear accidents: a review of the environmental impacts”. In: *Science of the Total Environment* 470 (2014), pp. 800–817.
- [11] Brit Salbu and Trygve Krekling. “Characterisation of radioactive particles in the environment”. In: *Analyst* 123.5 (1998), pp. 843–850.
- [12] International Atomic Energy Agency. *Radioactive Particles in the Environment: Sources, Particle Characterization and Analytical Techniques*. IAEA-TECDOC-1663. Vienna: IAEA, 2011.
- [13] Clemens Walther and Melissa A Denecke. “Actinide colloids and particles of environmental concern”. In: *Chemical reviews* 113.2 (2013), pp. 995–1015.
- [14] Alexander P Novikov et al. “Colloid transport of plutonium in the far-field of the Mayak Production Association, Russia”. In: *Science* 314.5799 (2006), pp. 638–641.
- [15] Annie B Kersting and Mavrik Zavarin. “Colloid-facilitated transport of plutonium at the Nevada Test Site, NV, USA”. In: *Actinide nanoparticle research*. Springer, 2011, pp. 399–412.
- [16] PML Hedberg et al. “Multiple ion counting measurement strategies by SIMS—a case study from nuclear safeguards and forensics”. In: *Journal of Analytical Atomic Spectrometry* 30.12 (2015), pp. 2516–2524.
- [17] Johannes Stark and G Wendt. “Über das Eindringen von Kanalstrahlen in feste Körper”. In: *Annalen der Physik* 343.10 (1912), pp. 921–940.

- [18] Florian Meinerzhagen et al. “A new setup for the investigation of swift heavy ion induced particle emission and surface modifications”. In: *Review of Scientific Instruments* 87.1 (2016), p. 013903.
- [19] Rainer Behrisch and Wolfgang Eckstein. *Sputtering by particle bombardment: experiments and computer calculations from threshold to MeV energies*. Vol. 110. Springer Science & Business Media, 2007.
- [20] Gerhard Betz and Karl Wien. “Energy and angular distributions of sputtered particles”. In: *International Journal of Mass Spectrometry and Ion Processes* 140.1 (1994), pp. 1–110.
- [21] MW Thompson. “Atomic collision cascades in solids”. In: *Vacuum* 66.2 (2002), pp. 99–114.
- [22] Peter Sigmund. *Fundamental processes in sputtering of atoms and molecules (SPUT92): symposium on the occasion of the 250th anniversary of the Royal Danish Academy of Sciences and Letters, Copenhagen, 30 August-4 September, 1992: invited reviews*. Vol. 43. Kongelige Danske videnskabernes selskab, 1993.
- [23] Peter Sigmund. “Theory of sputtering. I. Sputtering yield of amorphous and polycrystalline targets”. In: *Physical review* 184.2 (1969), p. 383.
- [24] Peter Sigmund. “Mechanisms and theory of physical sputtering by particle impact”. In: *Nuclear Instruments and Methods in Physics Research Section B: Beam Interactions with Materials and Atoms* 27.1 (1987), pp. 1–20.
- [25] Michael Warwick Thompson. “II. The energy spectrum of ejected atoms during the high energy sputtering of gold”. In: *Philosophical Magazine* 18.152 (1968), pp. 377–414.
- [26] Michael Warwick Thompson. “Physical mechanisms of sputtering”. In: *Physics Reports* 69.4 (1981), pp. 335–371.
- [27] Hubert Gnaser. “Energy and angular distributions of sputtered species”. In: *Sputtering by particle bombardment*. Springer, 2007, pp. 231–328.
- [28] Yu Kudriavtsev et al. “Calculation of the surface binding energy for ion sputtered particles”. In: *Applied surface science* 239.3 (2005), pp. 273–278.
- [29] Wolfgang Demtröder. *Experimentalphysik 3: Atome, Moleküle und Festkörper*. Springer, Berlin, 2005.
- [30] Gordon WF Drake. *Springer handbook of atomic, molecular, and optical physics*. Springer Science & Business Media, 2006.
- [31] Wolfgang Demtröder. *Laserspektroskopie: Grundlagen und Techniken*. Springer-Verlag, 2007.
- [32] Ingolf Volker Hertel and Claus-Peter Schulz. *Atome, Moleküle und optische Physik 1: Atomphysik und Grundlagen der Spektroskopie*. Springer-Verlag, 2008.
- [33] Bahaa EA Saleh and Malvin Carl Teich. *Grundlagen der Photonik*. John Wiley & Sons, 2008.
- [34] Igor I Sobelman. *Atomic spectra and radiative transitions*. Vol. 12. Springer Science & Business Media, 2012.
- [35] Peter F Moulton. “Ti-doped sapphire: tunable solid-state laser”. In: *Optics News* 8.6 (1982), pp. 9–9.
- [36] Peter F Moulton. “Spectroscopic and laser characteristics of Ti: Al₂O₃”. In: *JOSA B* 3.1 (1986), pp. 125–133.
- [37] WR Rapoport and Chandra P Khattak. “Titanium sapphire laser characteristics”. In: *Applied optics* 27.13 (1988), pp. 2677–2684.
- [38] John M Eggleston, Larry G Deshazer, and Kenneth W Kangas. “Characteristics and kinetics of laser-pumped Ti: sapphire oscillators”. In: *IEEE journal of quantum electronics* 24.6 (1988), pp. 1009–1015.
- [39] RV Ambartzumian and VS Letokhov. “Selective two-step (STS) photoionization of atoms and photodissociation of molecules by laser radiation”. In: *Applied optics* 11.2 (1972), pp. 354–358.

- [40] George S Hurst, Marvin G Payne, and Edward B Wagner. *Resonance ionization for analytical spectroscopy*. US Patent 3,987,302. Oct. 1976.
- [41] VS Letokhov and VI Mishin. "Highly selective multistep ionization of atoms by laser radiation". In: *Optics Communications* 29.2 (1979), pp. 168–171.
- [42] GS Hurst et al. "Resonance ionization spectroscopy and one-atom detection". In: *Reviews of Modern Physics* 51.4 (1979), p. 767.
- [43] K Wendt et al. "Progress of ultra trace determination of technetium using laser resonance ionization mass spectrometry". In: *Analytical and Bioanalytical Chemistry* 404.8 (2012), pp. 2173–2176.
- [44] BH Isselhardt et al. "Improved precision and accuracy in quantifying plutonium isotope ratios by RIMS". In: *Journal of Radioanalytical and Nuclear Chemistry* 307.3 (2016), pp. 2487–2494.
- [45] VN Fedosseev, Yu Kudryavtsev, and VI Mishin. "Resonance laser ionization of atoms for nuclear physics". In: *Physica Scripta* 85.5 (2012), p. 058104.
- [46] N Lecesne et al. "GISELE: A resonant ionization laser ion source for the production of radioactive ions at GANIL a". In: *Review of Scientific Instruments* 81.2 (2010), 02A910.
- [47] Tobias Kron et al. "High efficiency resonance ionization of palladium with Ti: sapphire lasers". In: *Journal of Physics B: Atomic, Molecular and Optical Physics* 49.18 (2016), p. 185003.
- [48] P Müller et al. "⁴¹Ca ultratrace determination with isotopic selectivity > 10¹² by diode-laser-based RIMS". In: *Fresenius' journal of analytical chemistry* 370.5 (2001), pp. 508–512.
- [49] Joseph John Thomson. "XXVI. Rays of positive electricity". In: *The London, Edinburgh, and Dublin Philosophical Magazine and Journal of Science* 21.122 (1911), pp. 225–249.
- [50] Francis William Aston. "LXXIV. A positive ray spectrograph". In: *The London, Edinburgh, and Dublin Philosophical Magazine and Journal of Science* 38.228 (1919), pp. 707–714.
- [51] Jürgen H Gross. *Massenspektrometrie: Ein Lehrbuch*. Springer-Verlag, 2012.
- [52] E de Hoffmann, J Charette, and V Stroobant. "Mass spectrometry: principles and applications". In: (1996).
- [53] AJ Dempster. "A new method of positive ray analysis". In: *Physical Review* 11.4 (1918), p. 316.
- [54] W Paul and H Steinwedel. "A new mass spectrometer without a magnetic field". In: *Zeitschrift fuer Naturforschung (West Germany) Divided into Z. Naturforsch., A, and Z. Naturforsch., B: Anorg. Chem., Org. Chem., Biochem., Biophys.*, 8 (1953).
- [55] Wolfgang Paul. "Electromagnetic traps for charged and neutral particles (Nobel lecture)". In: *Angewandte Chemie International Edition in English* 29.7 (1990), pp. 739–748.
- [56] Sebastian Raeder et al. "Detection of plutonium isotopes at lowest quantities using in-source resonance ionization mass spectrometry". In: *Analytical and Bioanalytical Chemistry* 404.8 (2012), pp. 2163–2172.
- [57] DA Fink et al. "First application of the Laser Ion Source and Trap (LIST) for on-line experiments at ISOLDE". In: *Nuclear Instruments and Methods in Physics Research Section B: Beam Interactions with Materials and Atoms* 317 (2013), pp. 417–421.
- [58] RP De Groote et al. "Use of a continuous wave laser and pockels cell for sensitive high-resolution collinear resonance ionization spectroscopy". In: *Physical review letters* 115.13 (2015), p. 132501.
- [59] Igor V Veryovkin et al. "Mass spectrometry on the nanoscale with ion sputtering based techniques: What is feasible". In: *Nuclear Instruments and Methods in Physics Research Section B: Beam Interactions with Materials and Atoms* 261.1 (2007), pp. 508–511.
- [60] Hans Oechsner. "Secondary neutral mass spectrometry (SNMS)-recent methodical progress and applications to fundamental studies in particle/surface interaction". In: *International journal of mass spectrometry and ion processes* 143 (1995), pp. 271–282.

- [61] Roland Erich Horn. “Aufbau eines Systems gepulster, abstimmbarer Festkörperlaser zum Einsatz in der Resonanzionisations-Massenspektrometrie”. PhD thesis. Johannes Gutenberg-Universität Mainz, 2003.
- [62] Christoph Mattolat. “Spektroskopische Untersuchungen an Technetium und Silizium-Ein Festkörperlaser-System für die Resonanzionisationsspektroskopie”. PhD thesis. Johannes Gutenberg-Universität Mainz, 2010.
- [63] Pascal Naubereit. “Weiterentwicklung eines weitabstimmbaren Titan:Saphir-Lasers und sein Einsatz zur Spektroskopie hochliegender Resonanzen in Holmium”. Master thesis. Johannes Gutenberg-Universität Mainz.
- [64] Tobias Kron. “Pushing the Limits of Resonance Ionization Mass Spectrometry - Ionization Efficiency in Palladium and Spectral Resolution in Technetium”. PhD thesis. Johannes Gutenberg-Universität Mainz, 2016.
- [65] Sebastian Rothe. “An all-solid state laser system for the laser ion source RILIS and in-source laser spectroscopy of astatine at ISOLDE/CERN”. PhD thesis. Johannes Gutenberg-Universität Mainz, 2012.
- [66] Pascal Naubereit. “Resonatorinterne Frequenzverdopplung eines gepulsten Titan:Saphir-Lasers”. Bachelor thesis. Johannes Gutenberg-Universität Mainz.
- [67] Felix Kollmer et al. “Ultra high spatial resolution SIMS with cluster ions—approaching the physical limits”. In: *Surface and Interface Analysis* 45.1 (2013), pp. 312–314.
- [68] E Niehuis et al. “Analysis of organic multilayers and 3D structures using Ar cluster ions”. In: *Surface and Interface Analysis* 45.1 (2013), pp. 158–162.
- [69] Ewald Niehuis et al. “Dual beam depth profiling of organic materials: assessment of capabilities and limitations”. In: *Surface and Interface Analysis* 46.S1 (2014), pp. 70–73.
- [70] S Kayser et al. “Surface spectrometry using large argon clusters”. In: *Surface and Interface Analysis* 45.1 (2013), pp. 131–133.
- [71] Florian Martin Engelberger. “Adaption einer kommerziellen Flugzeit-Sekundärionen-Massenspektrometer-Apparatur zur Lasernachionisierung der zerstäubten Neutralteilchen”. Diploma thesis. Johannes Gutenberg-Universität Mainz.
- [72] Jens Steinhoff. “Entwicklung und Aufbau eines Flugzeitmassenspektrometers mit optimierter Akzeptanz und Transmission für den hocheffizienten Nachweis durch Ionenebeschuss zerstäubter Neutralteilchen nach resonanter Lasernachionisierung”. PhD thesis. Westfälische Wilhelms-Universität Münster, 2004. ISBN: 3-8334-2485-0.
- [73] MJ Pellin et al. “Sensitive, low damage surface analysis using resonance ionization of sputtered atoms”. In: *Nuclear Instruments and Methods in Physics Research Section B: Beam Interactions with Materials and Atoms* 18.1-6 (1986), pp. 445–451.
- [74] Z Ma et al. “New instrument for microbeam analysis incorporating submicron imaging and resonance ionization mass spectrometry”. In: *Review of scientific instruments* 66.5 (1995), pp. 3168–3176.
- [75] Igor V Veryovkin et al. “A new time-of-flight instrument for quantitative surface analysis”. In: *Nuclear Instruments and Methods in Physics Research Section B: Beam Interactions with Materials and Atoms* 219 (2004), pp. 473–479.
- [76] Andrew M Davis et al. “Nuclear astrophysics with CHILL, the CHicago Instrument for Laser Ionization”. In: *Proceedings of Nuclei in the Cosmos XIII* (2014).
- [77] Quentin P Vanbellingen et al. “Time-of-flight secondary ion mass spectrometry imaging of biological samples with delayed extraction for high mass and high spatial resolutions”. In: *Rapid Communications in Mass Spectrometry* 29.13 (2015), pp. 1187–1195.
- [78] JLS Lee et al. “Topography and field effects in the quantitative analysis of conductive surfaces using ToF-SIMS”. In: *Applied Surface Science* 255.4 (2008), pp. 1560–1563.
- [79] Igor V Veryovkin, Wallis F Calaway, and Michael J Pellin. “Calculating time-of-flight spectra of post-ionized sputtered neutrals”. In: *Nuclear Instruments and Methods in Physics Research Section B: Beam Interactions with Materials and Atoms* 219 (2004), pp. 1051–1057.

- [80] Bruce A Bushaw et al. "Triple-resonance autoionization of uranium optimized for diode laser excitation". In: *Spectrochimica Acta Part B: Atomic Spectroscopy* 62.5 (2007), pp. 485–491.
- [81] Sebastian Raeder. "Spurenanalyse von Aktiniden in der Umwelt mittels Resonanzionisationsmassenspektrometrie". PhD thesis. Johannes Gutenberg-Universität Mainz, 2010.
- [82] Michael Franzmann. "Resonanzionisations-Massenspektrometrie an Aktiniden mit der Mainzer Atomstrahlquelle MABU". Diploma thesis. Johannes Gutenberg-Universität Mainz, 2013.
- [83] Nicole Erdmann et al. "Resonance and nonresonant laser ionization of sputtered uranium atoms from thin films and single microparticles: Evaluation of a combined system for particle trace analysis". In: *Analytical Chemistry* 75.13 (2003), pp. 3175–3181.
- [84] David Willingham et al. "RIMS analysis of ion induced fragmentation of molecules sputtered from an enriched U3O8 matrix". In: *Journal of Radioanalytical and Nuclear Chemistry* 296.1 (2013), pp. 407–412.
- [85] Ylva Ranebo et al. "Production and Characterization of Monodisperse Plutonium, Uranium, and Mixed Uranium- Plutonium Particles for Nuclear Safeguard Applications". In: *Analytical Chemistry* 82.10 (2010), pp. 4055–4062.
- [86] Ronald Middendorp et al. "Characterization of the Aerosol-Based Synthesis of Uranium Particles as a Potential Reference Material for Microanalytical Methods". In: *Analytical Chemistry* 89.8 (2017), pp. 4721–4728.
- [87] KB Knight et al. "Uranium resonance ionization mass spectrometry in natural U-silicate". In: *Proc. Radiochim. Acta* 1 (2011), p. 37.
- [88] C Grüning et al. "Resonance ionization mass spectrometry for ultratrace analysis of plutonium with a new solid state laser system". In: *International Journal of Mass Spectrometry* 235.2 (2004), pp. 171–178.
- [89] Klaus Wendt and Norbert Trautmann. "Recent developments in isotope ratio measurements by resonance ionization mass spectrometry". In: *International Journal of Mass Spectrometry* 242.2 (2005), pp. 161–168.
- [90] Annika Voss et al. "High-resolution laser spectroscopy of long-lived plutonium isotopes". In: *Physical Review A* 95.3 (2017), p. 032506.
- [91] C Mattolat et al. "Determination of the first ionization potential of technetium". In: *Physical Review A* 81.5 (2010), p. 052513.
- [92] N Winograd, JP Baxter, and FM Kimock. "Multiphoton resonance ionization of sputtered neutrals: a novel approach to materials characterization". In: *Chemical Physics Letters* 88.6 (1982), pp. 581–584.
- [93] F Kollmer et al. "Nonresonant Laser–SNMS and TOF–SIMS analysis of sub- μm structures". In: *Applied surface science* 203 (2003), pp. 238–243.
- [94] Douglas E Goeringer, Warner H Christie, and Robert E Valiga. "Investigation of matrix effects on the neutral fractions ejected from ion-bombarded, uranium-containing solids using resonance ionization mass spectrometry". In: *Analytical Chemistry* 60.4 (1988), pp. 345–349.
- [95] Fabio Schwellnus. "Entwicklung von Ionenquellen zur Optimierung von Selektivität und Effizienz bei der resonanten Laserionisation". PhD thesis. Johannes Gutenberg-Universität Mainz, 2010.
- [96] N Erdmann et al. "Resonance ionization mass spectrometry for element- and isotope-selective trace analysis of actinides in environmental micro-particles". In: *Recent Advances in Actinide Science. ACTINIDES 2005*. Ed. by R Al-varez, N D Bryan, and I May. Vol. 305. 1. Royal Society of Chemistry, 2006, pp. 122–124. ISBN: 978-0-85404-678-2.
- [97] Mohammad R Tanha et al. "Measurements in AFGHANISTAN using an active radon exposure meter and assessment of related annual effective dose". In: *Radiation protection dosimetry* 178.1 (2017), pp. 122–130.
- [98] Linda Hamann. "Untersuchung radioaktiver Partikel mittels Sekundärionen-Flugzeit-Massenspektrometrie". PhD thesis. Leibniz Universität Hannover, 2017.

- [99] Mohammad Rahmatullah Tanha. "Environmental radioactivity studies in Kabul and northern Afghanistan". PhD thesis. Gottfried Wilhelm Leibniz University Hannover, 2017.
- [100] Hauke Bosco. "Erarbeitung eines Anregungsschemas zum Strontiumnachweis mittels resonanter Laser-SNMS". Master thesis. Leibniz Universität Hannover, 2016.

LIST OF PUBLICATIONS

Articles in preparation

- M. Franzmann, H. Bosco, L. Hamann, C. Walther and K. Wendt. "Resonant Laser-SNMS for spatially resolved and element selective ultra-trace analysis of radionuclides". In: *Journal of Analytical Atomic Spectrometry* (2018), in print.

Published articles

- M. Franzmann, H. Bosco, C. Walther and K. Wendt. "A new resonant Laser-SNMS system for environmental ultra-trace analysis: Installation and optimization." *International Journal of Mass Spectrometry* 423 (2017): 27-32.
- P. Naubereit, J. Marín-Sáez, F. Schneider, A. Hakimi, M. Franzmann, T. Kron, S. Richter and K. Wendt. "Resonance ionization spectroscopy of sodium Rydberg levels using difference frequency generation of high-repetition-rate pulsed Ti: sapphire lasers". 2016. *Physical Review A*, 93(5), 052518.
- M. Roth, M. Franzmann, M. D'Acunzi, M. Kreiter and G. K. Auernhammer. "Experimental analysis of single particle deformations and rotations in colloidal and granular systems". 2011. arXiv preprint arXiv:1106.3623.

CURRICULUM VITAE

Dipl.-Phys.

Michael Franzmann

Adresse: Dieter-Schro-Weg 6, 55128 Mainz
Geboren: 07.02.1985 in Kirn
Staatsangehörigkeit: deutsch
Familienstand: ledig

Ausbildung

05/2017-today Promotion, Fachrichtung: Physik
Leibniz Universität Hannover
Titel der Arbeit: "A New Tool for Ultra-Trace Analysis of Radionuclides -
Setup, Optimization and Characterization of the Resonant
Laser-SNMS System for IRS Hannover"
06/2013-04/2017 Promotionsversuch, Fachrichtung: Physik
Johannes Gutenberg-Universität Mainz
Abbruch wegen prüfungsbedingtem Wechsel der Hochschule
10/2007-06/2013 Diplom-Studium, Studiengang: Physik
Johannes Gutenberg-Universität Mainz
Titel der Arbeit: "Resonanzionisations-Massenspektrometrie an
Aktiniden mit der Mainzer Atomstrahlquelle MABU"
09/2004-06/2007 Abitur
Ketteler-Kolleg Mainz

Berufserfahrung

07/2017-today Entwicklungsingenieur
iC-Haus-GmbH, Bodenheim
06/2013-06/2017 Wissenschaftlicher Mitarbeiter in Rahmen eines Stipendiums
Institut für Radioökologie & Strahlenschutz, Leibniz Universität Hannover &
Institut für Physik, Johannes Gutenberg-Universität Mainz
07/2011-01/2012 Wissenschaftliche Hilfskraft
Institut für Physik, Johannes Gutenberg-Universität Mainz
07/2009-08/2010 Wissenschaftliche Hilfskraft
Max-Planck-Institut für Polymerforschung, Mainz
09/2001-07/2004 Ausbildung als Energieanlagenelektroniker
Procter & Gamble Manufacturing GmbH, Mainz

ACKNOWLEDGMENTS

Die Ziele, die im Rahmen dieser Doktorarbeit erreicht wurden, wären ohne die Unterstützung vieler Kollegen und Kolleginnen nie in dieser Form umsetzbar gewesen, weshalb ich allen Beteiligten vielmals danken will.

Allen voran danke ich meinen Doktorvätern Prof. Clemens Walther und Prof. Klaus Wendt dafür die Projektidee entwickelt und zu einem gut durchdachten Forschungsprojekt ausgearbeitet zu haben. Bei der Gestaltung von Arbeitsabläufen und Messreihen, sowie der Entwicklung des experimentellen Messsystems wurden mir von beiden großzügige Freiräume gelassen, wodurch es mir möglich war eigene Ideen vollständig umzusetzen. Gleichmaßen konnte ich mich bei auftretenden Problemen auf ihre Hilfsbereitschaft und Expertise verlassen. Allerdings ist das Gelingen dieser Forschungsarbeit auch den Anregungen und der Mitarbeit vieler Kollegen, sowohl der Arbeitsgruppe LARISSA an der Johannes Gutenberg-Universität Mainz als auch des Instituts für Radioökologie und Strahlenschutz an der Leibniz Universität Hannover zu verdanken. Die Entwicklung des Lasersystems wurde maßgeblich durch Diskussionen und Erfahrungsaustausch mit Tobias Kron und Fabian Schneider aus Mainz beeinflusst. Der Aufbau und die Lösung vieler technischer Probleme wurde durch die Hilfe von Sebastian Büchner und der mechanischen Werkstatt des IRS sehr beschleunigt. Linda Hamann, Michael Steppert, Wolfgang Schulz und Claudia Fournier haben mich nach der Inbetriebnahme des Laser-SNMS-Systems in Hannover mit Anregungen zur Analytik radioaktiver Proben unterstützt. Für die meiste Unterstützung bedanke ich mich ohne Zweifel bei Hauke Bosco, der parallel zu dieser Doktorarbeit seine Masterarbeit am Laser-SNMS-System am IRS durchgeführt hat und dieses inzwischen als Doktorand betreut.

Sowohl am Institut für Physik in Mainz als auch am Institut für Radioökologie und Strahlenschutz in Hannover habe ich im Rahmen dieser Doktorarbeit zwei Jahre verbracht und war dabei von vielen großartigen und hilfsbereiten Menschen umgeben, die den wissenschaftlichen Alltag auch durch nicht-wissenschaftliche Aktivitäten bereichert haben. Daher bedanke ich mich bei allen Teilnehmern der morgendlichen Kaffeerunde in Hannover und allen aktiven Kickerspielern in Mainz.

Der Aufbau eines großen experimentellen Systems und die Beschäftigung eines Doktoranden erfordern eine entsprechende Finanzierung. Hierfür möchte ich zum Einen dem Bundesministerium für Bildung und Forschung danken, das im Rahmen des Verbundprojekts SIRIUS Anschaffung und Aufbau des Laser-SNMS-Systems ermöglichte. Zum Anderen danke ich der Siebold-Sasse-Stiftung, die mir neben meinem Stipendium die Teilnahme an mehreren internationalen Konferenzen ermöglichte.

Abschließend danke ich meiner Familie und meinen Freunden für die fortwährende Unterstützung und Rückhalt während der Promotion. Insbesondere danke ich meiner Freundin Sabrina, die trotz zwischenzeitlichem räumlichem Abstand immer für mich da war und Stress und Frust, die gelegentlich in einer Promotion auftreten, abgemildert hat.